

Wet-chemical synthesis of mono- and bimetallic nanoparticles of group VIII to XI metals and their detailed characterisation

Dissertation

Zur Erlangung des akademischen Grades eines

Doktors der Naturwissenschaften

- Dr. rer. nat. -

vorgelegt von

Alexander Rostek

Fakultät für Chemie

Institut für Anorganische Chemie

Universität Duisburg-Essen

2019

DuEPublico

Duisburg-Essen Publications online

UNIVERSITÄT
DUISBURG
ESSEN

Offen im Denken

ub | universitäts
bibliothek

Diese Dissertation wird über DuEPublico, dem Dokumenten- und Publikationsserver der Universität Duisburg-Essen, zur Verfügung gestellt und liegt auch als Print-Version vor.

DOI: 10.17185/duepublico/70267

URN: urn:nbn:de:hbz:464-20190705-105906-3

Alle Rechte vorbehalten.

“The greatest challenge of knowledge is not ignorance; it is the illusion of knowledge.”

- Stephen William Hawking (*1942 - †2018) -

Die vorliegende Arbeit ist im Zeitraum von April 2016 bis März 2019 im Arbeitskreis von Prof. Dr. Matthias Epple im Institut für Anorganische Chemie an der Fakultät für Chemie der Universität Duisburg-Essen angefertigt worden.

1. Gutachter: Prof. Dr. Matthias Epple
2. Gutachter: Prof. Dr. Stephan Barcikowski

Vorsitzender: Prof. Dr. Sebastian Schlücker

vorgelegt von: Alexander Rostek

vorgelegt am: 12.03.2019

Tag der Disputation: 28.06.2019

List of contents

List of abbreviations	IV
Abstract.....	7
German Abstract.....	8
1 Introduction	10
2 Theoretical background.....	14
2.1 Colloids	14
2.2 Synthesis of nanoparticles.....	15
2.3 Stability of colloids	16
2.4 Crystallisation and growth	17
2.5 Metal nanoparticles	18
2.5.1 Noble metals and their physico-chemical properties.....	19
2.5.2 Optical properties of metal nanoparticles - Surface plasmon resonance (SPR).....	20
2.5.3 Bimetallic nanostructures and galvanic replacement	21
3 Methods.....	23
3.1 Dynamic light scattering (DLS) and Zeta Potential.....	23
3.2 Differential centrifugal sedimentation analysis (DCS).....	26
3.3 Ultraviolet-visible spectroscopy (UV/vis)	27
3.4 Atomic absorption spectrometry (AAS)	27
3.5 Electron microscopy	28
3.5.1 High-resolution transmission electron microscopy (HR-TEM) 29	
3.5.2 High-angle annular dark field (HAADF) imaging	30
3.5.3 Energy dispersive X-ray spectroscopy (EDX)	30
3.6 X-ray powder diffraction (PXRD).....	31
4 Results and discussion	34
4.1 Characterisation of monometallic nanoparticles of the platinum and coin metals group (4-8 nm).....	34
4.1.1 Ruthenium nanoparticles	35
4.1.2 Rhodium nanoparticles	43
4.1.3 Palladium nanoparticles.....	52

4.1.4	Silver nanoparticles	60
4.1.5	Osmium nanoparticles	68
4.1.6	Iridium nanoparticles	75
4.1.7	Platinum nanoparticles.....	82
4.1.8	Gold nanoparticles	90
4.1.9	Summary	97
4.2	Characterisation of bimetallic Pd-Au nanoparticles	104
4.2.1	Bimetallic AuPd (alloyed) nanoparticles by simultaneous reduction	105
4.2.3	Pd-Au core-shell nanoparticles by sequential reduction	109
4.2.2	Au-Pd core-shell nanoparticles by sequential reduction	122
4.2.4	Summary	131
4.3	Characterisation of bimetallic Ag-Pd nanoparticles	138
4.3.1	Bimetallic AgPd (alloyed) nanoparticles by simultaneous reduction	139
4.3.2	Ag-Pd core-shell nanoparticles by sequential reduction	145
4.3.3	Pd-Ag core-shell nanoparticles by sequential reduction	151
4.3.4	Summary	157
5	Experimental section.....	158
5.1	Chemicals.....	158
5.2	Software / Databases.....	162
5.3	Devices.....	163
5.4	Synthesis	165
5.4.1	Synthesis of monometallic Ru, Rh, Pd, Os, Ir, and Pt nanoparticles with <i>D</i> -glucose	165
5.4.2	Synthesis of monometallic Ag nanoparticles with sodium borohydride.....	167
5.4.3	Synthesis of monometallic Au nanoparticles with trisodium citrate and tannic acid	168
5.4.4	Synthesis of bimetallic AuPd alloyed nanoparticles	171
5.4.5	Synthesis of bimetallic Pd-Au core-shell nanoparticles	172
5.4.6	Synthesis of bimetallic Au-Pd core-shell nanoparticles	173
5.4.7	Synthesis of bimetallic AgPd (alloyed) nanoparticles.....	174
5.4.8	Synthesis of Ag-Pd core-shell nanoparticles	175

5.4.9	Synthesis of Pd-Ag core-shell nanoparticles	176
6	Conclusion	177
7.	Summary	181
8.	German Summary	183
9.	Appendix	185
9.1	List of publications	185
9.2	List of scientific conferences, poster contributions and oral presentations	187
9.3	Curriculum vitae	189
9.4	Acknowledgement	191
9.5	Statutory declaration / Eidesstaatliche Erklärung	193
10.	References	194

List of abbreviations

AAS:	Atomic absorption spectrometry
acac:	Acetylacetonate
ADC:	Analytical disc centrifugation
at%:	Atom percent
BSE:	Backscattered electrons
COD:	1,5-cyclooctadiene
COT:	1,3,5-cyclooctatriene
Da:	Dalton
DCS:	Differential centrifugal sedimentation
DFG:	Deutsche Forschungsgemeinschaft
DIN:	Deutsches Institut für Normung e.V.
DLS:	Dynamic light scattering
DLVO:	Derjaguin, Landau, Verwey, and Overbeek
EELS:	Electron energy loss spectroscopy
EDX:	Energy dispersive X-ray spectroscopy
EN:	European Norms
fcc:	Face-centred cubic
FCS	Fetal calf serum
FWHM:	Full width at half maximum
HAADF:	High-angle annular dark field
h:	Hour(s)
hcp:	Hexagonal close packed

hMSC:	Human mesenchymal stem cells
HOMO:	Highest occupied molecular orbital
HR-TEM:	High-resolution transmission electron microscopy
IEC:	International Electrotechnical Commission
ISO:	International Organisation of Standardisation
K:	Kelvin
LFS:	Liquid flame spray
LUMO:	Lowest unoccupied molecular orbital
min:	Minute(s)
mol%:	Mole percent
MWCO:	Molecular weight cut-off
NIST:	National Institute of Standards and Technology
OA:	Oleic acid
OAm:	Oleylamine
OD:	Octadecene
PAA:	Poly(acrylic acid)
p.a.:	Pro analysis, analytical reagent grade
PDF:	Powder diffraction file
PdI:	Polydispersity index
PE:	Primary electrons
PEI:	Polyethyleneimine
PLAL:	Pulsed laser ablation in liquids
PSS:	Polystyrene sulfonate
PVA:	Polyvinyl alcohol
PVC:	Poly(vinyl chloride)

PVP:	Poly(<i>N</i> -vinylpyrrolidone)
PXRD:	Powder X-ray diffraction
ROS:	Reactive oxygen species
rpm:	Rounds per minute
RPMI	Roswell Park Memorial Institute
SAXS:	Small-angle X-ray scattering
SE:	Secondary electrons
SEM:	Scanning electron microscopy
SERS:	Surface-enhanced Raman scattering or spectroscopy
SPR:	Surface plasmon resonance
STEM:	Scanning transmission electron microscopy
TEM:	Transmission electron microscopy
TOP:	Trioctylphosphine
TPPTS:	Tris(sodium- <i>m</i> -sulfonato-phenyl)phosphine
UV/vis:	Ultraviolet-visible
wt%:	Weight percent

Abstract

Nanotechnology has become increasingly important in recent decades and nanomaterials are widely used nowadays. In industrial applications, electronics and catalysis the use of noble metal nanoparticles enable higher performance and selectivity. Considering the medical use, the increasing resistance of bacteria against antibiotics is one of the main problems, which might be resolved by the development of new nanobased antimicrobial mechanisms. Bimetallic nanostructures might reveal a promising mechanism to suspend the careless use of antibiotics. For the investigation and further study of physical, mechanical, and chemical properties as well as the biological, antimicrobial and toxicological action of nanomaterials, especially bimetallic (core-shell, alloy) nanoparticles, well-characterised nanoparticles of the corresponding single metals are promising to allow a careful and accurate evaluation and comparison. The fundamental prerequisites are equal sizes, shapes and surface functionalisation of these nanoparticles. First, spherical Ru, Rh, Pd, Ag, Os, Ir, Pt, and Au nanoparticles (4 to 8 nm) were prepared in aqueous media, stabilised with poly(*N*-vinylpyrrolidone) (PVP), and characterised in a comprehensive way. In addition, a comparative cytotoxicity study on human mesenchymal stem cells (hMSCs) after exposure to selected nanoparticles (Rh, Pd, Ag, Pt, Au) was carried out to determine their biological effects. Furthermore, spherical bimetallic nanostructures (4 to 8 nm, alloy and core-shell) of gold and palladium as well as silver and palladium with a nominal molar ratio of 50:50 at% (*n/n*) were wet-chemically synthesised and functionalised with PVP. The detailed characterisation and the confirmation of the bimetallic character were performed by scanning transmission electron microscopy (STEM) including high-angle annular dark field (HAADF) imaging and elemental mapping from energy-dispersive X-ray spectroscopy (EDX). In general, the size and morphology of the nanoparticles were determined by dynamic light scattering (DLS), differential centrifugal sedimentation (DCS) analysis, and high-resolution transmission electron microscopy (HR-TEM). Furthermore, the ultra- and microstructure of obtained particles were investigated by X-ray powder diffraction (PXRD) and an extensive analysis by Rietveld refinement.

German Abstract

Die Nanotechnologie hat in den letzten Jahrzehnten an Bedeutung gewonnen und Nanomaterialien sind heutzutage weit verbreitet. In industriellen Anwendungen, in der Elektronik und in der Katalyse ermöglicht der Einsatz von Edelmetallnanopartikeln eine höhere Leistungsfähigkeit und Selektivität. In Anbetracht der medizinischen Verwendung ist die zunehmende Resistenz von Bakterien gegen Antibiotika eines der Probleme, das durch die Entwicklung neuer nanobasierter antimikrobieller Mechanismen gelöst werden könnte. Bimetallische Nanostrukturen könnten einen vielversprechenden Mechanismus zur Einstellung des unachtsamen Einsatzes von Antibiotika aufzeigen. Für die Untersuchung und weitere Untersuchung der physikalischen, mechanischen und chemischen Eigenschaften sowie der biologischen, antimikrobiellen und toxikologischen Wirkung von Nanomaterialien, insbesondere von bimetallischen Nanopartikeln (Core-Shell und Legierungen), sind gut charakterisierte Nanopartikel der entsprechenden Einzelmetalle geeignet vielversprechend, um eine sorgfältige und genaue Bewertung und einen Vergleich zu ermöglichen. Grundvoraussetzung sind vollkommen gleiche Größen, Formen und Oberflächenfunktionalisierung dieser Nanopartikel. Zunächst wurden kugelförmige Ru-, Rh-, Pd-, Ag-, Os-, Ir-, Pt- und Au-Nanopartikel (4 bis 8 nm) in wässrigem Medium hergestellt, mit Poly (N-vinylpyrrolidon) (PVP) stabilisiert und umfassend charakterisiert. Darüber hinaus wurde eine vergleichende Zytotoxizitätsstudie an humanen mesenchymalen Stammzellen (hMSCs) nach Exposition gegenüber ausgewählten Nanopartikeln (Rh, Pd, Ag, Pt, Au) durchgeführt, um deren biologischen Wirkungen zu bestimmen. Des Weiteren wurden sphärische bimetallische Nanostrukturen (4 bis 8 nm, Legierung und Kern-Schale Partikel) aus Gold und Palladium sowie Silber und Palladium mit einem nominalen Molverhältnis von 50:50 at% (n/n) nasschemisch synthetisiert und mit PVP funktionalisiert. Die detaillierte Charakterisierung und die Bestätigung des bimetallischen Charakters wurden durch Rastertransmissionselektronenmikroskopie (STEM) durchgeführt, einschließlich spezieller Abbildungstechniken (engl. *High-angle annular dark field imaging*, HAADF) und der Elementbestimmung aus der energie-dispersive Röntgenspektroskopie (EDX). Im Allgemeinen wurde Größe und Morphologie der Nanopartikel durch dynamische Lichtstreuung (DLS), differentielle zentrifugale Sedimentationsanalyse (DCS) und hochauflösende Transmissionselektronenmikroskopie (HR-TEM) bestimmt.

Außerdem wurde die Ultra- und Mikrostruktur der erhaltenen Partikel durch Röntgenpulverdiffraktometrie (PXRD) und eine umfangreiche Analyse durch Rietveld-Verfeinerung untersucht.

1 Introduction

Nanotechnology represents one of the key technologies of the 21st century. Today inorganic and metallic nanoparticles are widely used in medicine, industry, electronics, and catalysis.^[1-6] Noble metals like rhodium, palladium, iridium, platinum, silver and gold are of special interest due to their outstanding in optical sensing, nanocatalysis and electrocatalysis.^[7-11] Furthermore, nanoparticles of noble metals (Au, Pt, Pd, and Rh) have distinct catalytic properties in biology and are reported to show several enzyme-like activities *in vitro*, including reactive oxygen species scavenger activity.^[12-17] Bimetallic nanostructures with a core-shell composition as well as nanoalloys have numerous applications and open up new scientific fields due to their tuneable properties, e.g. in heterogeneous catalysis, electrocatalysis, magnetism, and biomedical applications.^[18-23] Compared to bulk materials, nanomaterials show size dependent chemical, physical, and optical properties and form the bridge between the atomic and the macroscopic scale. The decrease in size is related to the exponential increase of the surface to volume ratio, which results in higher surface energy. In addition, nanoparticles entail crystallographic (e.g. lattice contraction, defects), electronic (e.g. quantum dots), and optical (e.g. auto-fluorescence, surface plasmon resonance (SPR)) changes. Thermal properties (e.g. melting points) show a strong size dependence as well.^[24]

At the present day, a major challenge is the development of new bactericidal agents in (bio-) medicine because of increasing resistance of bacteria against antibiotics. Post-operative and implant-associated infections still present a great problem in clinical use.^[25] The inhibition of initial bactericidal colonisation of implant surfaces can prevent those infections and can reduce the hazard of biofilm generation.^[26] A viable approach might be the application of nanostructures of antibacterial active metals like silver or copper. The antimicrobial action of copper and silver is based on the oxidative release of Cu^{2+} and Ag^+ ions and is well studied.^[27, 28] The metal ions interact with numerous bacterial structures and damage them. They affect the intracellular metabolism and increase the generation of reactive oxygen species, which also destroy cellular and bacterial structures and molecules.^[29, 30] The bactericidal effect of silver correlates with the quantity of the released ions caused by oxidative processes.^[31-34] An enhanced silver ion release can be achieved by smaller particle sizes which correlates with an enlargement of the specific

surface area.^[35] Another possibility for an increased antibacterial performance is the combination of Ag with an electrochemical more noble metal (gold, platinum metals). This might accelerate the release kinetics and lead to higher Ag⁺ release by a sacrificial anode effect and an electrochemically polarisation of silver.^[36-38] Bimetallic nanostructures might constitute a promising approach to diminish the extensive use of antibiotics and open a field of new antimicrobial and bactericidal mechanisms.

For a detailed study of physical, biological and chemical properties of nanostructures, especially bimetallic (core-shell, alloy) nanoparticles, well-characterised nanoparticles of the corresponding single metals are necessary to allow a careful and accurate evaluation and comparison of the biological effects and antibacterial action. The fundamental prerequisite is a completely equal size, shape and surface functionalisation of these nanoparticles. Numerous physical and chemical methods to synthesize nanoparticles of the noble metals has been described in the literature.^[39-41] Chemical synthesis is generally based on the reduction of dissolved cationic metal species by appropriate reducing agents and subsequent stabilisation of the formed nanoparticles.^[2] A great challenge is the shape-controlled synthesis of noble metal nanostructures, e.g. spheres, rods, cubes or triangles that requires experimental approaches to control the nucleation, crystal growth, and colloidal stabilisation.^[5, 42-44] One of the most prominent methods is the polyol process. Representative characteristics are the use of compounds like ethylene glycol, which act as solvent, reducing, complexing, and stabilisation agent at the same time.^[45] In the last decade, laser ablation and other physical methods have become increasingly importance.^[46]

Bimetallic nanoparticles like core-shell nanostructures and nanoalloys represent an important material class in heterogeneous catalysis, electrocatalysis, magnetism, and biomedical applications.^[18-23, 47] Specifically, bimetallic nanostructures consisting of palladium and gold are of considerable interest in heterogeneous catalysis. Various reduction and oxidation reactions are catalysed by Pd-Au nanoparticles due to the modulated electronic and structural properties of palladium by alloying it with gold.^[48] Numerous theoretical and experimental reports of the Pd-Au system can be found in the literature ranging from alloyed particles to thin films. Non-porous as well as porous alloyed PdAu nanoparticles with a size of 50 to 60 nm in diameter can be synthesized by co-reduction in the presence of Cu²⁺ ions.^[49] A microwave-based polyol process leads to small (about 2.5 nm diameter) PdAu nanoalloys with variable composition for possible applications in catalytic hydrogenation of alkenes.^[50] Thin films of palladium and gold with a thickness

of 100 to 150 nm can be prepared by an electron-beam co-deposition approach which can be used for the electrocatalytic CO₂ reduction.^[51]

Two variants of bimetallic core-shell nanoparticles can be synthesised: Palladium core/gold shell (Pd-Au) and gold core/palladium shell (Au-Pd) structures. The preparation of the second system is easier prepared as a galvanic replacement of Pd by gold is avoided.^[48] This system is also of direct interest to palladium-based heterogeneous catalysis. Gold nanocubes with a layer of Pd and a full diameter down to 12 nm can be prepared using a seed-mediated a synthesis approach.^[52] Au-Pd core-shell nanostructures with different sizes and shapes can be prepared by a seeded-growth method and variation of the reaction parameters.^[53] *Spitale et al.* has reported a synthesis approach to prepare small Au-Pd core-shell nanoparticles (6 nm Au core, 2 nm Pd shell thickness) for the investigation of the structural behaviour using atomistic simulations.^[54] A galvanic replacement of the less noble Pd metal by gold ions must be avoided during the synthesis of Pd-Au core-shell nanoparticles. Here, the reducing agent must be properly chosen to protect the palladium core against oxidative etching. *Gopalan et al.* have studied the catalytic performance of Pd-Au core-shell nanostructures synthesised by a seed-mediated polyol process.^[55] Palladium nanocubes (~5 nm edge length) with a thin layer of gold (1-2 nm) can be prepared via controlled overgrowth approach using L-ascorbic acid in the presence of bromide ions as promoting capping agent.^[56] Furthermore, core-shell nanoparticles of Pd (5 nm) with a variation of the gold shell thickness (1-2 nm, depending on the reaction parameters) can be synthesised in non-aqueous media.^[57] The galvanic replacement of the less noble metal during the wet-chemical synthesis of bimetallic nanostructures represents a resolving problem. Considering the standard electrochemical potential for the redox reaction of both precursors, Na₂PdCl₄ and HAuCl₄ (Pd²⁺/Pd⁰: +0.915 V and Au³⁺/Au⁰: +1.498 V), the chloridopalladium complex as well as palladium are less noble than gold. Therefore, a galvanic replacement reaction can occur which leads to the oxidation of formed palladium clusters, seeds, or nanoparticles (Pd⁰ to Pd²⁺) and reduction of the ionic gold species (Au³⁺ to Au⁰). To avoid such a galvanic replacement, the reaction must be kinetically controlled using e.g. stronger reducing agents, higher temperatures, or reduced precursor concentrations.^[58-62]

Monodisperse AgPd alloyed nanoparticles can be obtained by co-reduction of silver nitrate and palladium chloride in the presence of oleylamine (OAm).^[63] Small AgPd nanoparticles (~2 nm) can be synthesised by gradually heating silver acetate and palladium(II) acetylacetonate (Pd(acac)₂) in oleic acid and 1-octadecene in the presence of OAm.^[64, 65]

An enrichment of palladium (up to 5 %) on a silver core can be obtained by an aqueous synthesis using citrate as reducing and stabilizing agent.^[66] Silver-palladium core-shell can be prepared by a successive reduction method using preformed Ag and Pd nanoparticles in the presence of sodium borohydride.^[67] A further method is the liquid flame spray (LFS) process, in which the Ag-Pd alloy particles can be generated in a high temperature aerosol.^[68]

The studies presented here are part of a collaboration project between the groups of Prof. Dr. Matthias Epple (Institute of Inorganic Chemistry, University Duisburg-Essen, Essen), Dr. Marc Heggen (Peter Grünberg Institute and Ernst-Ruska Centre for Microscopy and Spectroscopy with Electrons, Forschungszentrum Jülich, Jülich), Jun.-Prof. Dr. Christina Sengstock, and Prof. Dr. Manfred Köller (both Surgical Research, University Hospital Bergmannsheil/Ruhr-University Bochum, Bochum). The aim of the project is to synthesize uniform, spherical mono- and bimetallic nanoparticles of the platinum and coin metals (group VIII-XI) in the size range between 5 and 10 nm for structural investigation, cell biological, and antimicrobial studies. The focus of this thesis is the preparation of the desired nanostructures via different synthesis approaches and subsequent thorough characterisation by spectroscopic and colloid-chemical methods. The first part consists of the establishment of reproducible wet-chemical syntheses of spherical nanoparticles of group VIII to XI metals (Ru, Rh, Pd, Ag, Os, Ir, Pt, Au) with 5-10 nm diameter using different reducing agents, i.e. trisodium citrate, D-glucose, tannic acid, and sodium borohydride. The nanoparticles have the same surface functionalisation, in this case poly(*N*-vinylpyrrolidone) (PVP). The second and third part describes with wet-chemical syntheses of bimetallic nanostructures (alloy, core-shell) of two different noble metals (Au-Pd, Ag-Pd). Their detailed characterisation comprises colloid-chemical and spectroscopic methods like dynamic light scattering (DLS), differential centrifugal sedimentation analysis (DCS), UV/vis spectroscopy, and atomic absorption spectrometry (AAS). Furthermore, a detailed electron microscopy study is carried out including high-angle annular dark field imaging (HAADF) and energy-dispersive X-ray spectroscopy (EDX). X-ray powder diffraction (PXRD) and Rietveld refinement are performed to investigate the ultrastructure of the obtained nanoparticles.

2 Theoretical background

2.1 Colloids

Colloid science is concerned with the physical and chemical properties of dispersed systems and surface boundaries phenomena at the nanometre scale. Colloidal systems consist of small solid or liquid particles (10^{-9} m) which are homogeneously distributed in another phase, the dispersion medium. A general definition of the size range does not exist but it is usually applicable between one nm up to 500 nanometre.^[69, 70] A simple classification of colloids based on the aggregation state of the dispersion medium and the dispersed phase. Table 1 show the classes of colloidal systems in dependence of the aggregation state.

Table 1: Classification of colloidal systems based on the state of aggregation of the dispersed phase and the dispersion media. Adapted from reference.^[71]

Dispersed phase	Dispersion medium		
	Solid	Liquid	Gas
Solid	Solid sol	Sol	Solid aerosol
Liquid	Solid emulsion	Liquid emulsion	Liquid aerosol
Gas	Solid foam	Foam	---

According to a classification by *Staudinger*, the group of colloids can be roughly distinguished in three classes. The association or micellar colloids consist of micelles of homogeneously structured droplets. They are thermodynamically stable, hydrophilic colloids that are formed spontaneously by reversible association of tensides into micelles. The second class are molecular colloids of macromolecules. Similar to association colloids, they represent a thermodynamically stable, hydrophilic system of polymers, which build up spherical-like colloids. Unlike the micellar and the molecular colloids, the dispersion colloids are thermodynamically unstable, hydrophobic colloids with polydisperse size

distributions and different morphologies. Metallic nanoparticles are prominent representatives of such sub-group.^[72] In comparison to macroscopic objects, nanoparticles and colloids with the same volume have a significantly higher surface area. Due to their very high surface to volume ratio, they often have different physico-chemical properties. Because of the high surface energy, nanoparticulate systems are generally more reactive than the respective bulk material.^[73]

2.2 Synthesis of nanoparticles

In general, there are two different ways to synthesise nanomaterials: The top-down and the bottom-up method. First, the so-called top-down approach starts from a macroscopic object (bulk material) from which nanoscopic particles are generated by the use of physical forces. The most prominent and common method is the grinding of bulk materials by classical milling processes.^[74]

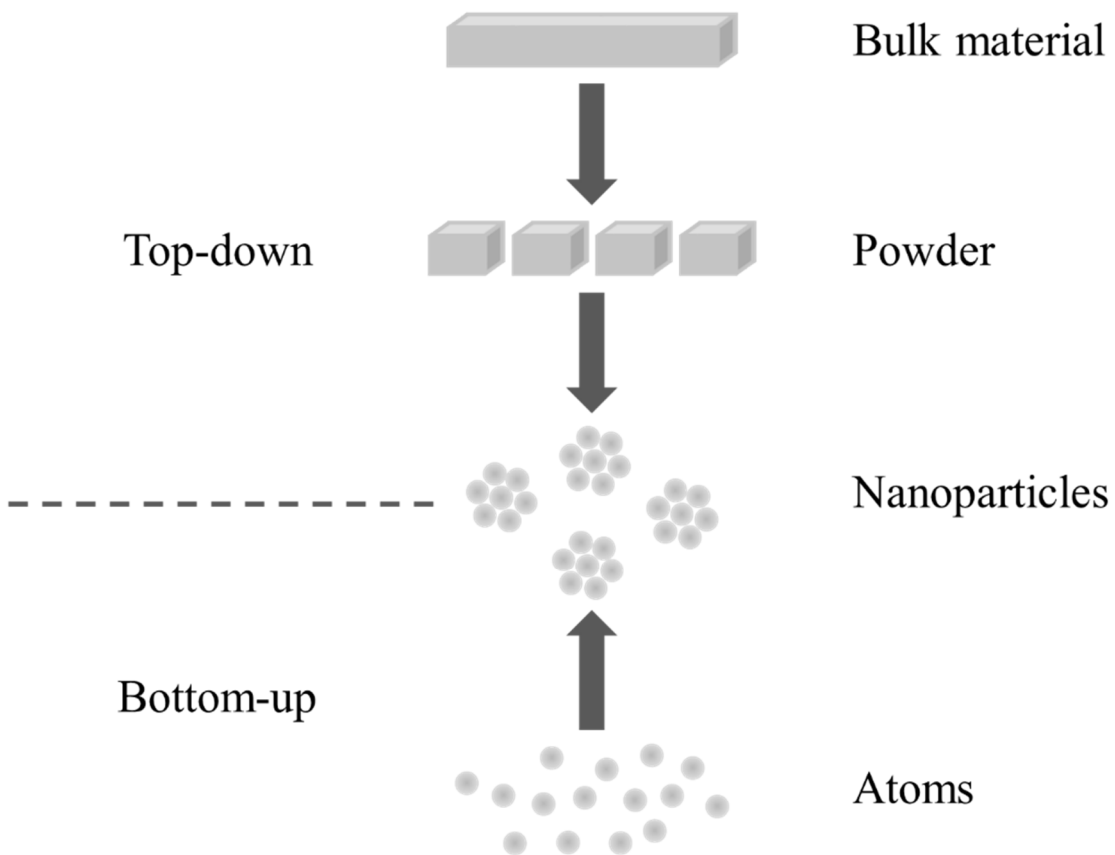


Figure 1: Scheme of nanomaterials generation by a top-down and bottom-up approach.

A second, prominent top-down method is the laser ablation where the macroscopic material is vaporized in a cavitation bubble and forms clusters and nanoparticles.^[75-77] In contrast, the bottom-up approach starts from a molecular or atomic state by reduction of ionic species in solution. All approaches have their own limitations and advantages particularly in terms of the size and morphology control. Milling processes have a high performance, but it is almost not possible to control the size and morphology of the particles. High yields can also be reached in a short time-range by pulsed laser ablation in liquids (PLAL). The size distribution of particles obtained by PLAL is quite broad and an additional and time-consuming separation step (e.g. centrifugation or sedimentation) is necessary. Furthermore, only spherical-like particles can be generated due to the lack of morphology control. If the reaction parameters are thoroughly controlled, the reduction of ionic precursors in liquid phase leads to well-defined nanostructures (e.g. spheres, cubes, rods) and a quite narrow size distribution. However, the performance and yield of such bottom-up approaches are comparatively small due to limitations in the reaction and purification steps.

2.3 Stability of colloids

The stability of colloidal systems can be described as an interplay of forces such as van der Waals attraction, double-layer repulsion, and steric interaction. The fundamental theory is described by the works of Derjaguin and Landau^[78] and Verwey and Overbeek^[79], known as the DLVO theory. The balance between attractive and non-attractive interactions governs the overall stability. In a colloidal system, the van der Waals interactions in form of London (dispersion) forces between particles in solution represent the attractive interaction. If the particle surface is considered as a double layer of ions, a further convergence of two particles leads to strong repulsion of electrochemical double layer. This results in a secondary minimum in an energy-distance diagram that represents a stable dispersion (Figure 2). A coagulation is observed if the double layer is penetrated and the attractive interaction between the particle surfaces predominates (primary minimum in the total energy curve).^[80] The coagulation is driven by the attractive van der Waals interaction and can be prevented by coating the nanoparticles with bulky ligands (steric stabilisation), e.g. polymers like poly(*N*-vinylpyrrolidone) (PVP) and poly(vinyl alcohol)

(PVA), or charged molecules (electrostatic stabilisation), e.g. trisodium citrate.^[73] A combination of both (electrosteric stabilisation) can be realised by using charged polymers like sodium polystyrene sulfonate (PSS).

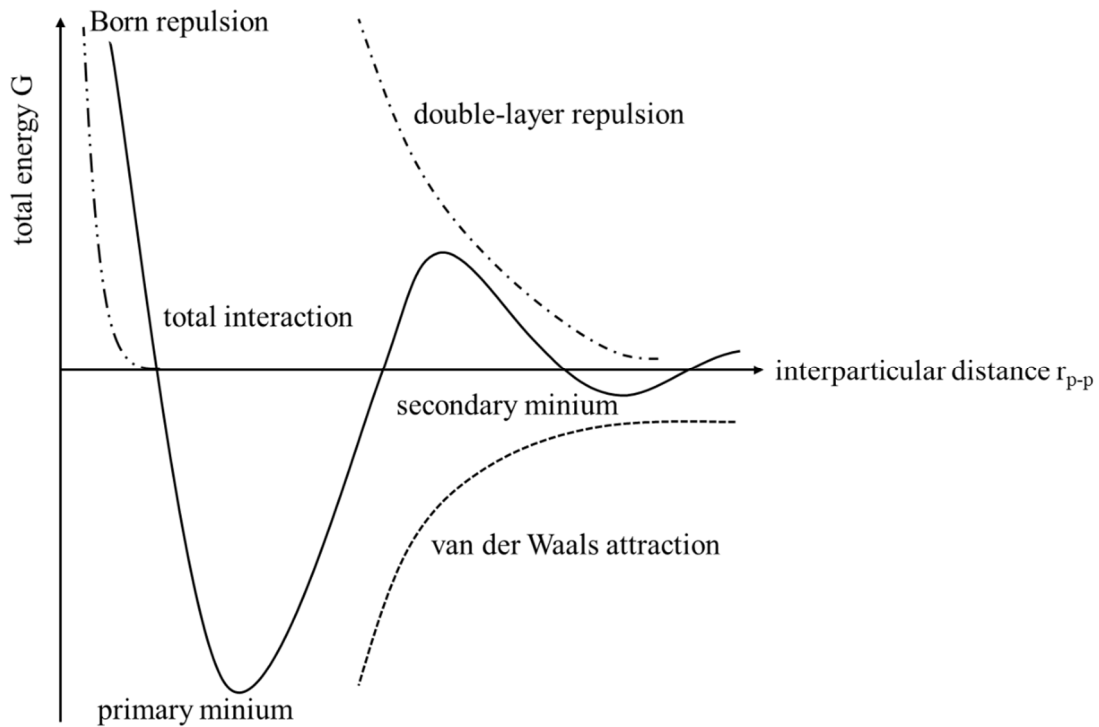


Figure 2: Energy-distance diagram in colloidal systems.

2.4 Crystallisation and growth

The bottom-up approach of particle synthesis can be described as a crystallisation process that can be modified by several parameters to influence the resulting particle size and shape. The formation mechanism of monodisperse hydrosols was described already in 1950 by LaMer and co-workers.^[81, 82] The model concept divides the nucleation and growth process into three stages (Figure 3). The initial formation of nuclei (c_{\min}) in a supersaturated stage (II) is a result of the increase of forming atoms in the first stage (I). The further consumption of atoms leads to a decrease in concentration until the second stage is left. If the concentration undercuts the critical point c_{\min} , no more nuclei are formed and the particle size increases because of a growth process (III). The formation of seeds depends on the strength of the reducing agent. Consequently, weaker reducing

agents, e.g. ascorbic acid, lead to a lower number of nuclei than strong agents, e.g. sodium borohydride.

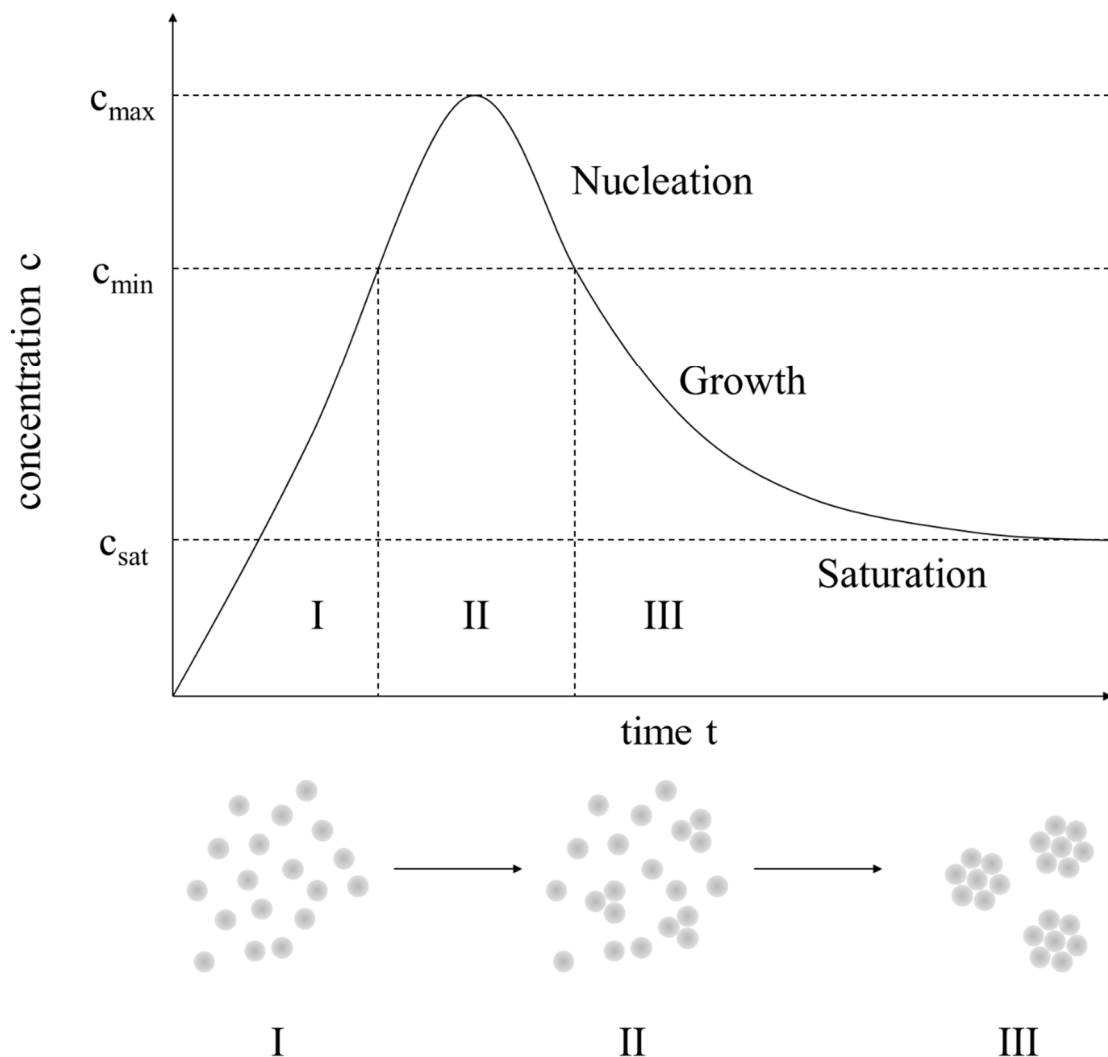


Figure 3: Scheme of the nucleation and growth process according to LaMer.

2.5 Metal nanoparticles

Metal nanoparticles are of particular interest in nanoscience and nanotechnology due to their easy synthesis and chemical modification. Their electronic and optical properties, e.g. the dielectric or optical constants, at the nanoscale are similar to those of the macroscopic bulk materials.

2.5.1 Noble metals and their physico-chemical properties

The noble metals are the elements of group VIII-XI and show a high resistance against corrosion and oxidation. The group of the platinum metals (group VIII-X) comprises the metals ruthenium, rhodium, palladium, osmium, iridium, and platinum. The group XI metals, so-called coin metals, are (copper), silver and gold.

Ruthenium (element symbol Ru) is a brittle, silver-white metal with a density of 12.45 g cm^{-3} and a melting point of $2310 \text{ }^\circ\text{C}$. Osmium (element symbol Os) is also a brittle, but bluish-grey metal with a high density of 22.61 g cm^{-3} and a melting point of $3045 \text{ }^\circ\text{C}$. Both crystallise in a hexagonal-close packed (hcp) structure. The most frequent oxidation states are **+III** (Ru) and **+IV** (Os), respectively. The electrochemical standard potential of the two-step redox reaction under acidic conditions ($\text{pH} = 0$) of $\text{Ru}^{3+}/\text{Ru}^{2+}$ is $+0.249 \text{ V}$ and $+0.815 \text{ V}$ of $\text{Ru}^{2+}/\text{Ru}^0$, respectively. The standard potential of $\text{Os}^{4+}/\text{Os}^0$ is $+0.846 \text{ V}$ at $\text{pH} = 0$.

Rhodium (element symbol Rh) is a ductile, silver-white metal with a density of 12.41 g cm^{-3} and a melting point of $1966 \text{ }^\circ\text{C}$. Iridium (element symbol Ir) is a brittle, silver-white metal with a melting point of $2410 \text{ }^\circ\text{C}$ and a density of 22.65 g cm^{-3} , the highest of all elements. Both metals crystallise in the face-centred cubic (fcc) structure. The most frequent oxidation states are **+III** (Rh, Ir) and **+IV** (Ir). The standard potential at $\text{pH} = 0$ of $\text{Rh}^{3+}/\text{Rh}^0$ is 0.760 V . The redox reaction of iridium(IV) is a two-step process with the standard potentials of $+0.867 \text{ V}$ ($\text{Ir}^{4+}/\text{Ir}^{3+}$) and $+0.860 \text{ V}$ ($\text{Ir}^{3+}/\text{Ir}^0$) under acidic conditions ($\text{pH} = 0$).

Palladium (element symbol Pd) is a ductile, silver-white metal with a density of 12.02 g cm^{-3} and melting point of $1554 \text{ }^\circ\text{C}$, the lowest of all platinum metals. Platinum (element symbol Pt) is a ductile, silver-grey metal with a melting point of $1772 \text{ }^\circ\text{C}$ and a density of 21.45 g cm^{-3} . Both metals are not so tough and crystallise in an fcc structure. The most frequent oxidation states are **+II** and **+IV** (especially for Pt). The standard potential at $\text{pH} = 0$ of $\text{Pd}^{2+}/\text{Pd}^0$ in aqueous media (e.g. in the presence of $\text{Pd}(\text{NO}_3)_2$ in form of $\text{Pd}(\text{H}_2\text{O})_4^{2+}$) is $+0.915 \text{ V}$. The presence of the square planar complex $[\text{PdCl}_4]^{2-}$ reduces the electrochemical potential. The standard potential of $[\text{PdCl}_4]^{2-}/\text{Pd}^0$ is $+0.620 \text{ V}$. The redox reaction of platinum(IV) under acidic conditions is a two-step process with the standard potentials of $+0.726 \text{ V}$ ($\text{Pt}^{4+}/\text{Pt}^{2+}$) and $+0.758 \text{ V}$ ($\text{Pt}^{2+}/\text{Pt}^0$).

Silver (element symbol Ag) is a soft, ductile, shining white metal with a density of 10.49 g cm^{-3} and a melting point of $962 \text{ }^\circ\text{C}$. Ag crystallises in an fcc structure in form of regular octahedra. Furthermore, silver has the best thermal ($\lambda = 418 \text{ W m}^{-1} \text{ K}^{-1}$) and electrical

conductivity ($\kappa = 6.31 \cdot 10^5 \Omega^{-1} \text{ cm}^{-1}$) of all metals. The most stable oxidation state is **+I**. The standard potential of Ag^+/Ag^0 is +0.799 V at $\text{pH} = 0$.

Elemental gold (element symbol Au) is a ductile, soft, rutilant (reddish-yellow) metal with a high density of 19.32 g cm^{-3} and a melting point of $1064 \text{ }^\circ\text{C}$. Au crystallises in an fcc structure and the thermal and electrical conductivity amounts to 70 % of those of silver. The most frequent oxidation states are **+I** and **+III**. The electrochemical standard potential of $\text{Au}^{3+}/\text{Au}^0$ is +1.498 V under acidic conditions ($\text{pH} = 0$).

2.5.2 Optical properties of metal nanoparticles - Surface plasmon resonance (SPR)

Nanoparticles often exhibit interesting optical and electronically properties in dependence of their size, morphology, composition, and dielectric constant. A few metals, especially copper, silver and gold, may absorb ultraviolet and visible light and show a distinct visible colour. These optical properties are caused by so-called surface plasmon resonance (SPR). SPR is the result of the collective motion of the electron gas (electrons in the conductive band) relative to the particle core by excitation with electromagnetic radiation. The absorbed wavelength corresponds to the specific excitation energy. The oscillation of the electron gas is caused by the electric field component of the radiation and Coulomb attractions between the electrons and the nuclei.^[83, 84] The frequency of the electron oscillation depends on the electron density and charge distribution. The particles must be smaller than the incident light wavelength to show SPR.

Additionally, the localised SPR can be utilised for studying both the optical properties (UV/vis) and surface chemistry like reactions on the surface or adsorption of molecules and ligands. The latter surface-sensitive phenomena can be investigated using surface-enhanced Raman spectroscopy (SERS). A side effect of the plasmon resonance is the amplification of Raman signals, which originate from molecules adsorbed or very close ($\leq 10 \text{ nm}$) to the surface of the metal substrate. This effect is known as surface-enhanced Raman scattering. The signal enhancement is provided by the SPR and is associated to the electromagnetic interactions with laser light. Nowadays, SERS represents a multidisciplinary technique in analytical chemistry, biotechnology and forensic science.^[85, 86]

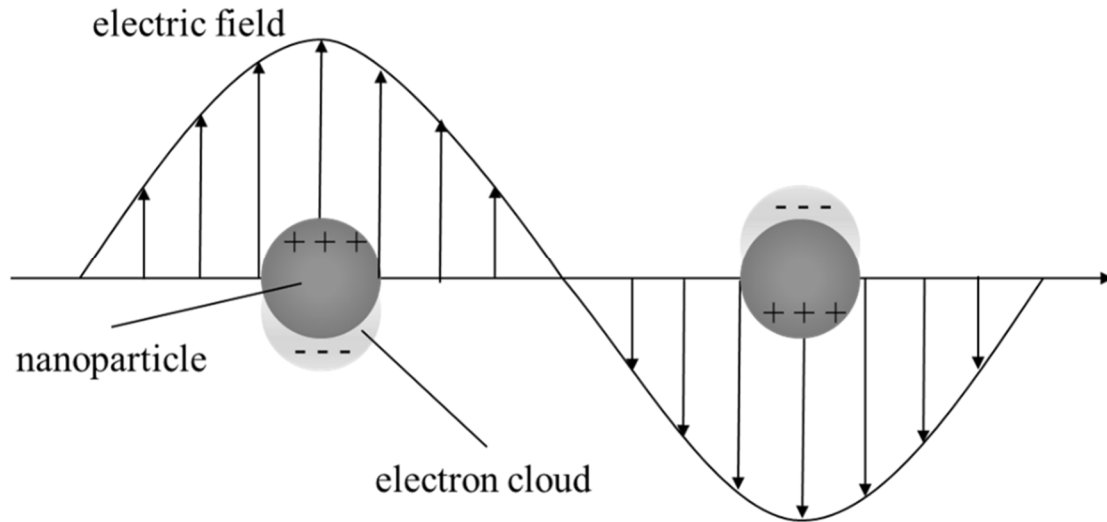


Figure 4: Schematic illustration of surface plasmon resonance (SPR) due to the oscillation and dipole induction of the electron gas in a nanoparticle by the electric field component of the incident light.

2.5.3 Bimetallic nanostructures and galvanic replacement

In general, bimetallic nanostructures can be classified into three main types (Figure 5). Core-shell and Janus nanoparticles show a strict phase separation of both metals in the same particle. Whereas the former are composed of a core which is fully covered with one or more layer of another metal, Janus particles structurally resemble a bar magnet with North and South Pole. Alloys constitute the third group of bimetallic nanoparticles and show a homogenous distribution of both elements.

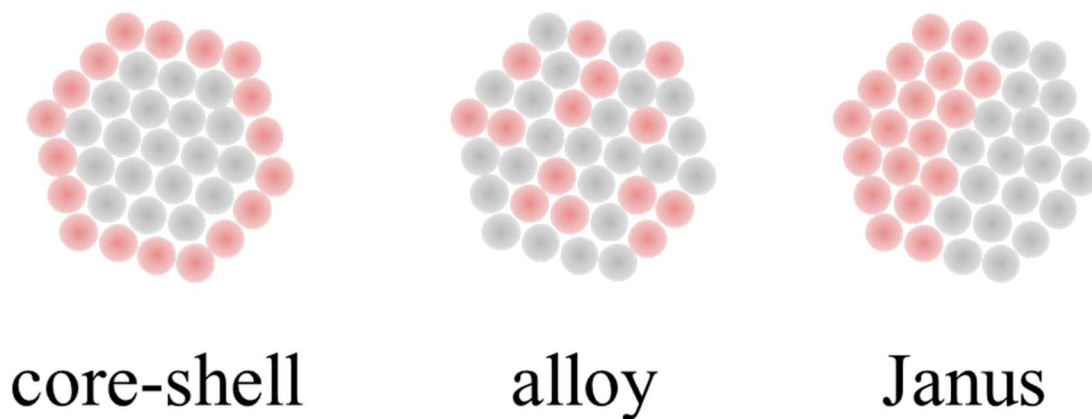


Figure 5: Three types of bimetallic nanostructures.

Typically, core-shell nanoparticles are synthesised by a seed and growth approach where the core is formed in the first step. The shell formation is induced by the addition of a second precursor and the crystallisation on the particle surface.^[19, 87-89] Alloys are produced by a simultaneous co-reduction of both metal precursors.^[90, 91] Janus nanostructures are normally formed by a two-step method where nanoparticles are masked in a matrix and the second metal is subsequently applied by sputtering, chemical reaction or stamping interface.^[83]

The synthesis of bimetallic nanoparticles depends on numerous parameters. Whereas the size and shape can be controlled by variation of typical reaction parameters like temperature, concentrations of precursors or reducing agents, the successful generation of heterogeneous nanoparticles of two different metals must fulfil certain requirements. The co-crystallisation of two elements strongly depends on the atomic radii and lattice parameters. The tolerance of the maximum deviation of both parameters is ca. 5 %.^[92] Furthermore, the solubility of the compounds and the electrochemical standard potential of the precursor molecules are important and must be taken into account when the co-crystallisation is performed in solution. If one metal is nobler than the other one, the obtained nanoparticles will show a gradient elemental distribution with an enrichment of the nobler metal in the inner part of the particle. A higher standard potential leads to a lower reducing potential in the redox reaction. The consequence is that the nobler metal will be reduced easier and the number of atoms of that element will be much higher compared to the less noble material.^[91] In the case of core-shell nanoparticles as well as Janus nanostructures, the difference in the electrochemical standard potential leads to another problem. A galvanic replacement reaction may occur if the core consists of the less noble metal and the nobler element is designated to form the shell. The less noble metal will dissolve by oxidation due to the transfer of electrons to the metal with the higher standard potential.^[91]

3 Methods

3.1 Dynamic light scattering (DLS) and Zeta Potential

The size distribution of dispersed colloids and particles can be determined by using dynamic light scattering (DLS). This method is based on Rayleigh scattering on suspended particles that undergo Brownian motion. If the particles are moving, changes in the scattered intensity with time directly reflect the Brownian motion of the scattering particles. The time-dependent fluctuation of the scattered intensity can be mathematically expressed by an autocorrelation function, which enables the determination of the diffusion coefficient D . The Stokes-Einstein equation (eq. 1) is used to calculate the hydrodynamic radius R_H of the scattering particles with k_B the Boltzmann constant, T the temperature, and η the viscosity of the dispersant.^[93] The hydrodynamic radius represents the size of the suspended particle with the hydration shell of ions, fluid molecules and stabilizing agents.

$$D = \frac{k_B \cdot T}{6\pi \cdot \eta \cdot R_H} \Rightarrow R_H = \frac{k_B \cdot T}{6\pi \cdot \eta \cdot D} \quad (\text{eq. 1})$$

Nanoparticles in solution form an electrochemical double layer consisting of counter ions in a rigid Stern layer and a diffuse layer. If a potential is applied, the charged particles move to the electrode of opposite charge. The diffuse layer is constrained to a slipping plane, which is sheered away upon particle diffusion. The potential at the slipping plane defines the zeta-potential (Figure 6). Consequently, the ζ -potential can be measured by the determination of the diffusion rate in an applied electrical field due to the direct correlation between the diffusion velocity and the particle charge.

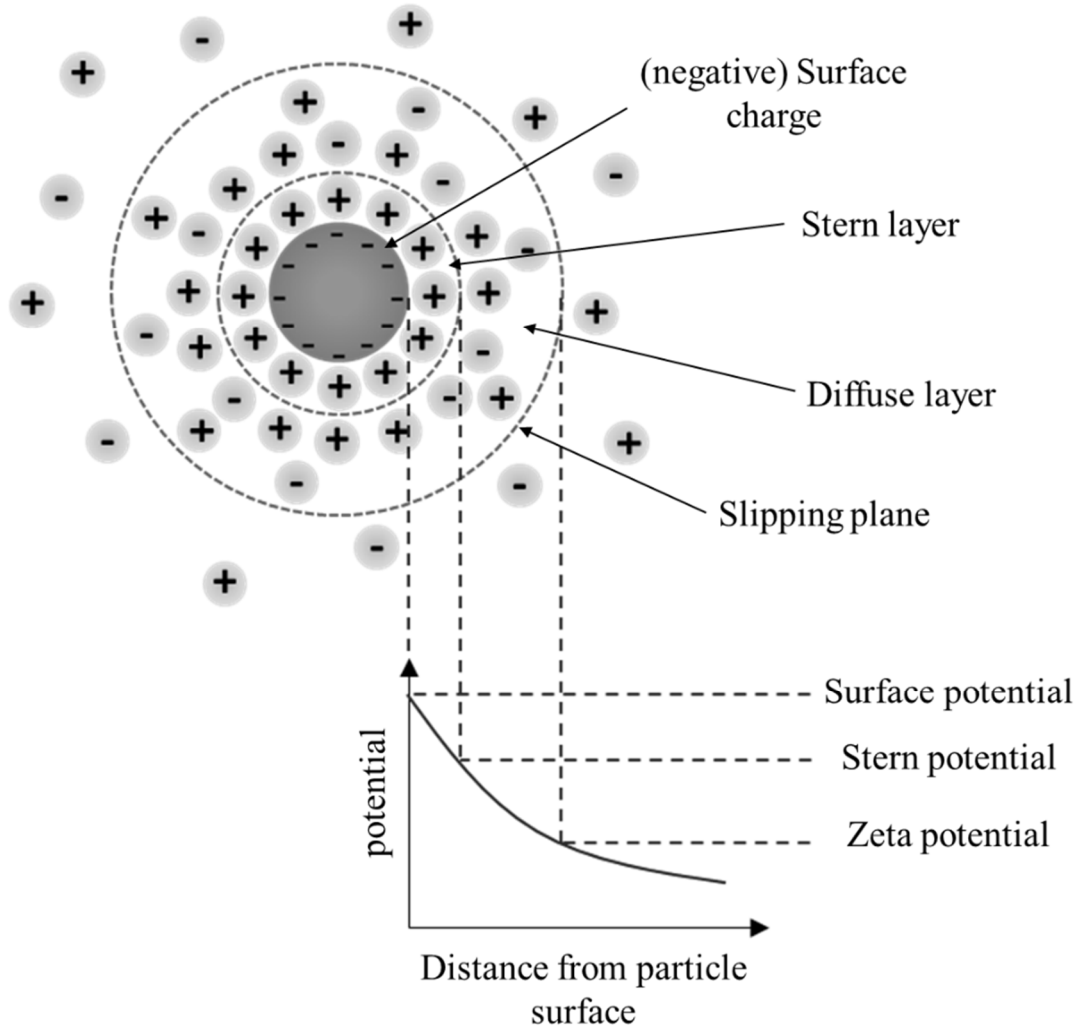


Figure 6: Schematic illustration of the potential as function of the distance.

Dynamic light scattering for particle size analysis and zeta-potential determination were carried out with a Malvern Zetasizer Nano ZS ZEN 3600 instrument (Malvern Panalytical Ltd.; 25 °C, laser wavelength 633 nm). The scattering was monitored at a fixed angle of 173° in backward scattering mode. The peak profile of the size distribution was analysed by a log-normal as well as a Gaussian distribution fit to calculate the maximum of size distribution and to determine the full-weight at half maximum β (FWHM) to calculate the polydispersity index (PdI) by following equation (eq. 2).

$$\text{PdI} = \left(\frac{\beta_{\text{Gauss}}}{d_{\text{Gauss}}} \right)^2 \quad (\text{eq. 2})$$

The average diameter is given as mean value of the maximum of the size distribution x_c from log-normal and Gaussian distribution fit analysis and the empirical standard deviation s . The arithmetic mean or average of the measured values x is commonly used to interpret the central tendency of a data set and defines the mean value \tilde{x} (eq. 3).^[94] Here, the average diameter d_{ave} is calculated using the following equation (eq. 4) with d_{LogN} the x_c value of the log-normal distribution fit, d_{Gauss} the x_c value of the Gaussian fit.

$$\tilde{x} = \frac{1}{N} \cdot \sum_{i=1}^N x_i = \frac{x_1 + x_2 + \dots + x_i}{N} \quad (\text{eq. 3})$$

$$d_{ave} = \frac{d_{LogN} + d_{Gauss}}{2} \quad (\text{eq. 4})$$

The deviation of the individual measured values x from the mean value \tilde{x} is called error u_i and is given as the sum of the subtraction of the measured value and the mean value (eq. 5). A suitable measure of the error is the standard deviation s which is the square root of the sum of the square error u_i^2 (eq. 6).^[94]

$$u_i = x_i - \tilde{x} \quad (\text{eq. 5})$$

$$s = \sqrt{s^2} = \sqrt{\frac{1}{N} \cdot \sum_{i=1}^N u_i^2} = \sqrt{\frac{1}{N} \cdot \sum_{i=1}^N (x_i - \tilde{x})^2} \quad (\text{eq. 6})$$

Here, the empirical standard deviation s is calculated using the following equations (eq. 7 and 8)

$$s^2 = \frac{(d_{LogN} - d_{ave})^2 + (d_{Gauss} - d_{ave})^2}{2} \quad (\text{eq. 7})$$

$$s = \sqrt{s^2} \quad (\text{eq. 8})$$

3.2 Differential centrifugal sedimentation analysis (DCS)

Differential centrifugal sedimentation analysis (DCS), commonly called analytical disc centrifugation (ADC), represents a high-resolution particle sizing method. According to Stokes' law, the sedimentation time of particles in a centrifugal field is measured to estimate the particle size distribution of an unknown sample in a fluid of known density and viscosity. For this, a hollow disc is filled with a density gradient and rotated at a defined speed. An advanced Stokes' equation (eq. 9) is used to calculate the hydrodynamic diameter D_H of sedimenting particles with η the fluid viscosity, R_f the outer disc radius, R_0 the inner disc radius, ρ_p the particle density, ρ_f the fluid density, ω the angular velocity, and t the sedimentation time.

$$D_H = \sqrt{\frac{18 \cdot \eta \cdot \ln\left(\frac{R_f}{R_0}\right)}{(\rho_p - \rho_f) \cdot \omega^2 \cdot t}} \quad (\text{eq. 9})$$

Note that the hydrodynamic diameter determined by differential centrifugal sedimentation analysis (DCS) is systematically underestimated due to the lower density of the hydration shell compared to the metal nanoparticle.^[95, 96]

Analytical disc centrifugation was performed with a DC 24000 disc centrifuge (CPS Instruments, Inc.). The rotor speed was set to 24,000 rpm (28,978 g). Two aqueous sucrose solutions (8 wt% and 24 wt%) formed a density gradient which was capped with 0.5 ml

dodecane as a stabilizing agent. The calibration standard was a poly(vinyl chloride) (PVC) latex in water with a particle size of 483 nm provided by CPS Instruments. The calibration was carried out prior to each run. A calibration and sample volume of 100 μl was used.

3.3 Ultraviolet-visible spectroscopy (UV/vis)

The excitation of electrons of molecules by light provides the basis of ultraviolet-visible spectroscopy (UV/vis). A transfer of electrons from the ground state into an excited state takes place by absorption of suitable energy in form of photons. The proportionality of absorbed light intensity and sample concentration can be described by the *Bouguer-Lambert-Beer* law (eq. 10) with E the extinction, I_0 the intensity of incident light, I the intensity of transmitted light, ε the extinction coefficient, c the sample concentration, and d the thickness of the cuvette.

$$E = \log\left(\frac{I_0}{I}\right) = \varepsilon \cdot c \cdot d \quad (\text{eq. 10})$$

Ultraviolet-visible spectroscopy (UV/vis) was performed with a Varian Cary 300 instrument (Agilent Technologies, Inc.). Suprasil® micro quartz cuvettes with a sample volume of 750 μl were used after dilution and background correction. The UV/vis spectroscopy was used to determine the reaction progress.

3.4 Atomic absorption spectrometry (AAS)

The atomic absorption spectrometry (AAS) is based on the element specific absorption of optical radiation with characteristic wavelength by free atoms and ions in the gas phase. *Kirchhoff* described the basic principles of absorption and emission of characteristic wavelengths by atoms. The wavelength corresponds to the energy gaps between the different electronic states of an atom (eq. 11).

$$\Delta E = |E_1 - E_2| = h \cdot \frac{c}{\lambda} \quad (\text{eq. 11})$$

Walsh has utilized this physical phenomenon to determine the absorption of monochromatic light by atoms and ions in the gas phase. A quantitative and qualitative analysis is possible according to the *Boguer-Lambert-Beer* law.^[97]

Atom absorption spectrometry was carried out with a Thermo Electron M-Series instrument (Thermo Fisher Scientific) according to DIN EN ISO/IEC 17025:2005. Kerstin Brauner and Robin Meya performed the measurements in the Laboratory of Microanalysis at the University Duisburg-Essen. The samples were dissolute in *aqua regia* (Rh, Pd, Pt, and Au) and nitric acid (Ag). The AAS was used for a quantitative determination of the metal concentration. The metal concentrations of Ru, Os and Ir were externally determined.

3.5 Electron microscopy

Scanning (SEM) as well as transmission electron microscopy (TEM) are based on the diffraction of electrons on the valence electrons of atoms. Electrons are used for visualisation of specimen smaller than the wavelength of visible light (400 – 700 nm) to overcome the optical *Abbé* limit (eq. 12) with d the resolution, λ the wavelength of the electron beam, n the refractive index of the immersion medium, α the aperture angle, and NA the numerical aperture.

$$d = \frac{\lambda}{2n \cdot \sin \alpha} = \frac{\lambda}{2 \cdot NA} \quad (\text{eq. 12})$$

The advantage of electron beams over x-ray radiation is based on the easy handling, i.e. focusing, scanning, and deflection by electromagnetic fields. Considering that SEM has obvious limitations due to the fact that only an imaging of the specimen's surface features is easily accessible, TEM shows more resolution in the subnanometer and atomic region and can be used for more detailed imaging and analysis of very small probes.^[98]

3.5.1 High-resolution transmission electron microscopy (HR-TEM)

Modern transmission electron microscopes can be operated in different imaging modes and can be equipped with a number of supplementary analysis tools. In addition to the “classical” diffraction patterns, the variations in diffraction across the specimen (contrast imaging) and the phase contrast of the specimen (high-resolution imaging) can be used to obtain various images and information on the sample. In addition to the spatial and diffraction imaging, the high-energy electrons of the small, focused electron beam (1-10 Å) in TEM induce electronic excitations of the atoms that can be simultaneously used to perform electron-energy loss (EELS) and energy-dispersive x-ray (EDX) spectroscopy measurements. The performance in resolution of TEM images is not only affected by the sample quality, but also by spherical and chromatic aberrations from the focusing lenses and electromagnetic fields. Elastic scattering of primary electrons from the incident beam on the sample atoms results in a bright-field contrast image. Secondary electrons (SE) with low energy (between 0 and 50 eV) originate from inelastic scattering of primary electrons. Whereas the so-called backscattered electrons (BSE) with high energy (between the beam energy E_0 and 50 eV) from elastic scattering give information on the material contrast, the SE carry information on the surface topography of the specimen.^[98] High-resolution imaging was performed using an aberration-corrected FEI Titan transmission electron microscope equipped with a Cs-probe corrector (CEOS Company), operated at 300 kV.^[99] Scanning transmission electron microscopy (STEM) was performed using a FEI Titan microscope, equipped with a Cs-probe corrector (CEOS Company) and a high-angle annular dark field (HAADF) detector, operated at 200 kV. Z-contrast conditions were achieved using a probe semi-angle of 25 mrad and an inner collection angle of the detector of 70 mrad. The elemental mapping using energy-dispersive X-ray spectroscopy (EDX) was conducted on a probe-corrected FEI Titan 80–300 ChemiSTEM electron microscope, equipped with four symmetrical SDD detectors.^[100, 101] The high-resolution transmission electron microscopy incl. HAADF imaging, and EDX spectroscopy was performed by Dr. Kateryna Loza in Dr. Marc Heggen’s group at the Ernst-Ruska Centre for Microscopy and Spectroscopy with Electrons in Jülich.

3.5.2 High-angle annular dark field (HAADF) imaging

Elastic and inelastic scattering as well as backscattering are the generally mentioned primary electron-specimen interactions in the TEM. Furthermore, an interaction between the atom's nuclei and the electrons of the beam is taking place that is known as Rutherford forward scattering. The technique of high-angle annular dark field (HAADF) imaging based on the detection of Rutherford-scattered electron on a high angle ($> 5^\circ$). In contrast to the typical bright-field image of electron microscopes, a dark field detector reproduces an image which is highly sensitive to atomic number contrast, i.e. $Z^{2/3}$ (at low angles) and Z^2 (at high angles) dependence. In dark-field images can be clearly distinguish between particles and matrix and show a much more even contrast.^[102]

3.5.3 Energy dispersive X-ray spectroscopy (EDX)

Energy dispersive X-ray spectroscopy (EDX) enables a qualitative and quantitative elemental analysis of specimen. Interactions, i.e. inelastic scattering, between the electrons of the incident electron beam and electrons of the sample's atoms lead to an ionization of an inner electron shell. The vacancy can be refilled by an electron from an outer shell causing emission of characteristic x-rays according to their energy level. The detected X-ray radiation energies can be classified with the element specific X-ray spectrum from literature data bases.^[98]

3.6 X-ray powder diffraction (PXRD)

The crystallographic structure as well as the verification of crystallographic phases of samples can be investigated by X-ray powder diffraction (PXRD). The wavelength of X-ray radiation (0.1 to 100 Å) is in the order of magnitude of interatomic distances and can be used to determine the atomic structure of crystalline materials. In crystalline materials, the position of atoms is periodic allocated and generate a three dimensional lattice. The phenomenon of diffraction can be described by the coherent scattering of the incident (primary) beam on the electron shells of the lattice atoms (Figure 7). Because the diffraction occurs at several atomic layers, the scattered beams can interfere in a destructive and constructive way.^[103]

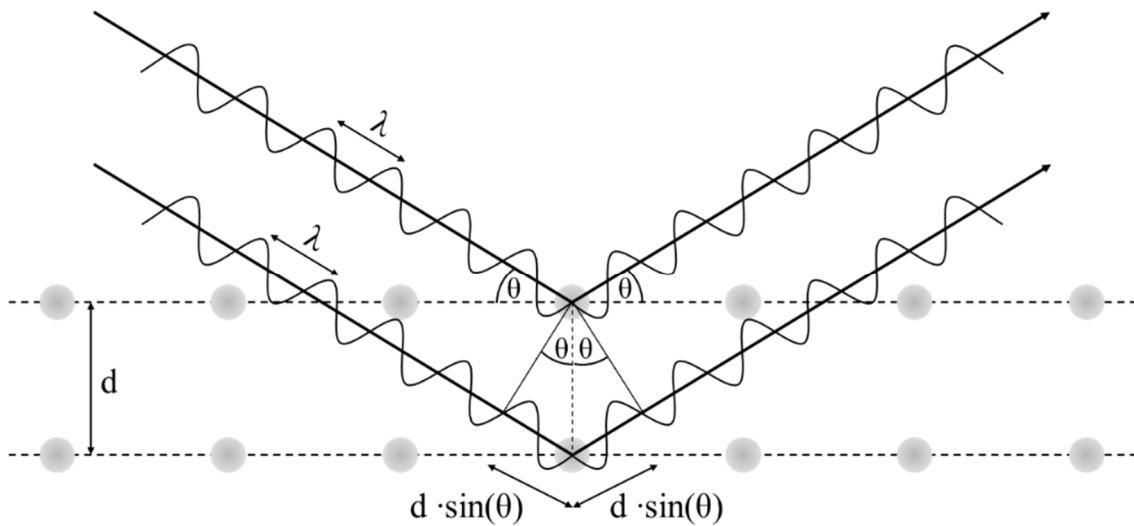


Figure 7: Schematic illustration of constructive interference according to the *Bragg* law with λ the wavelength of incident X-ray beam, θ the *Bragg* angle, d the distance between two atomic layers, and $d \cdot \sin(\theta)$ the path difference.

Only constructive interference results in detectable intensities of a diffraction pattern. According to the *Bragg* law (eq. 13), constructive interference only occurs if the path difference $d \cdot \sin(\theta)$ is an integral multiple n of the wavelength λ .

$$n \cdot \lambda = 2 \cdot d \cdot \sin(\theta) \quad (\text{eq. 13})$$

The signal width in a diffraction pattern allows to calculate the crystallite size D with the help of the *Scherrer equation*^[104] (eq. 14) where K is the *Scherrer factor* (constant set to 0.89), λ the wavelength of the incident X-ray beam, β the full width at half maximum (FWHM) of the regarded reflex, and θ the *Bragg angle*.

$$D = \frac{K \cdot \lambda}{\beta \cdot \cos(\theta)} \quad (\text{eq. 14})$$

Further, the microstrain ε can be calculate using the *Stokes-Wilson equation*^[105] (eq. 15) where β is the full width at half maximum (FWHM) of the regarded reflex, and θ the *Bragg angle*.

$$\varepsilon = \frac{\beta}{4 \cdot \tan(\theta)} \quad (\text{eq. 15})$$

For a cubic system, e.g. gold in fcc structure, the lattice parameter α can be calculated using following equation (eq. 16) with θ the *Bragg angle*, λ the wavelength of the incident X-ray beam, and hkl the *Miller indices* of the corresponding atomic plane.^[103]

$$\alpha = \frac{\lambda}{2 \cdot \sin(\theta)} \cdot \sqrt{h^2 + k^2 + l^2} \quad (\text{eq. 16})$$

The density of the crystals ρ_{cr} can be calculated using the following equation (eq. 17) with n_{cell} the number of atoms in the unit cell, M the molar mass, V_{cell} the volume of the unit cell, and N_A the Avogadro constant ($N_A = 6.02 \cdot 10^{23} \text{ mol}^{-1}$). The number of atoms in the unit cell is 4 (fcc) and 6 (hcp), respectively.

$$\rho_{cr} = \frac{n_{cell} \cdot M}{V_{cell} \cdot N_A} \quad (\text{eq. 17})$$

X-ray powder diffraction was performed with a Bruker D8 ADVANCE (Bruker Corp.) in *Bragg-Brentano* geometry with Cu $K\alpha$ radiation ($\lambda_{Cu \text{ } K\alpha} = 1.54 \text{ \AA}$, 40 kV and 40 mA), using a single-crystalline silicon sample holder with a crystallographic (911) plane to minimize scattering. The instrumental broadening is determined by using lanthanum hexaboride (LaB_6) from NIST (National Institute of Standards and Technology) as internal standard. Rietveld refinement (Le Bail method) with the program package TOPAS 4.2 (Bruker Corp.) was performed to calculate the average crystallite size and lattice parameter. The instrumental peak broadening was taken into account for each Rietveld refinement.

4 Results and discussion

4.1 Characterisation of monometallic nanoparticles of the platinum and coin metals group (4-8 nm)

The first part of the present work is concerned with the syntheses of spherical nanoparticles of the noble metals (Ru, Rh, Pd, Ag, Os, Ir, Pt, Au) with a nominal size of 5 to 10 nm in diameter and the same surface-functionalisation, i.e. poly(*N*-vinylpyrrolidone) (PVP). Several synthesis parameters, primarily the reducing agents, and / or precursor and reductant concentration, are varied to accomplish easy, reproducible, and water-based syntheses. All particles are characterised in detail with common colloid-chemical and spectroscopic method, e.g. dynamic light scattering, differential centrifugal sedimentation analysis, and UV/vis spectroscopy. Furthermore, high-resolution electron microscopy and X-ray diffraction are performed to investigate the structural characteristics of obtained nanoparticle systems. Additional biological effects on human mesenchymal stem cells (hMSC) are studied in order to compare different metal nanoparticles with identical surface-functionalisation and the same size range. Dr. Kateryna Loza performs the high-resolution and scanning transmission electron microscopy in cooperation with Dr. Marc Heggen's group at the Ernst-Ruska Centre for Microscopy and Spectroscopy with Electrons in Jülich. Ms. Marina Breisch, Jun.-Prof. Dr. Christina Sengstock, and Prof. Dr. Manfred Köller in the Surgical Research at the University Hospital Bergmannsheil in Bochum carry out cell biological studies.

4.1.1 Ruthenium nanoparticles

Very small Ru nanoparticles (< 2 nm) can be synthesised by photochemical reduction in aqueous ethanol solution in the presence of PVP and a photo-activator (e.g. benzoin or benzophenone).^[106] Furthermore, those particles can be also obtained by reduction of a mixture of PVP and RuCl₃ in alcohols like ethanol, *n*-propanol, or *n*-butanol.^[107] Small (< 6 nm) and cluster-like (< 2 nm) Ruthenium nanoparticles are available by the polyol process.^[108-110] Ligand-stabilised cluster-like Ru nanoparticles (< 2 nm) can be obtained by decomposition of Ru-(COD)(COT) (COD = 1,5-cyclooctadiene, COT = 1,3,5-cyclooctatriene) in THF and 1 to 3 bar H₂ at room temperature in the presence of PVP.^[111] Zero-valent ruthenium nanoparticles can be synthesised by a solvent less method using sodium borohydride.^[112]

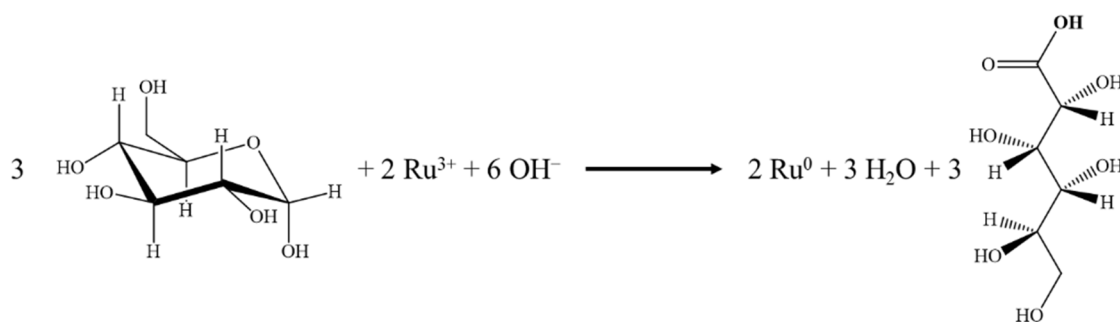


Figure 8: Reaction scheme of the reduction of RuCl₃ with *D*-glucose.

In this work, spherical ruthenium nanoparticles are obtained by a wet-chemical reduction of RuCl₃ with *D*-glucose in the presence of PVP (Figure 8). The hydrodynamic particle size is measured by dynamic light scattering (DLS) and differential centrifugal sedimentation (DCS) analysis. For this purpose, the particles are diluted and dispersed in ultrapure water. From the measured data, a log-normal and a Gaussian distribution can be derived and the mean size can be calculated in form of the x_c values using the corresponding mathematical fitting model. All average diameters are given as mean values of x_c of both distribution fit analyses with the standard deviation. Dynamic light scattering is based on the monitoring of the Rayleigh scattering fluctuations in dependence of the Brownian motion of dispersed particles. The fact that the Brownian motion as well as the scattering intensity ($I \sim r^6$) are strongly size dependent, DLS measurements result in larger particle sizes if a stabilising agent like PVP covers the particle surface. With a handful of assumptions (e.g. spherical morphology, monodisperse size distribution), it is possible to calcu-

late the number-weighted particle size distribution from the scattering intensity. The number-weighted hydrodynamic diameter is 6.6 nm with a standard deviation of ± 1.2 nm and a polydispersity index (PdI) of 0.17 as determined by DLS (Figure 9). A further technique to determine the size distribution of the particle dispersions is the analytical disc centrifugation or differential centrifugal sedimentation (DCS) analysis. The average size (by number) from DCS is 5.8 nm with a standard deviation of ± 1.2 nm in diameter and a calculated PdI of 0.22 (Figure 10). The difference between the particle size from DLS and DCS results from the influence of the hydration shell. Whereas the dynamic light scattering overestimates the particle size because of the swollen polymer shell in solution, the analytical disc centrifugation underestimates the hydrodynamic diameter due to the lower density of the polymer coverage compared to the metal core.^[95, 113] The zeta potential at pH 7 is $+1 \pm 4$ mV, which indicates a pure steric stabilisation by the polymer PVP.

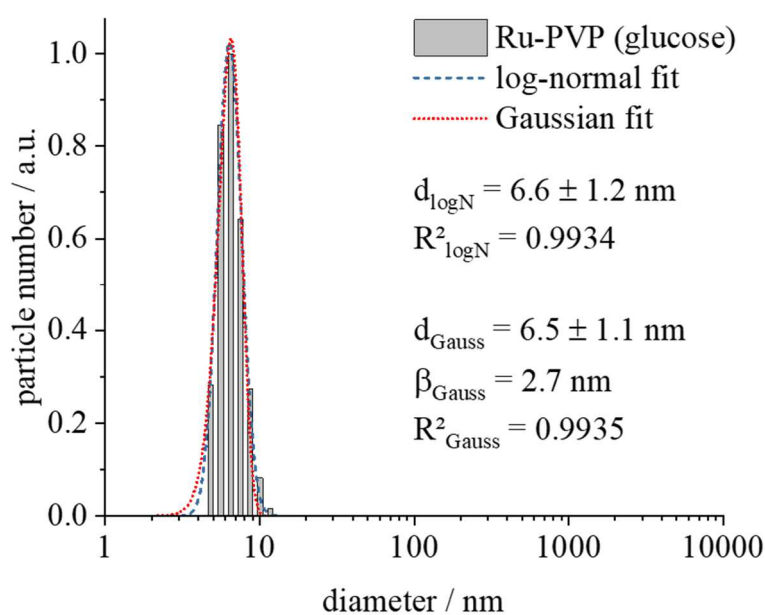


Figure 9: Number-weighted size distribution of PVP-stabilised ruthenium nanoparticles synthesised by reduction with *D*-glucose determined by DLS. The peak profile is analysed by a log-normal as well as a Gaussian distribution fit. The polydispersity index (PdI) is 0.17.

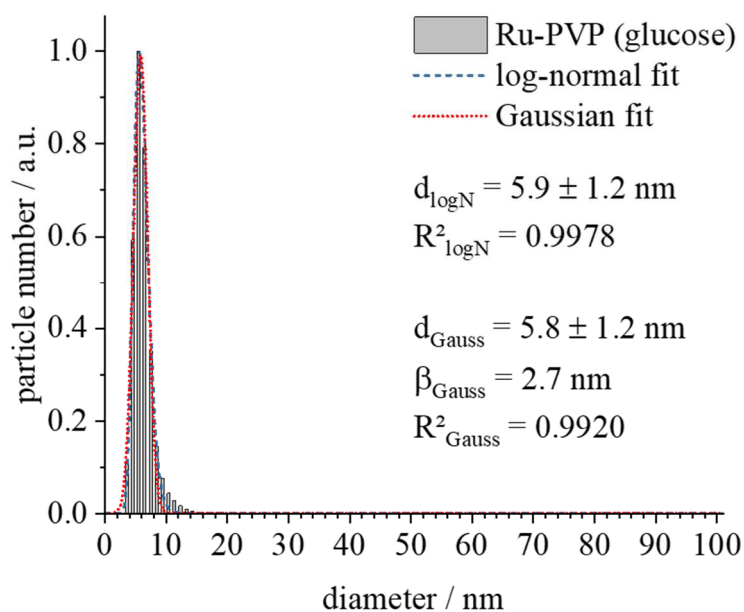


Figure 10: Number-weighted size distribution of PVP-stabilised ruthenium nanoparticles synthesised by reduction with *D*-glucose determined by DCS. The peak profile is analysed by a log-normal as well as a Gaussian distribution fit. The PDI is 0.22.

After reduction and purification, a brownish to almost black dispersion is obtained. The progress of the reaction can be followed by UV/vis spectroscopy. The UV/vis spectrum of RuCl₃ in 2 % HCl indicates a small blue shift compared to the typical absorption of a RuCl₃ solution.^[107] This can be attributed to the formation of the ruthenium chloride complex [RuCl₅(H₂O)]²⁻ from aqueous solution of RuCl₃ in the presence of excess chloride (see black arrows in Figure 11).^[114] In contrast, ruthenium nanoparticles show the typical absorption behaviour of Ru metal without any pronounced absorption in the visible range (400 to 800 nm) (Figure 11).^[115] The high absorption in the ultraviolet region (below 300 nm) comes from the polymer PVP and can be ascribed to the $\pi \rightarrow \pi^*$ and $n \rightarrow \pi^*$ transitions in the C=O bond and between the lone pairs of oxygen and the pyrrolidone ring, respectively.^[116, 117]

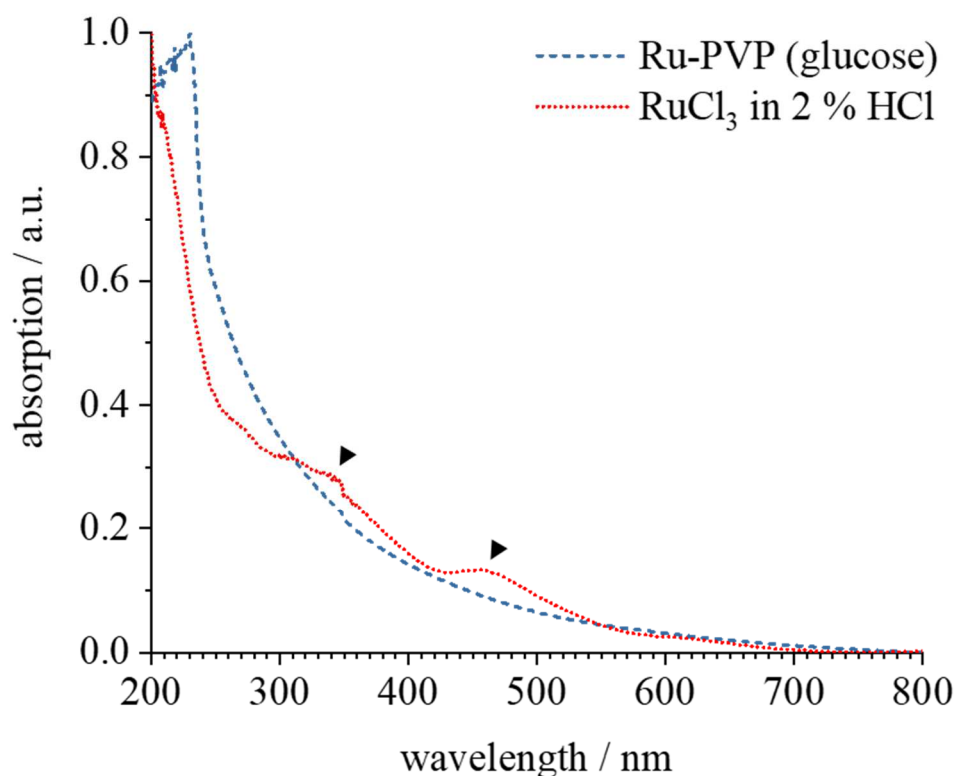


Figure 11: UV/vis spectra of RuCl₃ (in 2 % HCl; red dotted line) and PVP-stabilised ruthenium nanoparticles (blue dashed line) synthesised by reduction with *D*-glucose. The data is normalised for better comparison. The black arrows show the absorption peaks of the [RuCl₅(H₂O)]²⁻ complex from the precursor RuCl₃ (in 2 % HCl) in aqueous medium.

The transmission electron micrographs (Figure 12) show very small, spherical-like particles with a more or less single crystalline structure. In the overview, no aggregates or bigger particles can be observed which confirms a monodisperse system. In higher magnification, the single crystalline characteristic of the obtained particles can be visually substantiated.

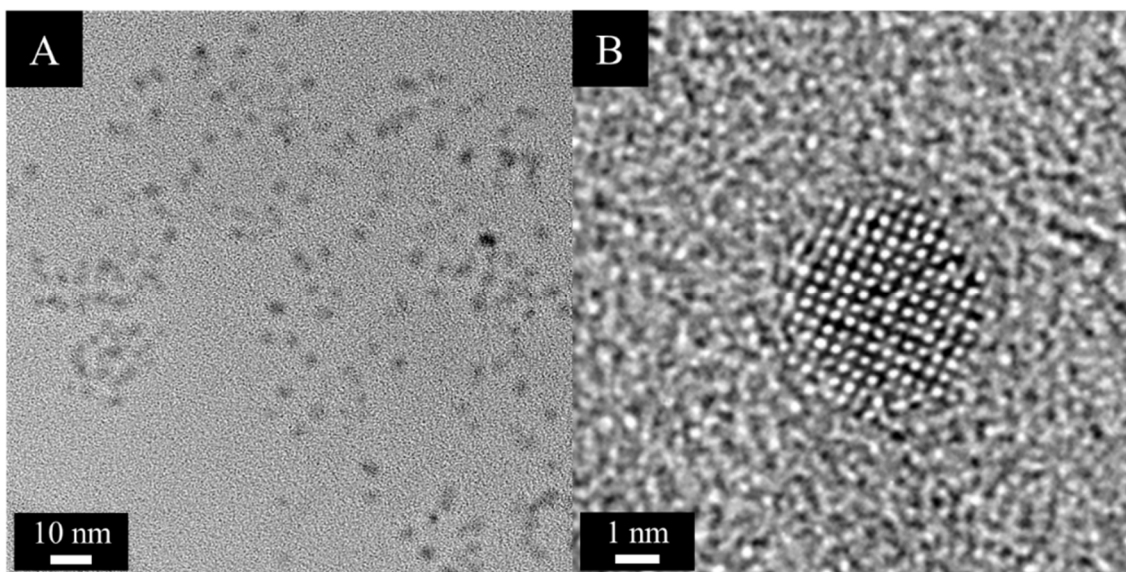


Figure 12: High-resolution TEM image of PVP-stabilised ruthenium nanoparticles synthesised by reduction with *D*-glucose (A) and a higher magnification of a single particle indicating a single crystalline structure without any grain boundaries (B).

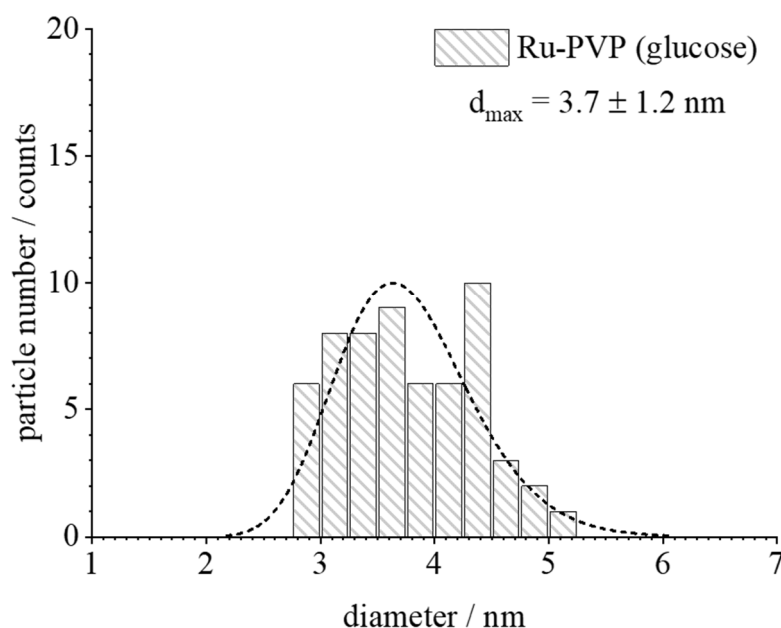


Figure 13: Histogram of particle size analysis from high-resolution TEM of PVP-stabilised Ru nanoparticles synthesised by reduction with *D*-glucose. The size distribution was analysed by a log-normal distribution fit.

The size of ruthenium particles are determined manually by measuring the size of 59 particles using the software *ImageJ* and compiling a histogram (Figure 13). The average size is 3.7 nm with a standard deviation of ± 1.2 nm in diameter. The differences between the sizes from DLS, DCS and TEM result from the measurement characteristics. Whereas in DLS and DCS a hydrodynamic diameter is measured, i.e. metallic core with the hydration shell, TEM depicts only the dense metal core of the particle. The detected X-ray intensity at 2Θ values between 15° and 40° results from the presence of amorphous PVP (not shown).^[118-120] The diffraction pattern shows three broad reflexes with weak intensity despite freeze-drying of the concentrated sample. The first broad reflex between 2Θ values of 35° and 45° corresponds to the scattering of the (100), (002) and (101) crystallographic planes of Ru (space group P63/mmc, lattice constants $a = 2.7058 \text{ \AA}$ and $c = 4.2819 \text{ \AA}$, cell volume $V_{\text{cell}} = 27.149 \text{ \AA}^3$, crystal density $\rho_{\text{crystal}} = 12.362 \text{ g cm}^{-3}$).^[121]

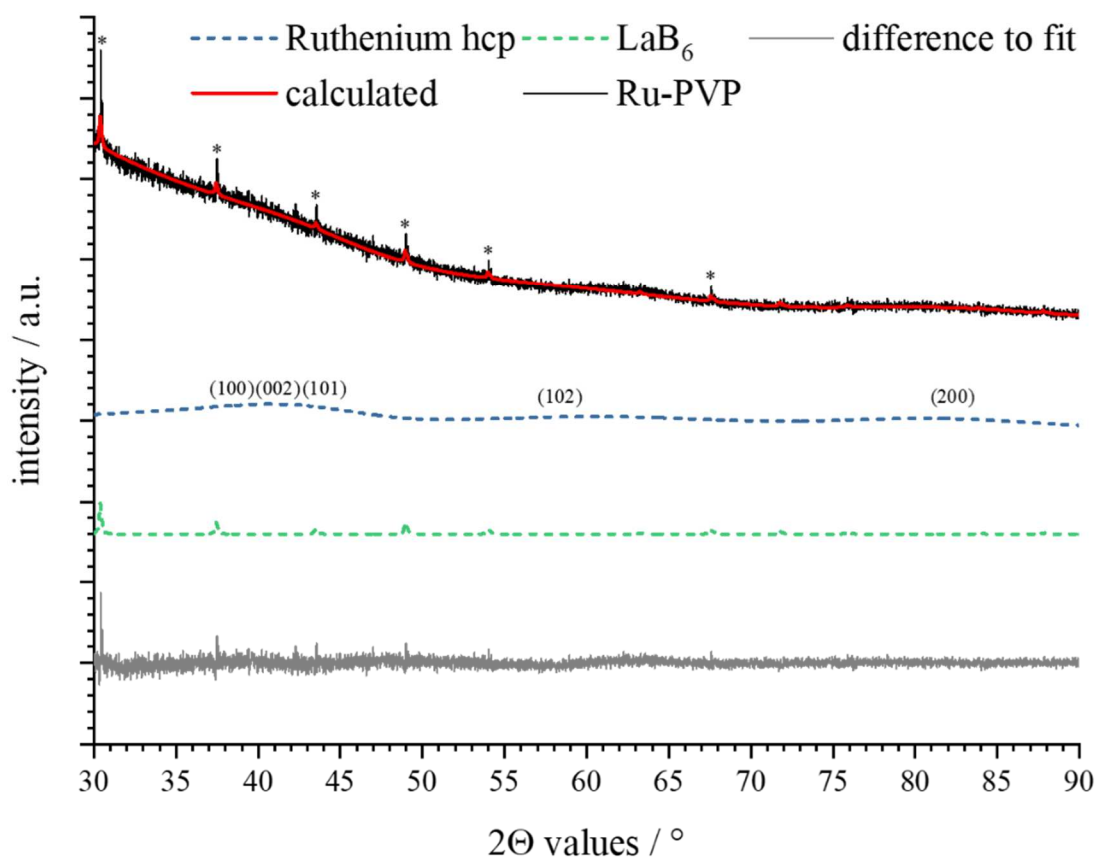


Figure 14: Powder diffraction pattern (not $K\alpha$ stripped) of PVP-stabilised Ru nanoparticles synthesised by reduction with *D*-glucose. The peak profile is calculated using the hcp phase of ruthenium. The asterisks mark the lanthanum hexaboride (LaB₆, PDF 00-034-0427).^[122] The reflexes of ruthenium are compared to powder diffraction file 00-006-0663 (Ru).^[123]

The assignment of the observed reflexes to the reference data is difficult due to the distinct broadening of the diffraction pattern. Small crystallites as well as strong microstrain lead to a high anisotropic broadening which directly corresponds to the small number of lattice planes in the sample.^[124] However, a Rietveld refinement is possible to calculate the crystallographic properties as well as the lattice parameter of ruthenium nanoparticles.

Table 2: Results of the Rietveld refinement from X-ray powder diffraction analysis of freeze-dried Ru nanoparticles. The reference values for the lattice parameters a and c were taken from AMCSD 0020237 (Ru).^[121]

Parameter	Ru hcp
Tabulated lattice parameter a (bulk metals) / Å	2.7058
Tabulated lattice parameter c (bulk metals) / Å	4.2819
Calculated lattice parameter a / Å	2.70(6)
Calculated lattice parameter c / Å	4.23(9)
Calculated cell volume / Å ³	26.8(8)
Calculated crystallite size / nm	1.6(2)
Calculated crystal density / g cm ⁻³	12.4(9)

The lattice constants a and c of PVP-stabilised Ru nanoparticles and the corresponding bulk material are comparable despite the small number of present crystallographic planes in the sample (Table 2). Consequently, the cell volume and crystal density is not influenced much. Notably, the high index (102) and (200) crystallographic planes cannot be identified in the diffraction pattern and the calculation of the microstrain is not possible or practical by Rietveld refinement.

In summary, the wet-chemical synthesis by reduction with *D*-glucose yields spherical-like ruthenium nanoparticles with a hydrodynamic diameter of about 6 nm. The average metal core size is approximately 4 nm. The investigation of the crystallographic structure by X-ray powder diffraction and Rietveld refinement illustrates the presence of the pure

hcp phase of ruthenium with a crystallite size of roughly 1.5 nm. Notably, the small particle size leads to a pronounced peak broadening that has a strong impact on the calculation accuracy.^[124] The obtained particles show no distinct absorption in the visible range corresponding to bulk material of ruthenium.

4.1.2 Rhodium nanoparticles

Rhodium nanoparticles can be synthesised by reduction of the metal cations in the presence of suitable capping agents. The reaction kinetics can be easily manipulated by variation of the synthesis parameters, e.g. temperature or concentration, which leads to different sizes and shapes.^[125, 126] Sponge-like Rh nanoparticles can be achieved by a hydrogen-based reduction in methanol, ethanol, heptanol, and propanol.^[127] Small rhodium nanoparticles (< 3 nm) can be synthesised using a modified phase transfer approach according to the Brust method.^[128] A green synthesis in water based on the reduction of Rh(acac)(CO)₂ (acac = acetylacetonate) in the presence of PVP or polyvinyl alcohol (PVA) leads to polymer-stabilised Rh nanoparticles (2 – 2.5 nm).^[129]

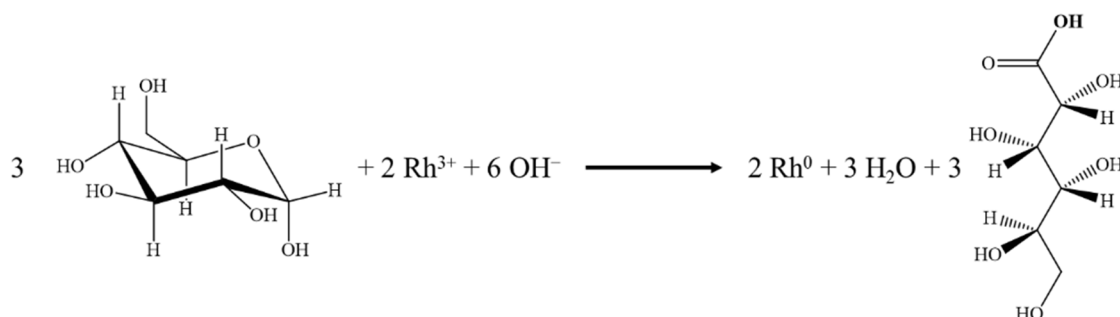


Figure 15: Reaction scheme of the reduction of RhCl₃ with *D*-glucose

Here an adapted synthesis approach based on *D*-glucose as reducing agent is used to synthesize rhodium nanoparticles stabilised by poly(*N*-vinyl pyrrolidone) (PVP) due to the electrochemical similarity to ruthenium. The synthesis leads to small nanoparticles with an average size of 6.2 nm with a standard deviation of ± 1.4 nm in diameter and a PDI of 0.24 as determined by dynamic light scattering (Figure 16). In solution, the capping polymer slows the Brownian motion of the nanoparticles, which results in the determination of an overestimated size by DLS. The zeta potential is $+3 \pm 4$ mV that indicates a steric stabilisation. The average diameter obtained by analytical disc centrifugation is 5.6 nm with a standard deviation of ± 2.0 nm (Figure 17). The polydispersity index calculated from DCS measurement is 0.56. The higher PDI from DCS might indicate an unstable dispersion but an aggregation or precipitation of Rh nanoparticles cannot be observed. Because of the higher density of the rhodium core, the measured size by DCS is slightly underestimated compared to the particle diameter from DLS. Overall, both size distributions correspond to each other with respect to the limitations of the detection method.

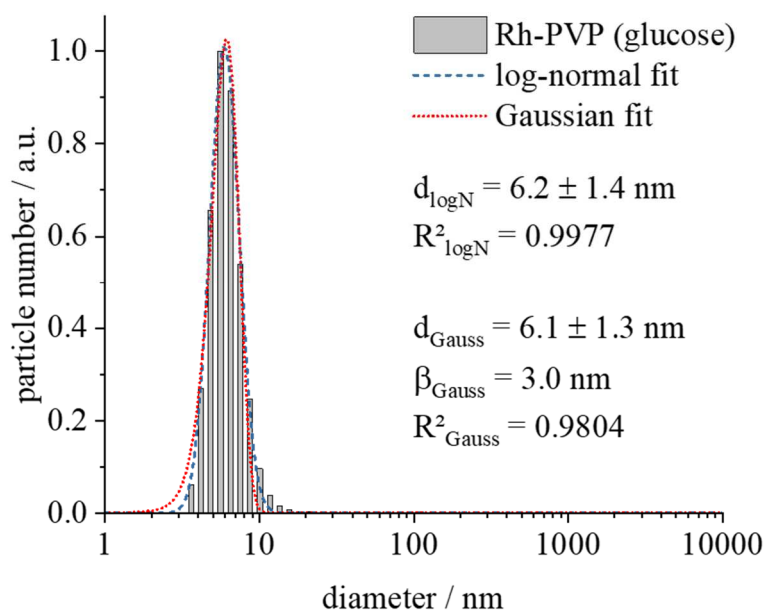


Figure 16: Number-weighted size distribution of PVP-stabilised rhodium nanoparticles synthesised by reduction with *D*-glucose determined by DLS. The peak profile is analysed by a log-normal as well as a Gaussian distribution fit. The PDI is 0.24.

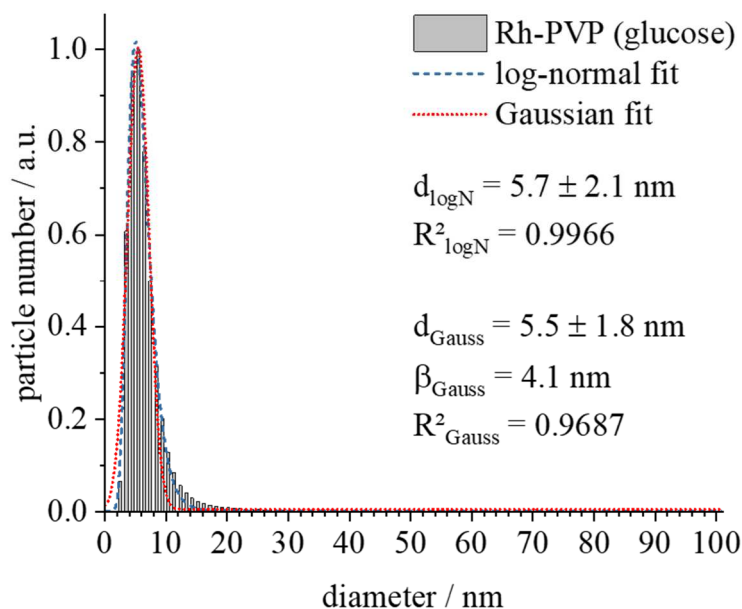


Figure 17: Number-weighted size distribution of PVP-stabilized rhodium nanoparticles synthesised by reduction with *D*-glucose determined by DCS. The peak profile is analysed by a log-normal as well as a Gaussian distribution fit. The PDI is 0.56.

The reduction of Rh^{3+} with glucose leads to a brownish dispersion without any absorption between 400 and 800 nm (Figure 18). The measured UV/vis spectrum corresponds to the absorption of Rh metal as described in literature.^[115] The initial aqueous solution of RhCl_3 shows two absorption maxima at 350 and 450 nm (see black arrows in Figure 18). Compared to the literature, a small blue shift can be observed which can be assigned to the formation of other Rh chloride species in the presence of an excess of chloride.^[130, 131]

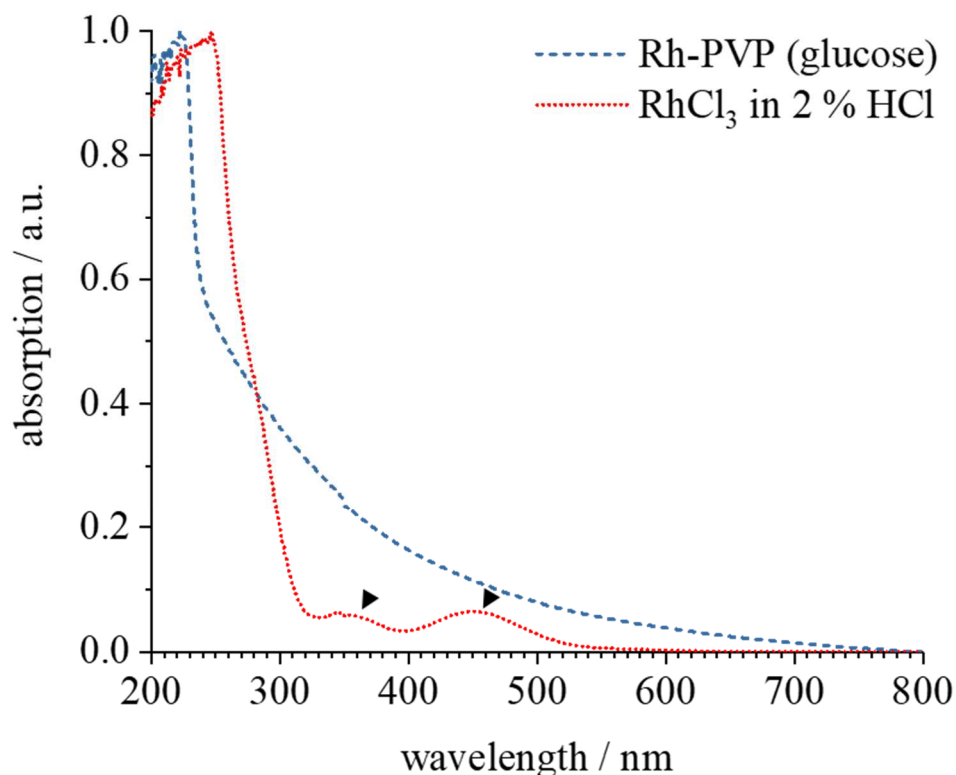


Figure 18: UV/vis spectra of RhCl_3 (in 2 % HCl; red dotted line) and PVP-stabilised rhodium nanoparticles (blue dashed line) synthesised by reduction with *D*-glucose. The data is normalised for better comparison. The black arrows show the absorption of present rhodium chloride species from the precursor RhCl_3 in aqueous medium.

The investigation of the structure and morphology of Rh nanoparticles by high-resolution TEM reveals small nanoparticles with spherical shape (Figure 19). The magnification of a single particle leads to believe that the obtained nanostructures are (partially) single crystalline. The particle size is determined manually by measuring the size of 101 particles and compiling a histogram (Figure 20). The particle size is 4.3 nm with a standard

deviation of ± 1.2 nm in diameter. The sizes determined by DLS, and DCS is in correspondence with the diameter from TEM. All three methods, DLS, DCS and TEM, result in different particle sizes. This behaviour originates from the underlying physical principles and the differences in detection of each analysis method. Additionally, electron microscopy probes dry samples, which influences the nature of the capping polymer. The polymer shell collapses in the vacuum and only the metallic core is depicted.^[95]

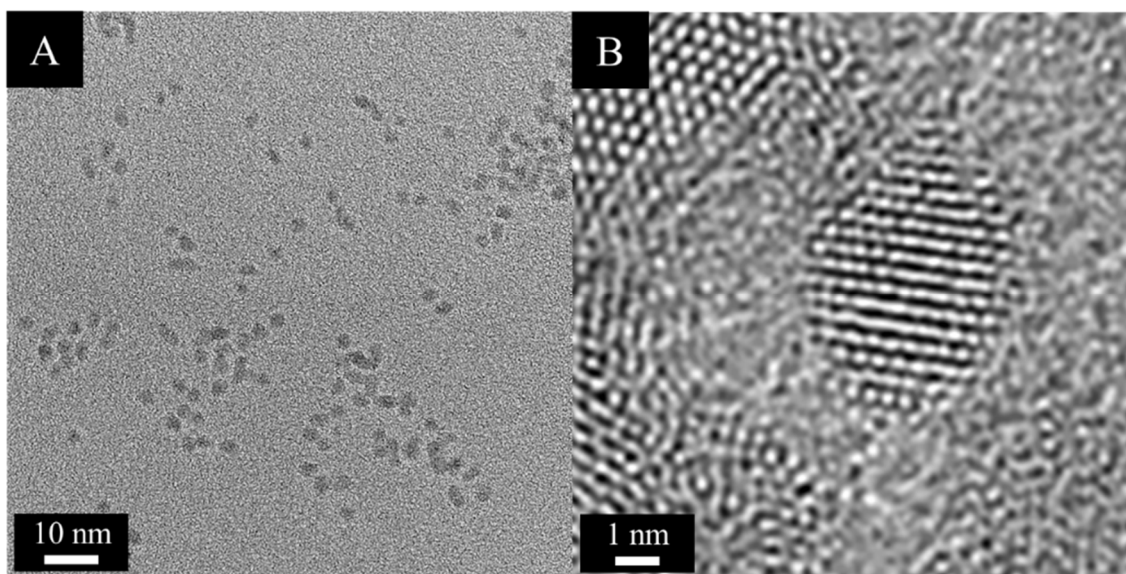


Figure 19: High-resolution TEM image of PVP-stabilised rhodium nanoparticles synthesised by reduction with *D*-glucose (A) and a higher magnification of a single particle (B).

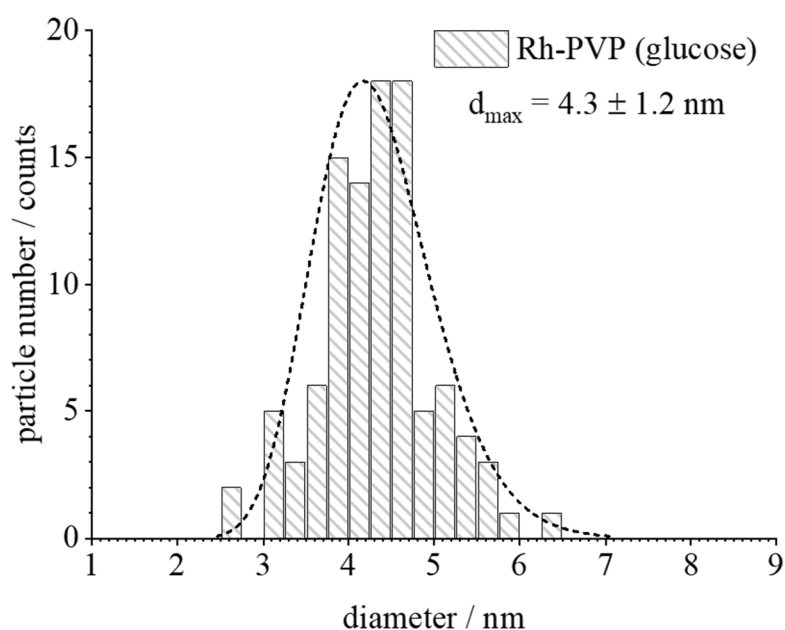


Figure 20: Histogram of particle size analysis from high-resolution TEM of PVP-stabilised Rh nanoparticles synthesised by reduction with *D*-glucose. The size distribution was analysed by a log-normal distribution fit.

For a detailed study the structure of rhodium nanoparticles, X-ray diffraction on a freeze-dried sample is carried out. First, the observable reflexes at 2Θ values 11.7° and 20.8° correspond to the stabilising polymer PVP.^[118, 132, 133] To corroborate this, the diffraction pattern of pure poly(*N*-vinylpyrrolidone) sample was recorded. Two broad but distinct reflexes can be identified at 2Θ values of 10.9° and 20.9° (Figure 22), in accordance with the literature diffraction data of the polymer PVP (Table 3).

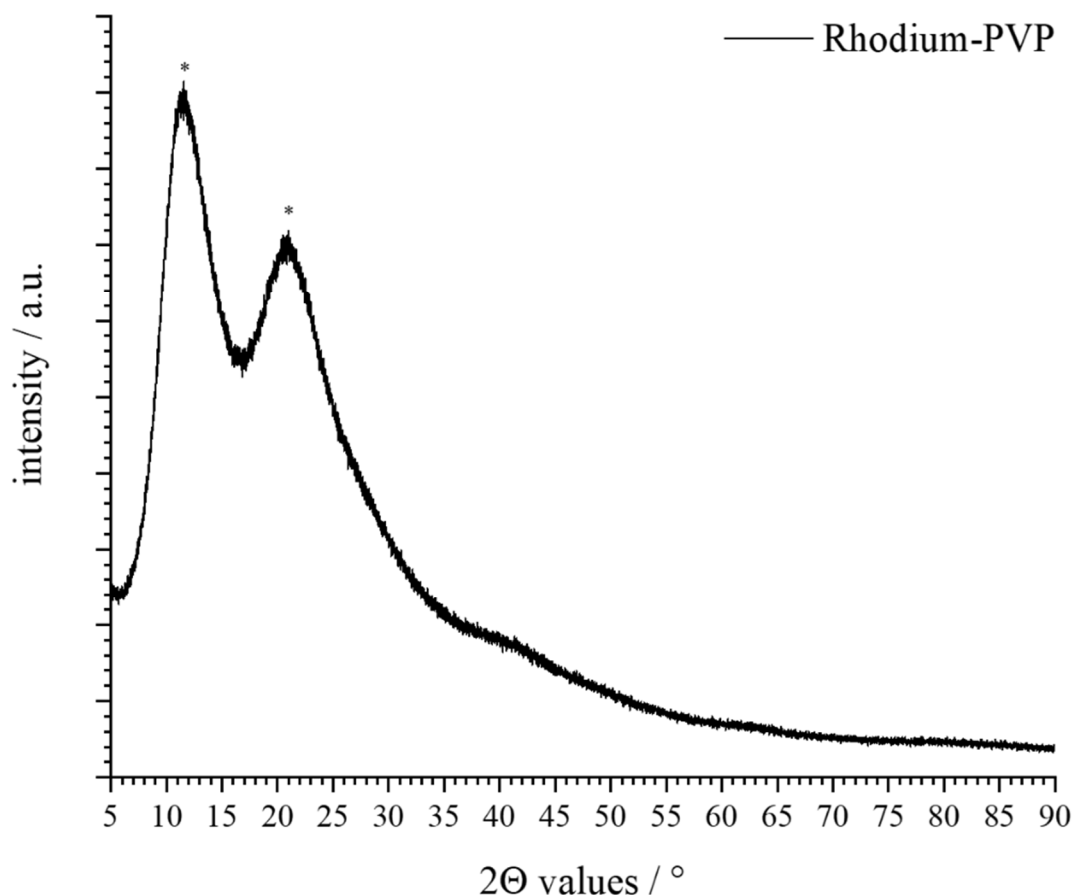


Figure 21: Powder diffraction pattern (not $K\alpha$ stripped) of PVP-stabilised Rh nanoparticles synthesised by reduction with *D*-glucose. The asterisks marked the crystalline phase of poly(*N*-vinylpyrrolidone).

The diffraction pattern of PVP-stabilised Rh nanoparticles furthermore shows a very broad reflex which originates from the coalescence of the scattering on the (111) and (200) crystallographic lattice planes of rhodium. (Figure 23). The small crystallites of Rh with lateral dimensions of around 2 nm lead to the enormous peak broadening. The higher indexed planes cannot be observed or identified. Those are strongly influenced by the anisotropic broadening caused by the very small crystallite size. In addition, the microstrain must be very high because of a strong distortion of the crystal phase. Since the missing reflexes of the high indexed lattice planes, a calculation of the microstrain is not practical. However, a Rietveld refinement is possible to get some information about the structural behaviour of rhodium nanoparticles.

Table 3: Overview of the poly(*N*-vinylpyrrolidone) reflex position between 5-90° from Rietveld refinement. Two phases can be identified and compared to the literature.

Peak phase	Reflex position (observed) $2\Theta / ^\circ$	Reflex position (Qian <i>et al.</i>) ^[118] $2\Theta / ^\circ$	Reflex position (Eisa <i>et al.</i>) ^[134] $2\Theta / ^\circ$	Reflex position (Abou_Taled) ^[132] $2\Theta / ^\circ$
1	10.9	11.7	11	11.5
2	20.9	20.8	21.5	22.5

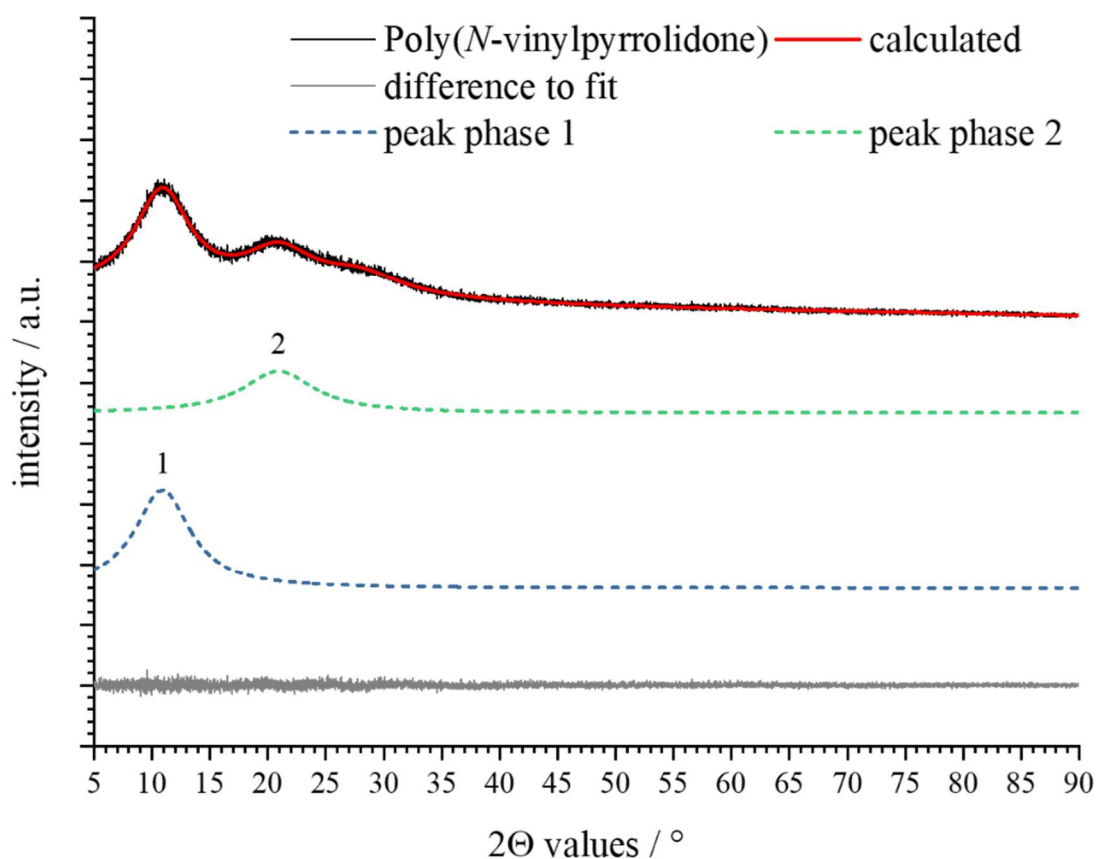


Figure 22: Powder diffraction pattern (not $K\alpha$ stripped) of poly(*N*-vinylpyrrolidone) (PVP). The two peak phases are used to identify the reflex positions.

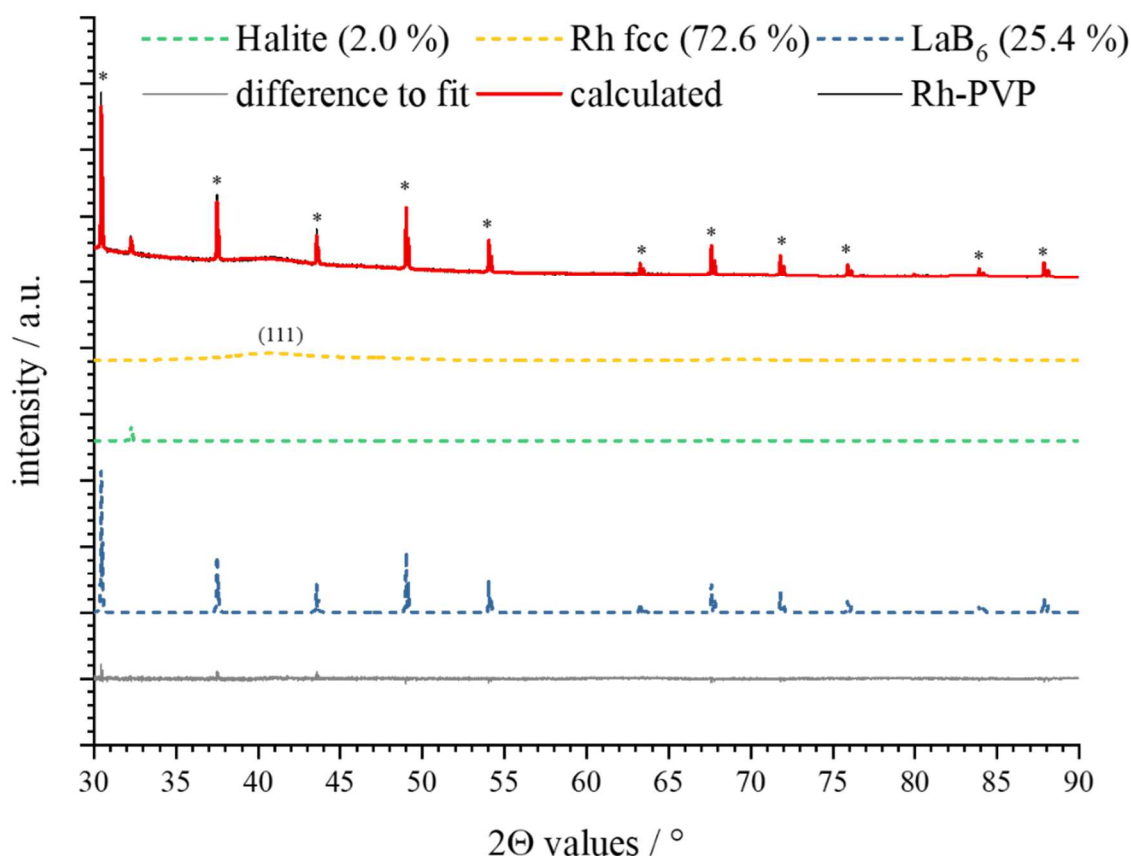


Figure 23: Detailed powder diffraction pattern (not $K\alpha$ stripped) between 2θ values of 30 to 90° and Rietveld refinement of PVP-stabilised Rh nanoparticles synthesised by reduction with glucose. The diffraction pattern is a The peak profile is calculated using the fcc phase of rhodium. The asterisks mark the lanthanum hexaboride (LaB_6 , PDF 00-034-0427).^[122] The reflexes of rhodium are compared to the powder diffraction file 00-005-0685 (Rh).^[135] Minor impurity of sodium chloride is found and compared to the powder diffraction file 00-005-0628 (Halite, NaCl).^[136]

Wondering, an impurity with a small amount of sodium chloride (halite; $\leq 2\%$) is found during the phase analysis notwithstanding any use of sodium containing chemicals during the synthesis process (Figure 23). Except those impurities, the obtained nanoparticles consist of the face-centred phase (fcc) of rhodium. The crystallographic properties are in accordance with the values of the bulk material (space group $Fm\bar{3}m$, lattice constant $a = 3.803 \text{ \AA}$, cell volume $V_{\text{cell}} = 55.006 \text{ \AA}^3$, crystal density $\rho_{\text{crystal}} = 12.424 \text{ g cm}^{-3}$).^[137] The results of the Rietveld refinement are summarised in Table 4.

Table 4: Results of the Rietveld refinement from X-ray powder diffraction analysis of freeze-dried Rh nanoparticles. The reference values for the lattice parameter a were taken from AMCSD 0011159 (Rh).^[137]

Parameter	Rh fcc
Tabulated lattice parameter a (bulk metals) / Å	3.803
Calculated lattice parameter a / Å	3.84(5)
Calculated cell volume / Å ³	56.8(1)
Calculated crystallite size / nm	2.1(2)
Calculated crystal density / g cm ⁻³	12.0(3)

To sum up, the reduction of RhCl₃ with *D*-glucose yields rhodium nanoparticles with a hydrodynamic size of about 6 nm. Those particles have spherical morphology and a diameter of the metallic core approximately 4 nm determined by TEM. The Rietveld refinement of the diffraction pattern must be considered carefully due to the high peak broadening because of the small particle size and missing reflexes of higher indexed lattice planes.^[124] However, the diffraction data confirms the presence of the fcc phase of rhodium. Similar to the bulk metal, the obtained rhodium nanoparticles have no distinct absorption in the visible range (400 to 800 nm).

4.1.3 Palladium nanoparticles

In general, Pd nanoparticles can be obtained either by the polyol process or by wet-, electro-, and sonochemical methods.^[138, 139] The reduction with strong reducing agents like sodium borohydride leads to small particles (< 10 nm).^[140] Amorphous and crystalline palladium nanoparticles (2 – 6 nm) can be synthesised in ethanol using NaBH₄ as reductant.^[141] The thermal decomposition of the Pd-TOP complex (obtained from Pd(acac)₂ in trioctylphosphine (TOP)) leads to spherical, monodisperse Pd nanoparticles (3.5, 5, and 7 nm).^[142] Furthermore, palladium nanocrystals (cubes, tetrahedrons, octahedrons) are available by reduction in the presence of alcohols.^[143]

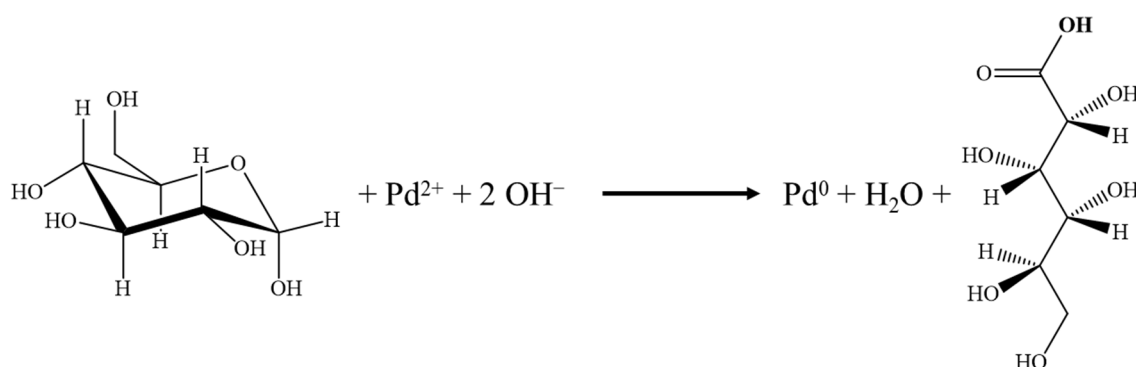


Figure 24: Reaction scheme of the reduction of Pd²⁺ species (here Na₂PdCl₄ or Pd(NO₃)₂) with *D*-glucose.

In this work, palladium nanoparticles are synthesised by reduction of Pd²⁺ in aqueous solution with *D*-glucose. A slightly brownish dispersion is obtained with an average hydrodynamic particle diameter of 12.5 nm with a standard deviation of ±2.6 nm determined by DLS (Figure 25). The PdI is 0.20, which indicates a stable colloidal dispersion. The average diameter from DCS is 8.4 nm with a standard deviation of ±3.7 nm. In fact, it is possible to calculate a polydispersity index from the Gaussian distribution fit but there is no useful interpretation of the high value of 0.95. Considering the correlation coefficient of the Gaussian distribution fit ($R^2 = 0.9791$), no sign of aggregation or polydispersity is observable. In addition, neither aggregation nor precipitation of palladium nanoparticles can be observed which indicates a stable dispersion. Compared to the size from DCS, dynamic light scattering overestimates the hydrodynamic diameter by a factor of 1.5. This is because the polymer is swollen in water, which slows the Brownian motion in solution.

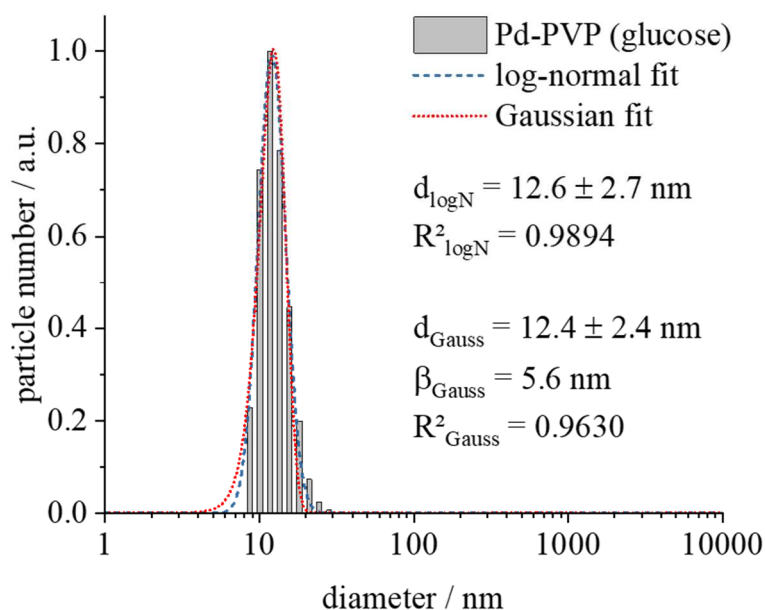


Figure 25: Size distribution of PVP-stabilised palladium nanoparticles synthesised by reduction with *D*-glucose determined by DLS. The peak profile is analysed by a log-normal as well as a Gaussian distribution fit. The PdI is 0.20.

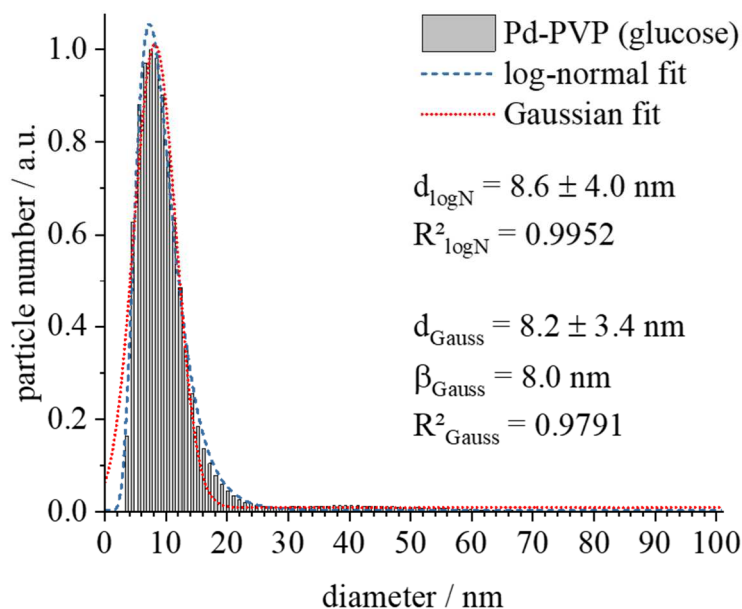


Figure 26 Size distribution of PVP-stabilised palladium nanoparticles synthesised by reduction with *D*-glucose determined by DCS. The peak profile is analysed by a log-normal as well as a Gaussian distribution fit. The PdI is 0.95.

The UV/vis spectra of aqueous solution of Na_2PdCl_4 and $\text{Pd}(\text{NO}_3)_2$ show the typical absorption behaviour (see black arrows in Figure 27). In the case of H_2PdCl_4 the absorption under 300 nm as well as at 450 nm can be ascribed to the absorption of the PdCl_4^{2-} anion.^[144, 145] The peak maximum at 380 nm in the absorption spectrum of $\text{Pd}(\text{NO}_3)_2$ is attributed to a d-d transition inside the aqua complex $\text{Pd}(\text{H}_2\text{O})_4^{2+}$.^[146] The absorption behaviour at 285 nm and below 240 nm can be assigned to the square planar Pd complex $\text{Pd}(\text{NO}_2)_4^{2-}$.^[147] The palladium nanoparticles show no distinct absorption in visible range (400 to 800 nm) which correspond very well to the electronic spectra of Pd metal as described in literature.^[115]

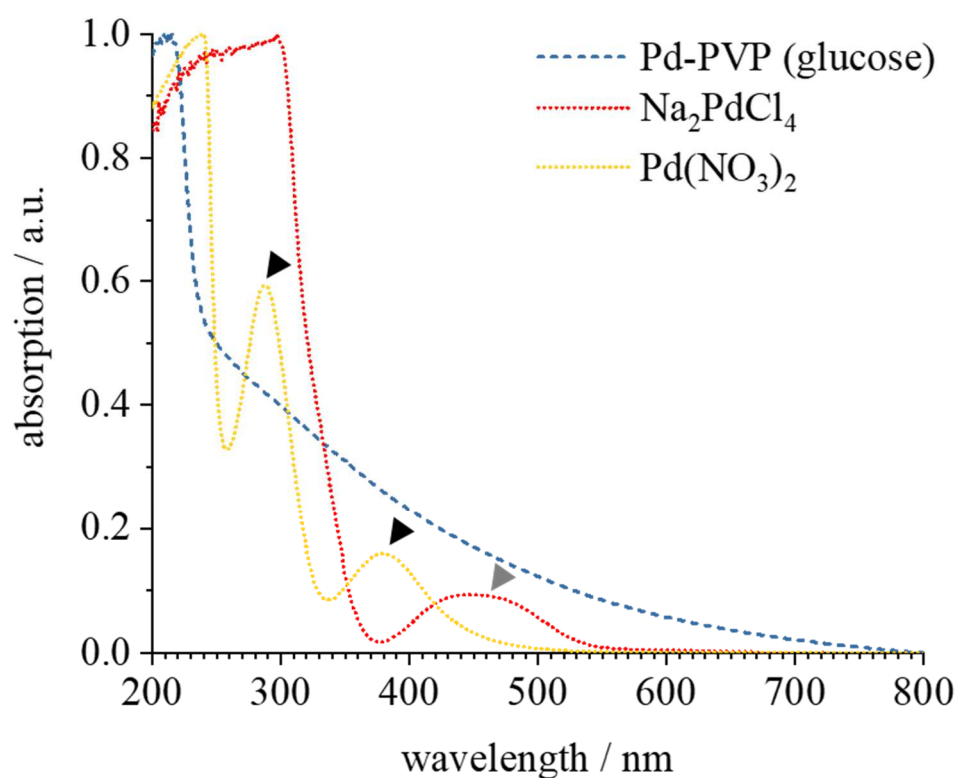


Figure 27: UV/vis spectra of Na_2PdCl_4 (red dotted line), $\text{Pd}(\text{NO}_2)_3$ (yellow dotted line), and PVP-stabilised palladium nanoparticles (blue dashed line) synthesised by reduction with *D*-glucose. The data are normalised for better comparison. The grey arrow shows the absorption peaks of the PdCl_4^{2-} anion from the precursors Na_2PdCl_4 . The black arrows show the absorption peaks of $\text{Pd}(\text{H}_2\text{O})_4^{2+}$ and $\text{Pd}(\text{NO}_2)_4^{2-}$ complexes from the precursor $\text{Pd}(\text{NO}_3)_2$.

The reduction of Pd²⁺ with *D*-glucose results in spherical-like particles with an evident single-crystalline structure (Figure 28). The size of Pd nanoparticles are determined manually by measuring the size of 101 particles and compiling a histogram (Figure 29). The average diameter is 4.4 nm with a standard deviation of ± 1.2 nm. The size determined by DLS and DCS compared to TEM is overestimated by a factor of 3 and 2, respectively. This deviation originates from the measurement characteristics. In scanning as well as transmission electron microscopy, only the particle core (here: Pd) is depicted because of the collapsed polymer shell in the high vacuum.

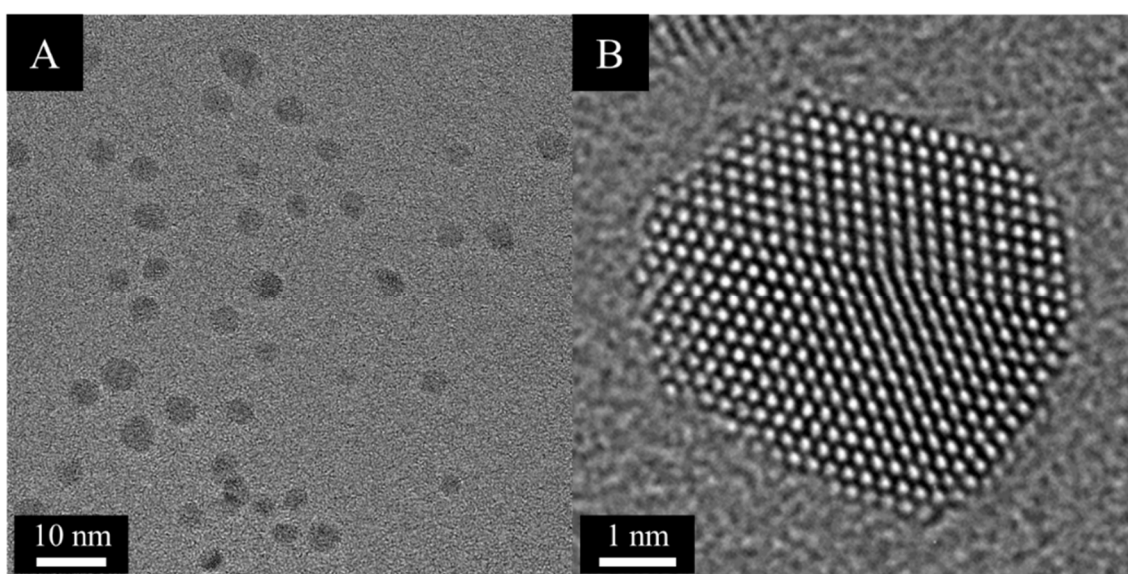


Figure 28: High-resolution TEM image of PVP-stabilised palladium nanoparticles synthesised by reduction with *D*-glucose (A) and higher magnification of a single particle indicating a single crystalline structure without any grain boundaries (B).

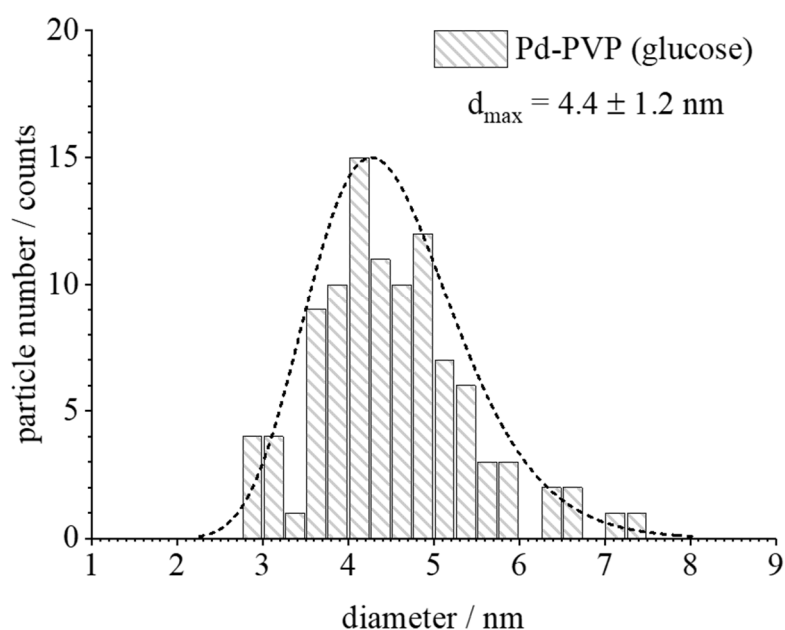


Figure 29: Histogram of particle size analysis from high-resolution TEM of PVP-stabilised Pd nanoparticles synthesised by reduction with *D*-glucose. The size distribution was analysed by a log-normal distribution fit.

For the investigation of structural parameter (e.g. lattice constant, crystallite size) powder X-ray diffraction is performed. All expected reflexes of the fcc phase of palladium could be observed (Table 5). The small shift of observed reflex positions to smaller 2Θ values is a result of a small extension of the unit cell and an increase in the lattice parameter (Table 6).

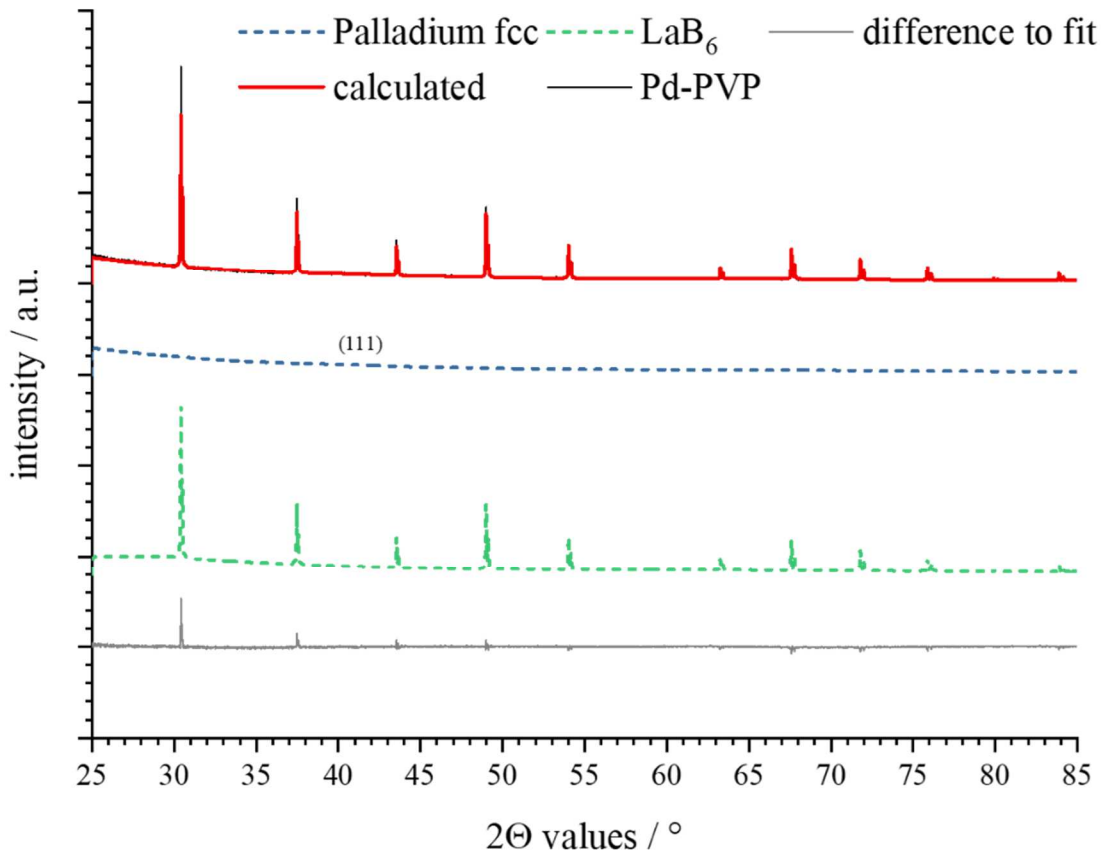


Figure 30: Powder diffraction pattern (not $K\alpha$ stripped) and Rietveld refinement of PVP-stabilised Pd nanoparticles synthesised by reduction with glucose. The peak profile is calculated using the fcc phase of palladium. The asterisks mark the lanthanum hexaboride (LaB_6 , PDF 00-034-0427).^[122] The reflexes of palladium are compared to the powder diffraction file 00-046-1043 (Pd).^[148]

The sharp reflexes in the diffraction pattern (see asterisks in Figure 30) derive from lanthanum hexaboride that was added to the sample as an internal standard for the determination of the instrumental broadening. This can be ignored because of the small particle size that leads to a higher broadening from the sample crystals. For a successful Rietveld refinement, the addition of LaB_6 was renounced because of the strong anisotropic broadening and the small X-ray scattering intensity of the sample (Figure 31). The calculated crystallographic properties correlate with the data of the bulk material (space group $\text{Fm}\bar{3}\text{m}$, lattice constant $a = 3.8930 \text{ \AA}$, cell volume $V_{\text{cell}} = 59.000 \text{ \AA}^3$, crystal density $\rho_{\text{crystal}} = 11.979 \text{ g cm}^{-3}$).^[149]

Table 5: Overview of the palladium fcc reflex position between 25-85° from Rietveld refinement in comparison to the ICDD database (Pd, PDF 00-046-1043).^[148]

Reflex position (observed) $2\Theta / ^\circ$	Reflex position (reference) $2\Theta / ^\circ$	Lattice plane (hkl)
40.161	40.122	(111)
46.469	46.664	(200)
67.520	68.118	(220)
81.292	82.099	(311)

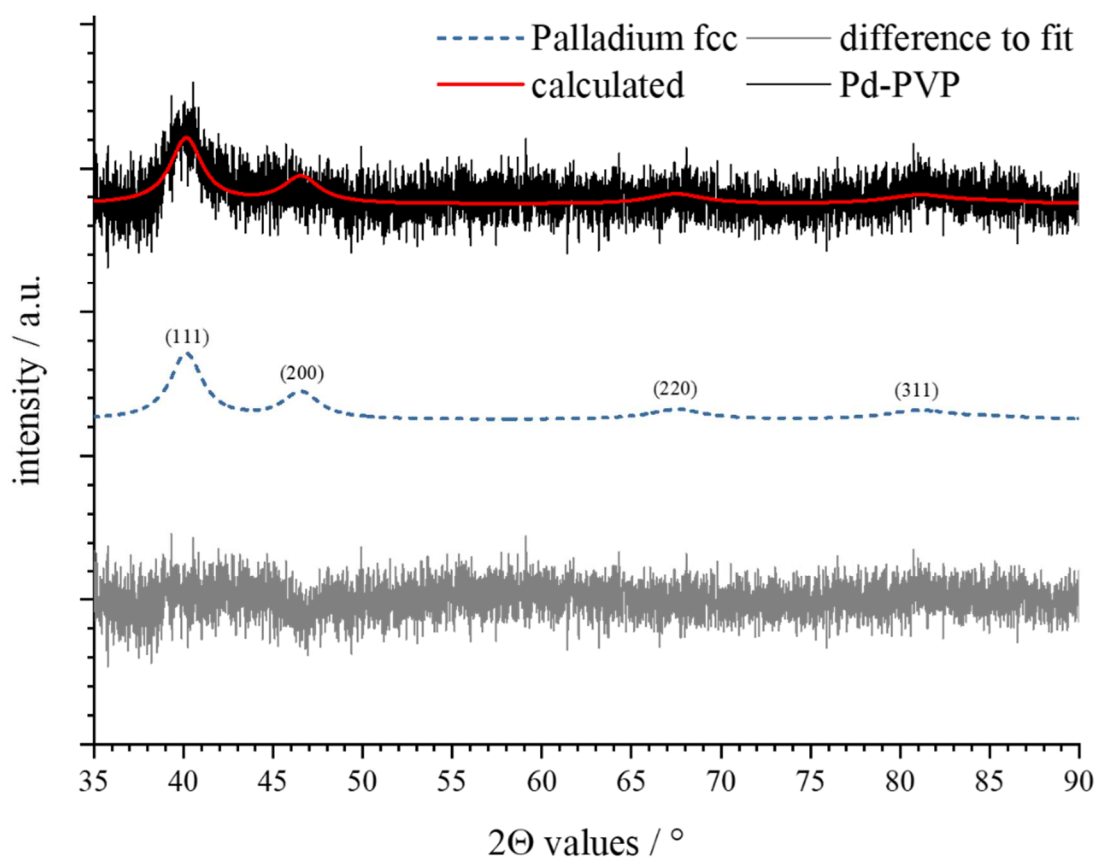


Figure 31: Powder diffraction pattern (not $K\alpha$ stripped) and Rietveld refinement of PVP-stabilised Pd nanoparticles synthesised by reduction with glucose. The peak profile is calculated using the fcc phase of palladium.

In good agreement with the diameter from TEM, the calculated crystallite size from the Rietveld refinement illustrates the single-crystalline structure of obtained palladium nanoparticles from reduction with *D*-glucose.

Table 6: Results of the Rietveld refinement from X-ray powder diffraction analysis of freeze-dried Pd nanoparticles. The reference values for the lattice parameter a were taken from AMCS D 0014146 (Pd).^[149]

Parameter	Pd fcc
Tabulated lattice parameter a (bulk metals) / Å	3.8930
Calculated lattice parameter a / Å	3.917(2)
Calculated cell volume / Å ³	60.12(9)
Calculated crystallite size / nm	5.0(7)
Calculated crystal density / g cm ⁻³	11.76(18)

In summary, it can be stated that the reduction of Pd(NO₃)₂ with *D*-glucose leads to uniform palladium nanoparticles with an average size of about 8 nm obtained from DCS analysis. The hydrodynamic diameter from dynamic light scattering is roughly 12 nm, which is slightly larger than from DCS. The difference between both arises from the effect of the hydration shell around the particles. In DLS the hydrated polymeric layer slows the Brownian motion resulting in an overestimated size, while in DCS the polymer shell increases the sedimentation time resulting in smaller diameters because of the lower effective density of the particles.^[113] The average metal core size is approximately 4 nm determined by HR-TEM. The investigation of the crystallographic structure by X-ray powder diffraction and Rietveld refinement illustrates the presence of the pure fcc phase of palladium with a crystallite size of around 5 nm. The obtained particles show no distinct absorption in the visible range corresponding to bulk material of Pd.

4.1.4 Silver nanoparticles

A numerous different methods are available to investigate silver nanostructures.^[35, 150] Bottom-up syntheses of Ag nanoparticles can be performed either in aqueous solution or in organic solvents like ethylene glycol (EG), and oleylamine (cis-1-amino-9-octadecene, OAm).^[151] A variety of different morphologies and sizes can be realised by using additives and changing reaction conditions.^[35, 150, 152-158] Small silver nanoparticles (3-6 nm) are often used as a precursor for seed-mediated syntheses for subsequent more complex morphologies, as core for bimetallic nanostructures, or as sacrificial seed for hollow particles of a more noble metal, e.g. gold.^[152, 159-162] In addition to solution based methods, microwave-assisted syntheses of ultra-small silver nanoparticles are commonly available.^[163]

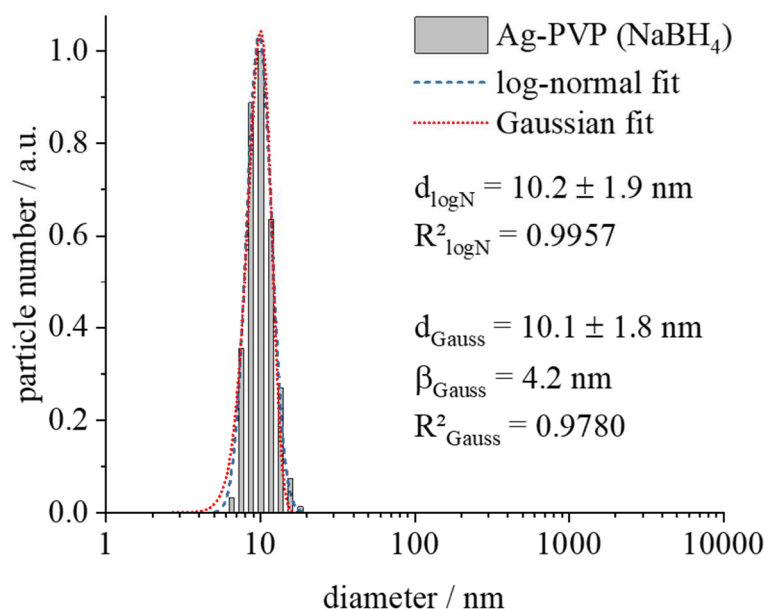


Figure 32: Number-weighted size distribution PVP-stabilized silver nanoparticles synthesised by reduction with sodium borohydride determined by DLS. The peak profile is analysed by a log-normal as well as a Gaussian distribution fit. The PDI is 0.17.

Here, silver nanoparticles are synthesised by reduction of AgNO_3 with sodium borohydride in the presence of citrate and PVP. The average hydrodynamic diameter is 10.2 nm with a standard deviation ± 1.9 nm determined by DLS. The obtained particles are well

dispersed, indicating by a low PdI value of 0.17. In addition, the particle size is determined by DCS. The average size is 5.5 nm with a standard deviation of ± 1.5 nm in diameter. The polydispersity index from analytical disc centrifugation is 0.35.

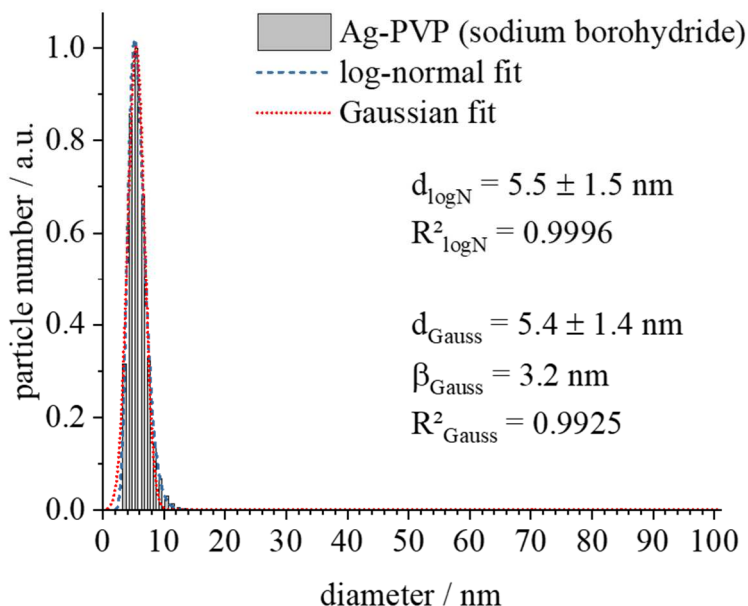


Figure 33: Number-weighted size distribution of PVP-stabilized silver nanoparticles synthesised by reduction with sodium borohydride determined by DCS. The peak profile is analysed by a log-normal as well as a Gaussian distribution fit. The PdI is 0.35.

The diameter from DLS is two times bigger than from DCS, which points towards the presence of a swollen hydrated polymer shell around the silver nanoparticles. The UV/vis spectrum AgNO_3 shows an absorption maximum at 302 nm, which is caused by the electronic structure of the NO_3^- anion (black arrow, Figure 34).^[164, 165] After reduction, the absorption of the NO_3^- anion is disappeared and the silver nanoparticles show the typical SPR absorption of Ag with a maximum around 395 nm.^[115] Silver nanoparticles stabilised with polyethyleneimine (PEI) or poly(acrylic acid) (PAA) show similar absorption behaviour with maxima around 400 nm.^[163, 166]

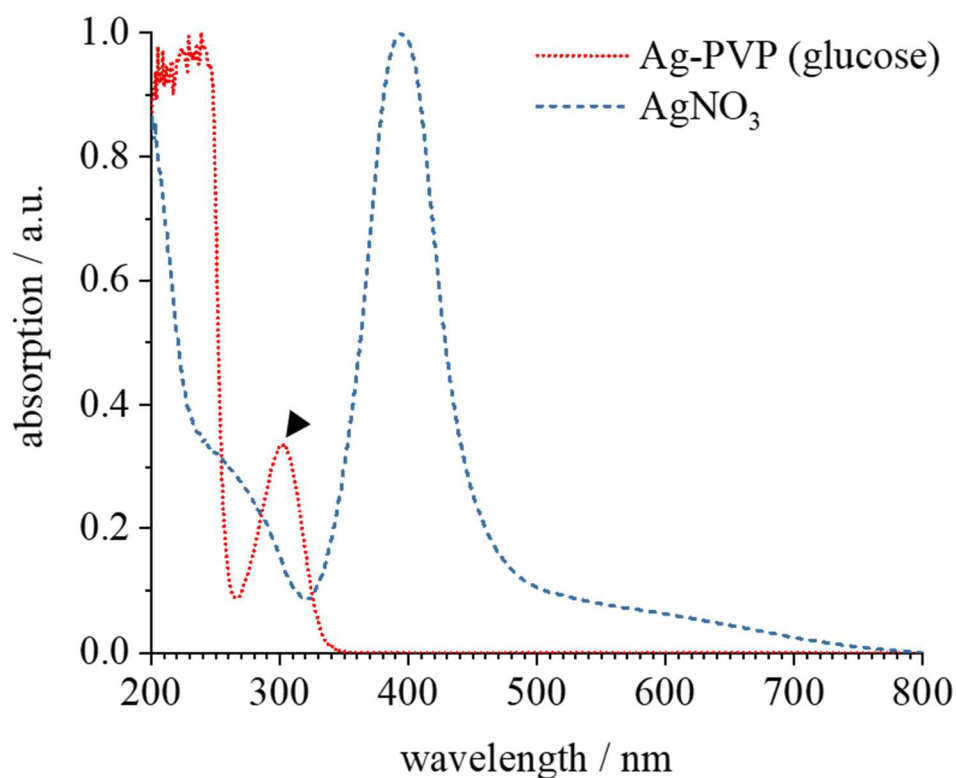


Figure 34: UV/vis spectra of AgNO₃ (red dotted line) and PVP-stabilised silver nanoparticles (blue dashed line) synthesised by reduction with *D*-glucose. The data are normalised for better comparison. The black arrow shows the absorption of NO₃⁻ anion from the precursor AgNO₃ in aqueous medium.

High-resolution TEM images show spherical-like particles of silver that appear to be more or less single crystalline. However, on a closer look most of the particles have stacking faults, which can be observed by visible grain boundaries (white arrows in Figure 35). The size of Ag particles are determined manually by measuring the size of 113 particles and compiling a histogram from TEM (Figure 33). The average size is 8.0 nm with standard deviation of ± 1.3 nm in diameter.

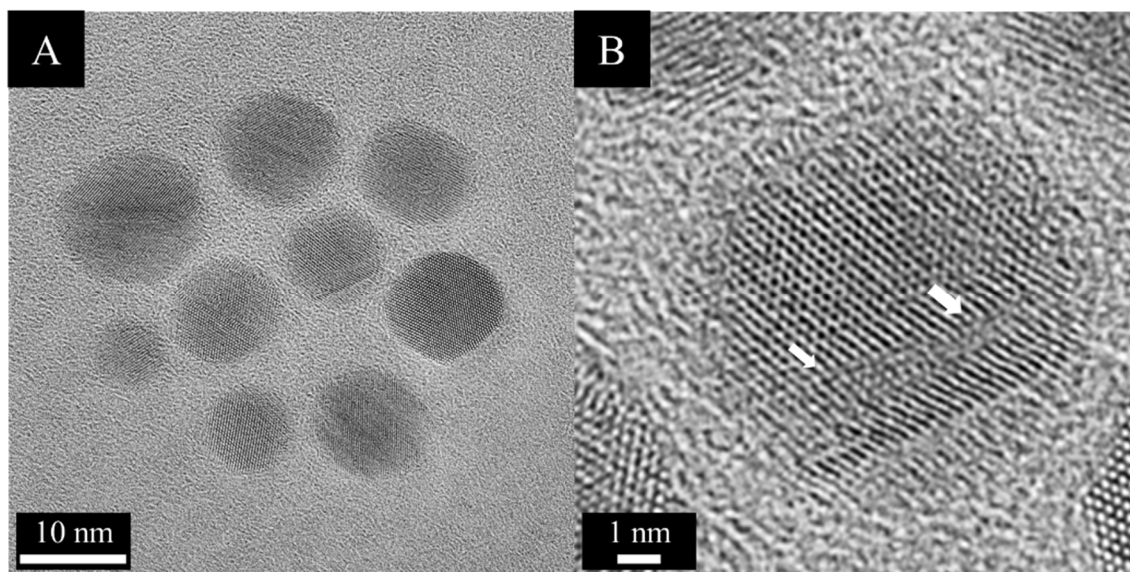


Figure 35: High-resolution TEM image of PVP-stabilised silver nanoparticles synthesised by reduction with sodium borohydride (A) and higher magnification of a single particle indicating a single crystalline structure with typical stacking faults (B, marked with white arrows).

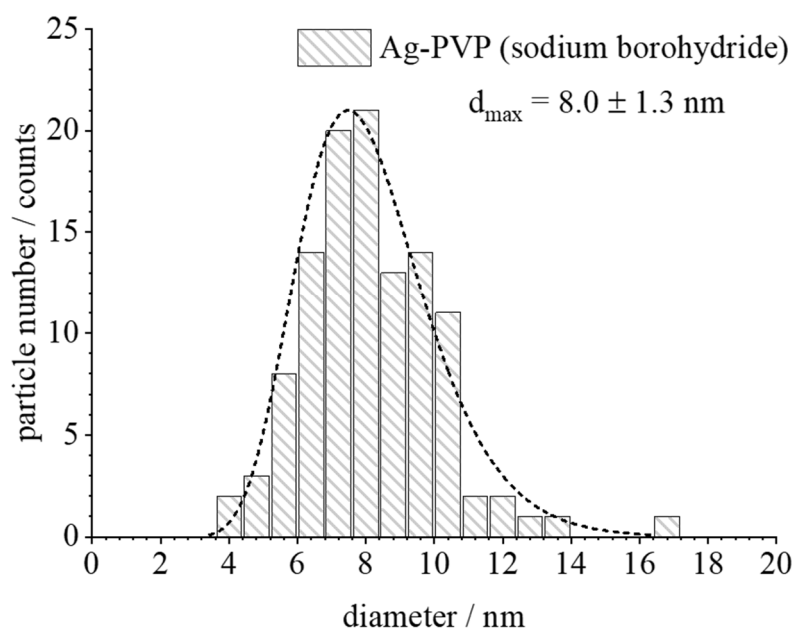


Figure 36: Histogram of particle size analysis from high-resolution TEM of PVP-stabilised Ag nanoparticles synthesised by reduction with sodium borohydride. The size distribution was analysed by a log-normal distribution fit.

The stacking faults might be a result of the very fast crystallisation of Ag in the presence of the strong reducing agent sodium borohydride. In dependence of the reduction potential of NaBH_4 ,^[167, 168] the number of silver atoms will be increase which leads to an immediately nucleation and crystallisation of particles. Therefore, the nucleation and growth process is kinetically driven which results in a high number of stacking faults. Further analysis of the crystallographic properties and the phase purity of obtained Ag nanoparticles, an X-ray diffraction pattern of a freeze-dried sample is recorded. All expected reflexes of the silver fcc lattice in the 2Θ range of 25-85° are observed and can be associated to the literature (Table 7).

Table 7: Overview of the silver fcc reflex position between 25-85° from Rietveld refinement in comparison to the ICDD database (Ag, PDF 00-004-0783).^[169]

Reflex position (observed) $2\Theta / ^\circ$	Reflex position (reference) $2\Theta / ^\circ$	Lattice plane (hkl)
38.150	38.110	(111)
44.343	44.281	(200)
64.521	64.438	(220)
77.500	77.464	(311)
81.631	81.529	(222)

With respect to the stacking faults which are observable in the TEM images, the Rietveld refinement of the obtained diffraction pattern using only the fcc phase of silver are not sufficient for an adequate description of the structural behaviour (Figure 37). Hence, an additional hcp phase of Ag is used for a better refinement. The use of a second phase to model the anisotropic shape of the reflexes, especially of the (111) and (200)-lattice plane reflex is necessary and is quite common in the investigation of the ultrastructure of silver nanoparticles.^[170, 171] Notably, it is not clearly proven that the crystallite defects and stacking faults develop a strict hcp phase of silver, but the modelling with an additional hcp phase during the Rietveld refinement yields good results. All crystallographic properties

of the fcc phase of silver nanoparticles correspond to the data of the bulk material (space group $Fm\bar{3}m$, lattice constant $a = 4.0860 \text{ \AA}$, cell volume $V_{\text{cell}} = 68.217 \text{ \AA}^3$, crystal density $\rho_{\text{crystal}} = 10.501 \text{ g cm}^{-3}$).^[172] Additionally, the results from Rietveld refinement for the observed hcp phase are in good agreement with the literature data for the bulk material of hcp silver (space group $P63/mmc$, lattice constants $a = 2.8800 \text{ \AA}$ and $c = 9.6200 \text{ \AA}$, cell volume $V_{\text{cell}} = 69.102 \text{ \AA}^3$, crystal density $\rho_{\text{crystal}} = 10.248 \text{ g cm}^{-3}$).^[173] The calculated lattice parameters by Rietveld refinement are summarised in Table 8.

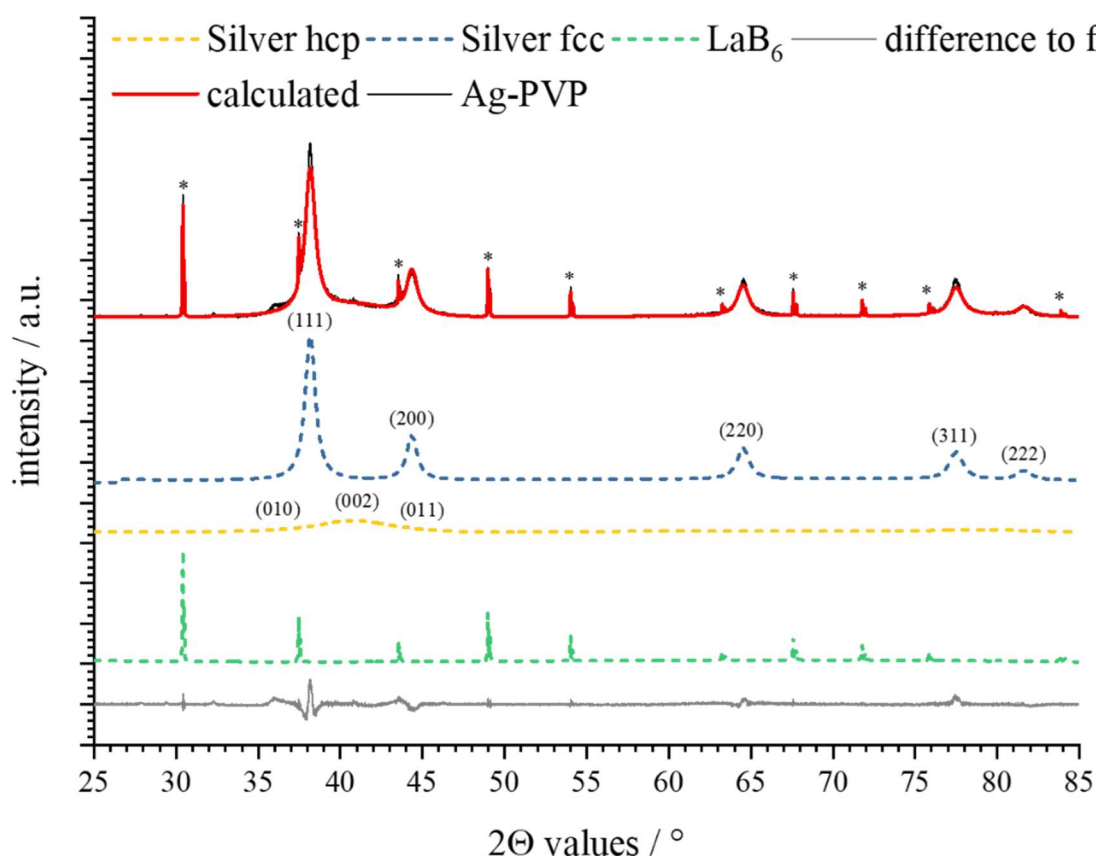


Figure 37: Powder diffraction pattern (not $K\alpha$ stripped) and Rietveld refinement of PVP-stabilised Ag nanoparticles synthesised by reduction with glucose. The peak profile is calculated using the fcc and hcp phase of silver.^[172, 173] The asterisks mark the lanthanum hexaboride (LaB_6 , PDF 00-034-0427).^[122] The reflexes of silver are compared to the powder diffraction file 00-004-0783 (Ag).^[169]

The sharp reflexes originate from additional lanthanum hexaboride (LaB_6 , marked with asterisks, Figure 37) for investigation of the instrumental broadening, which is negligible. Nanocrystalline materials lead to broader diffraction reflexes because of natural lattice

defects and interference effects.^[124] A slight shift in the reflex position to higher 2Θ values can be observed caused by a decrease of the lattice constants. This observation is well known for metal nanoparticles due to the decrease of available crystallographic lattice planes.^[174, 175]

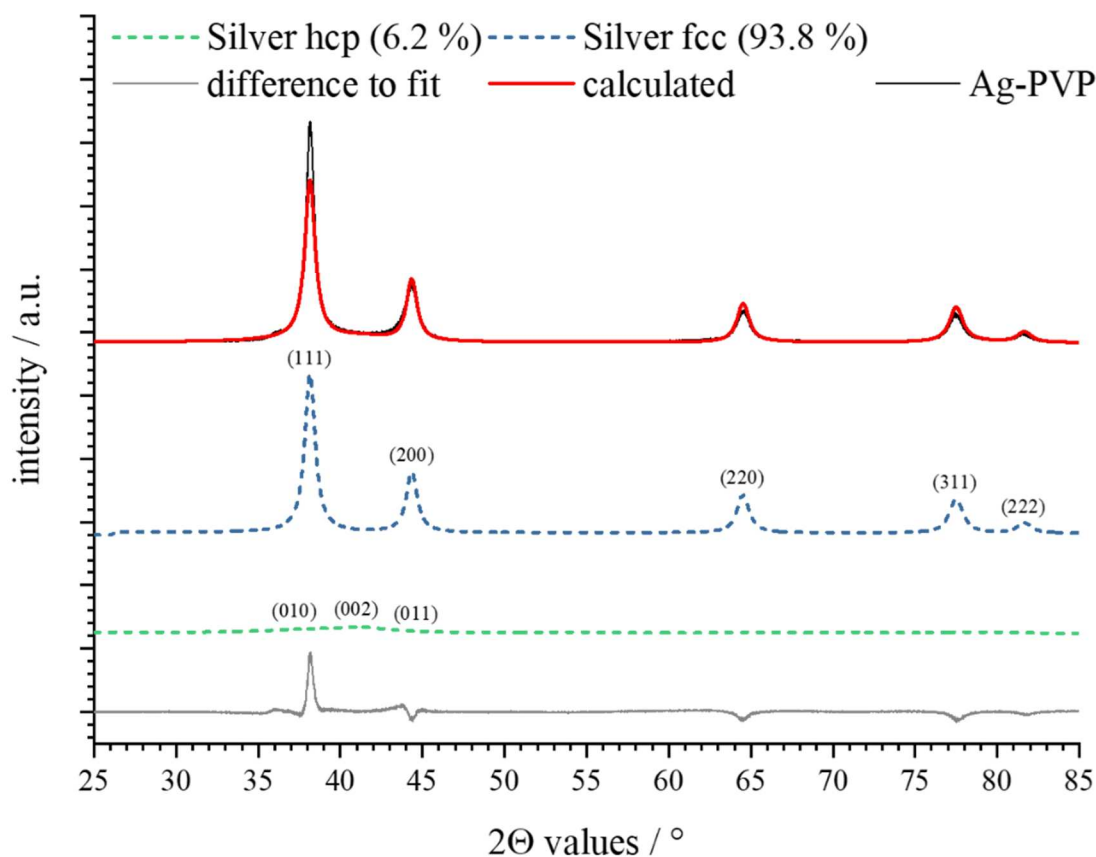


Figure 38: Detailed powder diffraction pattern (not $K\alpha$ stripped) in the 2Θ range between 25 to 85° and Rietveld refinement of PVP-stabilised Ag nanoparticles synthesised by reduction with glucose. The peak profile is calculated using the fcc and hcp phase of silver.^[172, 173]

Table 8: Results of the Rietveld refinement from X-ray powder diffraction analysis of freeze-dried Ag nanoparticles. The reference values for the lattice parameter a were taken from AMCSD 0013118 (Ag fcc) and AMCSD 0018575 (Ag hcp).^[172, 173]

Parameter	Ag fcc	Ag hcp
Tabulated lattice parameter a (bulk metals) / Å	4.086	2.880
Tabulated lattice parameter c (bulk metals) / Å	---	9.620
Calculated lattice parameter a / Å	4.0850(1)	2.862(7)
Calculated lattice parameter c / Å	---	4.71(2)
Calculated cell volume / Å ³	68.169(5)	66.8(2)
Calculated crystallite size / nm	13.15(8)	2.16(7)
Calculated crystal density / g cm ⁻³	10.51(1)	10.72(1)

In summary, it can be said, therefore, that the synthesis of Ag nanoparticles with sodium borohydride yields uniform particles within the size of about 5 to 10 nm in hydrodynamic diameter. The narrow size distributions from DLS as well as DCS indicate a monodisperse system. Quasi-spherical and single crystalline nanoparticles (metallic core size 8 nm) can be observed, but high-resolution TEM analysis also reveals that the obtained particles have a considerable amount of stacking faults. Those could be identified as a hexagonal silver phase (Ag hcp) that could be quantified by Rietveld refinement of the powder diffraction pattern (hcp 6 %, fcc 94 %). The particles show an absorption in the visible range with an absorption maximum at 395 nm corresponding to the SPR of silver.

4.1.5 Osmium nanoparticles

Osmium nanoparticles with defined sizes between 1.5 to 50 nm deposited on a graphitic surface can be synthesised using electron-beam irradiation.^[176] The thermal or photolytic decomposition of osmium carbonyl precursors dissolved in ionic liquids leads to very small Os nanoparticles (<3 nm).^[177, 178] A microwave-assisted synthesis in aqueous methanol yields in very small osmium electro catalysts.^[179]

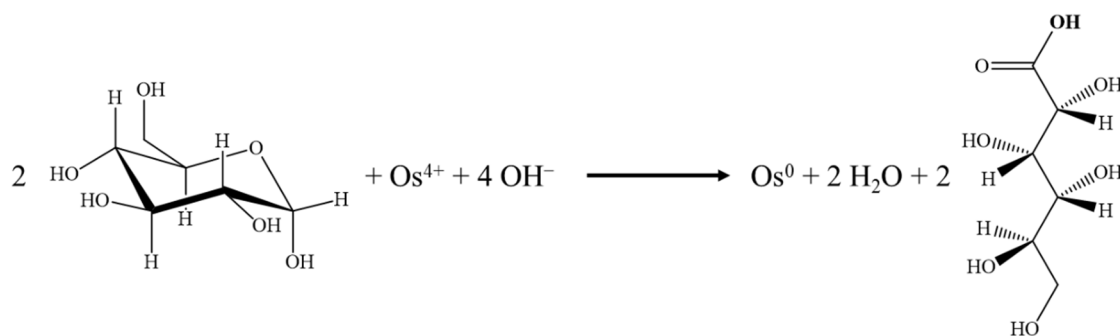


Figure 39: Reaction scheme of the reduction of H_2OsCl_6 with D -glucose.

In the present work, the wet-chemical reduction of the ionic osmium precursor H_2OsCl_6 with D -glucose in the presence of PVP results in nanoparticles with a hydrodynamic diameter of 13.4 nm with a standard deviation of ± 3.4 nm determined by DLS (Figure 40). The colloids are well dispersed which is indicated by a low PdI value of 0.31. The sizes of osmium particles are further investigated by analytical disc centrifugation. The diameter from DCS is 7.5 nm with a standard deviation of ± 3.6 nm. The very high polydispersity index of 1.2 suggests an unstable dispersion. However, neither an aggregation nor precipitation of osmium particles dispersed in ultrapure water is observed.

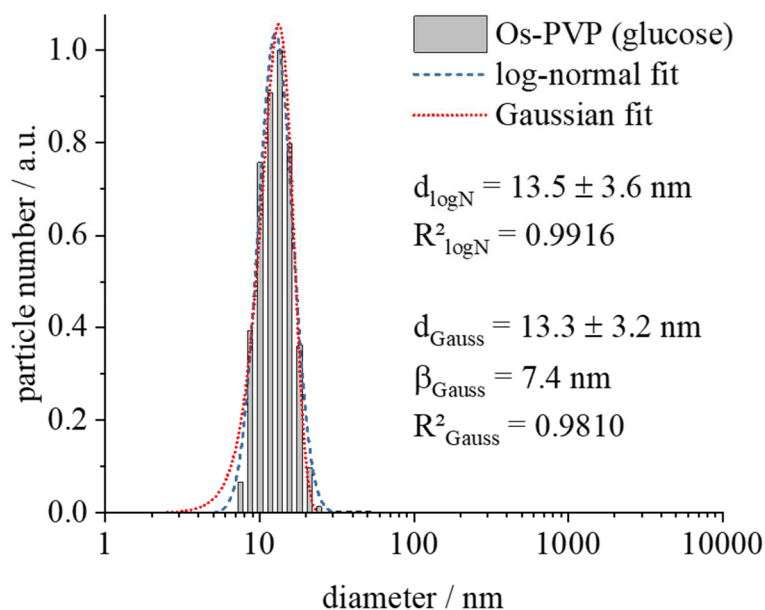


Figure 40: Number-weighted size distribution of PVP-stabilized osmium nanoparticles synthesised by reduction with *D*-glucose determined by DLS. The peak profile is analysed by a log-normal as well as a Gaussian distribution fit. The PdI is 0.31.

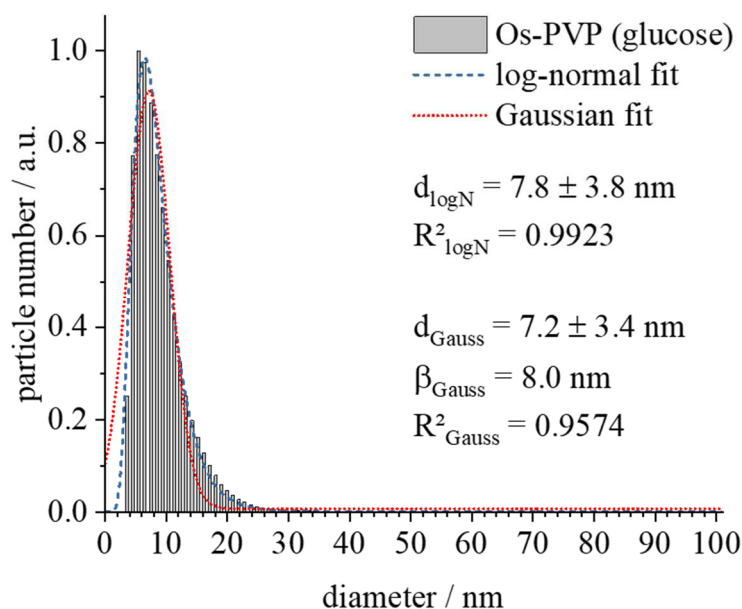


Figure 41: Number-weighted size distribution of PVP-stabilized osmium nanoparticles synthesised by reduction with *D*-glucose determined by DCS. The peak profile is analysed by a log-normal as well as a Gaussian distribution fit. The PdI is 1.2.

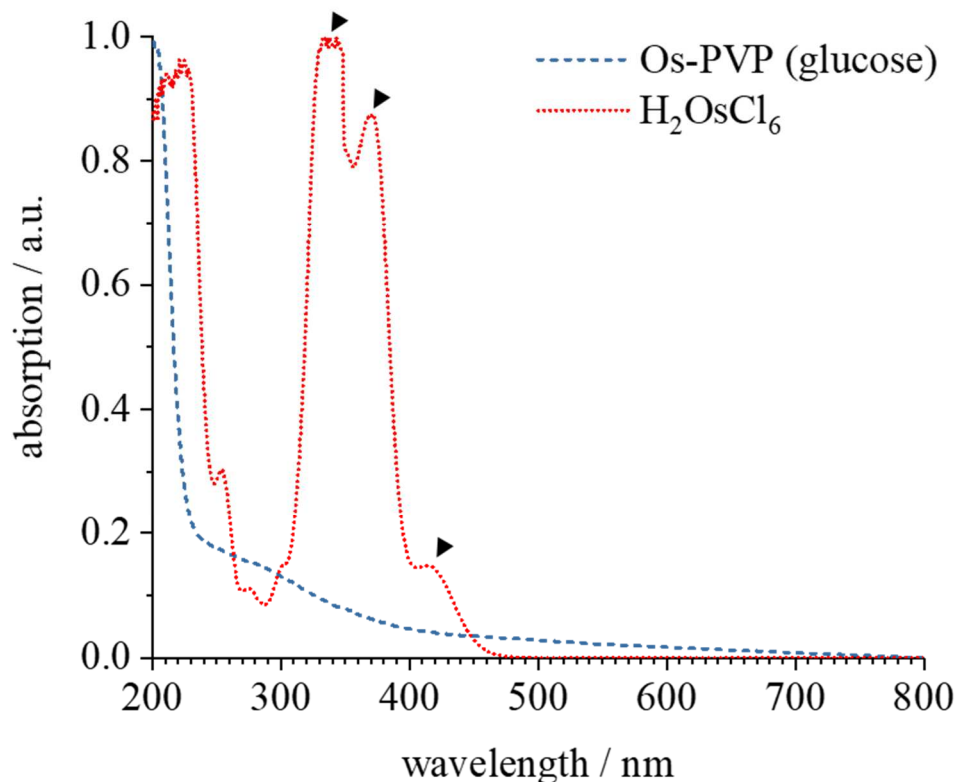


Figure 42: UV/vis spectra of H_2OsCl_6 (red dotted line) and PVP-stabilised osmium nanoparticles (blue dashed line) synthesised by reduction with *D*-glucose. The data were normalised for better comparison. The black arrows show the absorption of the octahedral $[\text{OsCl}_6]^{2-}$ complex from the precursor H_2OsCl_6 in aqueous medium.

The UV/vis spectrum of H_2OsCl_6 corresponds very well to the literature data. The absorption maxima assign to charge-transfer transitions in the octahedral $[\text{OsCl}_6]^{2-}$ complex (see black arrows in Figure 42).^[180, 181] Osmium nanoparticles show the typical absorption spectrum of Os metal without any distinct absorption in visible range (400 to 800 nm) as well as a small absorption band in the near ultraviolet region (2500 to 300 nm) (Figure 42).^[115] The transmission electron microscope images show very small osmium particles which seem to be aggregates to bigger, branched nanostructures with crystalline domains (Figure 43). The size of Os particles are determined manually by measuring the size of 21 particles and compiling a histogram (Figure 44). The average size is 2.4 nm with a standard deviation of ± 1.2 nm in diameter.

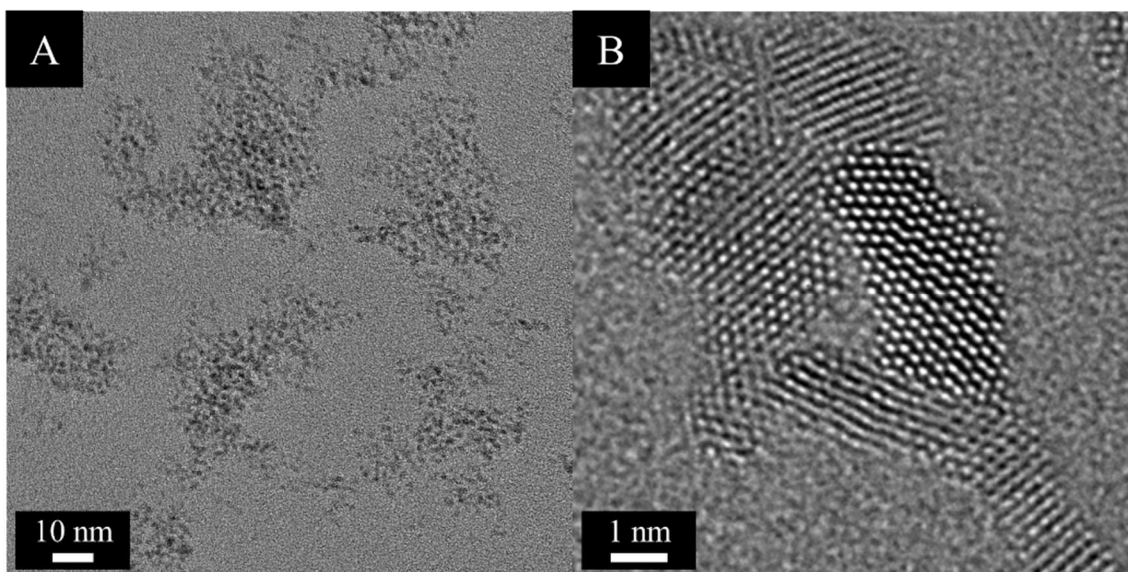


Figure 43: High-resolution TEM image of PVP-stabilised osmium nanoparticles synthesised by reduction with *D*-glucose (A) and a higher magnification of branched, single particles indicating an aggregation (B).

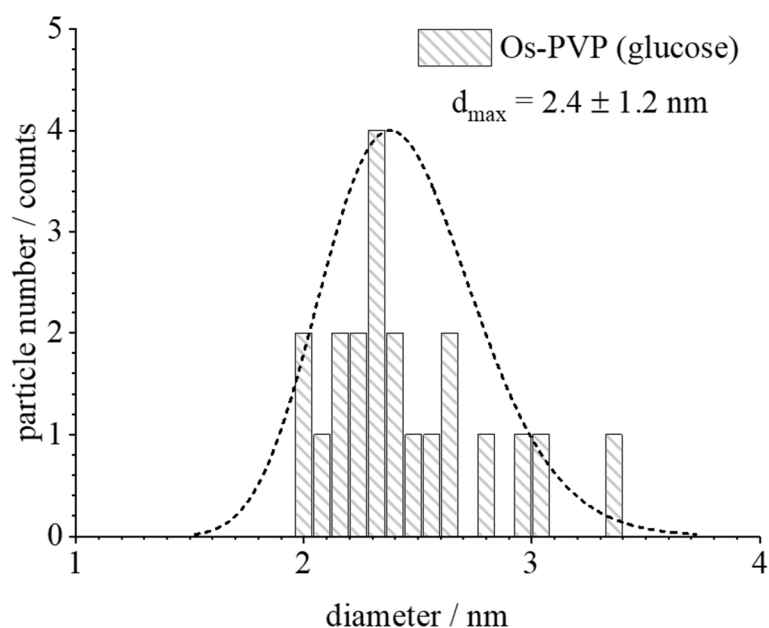


Figure 44: Histogram of particle size analysis from high-resolution TEM of PVP-stabilised Os nanoparticles synthesised by reduction with *D*-glucose. The size distribution was analysed by a log-normal distribution fit

The X-ray diffraction pattern of PVP-stabilised Os nanoparticles is shown in Figure 45. The assignment of the observed reflexes to the reference data is difficult due to the high broadening of the diffraction pattern. Small crystallites as well as strong microstrain lead to a high anisotropic broadening which directly corresponds to the small number of lattice planes in the sample.^[124] However, an adequate Rietveld refinement is possible to calculate the crystallographic properties as well as the lattice parameter of osmium nanoparticles. Those values correspond to the data of the bulk material (space group P63/mmc, lattice constants $a = 2.7240 \text{ \AA}$ and $c = 4.2950 \text{ \AA}$, cell volume $V_{\text{cell}} = 27.600 \text{ \AA}^3$, crystal density $\rho_{\text{crystal}} = 22.887 \text{ g cm}^{-3}$).^[182]

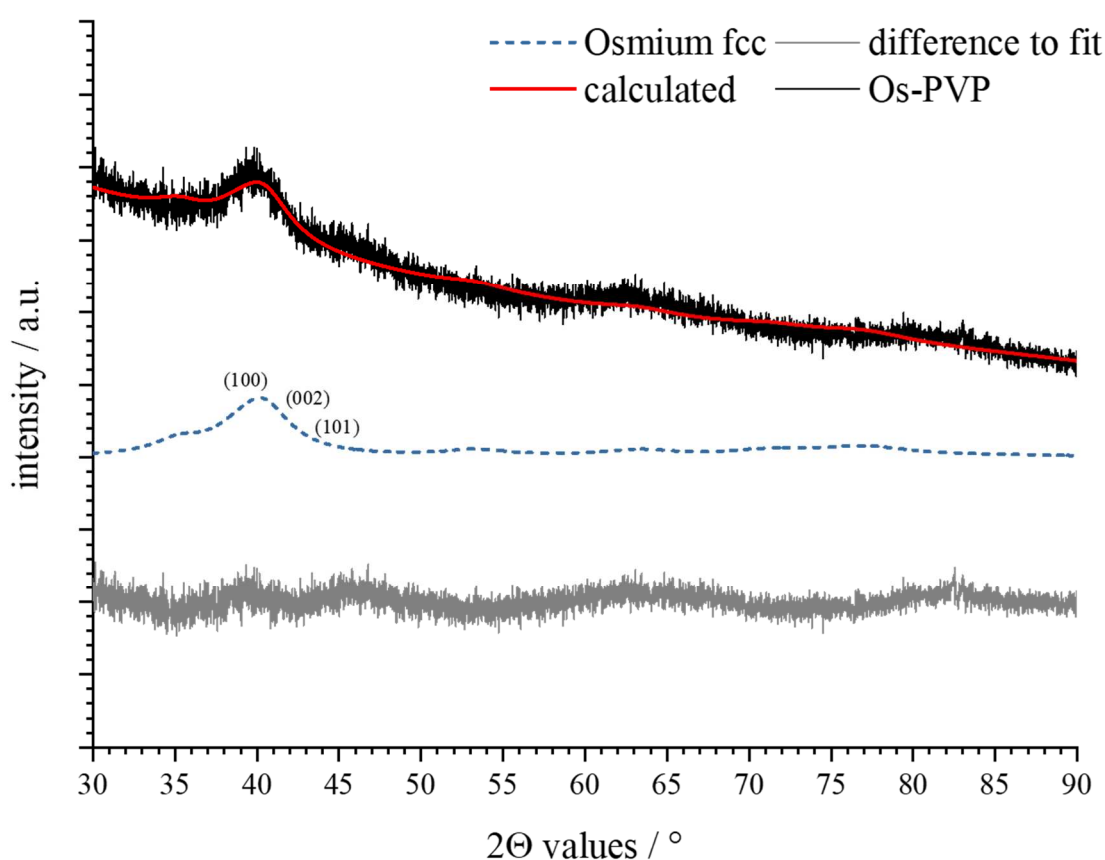


Figure 45: Powder diffraction pattern (not $K\alpha$ stripped) and Rietveld refinement of PVP-stabilised Os nanoparticles synthesised by reduction with glucose. The peak profile is calculated using the hcp phase of osmium. The reflexes of osmium are compared to the powder diffraction file 00-006-0662 (Os).^[183]

The PVP-stabilised osmium nanoparticles show similar lattice constants a and c in comparison to the bulk material (Table 9). Due to the small number of present crystallographic planes in the sample, the calculated values must be assessed carefully. As consequence,

the cell volume and crystal density is not influenced much. Notably, the high index (110) crystallographic planes cannot be identified in the diffraction pattern and the calculation of the microstrain is not possible or practical by Rietveld refinement.

The difference between crystallite size from PXRD ($d_{\text{CS}} = 4.7 \pm 1.6$ nm) and the particle diameter from HR-TEM ($d_{\text{TEM}} = 2.4 \pm 1.2$ nm) is based on the measurement characteristics. The PXRD is not able to identify single particles because of aggregation during the sample preparation and freeze-drying process. Additionally, there is a different emphasis on the size distribution analysis of the TEM data. The particle size from electron microscopy correlates to the size of primary particles and does not take into account the size of the aggregates, agglomerates or branched structures.

Table 9: Results of the Rietveld refinement from X-ray powder diffraction analysis of freeze-dried Os nanoparticles. The reference values for the lattice parameters a and c were taken from AMCSD 0016737 (Os).^[182]

Parameter	Os hcp
Tabulated lattice parameter a (bulk metals) / Å	2.724
Tabulated lattice parameter c (bulk metals) / Å	4.295
Calculated lattice parameter a / Å	2.732(7)
Calculated lattice parameter c / Å	4.383(8)
Calculated cell volume / Å ³	28.35(2)
Calculated crystallite size / nm	4.7(16)
Calculated crystal density / g cm ⁻³	22.28(3)

In summary, the wet-chemical synthesis by reduction with *D*-glucose yields spherical-like osmium nanoparticles within the size range of 8 to 14 nm in hydrodynamic diameter. The HR-TEM images depict aggregated nanostructures with a primary particle diameter of 2 to 3 nm. The investigation of the crystallographic structure by X-ray powder diffraction and Rietveld refinement reveals the presence of the pure hcp phase of osmium with a crystallite size of approximately 4 to 5 nm, which illustrates an aggregation of smaller particles. Notably, the small particle size leads to a considerable peak broadening that has

a strong impact on the calculation accuracy.^[124] The obtained particles show no distinct absorption in the visible range corresponding to bulk material of Os.

4.1.6 Iridium nanoparticles

Small (ca. 2-4 nm) iridium nanoparticles can be synthesised by reduction of Ir(III) chloride or dihydrogen hexachloroiridate(IV) with borohydride in aqueous media,^[184, 185] by hydrogen reduction in ionic liquids,^[186, 187] or using lithium triethylborohydride (superhydride) in tetrahydrofuran (THF).^[188] Furthermore, Ir nanoparticles can be obtained using a polyol process.^[189]

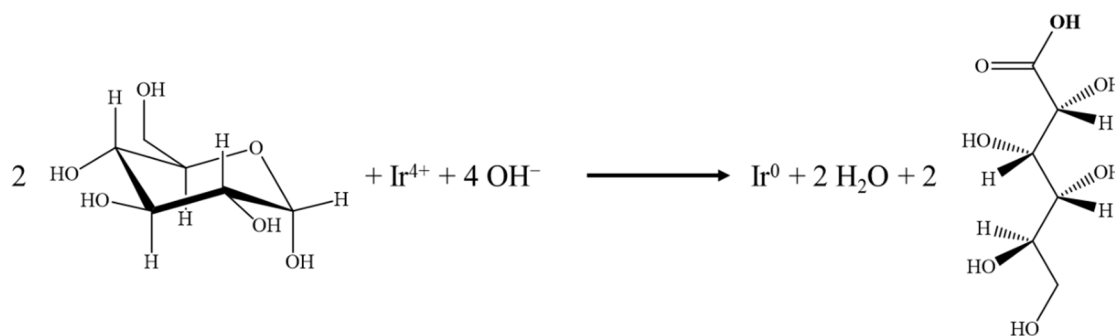


Figure 46: Reaction scheme of the reduction of H_2IrCl_6 with *D*-glucose.

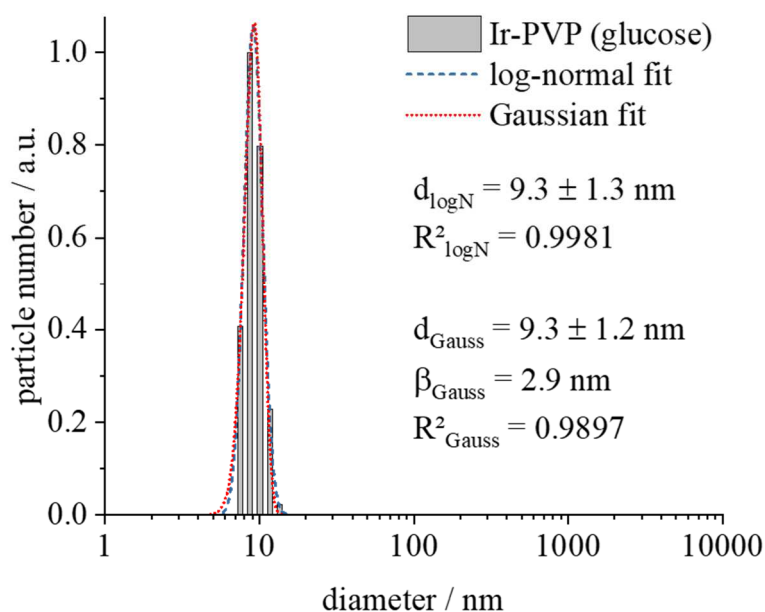


Figure 47: Number-weighted size distribution of PVP-stabilized iridium nanoparticles synthesised by reduction with *D*-glucose determined by DLS. The peak profile is analysed by a log-normal as well as a Gaussian distribution fit. The PdI is 0.10.

Here, iridium nanoparticles are synthesised by reduction of H_2IrCl_6 with *D*-glucose in aqueous media. Please note that the synthesis is taking long time and the reproducibility of such synthesis approach is unrewarding. The obtained particles are used to complete the row of noble metal nanoparticles in the size range of 5 – 10 nm from wet-chemical synthesis. Nevertheless, some characterisation data can be obtained from colloid-chemical and spectroscopic methods. The hydrodynamic diameter of Ir nanoparticles is 9.3 nm with a standard deviation of ± 1.3 nm determined by dynamic light scattering (Figure 47). The PdI of 0.1 is very low and indicates a well-dispersed solution. The diameter from DCS is 7.3 nm with a standard deviation of ± 1.5 nm and a PdI value of 0.21. Considering the measurement characteristics of DLS and DCS, the particle sizes are in good agreement with each other. Notably, iridium has the highest density of all platinum metals. Therefore, the influence of the dense metal core on the sedimentation is much higher than from the polymer shell, which results in an underestimated size by DCS.

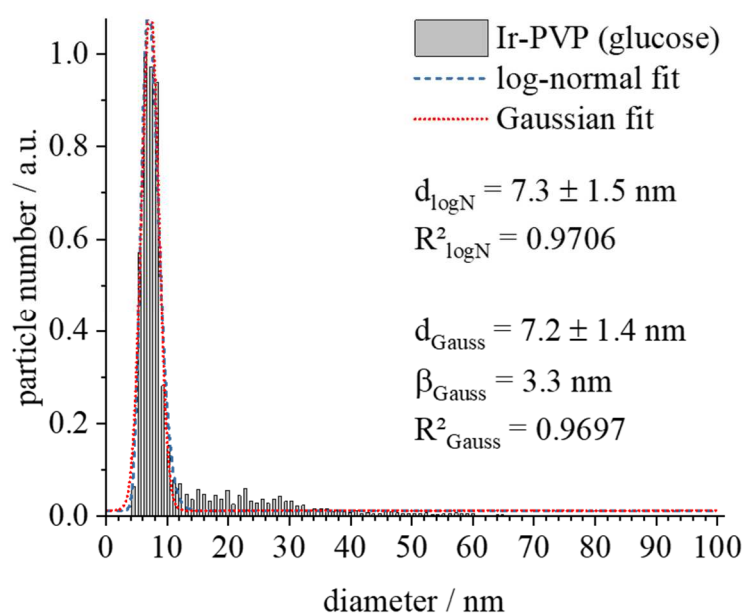


Figure 48: Number-weighted size distribution of PVP-stabilized iridium nanoparticles synthesised by reduction with *D*-glucose determined by DCS. The peak profile is analysed by a log-normal as well as a Gaussian distribution fit. The PdI is 0.21.

The complexity of the redox reaction of hexachloroiridate in aqueous media is due to the high stability of the newly formed $[\text{IrCl}_3(\text{H}_2\text{O})_3]^+$ aqua complex. The ligand exchange of Cl^- with water molecules leads to a rise of the electrochemical standard potential. The standard potential of the half reaction $[\text{IrCl}_3(\text{H}_2\text{O})_3]^+ / [\text{IrCl}_3(\text{H}_2\text{O})_3]$ is +1.30 V and much

more higher than of $[\text{IrCl}_6]^{2-}/\text{Ir}^0$ with a value of +0.83 V.^[190] In general, a strong reducing agent like sodium borohydride is needed. The (possible) conversion of *D*-glucose to pyruvic acid leads to a release of 4 electrons per molecule. This reaction can be promoted by catalytic active metals and by long-term thermal treatment (100 °C, > 4 h) under acidic conditions (pH < 6).^[191-194] This might be the reason why Ir nanoparticles are formed despite the weak reduction potential of glucose.

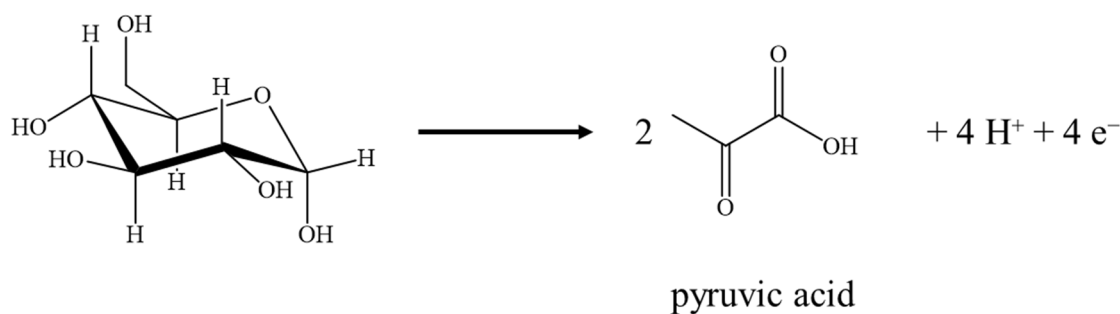


Figure 49: Conversion of *D*-glucose to pyruvic acid.^[195]

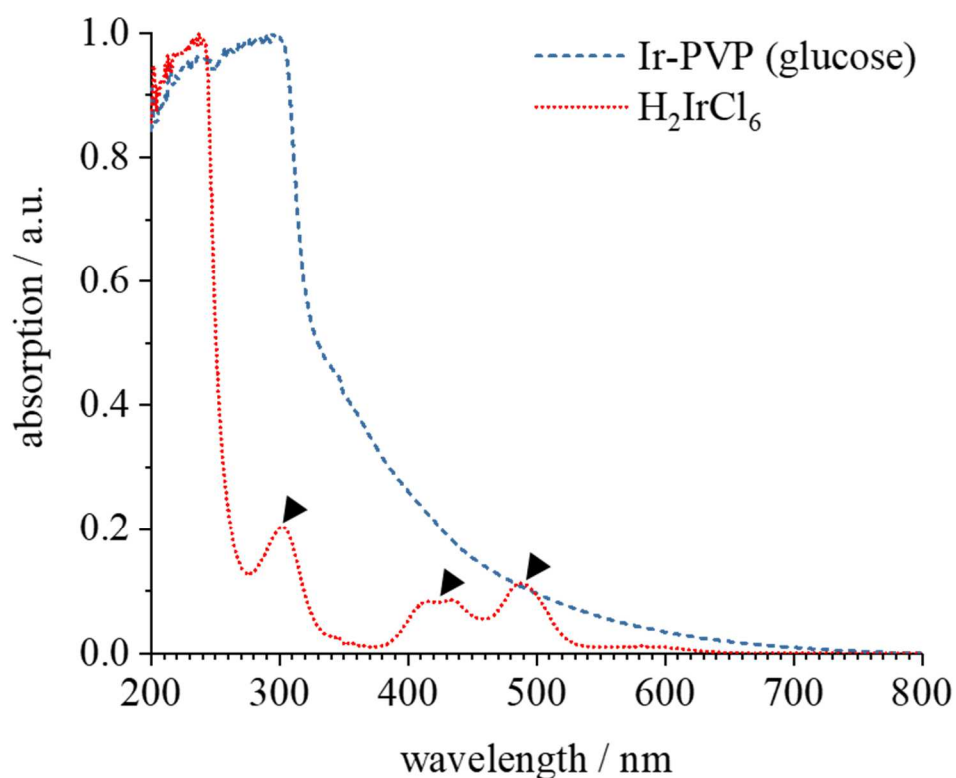


Figure 50: UV/vis spectra of H_2IrCl_6 (red dotted line) and PVP-stabilised iridium nanoparticles (blue dashed line) synthesised by reduction with *D*-glucose. The data are normalised for better comparison. The black arrows show the absorption of $[\text{IrCl}_6]^{2-}$ and $[\text{Ir}(\text{OH})_6]^{2-}$ complexes from the precursor H_2IrCl_6 in aqueous media.

The electronic spectrum of the ionic precursor H_2IrCl_6 displays three absorption bands in the visible range with maxima at 415, 433, and 487 nm due to d-d electron transition in the $[\text{IrCl}_6]^{2-}$ complex. The one distinct maximum in the ultraviolet region at 301 nm is based on the hydrolysis of the Ir(IV) chloride complex under formation the $[\text{Ir}(\text{OH})_6]^{2-}$ complex (see black arrows in Figure 50).^[196-201] The iridium nanoparticles show the typical UV/vis spectrum of Ir metal without any pronounced absorption in the visible range (400 to 800 nm) (Figure 50). The strong absorption below 350 nm comes from the polymer PVP and can be assigned to $n \rightarrow \pi^*$ transition of the oxygen lone pairs and the vacant π^* -orbital of the pyrrolidone ring and the high absorption coefficient of the C=O double bond due to $\pi \rightarrow \pi^*$ transition.^[116, 117]

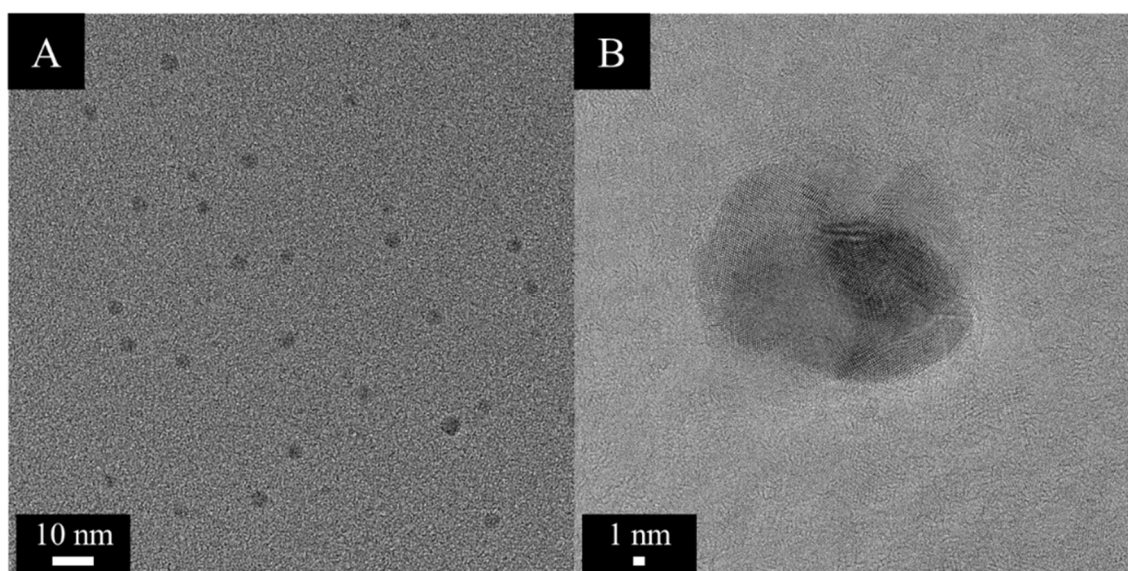


Figure 51: High-resolution TEM image of PVP-stabilised iridium nanoparticles synthesised by reduction with *D*-glucose (A) and higher magnification of a single particle even with a nanocrystalline or amorphous structure (B).

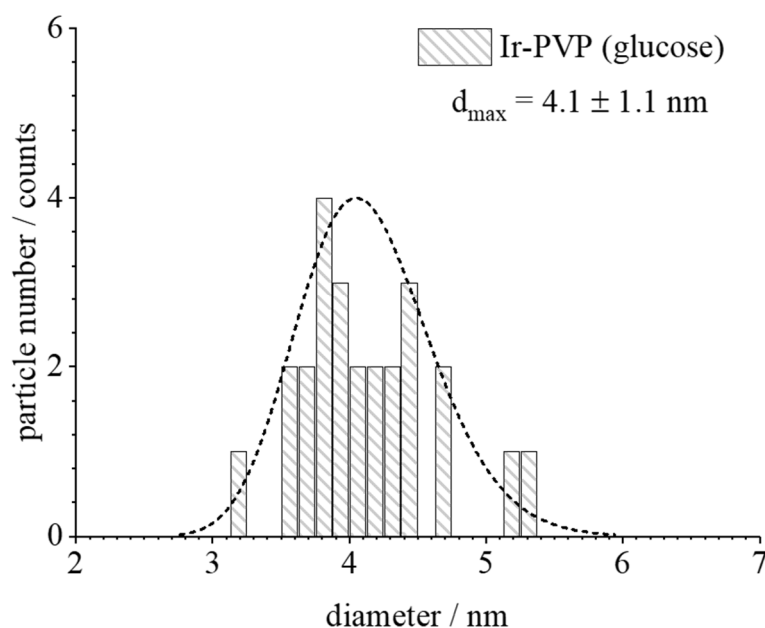


Figure 52: Histogram of particle size analysis from high-resolution TEM of PVP-stabilised Ir nanoparticles synthesised by reduction with *D*-glucose. The size distribution was analysed by a log-normal distribution fit.

For a further investigation of the crystallographic properties and for the calculation of the crystallite size of iridium nanoparticles, an X-ray diffraction pattern was measured (Figure 53). Since the high-resolution TEM shows very small particles with a nanocrystalline or amorphous structure, spin filtration and final freeze-drying was applied in order to enhance the scattering capability of the concentrated sample. The sharp reflexes originate from additional lanthanum hexaboride (LaB_6 , marked with asterisks, Figure 53) for investigation of the instrumental peak broadening, which is negligible. The reflexes of the iridium nanoparticles show a distinct broadening because of the nanocrystalline or amorphous nature. Small crystallite sizes as well as amorphous materials lead to broader diffraction reflexes because of natural lattice defects and interference effects.^[124]

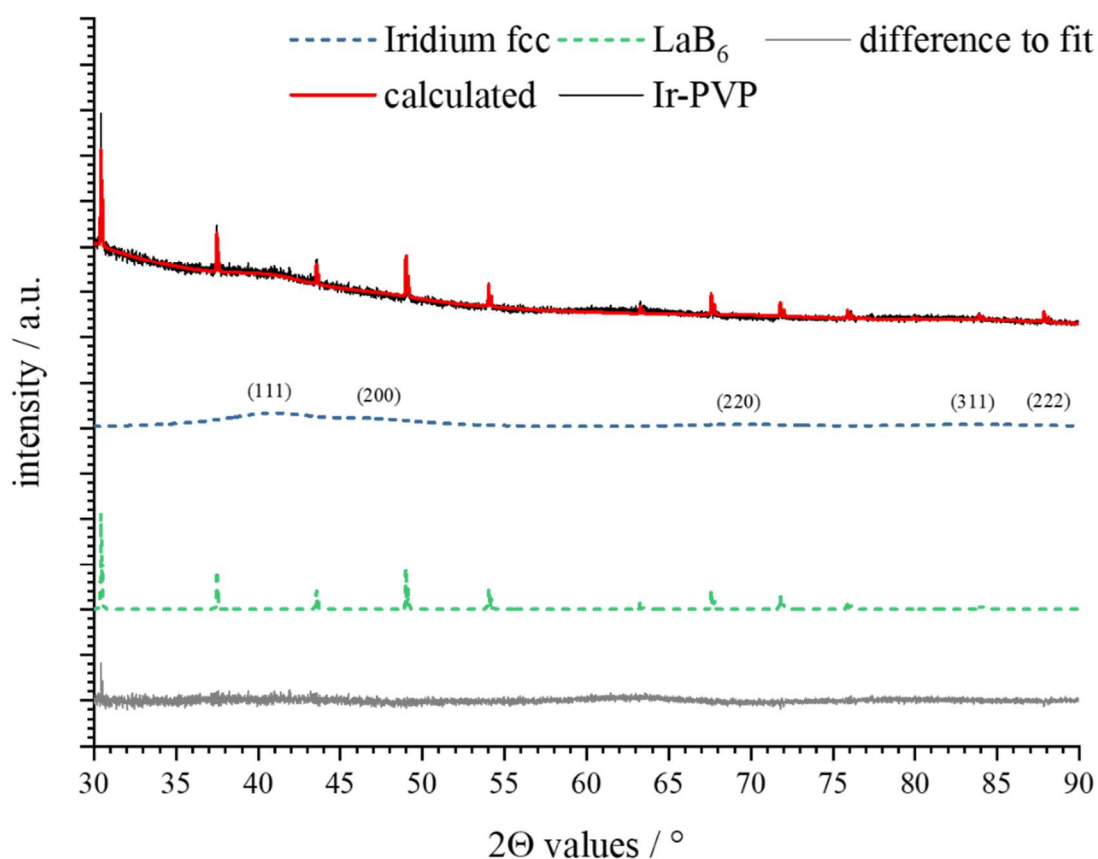


Figure 53: Powder diffraction pattern (not $K\alpha$ stripped) and Rietveld refinement of PVP-stabilised Ir nanoparticles synthesised by reduction with *D*-glucose. The peak profile is calculated using the fcc phase of iridium. The asterisks mark the lanthanum hexaboride (LaB_6 , PDF 00-034-0427).^[122] The reflexes of iridium are compared to the powder diffraction file 00-046-1044 (Ir).^[202]

The diffraction pattern shows two broad reflexes with weak intensity despite freeze-drying of the concentrated sample. These correspond to the scattering of the (111) and (200) crystallographic planes of iridium (space group $\text{Fm}\bar{3}\text{m}$, lattice constant $a = 3.8394 \text{ \AA}$, cell volume $V_{\text{cell}} = 56.597 \text{ \AA}^3$, crystal density $\rho_{\text{crystal}} = 22.555 \text{ g cm}^{-3}$).^[203] The small crystallite size and the anisotropic broadening strongly influences the reflex shapes. Nevertheless, the fcc-phase of iridium can be identified and the crystallographic properties (lattice parameter, cell volume, crystallite size, crystal density) can be calculated by Rietveld refinement. The results of the Rietveld refinement are summarised in Table 10.

Table 10: Results of the Rietveld refinement from X-ray powder diffraction analysis of freeze-dried Ir nanoparticles. The reference values for the lattice parameter a were taken from AMCSD 0011147 (Ir).^[203]

Parameter	Ir fcc
Tabulated lattice parameter a (bulk metals) / Å	3.8394
Calculated lattice parameter a / Å	3.838(8)
Calculated cell volume / Å ³	56.5(7)
Calculated crystallite size / nm	1.7(2)
Calculated crystal density / g cm ⁻³	22.5(7)

The PVP-stabilised Ir nanoparticles show a similar lattice constant a in comparison to the bulk material (Table 10) despite the small number of present crystallographic planes in the sample. Consequently, the cell volume and crystal density is not influenced much. Notably, the high index (220), (311) and (222) crystallographic planes cannot be observed or identified in the diffraction pattern and the calculation of the microstrain is not possible or practical by Rietveld refinement.

To sum up, the synthesis yields iridium nanoparticles with a hydrodynamic size of about 7 to 9 nm. Those particles are quasi spherical and have a metallic core diameter of about 4 nm as indicated by HR-TEM. The Rietveld refinement of the diffraction pattern must be considered carefully due to the distinct peak broadening because of the small particle size and missing reflexes of higher indexed lattice planes.^[124] However, the diffraction data confirms the presence of the fcc phase of iridium with a crystallite size of approximately 1 to 2 nm. Similar to the bulk metal, the obtained IR nanoparticles have no distinct absorption in the visible range (400 to 800 nm).

4.1.7 Platinum nanoparticles

Pt nanoparticles can be obtained in organic solvents by metal carbonyl-mediated synthesis.^[204] Catalysts of nanoscopic platinum were synthesised using sodium borohydride in octylamine.^[205] Pt nanoparticles with sizes below 10 nm are available using NaBH₄ in the presence of polyethyleneimine (PEI)^[206] or PVP.^[207] Polyhedral platinum nanostructures (< 10 nm) can be obtained by reduction of Pt(acac)₂ in octadecene (OD), oleic acid (OA), and oleylamine (OAm) in the presence of trace amounts of Fe(CO)₅. Furthermore, truncated cubes and nanocubes of Pt can be synthesised according the same synthesis protocol without Fe(CO)₅.^[208]

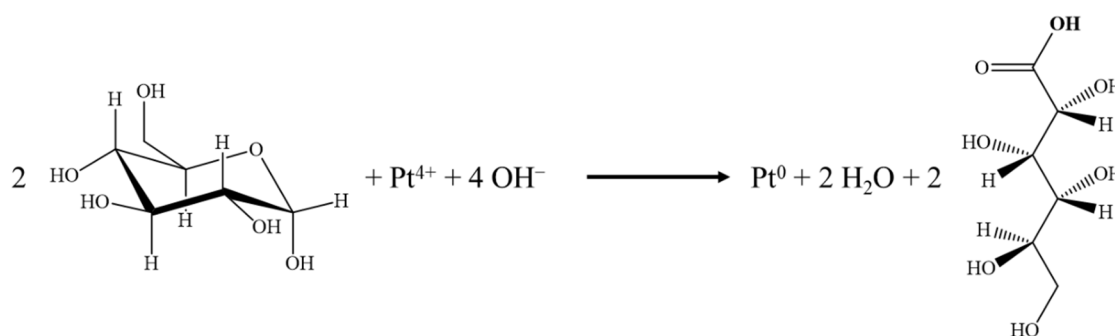


Figure 54: Reaction scheme of the reduction of H₂PtCl₆ with *D*-glucose.

In this work, small platinum nanoparticles are obtained by a wet-chemical synthesis using *D*-glucose in the presence of PVP. The hydrodynamic diameter is 8.5 nm with a standard deviation of ± 1.7 nm. The Pt particles are well dispersed in water indicating by a low polydispersity index of 0.18. Notably, the hydrodynamic diameter from DLS is often overestimated because of the adsorbed and hydrated polymer on the Pt nanoparticle surface. The size from DCS is 4.3 nm with a standard deviation of 1.1 nm in diameter. The PDI is 0.30. The difference in sizes from dynamic light scattering and differential centrifugal sedimentation analysis originate from the measurement characteristics of each method. The DLS measures the intensity of the Rayleigh scattering and is carried out in the dispersed state. Hence, the obtained particle sizes are generally larger than the metallic core due to the presence of the hydrated polymeric layer.^[95] Additionally, the polymer shell lowers the effective density of the particles, which influences the sedimentation during the DCS analysis. The increased sedimentation time leads to obviously smaller particle sizes compared to the results from DLS.^[113]

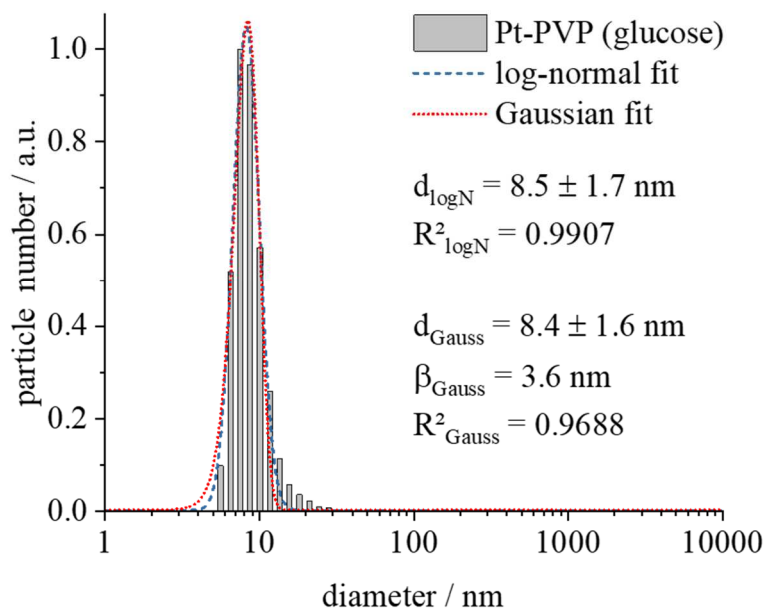


Figure 55: Number-weighted size distribution of PVP-stabilized platinum nanoparticles synthesised by reduction with *D*-glucose determined by DLS. The peak profile is analysed by a log-normal as well as a Gaussian distribution fit. The PDI is 0.18.

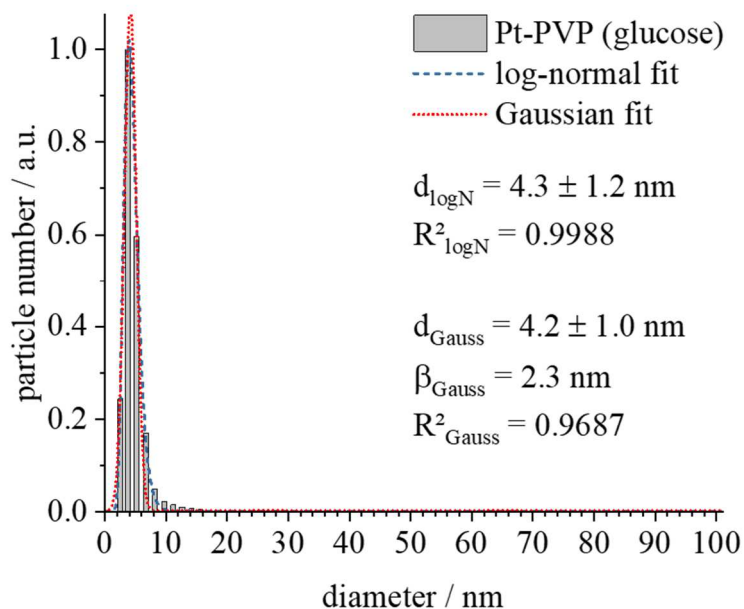


Figure 56: Number-weighted size distribution of PVP-stabilized platinum nanoparticles synthesised by reduction with *D*-glucose determined by DCS. The peak profile is analysed by a log-normal as well as a Gaussian distribution fit. The PDI is 0.30.

The synthesis leads to a brownish-black coloured dispersion. The absorption spectrum of colloidal Pt nanoparticles with an absorption maximum at 224 nm is conformed to literature data (Figure 57).^[115] This specific absorption is a result of the ligand field splitting of the Pt^{5d} orbital which arises from the expansion of the coordination sphere of N and O atoms of PVP to the Pt nanoparticles.^[209-211] The ionic precursor H_2PtCl_6 shows three steps in the electronic spectrum which can be assigned to electron transitions in the $[\text{PtCl}_6]^{2-}$ and $[\text{Pt}(\text{OH})_6]^{2-}$ complex, respectively.^[211-214]

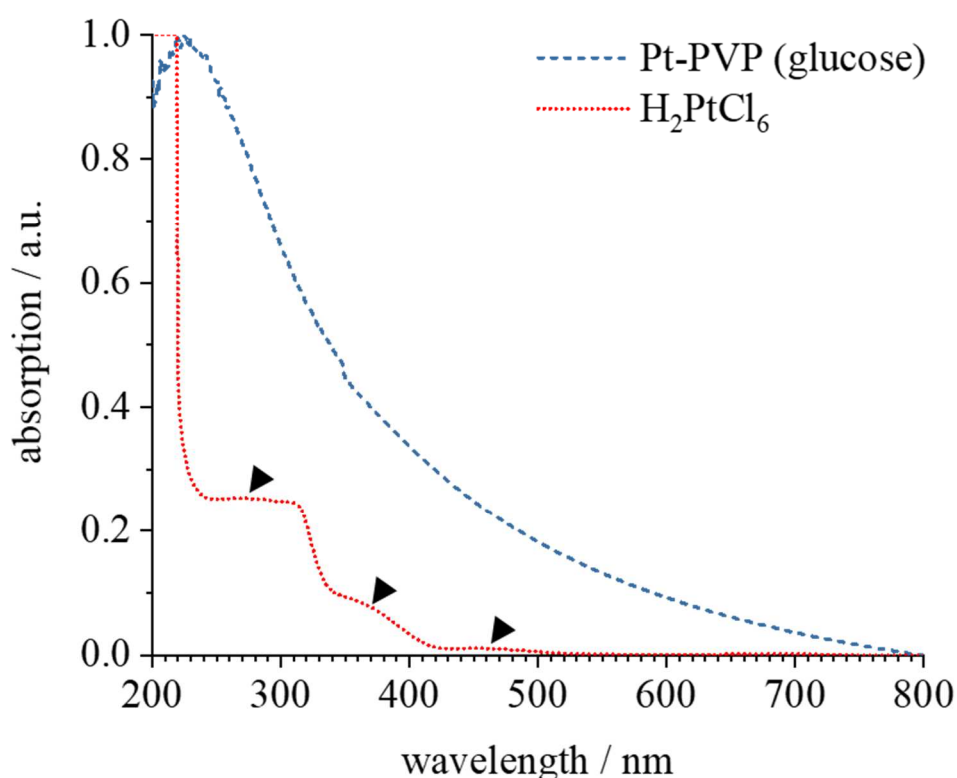


Figure 57: UV/vis spectra of H_2PtCl_6 (red dotted line) and PVP-stabilised platinum nanoparticles (blue dashed line) synthesised by reduction with *D*-glucose. The data are normalised for better comparison. The black arrows show the absorption peaks of the $[\text{PtCl}_6]^{2-}$ and $[\text{Pt}(\text{OH})_6]^{2-}$ complex from the ionic precursor H_2PtCl_6 in aqueous medium.

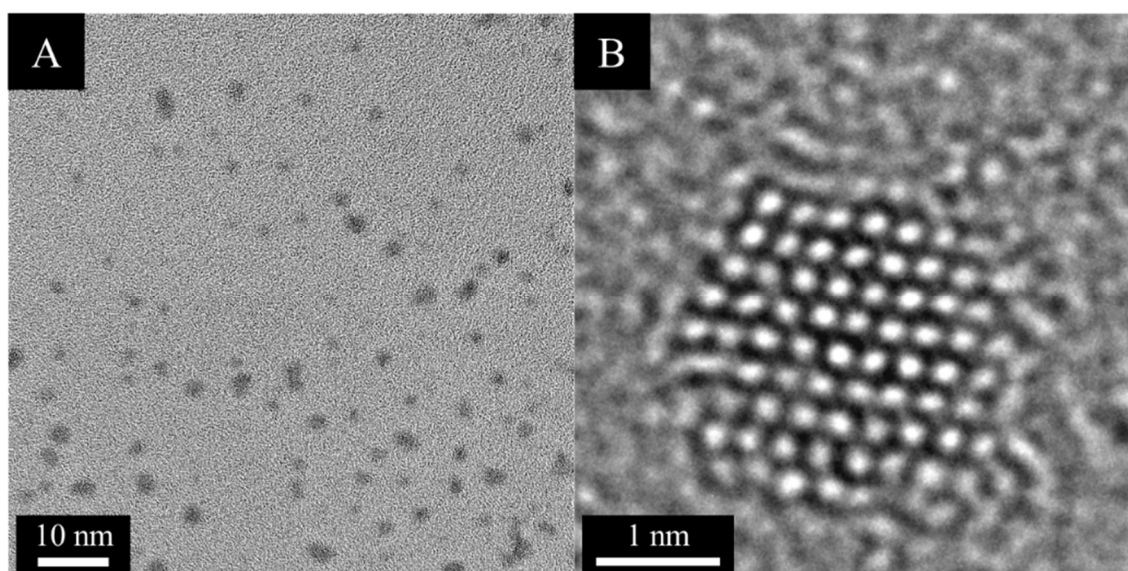


Figure 58: High-resolution TEM image of PVP-stabilised platinum nanoparticles synthesised by reduction with *D*-glucose (A) and higher magnification of a single particle indicating a single crystalline structure without any grain boundaries (B).

The HR-TEM images show small, spherical-like particles with an entire crystalline structure (Figure 58). The particle size is determined manually by measuring the size of 110 particles and compiling a histogram (Figure 59). The size is 4.8 nm with a standard deviation of ± 1.3 nm in diameter and corresponds very well to the hydrodynamic diameters from DCS. In the overview, no aggregates or bigger particles can be observed which confirms a monodisperse system. In higher magnification, the single crystalline characteristic of the obtained particles can be visually substantiated. Notably, electron microscopy depicts dried samples and gives information just about the metallic core of the particles because the hydration shell and adsorbed polymer collapsed in the high vacuum.

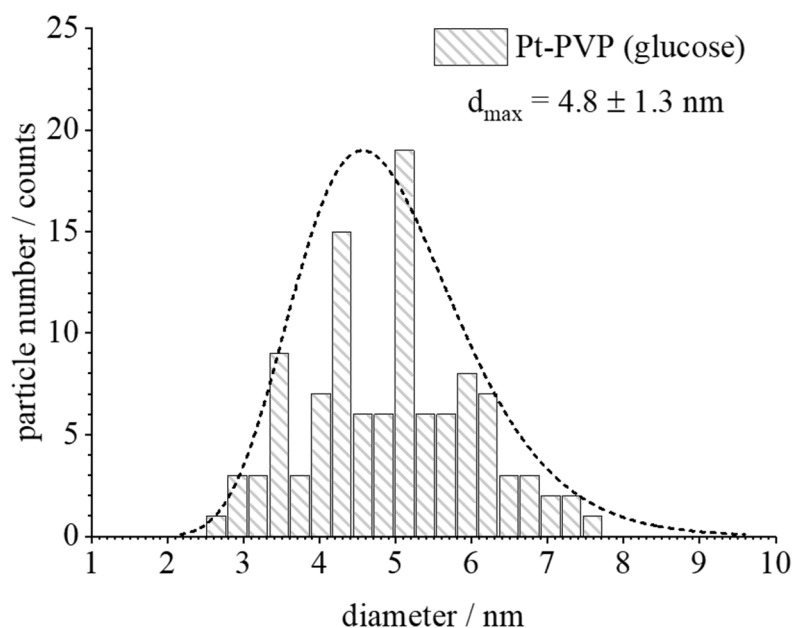


Figure 59: Histogram of particle size analysis from high-resolution TEM of PVP-stabilised Pt nanoparticles synthesised by reduction with *D*-glucose. The size distribution was analysed by a log-normal distribution fit.

Table 11: Overview of the platinum fcc reflex position between 25-85° from Rietveld refinement in comparison to the ICDD database (Pt, PDF 00-001-1194).^[215]

Reflex position (observed) $2\theta / ^\circ$	Reflex position (reference) $2\theta / ^\circ$	Lattice plane (hkl)
39.787	39.756	(111)
46.190	46.242	(200)
67.498	67.443	(220)
81.359	81.301	(311)
85.539	85.721	(222)

Powder X-ray diffraction is performed to investigate the structural behaviour of platinum nanoparticles (Figure 60). The diffraction pattern shows sharp reflexes, which originate

from the internal standard LaB_6 for the investigation of the instrumental broadening (marked with asterisk, Figure 60). This can be neglected because of the small particle and crystallite size, respectively. Small crystallites (few nanometres) have natural lattice defects that lead to broader diffraction reflexes and affect the reflex shape by interference effects. These effects result from the low number of lattice planes.^[124] The reflexes of platinum can be found and assigned to (111), (200), (220), (311), and (222) crystallographic planes according the reference data of the fcc phase of Pt (Table 11). Overall, the diffraction pattern corresponds to a face-centred cubic (fcc) phase without any other phases. Platinum crystallises in the fcc structure with the space group $\text{Fm}\bar{3}\text{m}$. The lattice parameter a is 3.923 \AA .^[216]

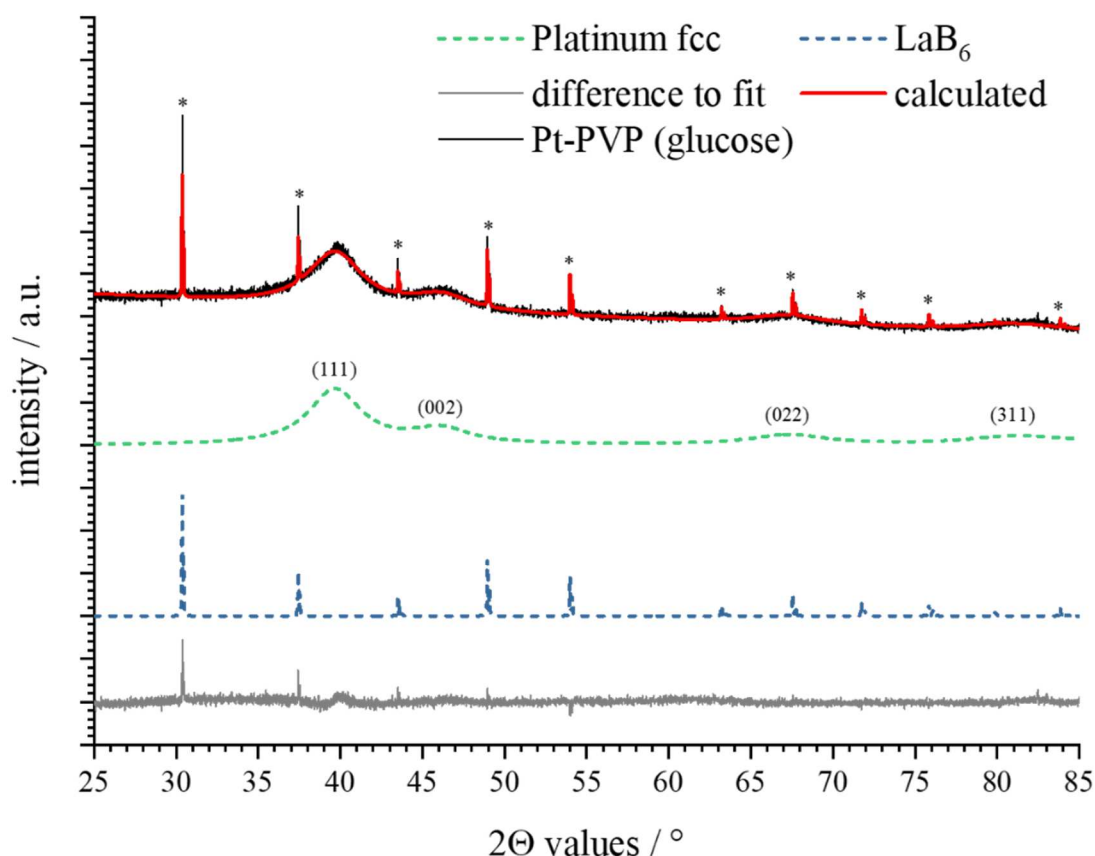


Figure 60: Powder diffraction pattern (not $K\alpha$ stripped) and Rietveld refinement of PVP-stabilised Pt nanoparticles synthesised by reduction with *D*-glucose. The peak profile is calculated using the fcc phase of platinum. The asterisks mark the lanthanum hexaboride (LaB_6 , PDF 00-034-0427).^[122] The reflexes of platinum are compared to the powder diffraction file 00-001-1194 (Pt).^[215]

For a more detailed investigation of the crystallographic and structural parameters, another diffraction pattern without lanthanum hexaboride is recorded. Wondering, an impurity with a small amount of sodium chloride (halite; 2.2 %) is found during the phase analysis notwithstanding any use of sodium containing chemicals during the synthesis process (Figure 61). The calculated lattice parameter from Rietveld refinement corresponds well with the reference (Table 12). An accurate calculation of the microstrain is not possible because of the small crystallite sizes.

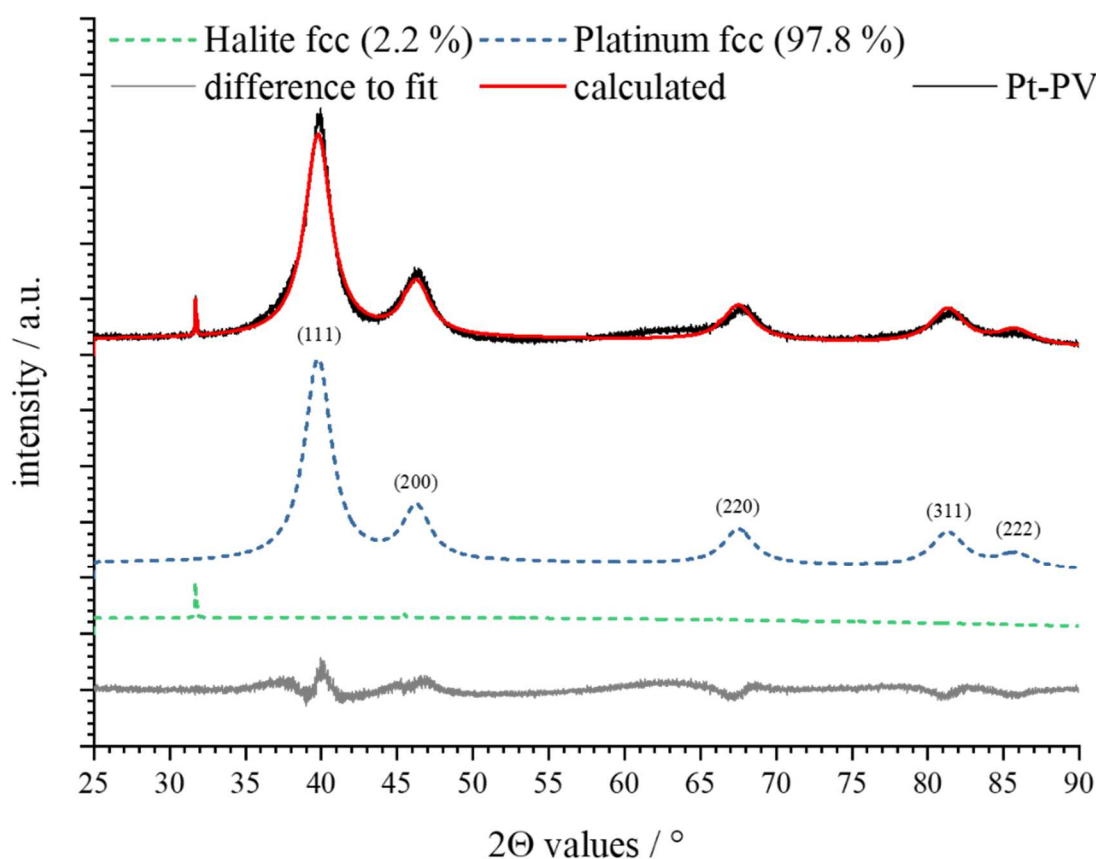


Figure 61: Powder diffraction pattern (not $K\alpha$ stripped) and Rietveld refinement of PVP-stabilised Pt nanoparticles synthesised by reduction with *D*-glucose. The peak profile is calculated using the fcc phase of platinum. The phase analysis reveals to a small amount of halite (NaCl) in the present sample (2.2 %).

The crystallite size of Pt particles is 4.46(2) nm. Considering the particle size from high-resolution TEM ($d_{\text{TEM}} = 4.8 \pm 1.3$ nm) and analytical disc centrifugation ($d_{\text{DCS}} = 4.3 \pm 1.1$ nm), the calculated crystallite size from Rietveld refinement illustrate the presence of a single-crystalline structure.

Table 12: Results of the Rietveld refinement from X-ray powder diffraction analysis of freeze-dried Pt nanoparticles. The reference values for the lattice parameter a were taken from AMCSD 0011157 (Pt).^[216]

Parameter	Pt fcc
Tabulated lattice parameter a (bulk metals) / Å	3.923
Calculated lattice parameter a / Å	3.9240(4)
Calculated cell volume / Å ³	60.42(2)
Calculated crystallite size / nm	4.46(2)
Calculated crystal density / g cm ⁻³	21.445(6)

Overall, the synthesis of platinum nanoparticles with *D*-glucose leads to particles within the size range of 4 to 8 nm without any distinct absorption in the visible range (400 to 800 nm). The investigation by high-resolution TEM shows small particles around 5 nm, which reveal that the obtained particles seem to be single crystalline. In addition, powder X-ray diffraction and supplemental Rietveld refinement confirms the obvious crystalline structure. Platinum nanoparticles show no distinct absorption in the visible range corresponding to the bulk metal.

4.1.8 Gold nanoparticles

Gold nanoparticles (< 10 nm) can be synthesised by wet-chemical approaches using strong reducing agents, e.g. NaBH₄, in the presence of strong-binding capping agents, e.g. 11-mercaptoundecanoic acid (11-MUA), or by a modified *Turkevich* method with citrate and tannic acid.^[217, 218]

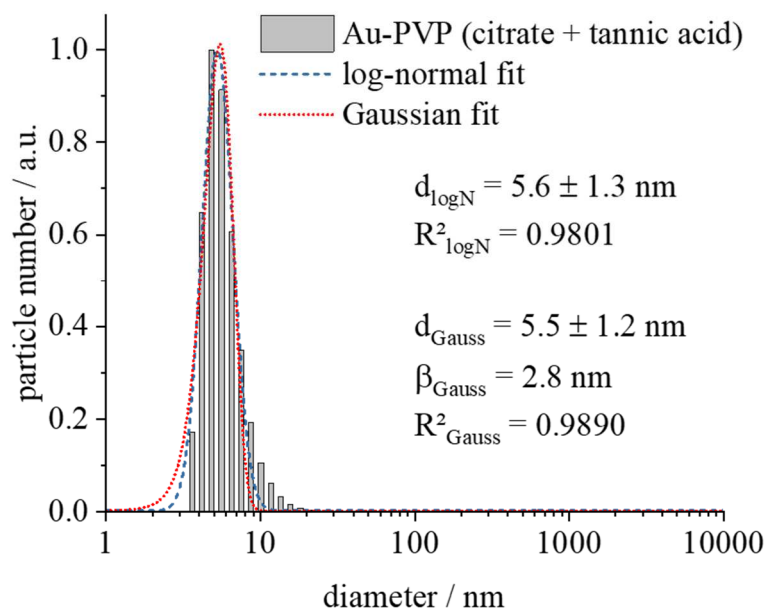


Figure 62: Number-weighted size distribution of PVP-stabilized gold nanoparticles synthesised by reduction with citrate and tannic acid determined by DLS. The peak profile is analysed by a log-normal as well as a Gaussian distribution fit. The PDI is 0.26.

Here, PVP-stabilised gold nanoparticles are synthesised by reduction with citrate and tannic acid in aqueous media. The particle size determined by dynamic light scattering is 5.6 nm with a standard deviation of ± 1.3 nm in hydrodynamic diameter (Figure 62). The PDI is 0.26 indicating a well-dispersed system. The results from differential centrifugal sedimentation analysis are comparable to the DLS. The diameter from DCS is 5.4 nm with a standard deviation of ± 1.2 nm and the PDI is 0.28 (Figure 63).

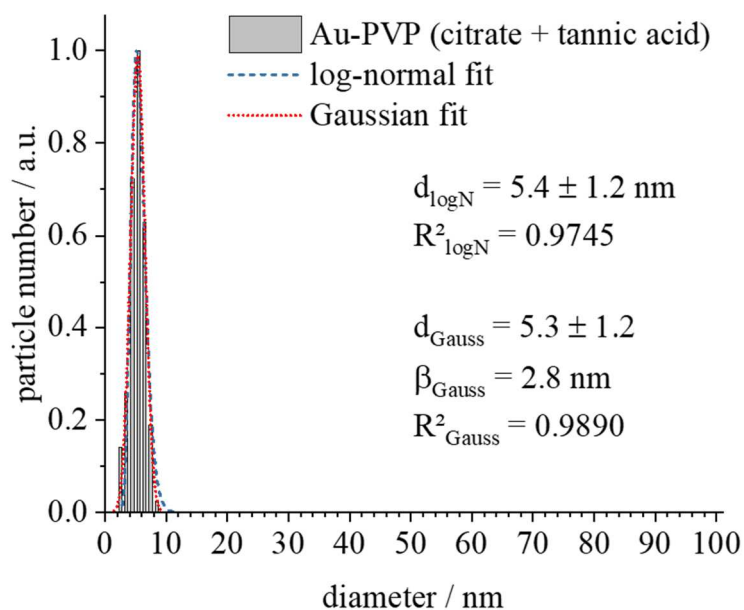


Figure 63: Number-weighted size distribution of PVP-stabilized gold nanoparticles synthesised by reduction with citrate and tannic acid determined by DCS. The peak profile is analysed by a log-normal as well as a Gaussian distribution fit. The PDI is 0.28.

Both UV/vis spectra correspond to the literature data and can be assigned to the surface plasmon resonance (SPR) absorption of gold nanoparticles (with an absorption maximum at 518 nm) as well as ligand-to-metal charge-transfer (LMCT) transition in the $[\text{AuCl}_4]^-$ complex (see black arrows in Figure 64).^[115, 219, 220] The absorption, especially in the ultraviolet region (below 350 nm), of tetrachloroauric(III) acid shows a very high pH-dependence which results in higher absorption coefficients at low pH (< pH 4).^[221]

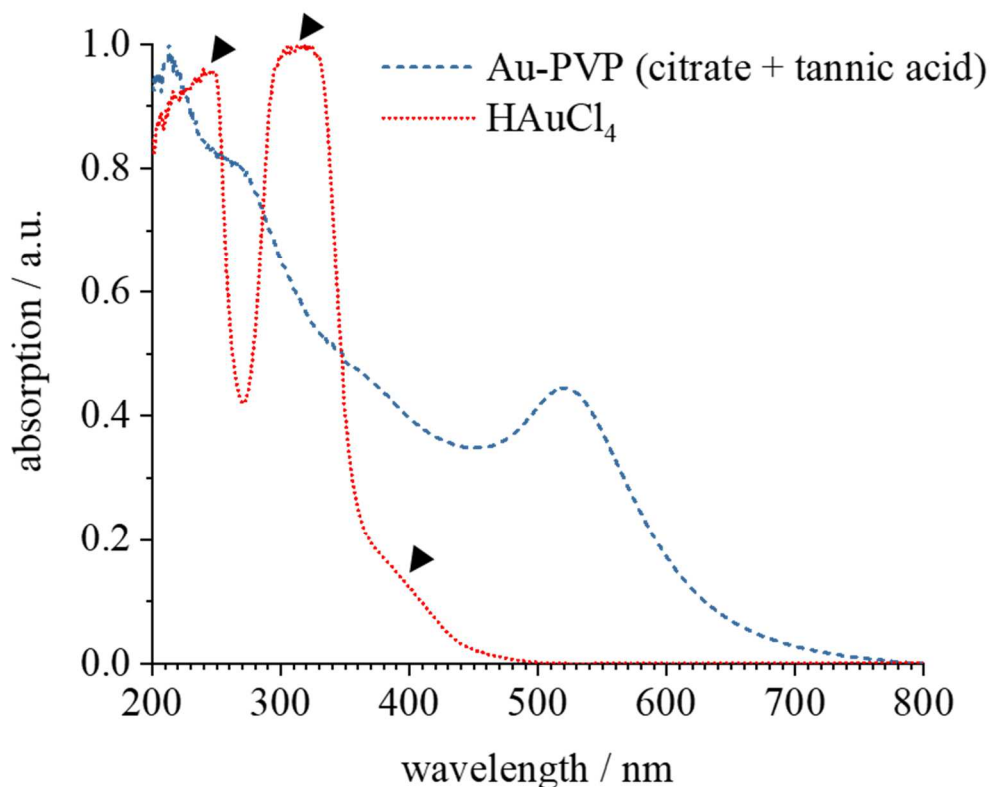


Figure 64: UV/vis spectra of HAuCl₄ (red dotted line) and PVP-stabilised gold nanoparticles (blue dashed line) synthesised by reduction with citrate and tannic acid. The data are normalised for better comparison. The black arrows show the absorption of the [AuCl₄]⁻ complex from the precursor HAuCl₄ in aqueous medium.

The transmission electron microscopy images (Figure 65) show nearly monodispersed, quasi-spherical, and polycrystalline particles with a penta-fold twinned structure. The particle size is determined manually by measuring the size of 101 particles and compiling a histogram (Figure 66). The particle size is 6.0 nm with a standard deviation of ± 1.4 nm in diameter.

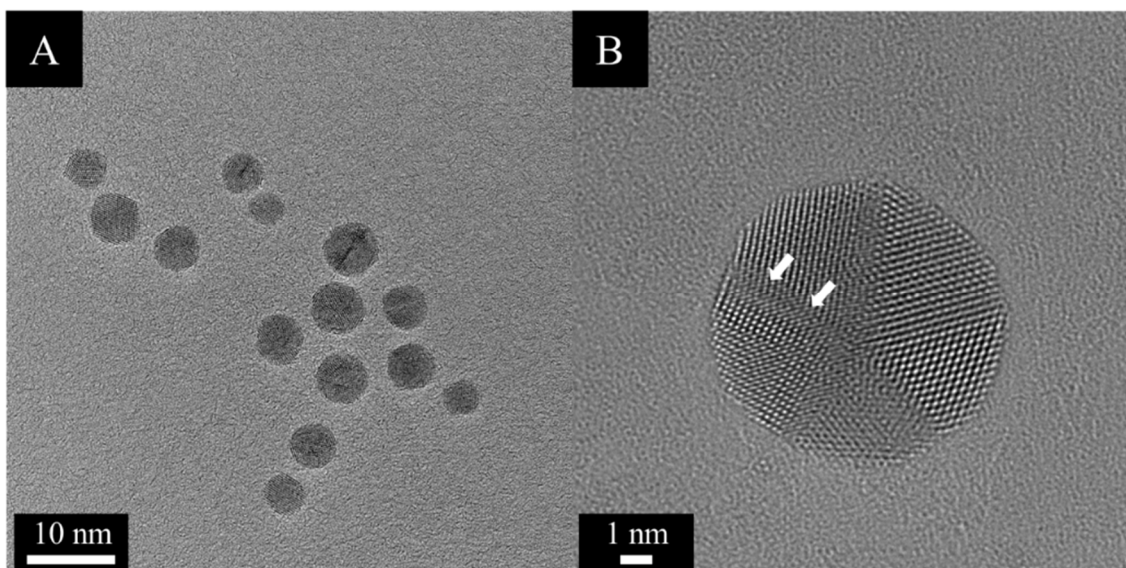


Figure 65: High-resolution TEM image of PVP-stabilised gold nanoparticles synthesised by reduction with citrate and tannic acid (A) and an image of a single particle showing a penta-twinned crystalline structure with stacking faults at the grain boundaries marked with a white arrow (B).

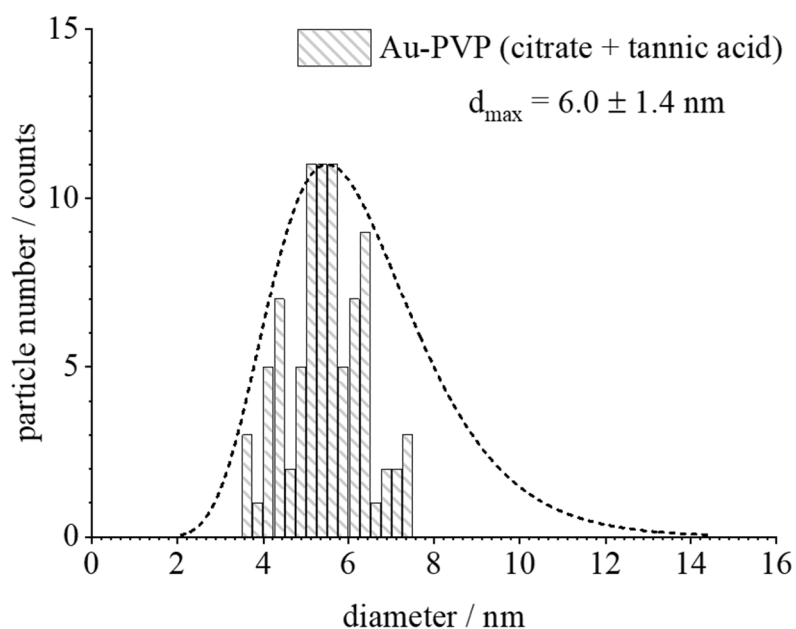


Figure 66: Histogram of particle size analysis from high-resolution TEM of PVP-stabilised Au nanoparticles synthesised by reduction with citrate and tannic acid. The size distribution was analysed by a log-normal distribution fit.

Table 13: Overview of the gold fcc reflex position between 30-80° from Rietveld refinement in comparison to the ICDD database (Au, PDF 00-004-0748).^[222]

Reflex position (observed) $2\Theta / ^\circ$	Reflex position (reference) $2\Theta / ^\circ$	Lattice plane (hkl)
38.200	38.178	(111)
44.402	44.397	(200)
64.614	64.565	(220)
77.616	77.547	(311)

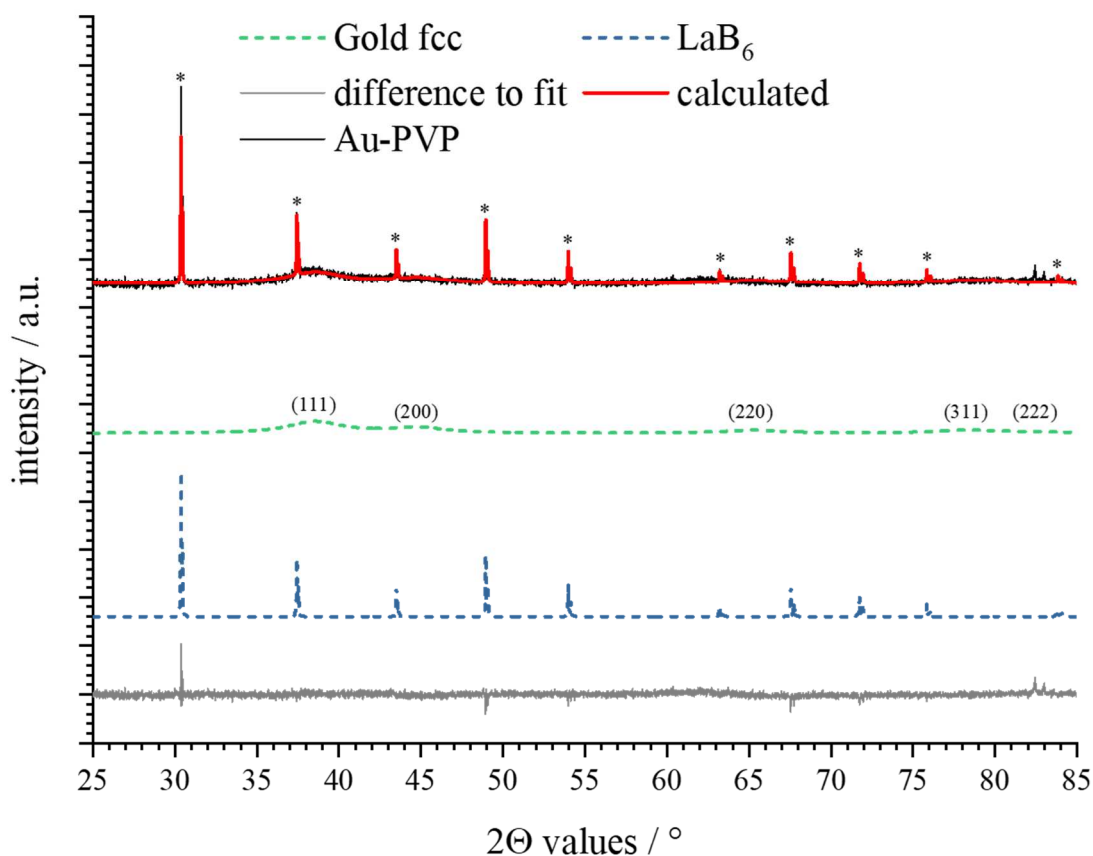


Figure 67: Powder diffraction pattern (not $K\alpha$ stripped) and Rietveld refinement of PVP-stabilised Au nanoparticles synthesised by reduction with citrate and tannic acid. The peak profile is calculated using the fcc phase of gold. The asterisks mark the lanthanum hexaboride (LaB_6 , PDF 00-034-0427).^[122] The reflexes of gold are compared to powder diffraction file 00-004-0784 (Au).^[222]

The further investigation of the ultrastructure is carried out by powder X-ray diffraction. The diffraction pattern corresponds to a pure face-centred cubic (fcc) phase. Gold crystallises in this structure with the space group $Fm\bar{3}m$. The lattice constant a is 4.072 \AA .^[223] The main reflexes of the (111), (200), (220), and (311) crystallographic plane can be assigned to the reference (Table 13). The sharp reflexes originate from additional lanthanum hexaboride (LaB_6 , marked with asterisks, Figure 67) for investigation of the instrumental broadening, which is negligible. The reflexes of the gold phase show a marked broadening because of nanocrystallinity. A small crystallite size leads to broader diffraction reflexes because of natural lattice defects and interference effects.^[124] For an adequate investigation of the crystallographic and structural properties, the diffraction pattern of gold nanoparticles is measured without any LaB_6 . The calculated crystallite size is $2.29(4) \text{ nm}$ and confirms the presence of a twinned crystal structure according to the structural observation from high-resolution TEM images.

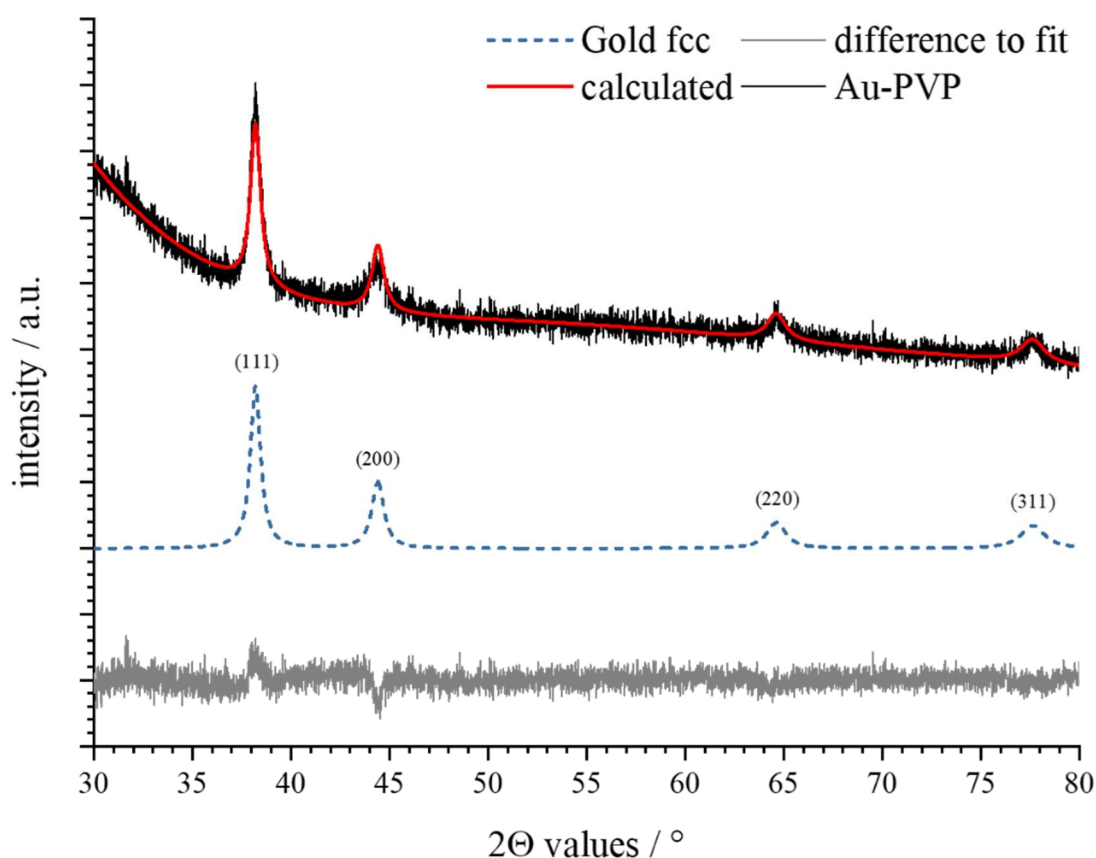


Figure 68: Powder diffraction pattern (not $K\alpha$ stripped) and Rietveld refinement of PVP-stabilised Au nanoparticles synthesised by reduction with citrate and tannic acid. The peak profile is calculated using the fcc phase of gold.

Table 14: Results of the Rietveld refinement from X-ray powder diffraction analysis of freeze-dried Au nanoparticles. The reference values for the lattice parameter a were taken from AMCSD 0013108 (Au).^[223]

Parameter	Au fcc
Tabulated lattice parameter a (bulk metals) / Å	4.072
Calculated lattice parameter a / Å	4.079(5)
Calculated cell volume / Å ³	67.9(2)
Calculated crystallite size / nm	2.29(4)
Calculated crystal density / g cm ⁻³	19.28(7)

In summary, the synthesis gold nanoparticles with a mixture of trisodium citrate and tannic acid yields particles within a size of about 5-6 nm. Transmission electron microscopy depicted spherical-like particles (core size around 6 nm) with a penta-twinned crystal structure and observable stacking faults at the grain boundaries. This could be confirmed by PXRD and Rietveld refinement. The calculated crystallite size is roughly 2 nm. The obtained particles possess an observable absorption in the visible range with an absorption maximum at 518 nm corresponding to the surface plasmon resonance of nanosized gold.

4.1.9 Summary

Overall, uniform, spherical nanoparticles of the platinum and coin metals (group VIII-XI) in a size range of 5 to 10 nm are available with a wet-chemical synthesis approach using different reducing agents. Except iridium nanoparticles, the syntheses result in a high degree of monodispersity and synthesis reproducibility. In addition, an extensive characterisation including physical, chemical, and structural properties is performed using different colloid-chemical, spectroscopic, and microscopic methods.

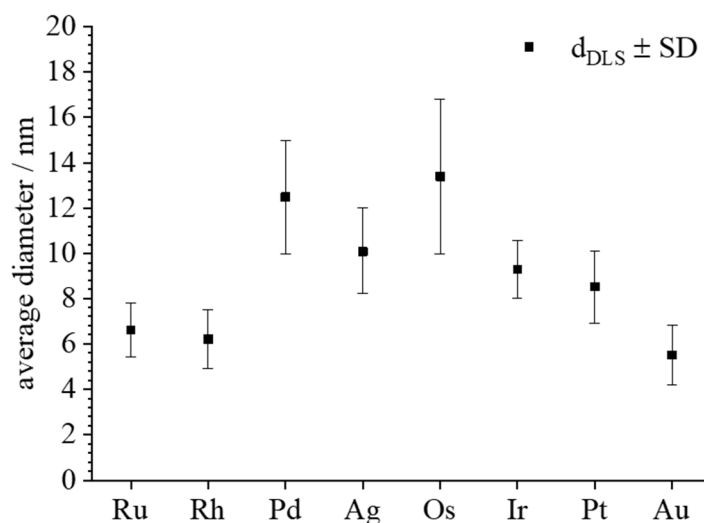


Figure 69: Hydrodynamic diameter determined by dynamic light scattering of monometallic nanoparticles (Ru, Rh, Pd, Ag, Os, Ir, Pt, and Au). All values are given as an average of 3 measurements with standard deviation

All nanoparticles have a neutral or (slightly) negative zeta potential (Figure 70). This behaviour is supposedly due to synthesis by-products that were not completely replaced by the stabilizing polymer PVP.^[224] The hydrodynamic diameter as determined by dynamic light scattering (DLS, Figure 69) and differential centrifugal sedimentation analysis (DCS, Figure 71) are comparable to each other. Note the fact that the hydrodynamic diameter from DCS is systematically underestimated because of the hydration shell.^[95]

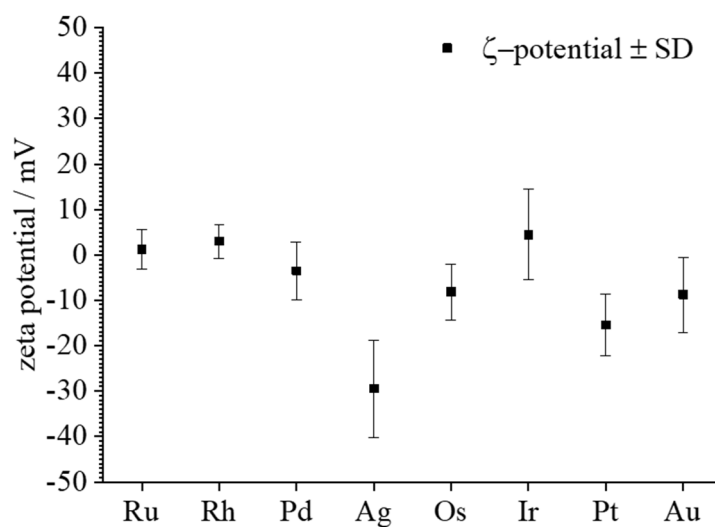


Figure 70: Zeta potential of monometallic nanoparticles (Ru, Rh, Pd, Ag, Os, Ir, Pt, and Au). All values are given as an average of 3 measurements with standard deviation.

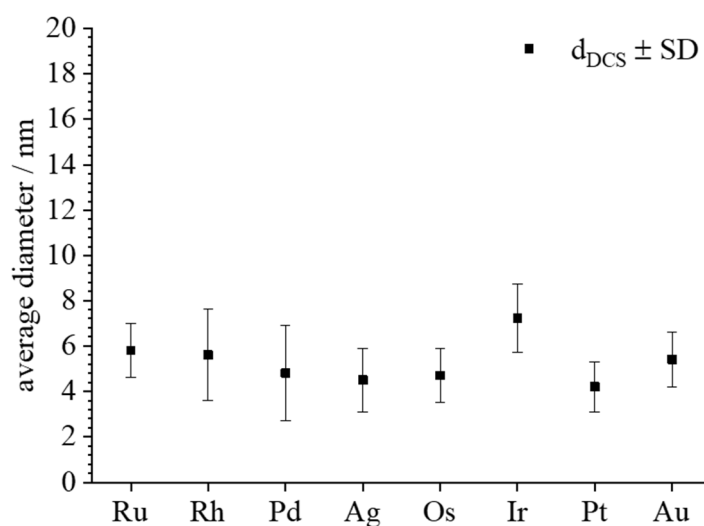


Figure 71: Particle diameter determined by differential centrifugal sedimentation analysis of monometallic nanoparticles (Ru, Rh, Pd, Ag, Os, Ir, Pt, and Au). All values are given as mean diameter with standard deviation.

All metals have almost spherical morphologies as identified by high-resolution electron microscopy. For the further analysis of the crystallographic properties and phase purity, powder X-ray diffraction of freeze-dried samples were performed. The crystallite size, cell volumes, crystal densities and lattice parameters were calculated by an extensive Rietveld refinement analysis. Considering the different method characteristics, the calculated crystallite sizes suggest the obtained structure as observed by high-resolution TEM imaging. However, the small particle size, especially in the case of Ru, Rh, Os and Ir, leads to a distinct peak broadening, which results in difference between the particle size from TEM and the crystallite size. Additionally, the diffraction pattern could explain the crystal structure of silver and gold nanoparticles. Whereas silver seems to be single crystalline with a few intrinsic stacking faults, gold shows typical penta-fold twinning of crystals. In general, the large surface-to-volume ration as well as the local configuration of atoms are causing specific properties of nanoparticles.^[157] The definition of particle morphology is contributed to the surface energy, the cohesion, the strain energy, and the twinning energy.^[225] The equilibrium shape of nanosized crystals is based on the Wulff construction and can be predicted by the minimisation of the free surface energy of crystals for a given volume. Face-centred cubic (fcc) crystals tend to form truncated octahedrons with large (111) and small (100) facets in accordance to the Wulff construction.^[226] Whereas metal nanoparticles smaller than 10 nm in diameter prefer an icosahedral structure, larger crystals prefer a truncated octahedral structure.^[225, 227] Those explicate the formation of twinned structure as observed in the case of gold. In contrast, the stacking faults, which can be identify as an hcp phase of silver, results from the instantly crystallisation of Ag. In dependence of the reduction potential of NaBH₄,^[167, 168] the atom number will be increase which leads to an immediately nucleation and crystallisation of Ag particles. Therefore, the nucleation and growth process is kinetically driven which results in a high number of stacking faults.

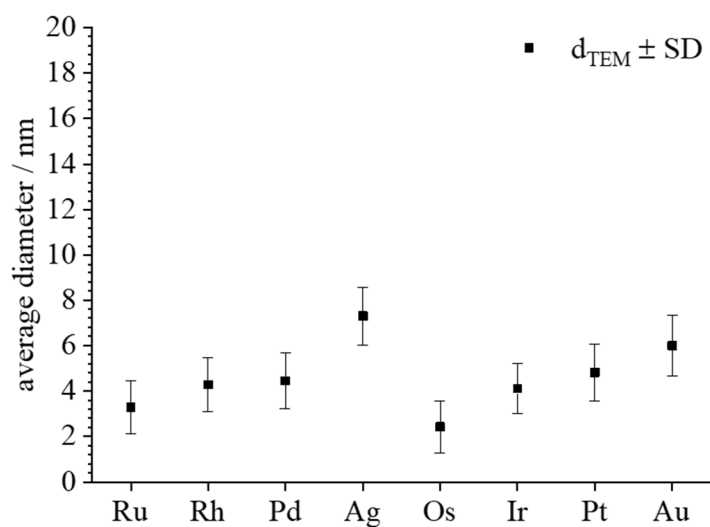


Figure 72: Particle diameter determined by high-resolution transmission electron microscopy of monometallic nanoparticles (Ru, Rh, Pd, Ag, Os, Ir, Pt, and Au). All values are given as mean diameter with standard deviation.

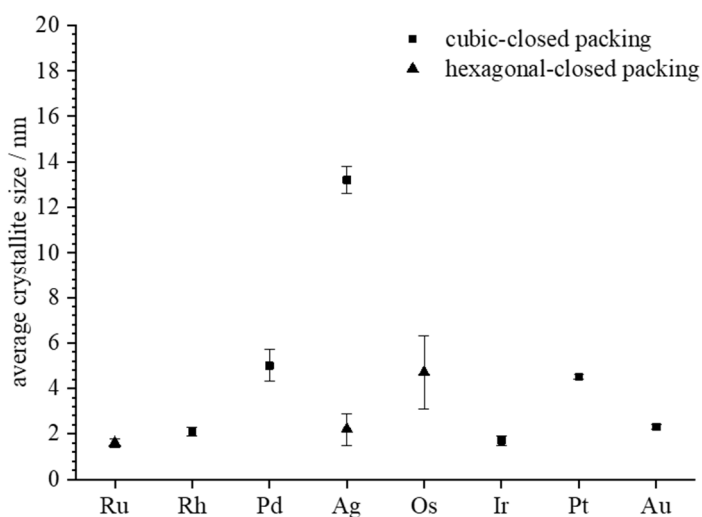


Figure 73: Crystallite size determined by PXRD and Rietveld refinement of monometallic nanoparticles (Ru, Rh, Pd, Ag, Os, Ir, Pt, and Au). All values are given as mean crystallite size with standard deviation concerning the packing density (cubic-closed packing (ccp) vs. hexagonal-closed packing (hcp)).

Table 15: Characterisation data of PVP-stabilised nanoparticles of the platinum and coin metal groups (VIII – XI). All particles were well dispersed in water and not agglomerated.

	Ru	Rh	Pd	Ag
reductant	glucose	glucose	glucose	NaBH ₄
d _{DLS} ¹ / nm	6.6 ± 1.2	6.2 ± 1.4	12.5 ± 2.6	10.2 ± 1.9
d _{DCS} ¹ / nm	5.8 ± 1.2	5.6 ± 2.0	8.4 ± 3.7	5.5 ± 1.5
d _{TEM} / nm	3.7 ± 1.2	4.3 ± 1.2	4.4 ± 1.2	8.0 ± 1.3
d _{XRD} ² / nm	1.6 ± 0.2	2.1 ± 0.2	5.0 ± 0.7	13.2 ± 0.6 (fcc) 2.2 ± 0.7 (hcp)
ζ-potential / mV	+1 ± 4	+3 ± 4	-4 ± 6	-30 ± 11
	Os	Ir	Pt	Au
reductant	glucose	glucose	glucose	citrate + tannic acid
d _{DLS} ¹ / nm	13.4 ± 3.4	9.3 ± 1.3	8.5 ± 1.7	5.6 ± 1.3
d _{DCS} ¹ / nm	7.5 ± 3.6	7.3 ± 1.5	4.3 ± 1.1	5.4 ± 1.2
d _{TEM} / nm	2.4 ± 1.2	4.1 ± 1.1	4.8 ± 1.3	6.0 ± 1.4
d _{XRD} ² / nm	4.7 ± 1.6	1.7 ± 0.2	4.5 ± 0.1	2.3 ± 0.1
ζ-potential / mV	-8 ± 6	1 ± 10	-16 ± 7	-9 ± 8

¹Average diameter calculated from log-normal and Gaussian distribution fit with standard deviation.

²Crystallite size calculated by Rietveld refinement

The dispersion of the platinum metals (Ru, Rh, Pd, Os, Ir, Pt) are all brownish-black without any distinct absorption in visible range (400 to 800 nm). In contrast, the coin metals silver and gold show the typical absorption band due to their surface plasmon resonances.^[115]

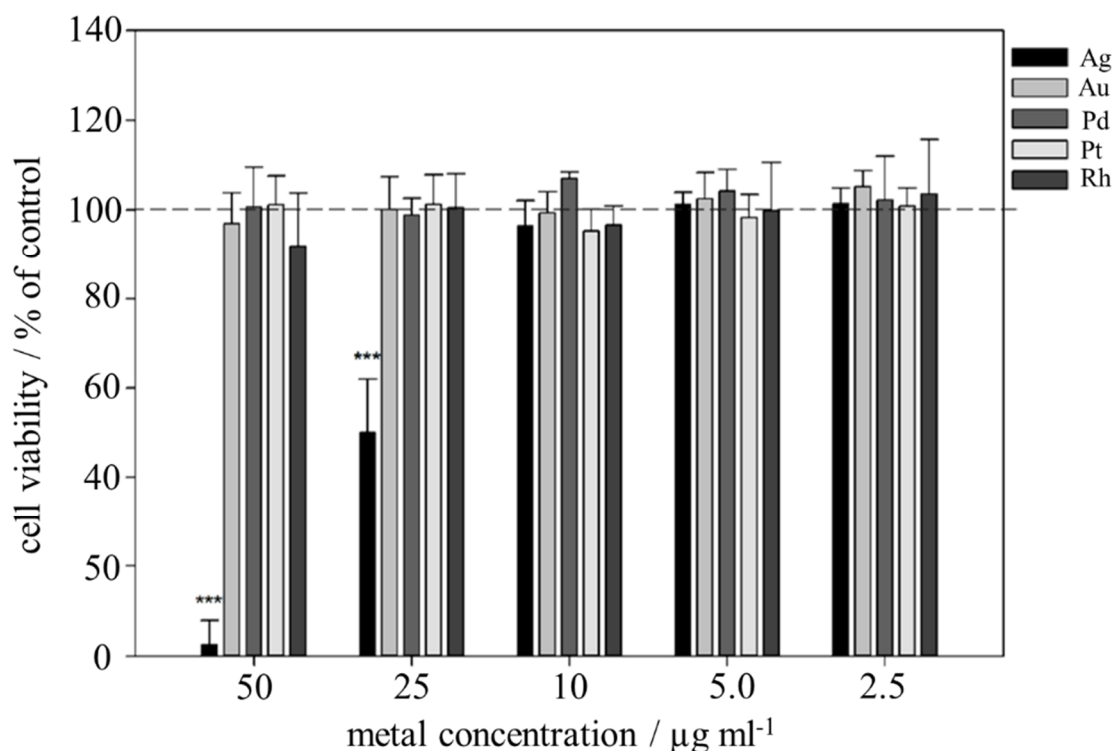


Figure 74: Effect of monometallic nanoparticles of the noble metals (Rh, Pd, Ag, Pt, and Au) on the viability of human mesenchymal stem cells (hMSC). The cells are treated with nanoparticles (2.5 to 50 $\mu\text{g ml}^{-1}$) for 24 h under cell culture conditions. Vital cells (green fluorescence) are quantified by digital image processing (phase analysis). The data are expressed as mean \pm standard deviation ($n = 5$ independent experiments) given as percentage of the control (cells cultured without nanoparticles). Asterisks (*) indicate significant differences in comparison to the control (*) $p \leq 0.001$). The graph is taken from the reference.^[228]**

In addition, cell biological studies on human mesenchymal stem cells (hMSC) from bone marrow are carried out to assess potential toxic effects after unintended exposure. Note that ruthenium, osmium, and iridium nanoparticles are not stable in cell cultured medium (RPMI plus 10 % FCS) and formed aggregates, which were precipitated during the experiments. Therefore, they were not further investigate in cell biological studies. All other

nanoparticles are well dispersed in RPMI plus 10 % fetal calf serum without neither any aggregation nor precipitation. Except for silver nanoparticles, there is no adverse effect on the viability of hMSC up to a concentration of $50 \mu\text{g ml}^{-1}$. Ag shows a concentration depending cytotoxicity from 25 to $50 \mu\text{g ml}^{-1}$ (Figure 74). The effects are known for silver, silver chloride, and silver ions.^[229-232] In contrast to toxic concentration ($\geq 25 \text{ mg ml}^{-1}$) of Ag nanoparticles, subtoxic concentration ($\leq 10 \mu\text{g ml}^{-1}$) of Ag show no cell detachment which is correlated to cell toxicity. Additional, subtoxic concentrations of silver have a reported adverse influence on differentiation of hMSC.^[233]

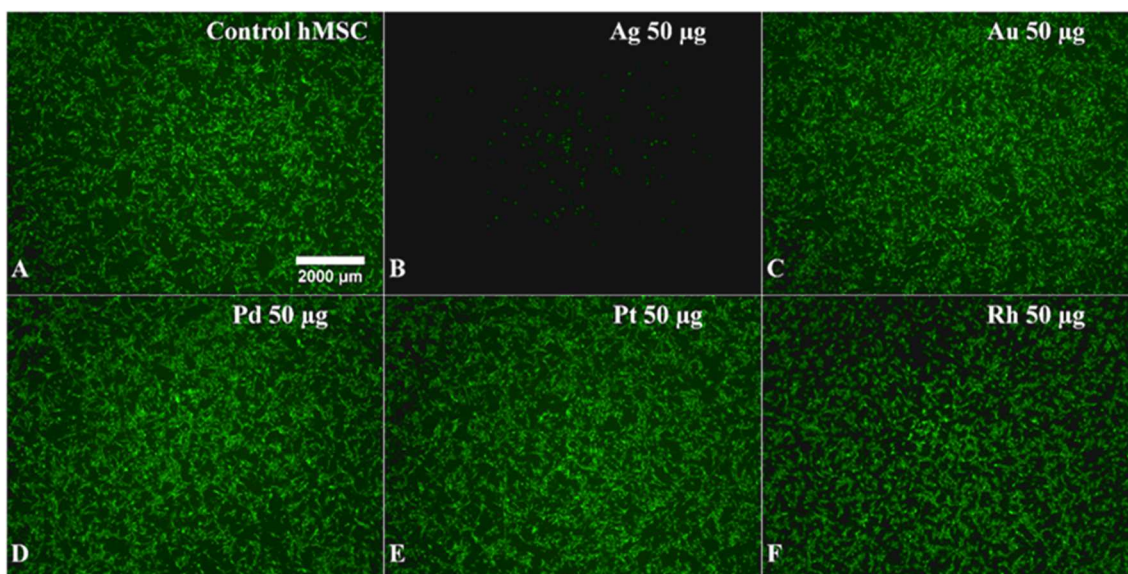


Figure 75: Effects on the viability and morphology of hMSC in the presence of noble metal nanoparticles (Rh, Pd, Ag, Pt, and Au). Subconfluent growing hMSC in 24-well cell culture plates are incubated in the absence (A, control) or in the presence of metal nanoparticles (B-F, $50 \mu\text{g ml}^{-1}$) for 24 h under cell culture conditions and subsequently stained with calcein-AM. Viable cells are indicated by green fluorescence. The image is taken from the reference.^[228]

4.2 Characterisation of bimetallic Pd-Au nanoparticles

The second part of the present work is concerned with the syntheses of alloyed and core-shell nanoparticles of palladium and gold to assess the possibility of such bimetallic systems, which consist of two metals with different electrochemical standard potential. Two approaches are pursued to achieve the synthesis of bimetallic Au-Pd nanostructures. On the one hand, a simultaneous reduction of the ionic metal precursors, Na_2PdCl_4 and HAuCl_4 , is carried out to prepared alloyed particles and on the other hand a seed-and-growth approach with sequential reduction is accomplished to form nanoparticles with a distinct core-shell structure. The detailed spectroscopic, colloid-chemical, and microscopic characterisation comprises size, shape and composition as well as the ultra- and microstructure. Dr. Kateryna Loza performs the high-resolution and scanning transmission electron microscopy including HAADF imaging and EDX spectroscopic analysis in cooperation with Dr. Marc Heggen's group at the Ernst-Ruska Centre for Microscopy and Spectroscopy with Electrons in Jülich. In addition, *in-situ* small-angle X-ray scattering (SAXS) measurements are performed to monitor the formation of Pd-Au core-shell nanoparticles. Mr. Paulo R. A. F. Garcia and Prof. Dr. Cristiano L. P. Oliveira in the Institute of Physics at the University of São Paulo in Brazil carry out the SAXS experiments. Ms. Marina Breisch, Jun.-Prof. Dr. Christina Sengstock, and Prof. Dr. Manfred Köller in the Surgical Research at the University Hospital Bergmannsheil in Bochum carry out cell biological studies.

4.2.1 Bimetallic AuPd (alloyed) nanoparticles by simultaneous reduction

Bimetallic AuPd nanoparticles are wet-chemically prepared in a one-pot synthesis using *D*-glucose. The formation of alloyed structures is anticipated using a simultaneous reduction approach of the ionic species in the presence of PVP as stabilizing agent. The average hydrodynamic diameter of the obtained particles is 16.0 nm with a standard deviation of ± 3.9 nm as determined by DLS (Figure 76). The PdI value is 0.28, indicating a well-dispersed system. The size distribution of AuPd nanoparticles obtained by differential centrifugal sedimentation analysis is shown in Figure 77. The average size is 4.0 nm with a standard deviation of ± 1.1 nm in diameter with a PdI of 0.36. It has to be taken into account that the size from DLS is overestimated because of the hydration shell (stabilizing agent).

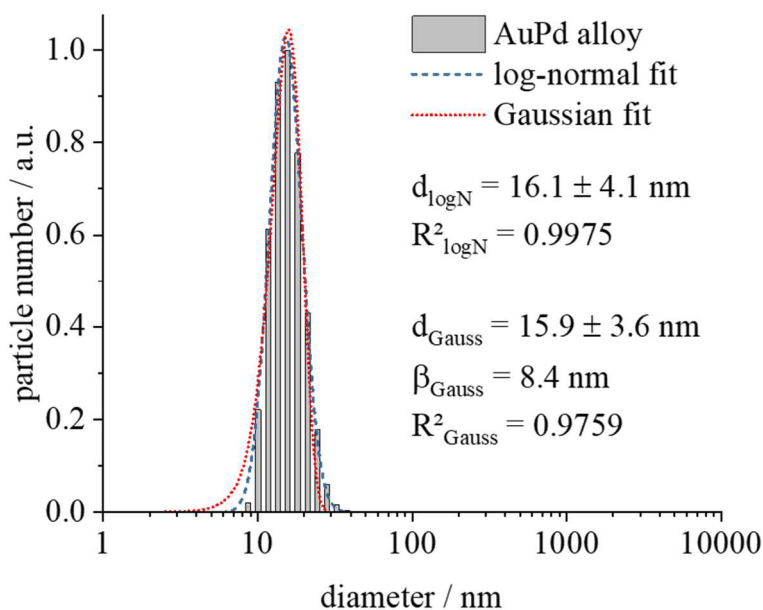


Figure 76: Number-weighted size distribution of AuPd alloyed nanoparticles synthesised by reduction with *D*-glucose determined by DLS. The peak profile is analysed by a log-normal as well as a Gaussian distribution fit. The PdI is 0.28.

The difference between DLS and analytical disc centrifugation arise from the different method characteristics. It is noteworthy that the particle diameter from DCS is smaller than the one determined by dynamic light scattering. This is probably due to the polymer shell around the particles, which affects the effective density of the particles and leads to

lower values. In consequence of a lower effective density, the sedimentation time is increasing, which results in smaller particle sizes.^[113]

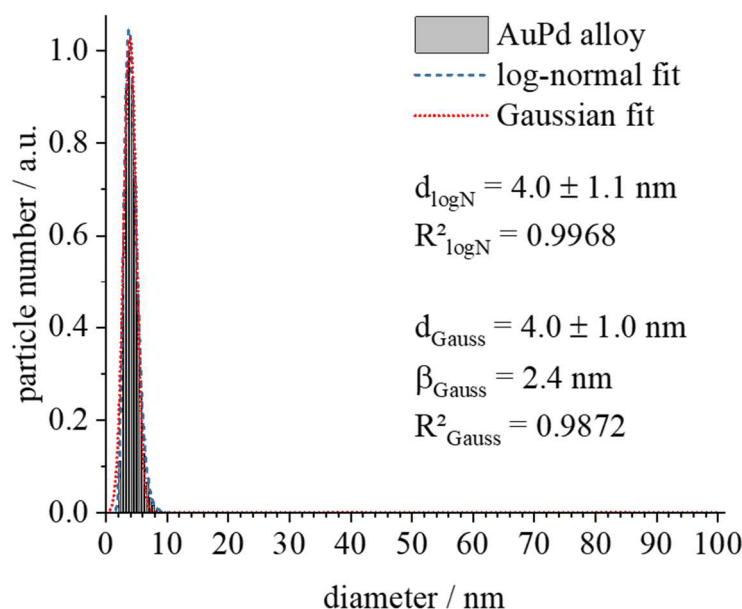


Figure 77: Number-weighted size distribution of AuPd alloyed nanoparticles synthesised by reduction with *D*-glucose determined by DCS. The peak profile is analysed by a log-normal as well as a Gaussian distribution fit. The PdI is 0.36.

In contrast to the UV/vis spectrum of pure Au particles with its typical SPR absorption band around 520 nm, the optical properties of AuPd are similar to pure palladium without any distinct absorption in the visible range (Figure 78).^[115] This observation gives rise to two possible scenarios. On the one hand a core-shell like structure might have formed on the other hand an alloying of both metals might have occurred. A core-shell structure with a gradual elemental distribution and an enrichment of palladium on the surface side shows the same optical properties as the pure metal if the shell is dense enough. In the case of an alloy, palladium is able to prevent the SPR of Au.^[234]

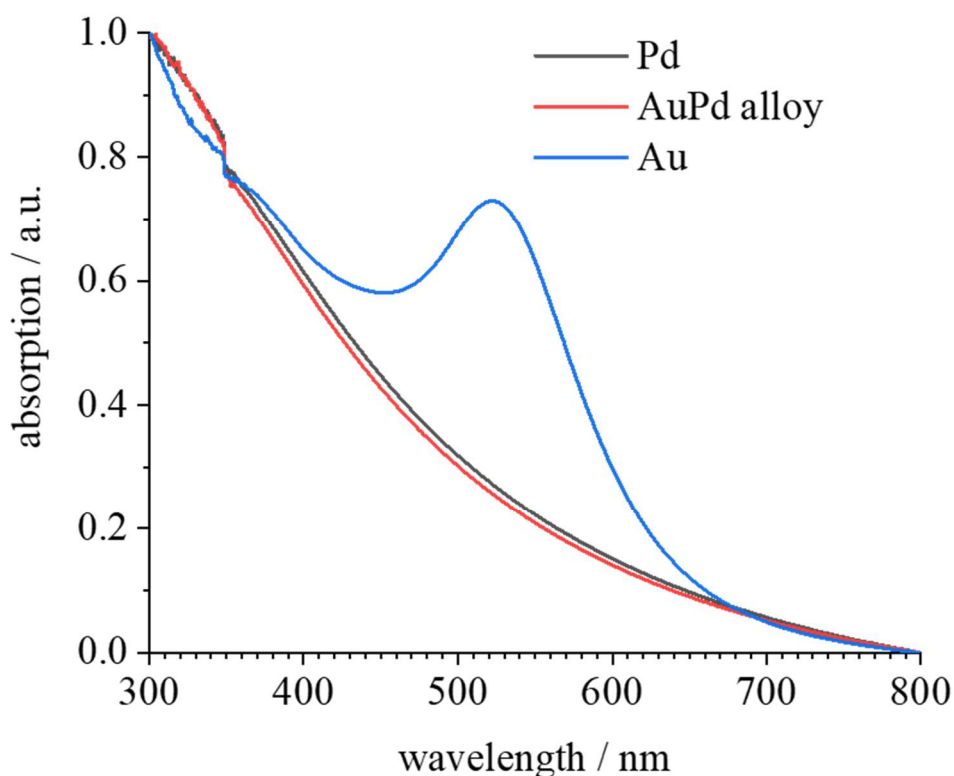


Figure 78: UV/vis spectra of Pd, Au and AuPd alloyed nanoparticles. The data is normalised for better comparison.

Considering the monomodal size distributions determined by DLS and DCS, the optical properties point towards the presence of bimetallic structures like an alloy or a core-shell construction with Pd on the surface. HAADF images show some non-spherical nanostructures (triangles, decahedra) and numerous small palladium nanoparticles. A closer look on the elemental mapping from EDX analysis confirms that the non-spherical nanostructures consist of Au that is decorated with thin shell of palladium (Figure 79). The size of the larger nanostructures is between 10 and 20 nm, whereas the small palladium nanoparticles are below 2 nm. Further, the formation of aggregates or agglomerates of Pd nanoparticles are observable on the HAADF-STEM image.

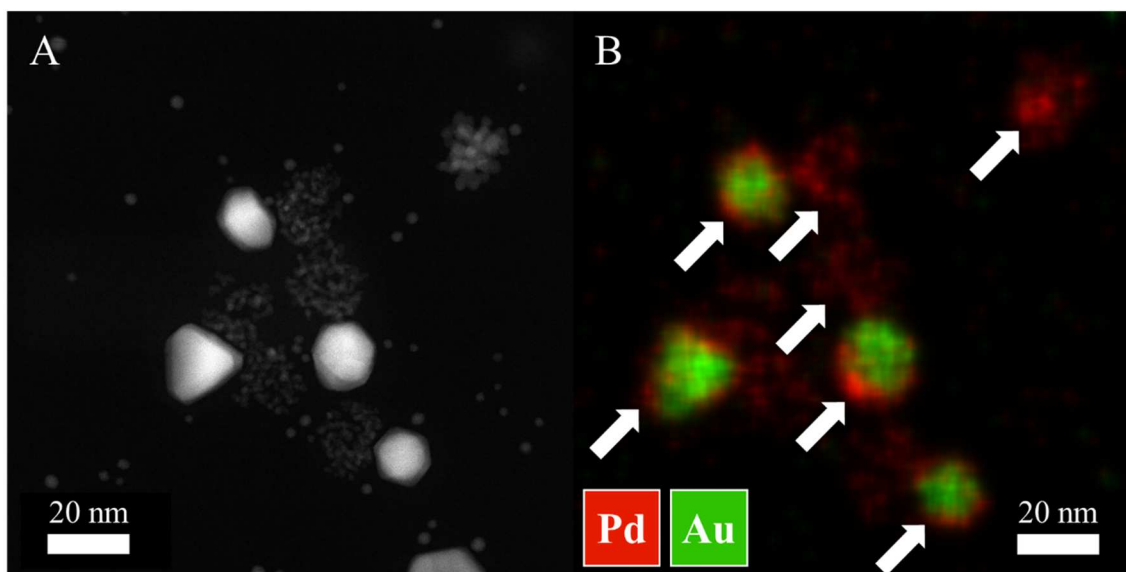


Figure 79: Representative HAADF image of AuPd alloyed nanoparticles and the corresponding elemental mapping from EDX analysis. The EDX maps clearly show the co-presence of Au-Pd core-shell and small Pd nanoparticles (white arrows).

In summary, the results show that no alloyed nanostructures could be obtained by a simultaneous reduction of Au^{3+} and Pd^{2+} with *D*-glucose in aqueous media. The data from dynamic light scattering and analytical disc centrifugation reveals that the particles are colloidally stable without any evidence of aggregation or agglomeration. However, the HAADF images and elemental mapping from EDX clearly illustrate the co-presence of very small palladium nanoparticles and gold nanostructures (triangles, non-spherical nanoparticles) with an obvious thin Pd shell.

4.2.3 Pd-Au core-shell nanoparticles by sequential reduction

The Pd-Au core-shell nanoparticles are wet-chemically prepared by one-pot synthesis using *D*-glucose. The formation of the core-shell structure is accomplished by a sequential reduction of the ionic species in the presence of PVP as stabilizing agent. First, the core is prepared by reduction of Pd²⁺ ions with *D*-glucose. The initial Pd seeds have an average diameter of 6.7 nm with standard deviation of ± 1.2 nm as determined by DLS (Figure 80). The low polydispersity index value of 0.16 indicates well-dispersed particles. Notably, all measurements of the Pd seeds are obtained from the unpurified dispersion because of the one-pot synthesis approach.

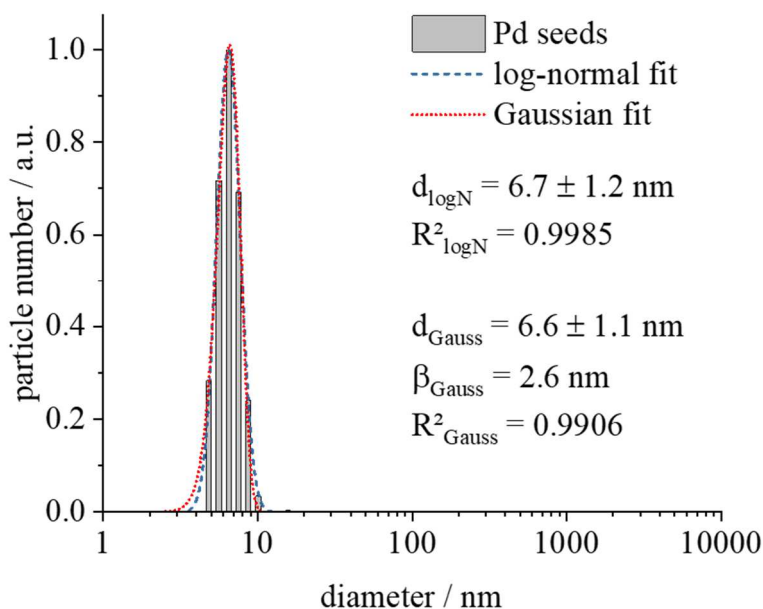


Figure 80: Number-weighted size distribution of Pd seeds synthesised by reduction with *D*-glucose determined by DLS. The peak profile is analysed by a log-normal as well as a Gaussian distribution fit. The PdI is 0.16.

The Pd seeds have a slightly negative ζ -potential of $-6(5)$ mV (at pH 7) due to the polyelectrolyte PVP and supposedly adsorbed reaction by-products on the nanoparticle surface. The size distribution of palladium seeds is further investigated by DCS measurements (Figure 81). The average diameter is 4.6 nm with a standard deviation of ± 2.1 nm and a PdI of 0.337. In fact, it is possible to calculate a polydispersity index from the Gaussian distribution fit but there is no useful interpretation of the high value of 2.44. Considering the correlation coefficient of the Gaussian distribution fit ($R^2 = 0.9583$), a

description with a symmetric “bell curve” shape of the Gaussian function is not suggestive and does not reflect the real size distribution of the Pd seeds. Overall, no sign of aggregation or polydispersity is observable.

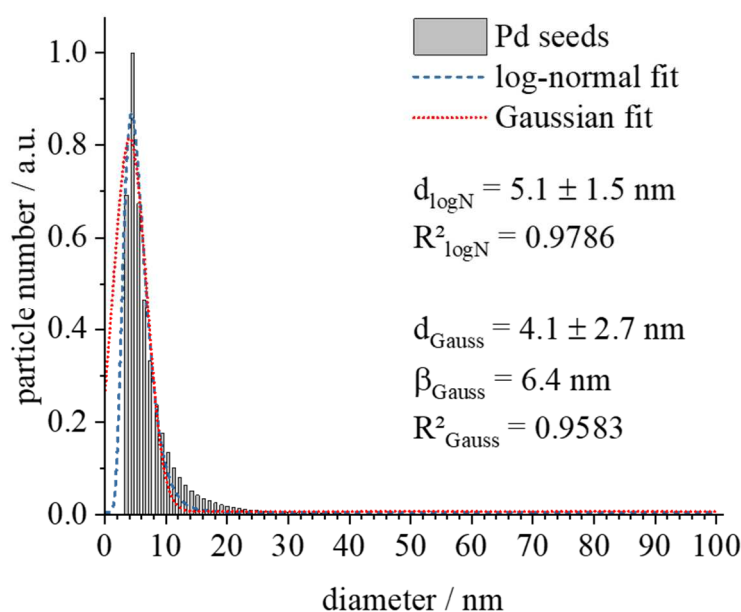


Figure 81: Number-weighted size distribution of Pd seeds synthesised by reduction with *D*-glucose determined by DCS. The peak profile is analysed by a log-normal as well as a Gaussian distribution fit. The PDI is 2.44.

In the next step, an Au(III)-precursor (HAuCl_4) ions are added to the dispersion of small Pd seeds to form a gold shell in the presence of remaining *D*-glucose. A possible galvanic replacement reaction is likely suppressed due to the excess PVP and glucose. The average particle size determined by DLS is 8.1 nm in diameter with a standard deviation of ± 1.8 nm (Figure 82). The polydispersity index is 0.21. An increase in diameter of 1.43(29) nm according to DCS can be observed as compared to the size of the initial Pd seeds. The size of Pd-Au nanoparticles is 6.6 nm with a standard deviation of ± 2.2 nm in diameter (Figure 83). The PDI from DCS is 0.52 that might indicate an unstable dispersion. Nevertheless, neither aggregation nor sedimentation is observed. The difference between DLS and analytical disc centrifugation is based on the method characteristics. Notably, the particle diameter from DCS is smaller than the one determined by dynamic light scattering. This is likely due to the polymeric layer around the particles, which shifts the effective density of the particles towards lower values. In consequence of a lower effective density, the sedimentation time is increasing, which results in smaller particle sizes.^[113]

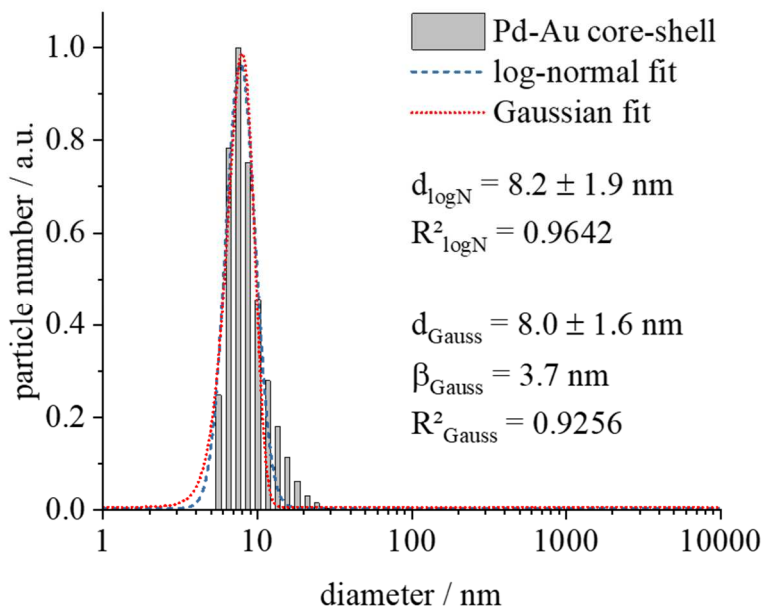


Figure 82: Number-weighted size distribution of PVP-stabilized Pd-Au core-shell nanoparticles synthesised by sequential reduction with *D*-glucose determined by DLS. The peak profile is analysed by a log-normal as well as a Gaussian distribution fit. The PdI is 0.21.

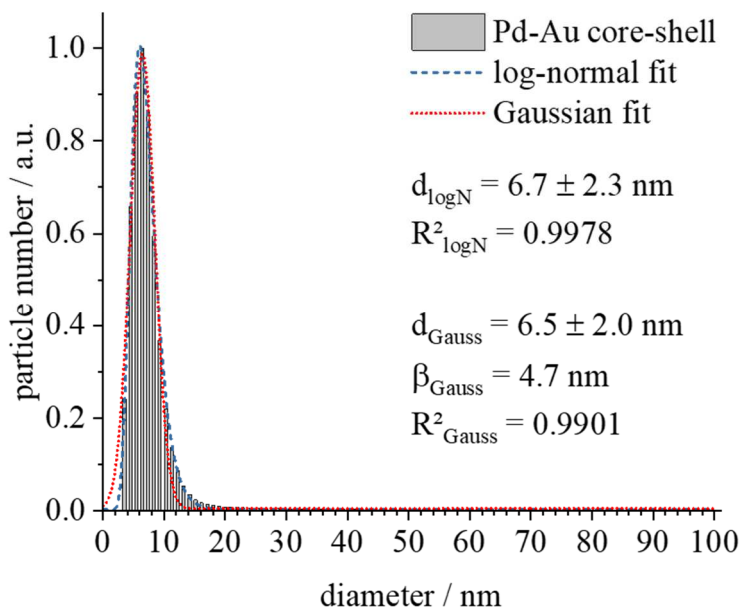


Figure 83: Number-weighted size distribution of PVP-stabilized Pd-Au core-shell nanoparticles synthesised by sequential reduction with *D*-glucose determined by DCS. The peak profile is analysed by a log-normal as well as a Gaussian distribution fit. The PdI is 0.52.

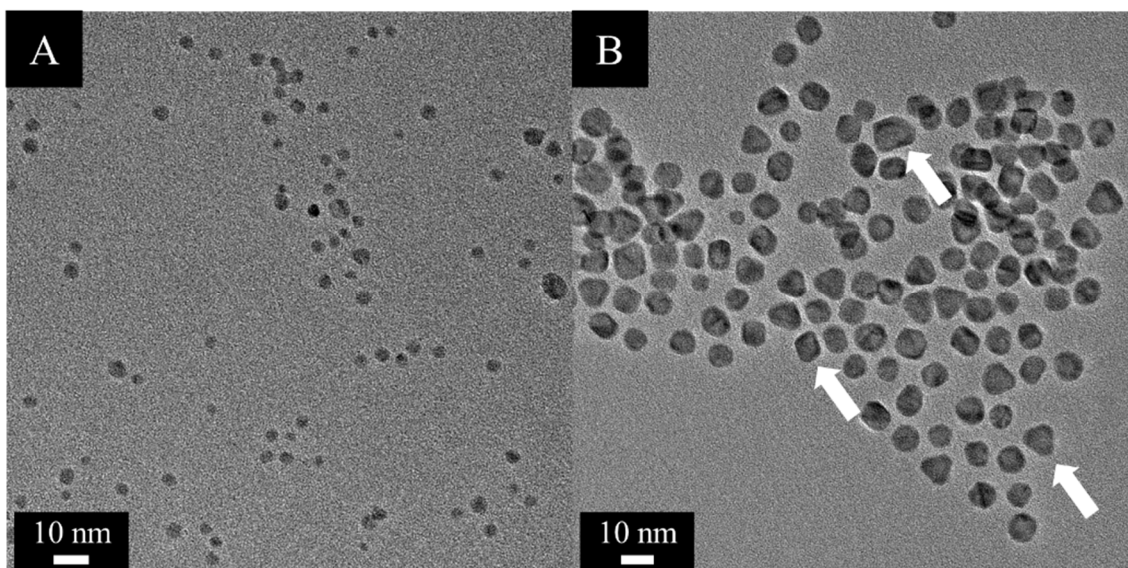


Figure 84: Representative overview TEM image of initial Pd seeds (A) and Pd-Au core-shell nanoparticles (B) synthesised by reduction with *D*-glucose. The image of Pd-Au core-shell nanoparticles (B) shows some particles of different morphologies (e.g. triangles, rhombs) marked with white arrows.

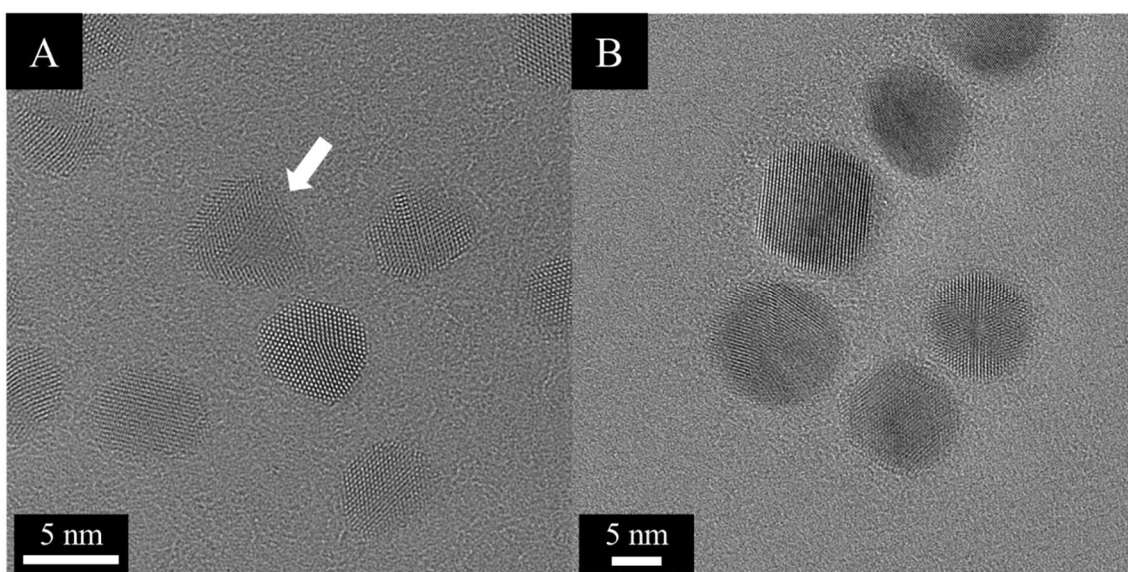


Figure 85: Representative high-resolution TEM image of initial Pd seeds (A) and Pd-Au core-shell nanoparticles (B) in higher magnification. The image of Pd seeds (A) shows a particle of non-spherical morphology (triangle) marked with a white arrow.

The transmission electron micrographs (Figure 84) show quasi-spherical Pd seeds and Pd-Au core-shell nanoparticles with a minor amount of non-spherical morphologies (triangles, rhombs). On a closer look, the particles seem to be single-crystalline with only some indications of stacking faults or twinned structure (Figure 85).

The particle size of initial Pd seeds and Pd-Au core-shell nanoparticles is determined manually by measuring the size of 46 and 50 particles, respectively. The data is compiled in histograms (Figure 86). The diameter of the Pd seeds is 5.4 nm with a standard deviation of 1.1 nm and the overall particle size of Pd-Au core-shell nanoparticles is 8.9 nm with a standard deviation of ± 1.1 nm.

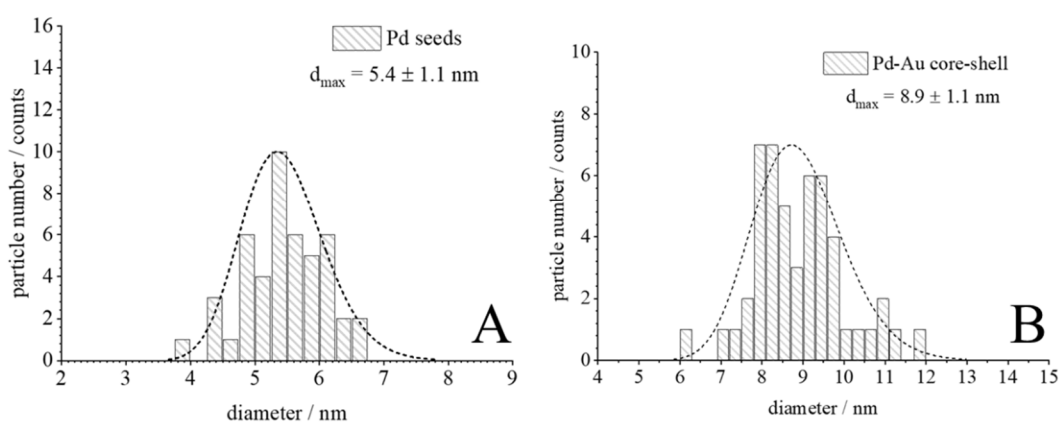


Figure 86: Histograms of particle size analysis from high-resolution TEM of Pd seeds (A) and Pd-Au core-shell nanoparticles (B) synthesised by reduction with *D*-glucose. The size distribution was analysed by a log-normal distribution fit.

Concerning the particle size from TEM, the thickness of the gold shell is about 1.7 nm with a standard deviation of ± 0.6 nm. The UV/vis spectra (Figure 87) show the typical absorption behaviour of palladium with no distinct absorption in the visible range which corresponds very well to the literature.^[115] After addition of gold, a development of an absorption band can be observed which conforms to the absorption region of nanoparticulate gold.^[115] The fact of an absorption band confirms the presence of a dense Au layer around the palladium core, which corresponds very well to the TEM results.

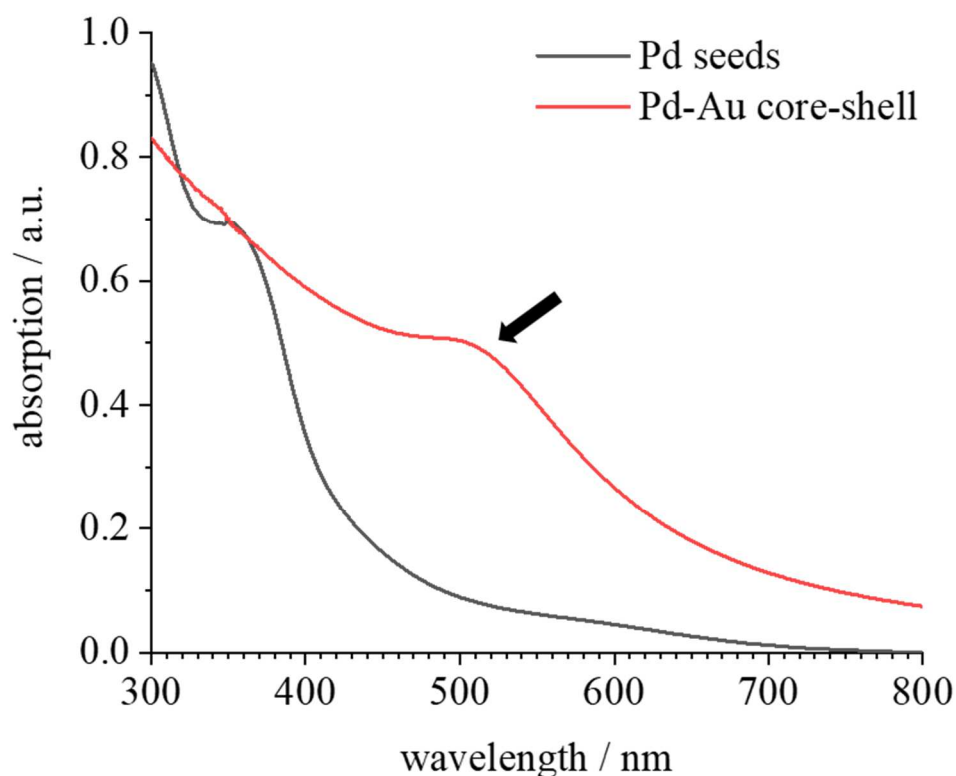


Figure 87: UV/vis spectra of Pd seeds and of the Pd-Au core-shell nanoparticles. The development of an absorption band according to the SPR of Au after addition of gold is marked with a black arrow. The data is normalised for better comparison.

In addition, high-angle annular dark field (HAADF) STEM is performed to elucidate the nanoparticle ultrastructure. HAADF-STEM images (Figure 88) as well as the EDX analysis (mapping and line scan, Figure 90) confirmed the presence of a core-shell structure. A clear phase boundary between the core and the shell can be observed due to the brighter Z-contrast of the heavier element gold ($Z = 79$) in comparison to palladium ($Z = 46$).

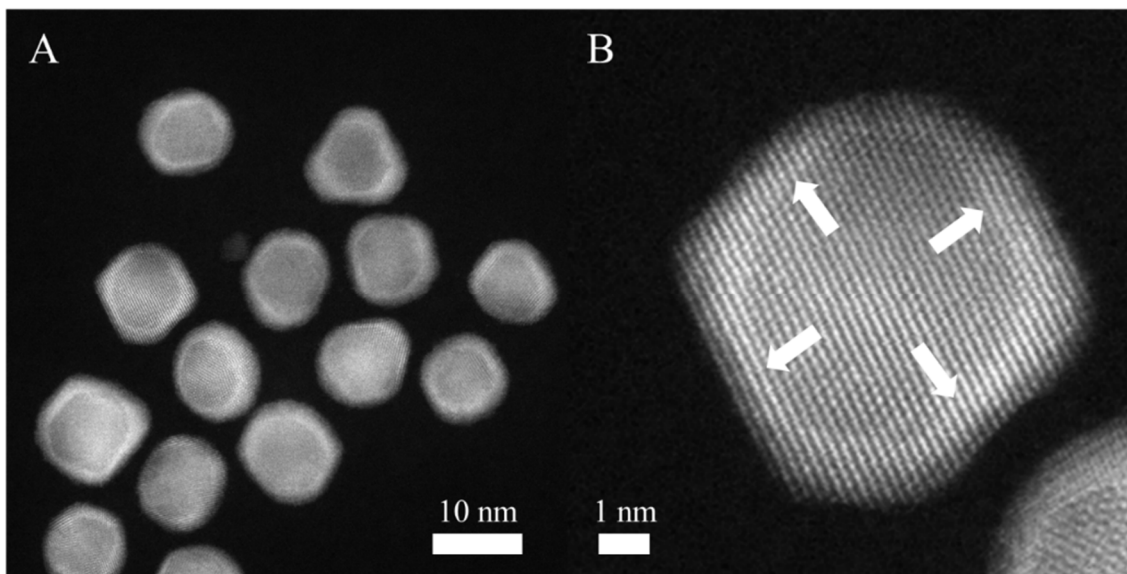


Figure 88: HAADF image of PVP-stabilised Pd-Au core-shell nanoparticles synthesised by sequential reduction with *D*-glucose (A) and a higher magnification of a single particle showing clearly the contrast difference at the boundary of the core and shell marked with white arrows.

The size of the inner and outer sphere from HAADF-STEM imaging is determined manually by measuring the size of 15 particles and compiling histograms (Figure 89). The thickness of the shell is 1.2 ± 0.7 nm.

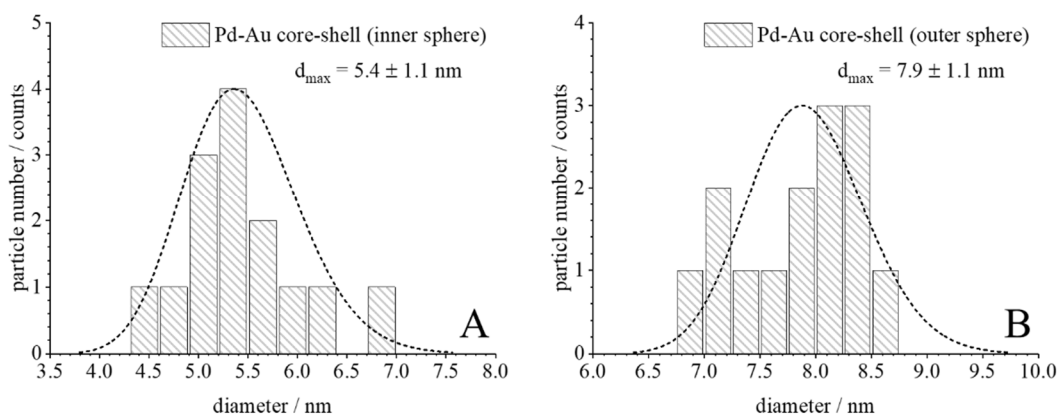


Figure 89: Histograms from the inner (A) and outer sphere (B) of Pd-Au core-shell nanoparticles as obtained from HAADF-STEM images. The particle size distribution is analysed by a log-normal distribution fit.

The quantitative EDX evaluation gives an average molar Pd: Au ratio of 59 at% to 41 at%, which is slightly lower for gold than expected from the stoichiometric synthesis where a 50:50 ratio was used. An alloying of the shell and core cannot be exactly quantified with the obtained data sets. An accurate EDX analysis can only be realised by partial cross sections with special single element calibration samples.^[235]

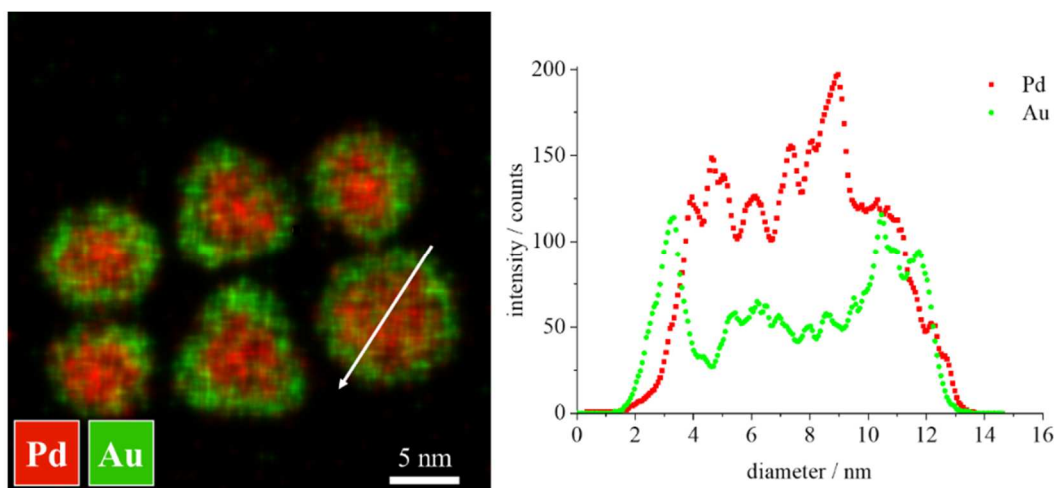


Figure 90: Elemental mapping from EDX analysis with an additional line scan (white arrow) of Pd-Au core-shell nanoparticles. The EDX maps and line scans clearly illustrate the co-presence of a palladium core (red) and a gold shell (green).

The obtained particles are mainly single crystalline, notwithstanding the core-shell structure and some isolated twins and grain boundaries (Figure 88), indicating an epitaxial growth of the Au shell onto the palladium core during the synthesis (Figure 90). Note that a few particles possess a triangular instead of a spherical shape. The more or less pronounced boundary between the Pd core and the Au shell indicates a sequential overgrowth with some alloying at the interface. Gold and palladium provide an unlimited row of mixed crystals, with a perfect match to Vegard's law concerning the lattice parameter for the cubic fcc crystal system (Figure 91).^[51, 236-241] X-ray powder diffraction on freeze-dried samples is carried out to investigate the internal structure of core-shell nanoparticles and an extensive Rietveld refinement is performed for quantitative phase analysis and calculation of the lattice parameters, the crystallite sizes, the crystal density, and cell volume. Despite the epitaxial overgrowth of gold, the two metal phases can be clearly distinguished in the diffraction pattern due to their different lattice parameters. The results of the Rietveld refinement are summarised in Table 18.

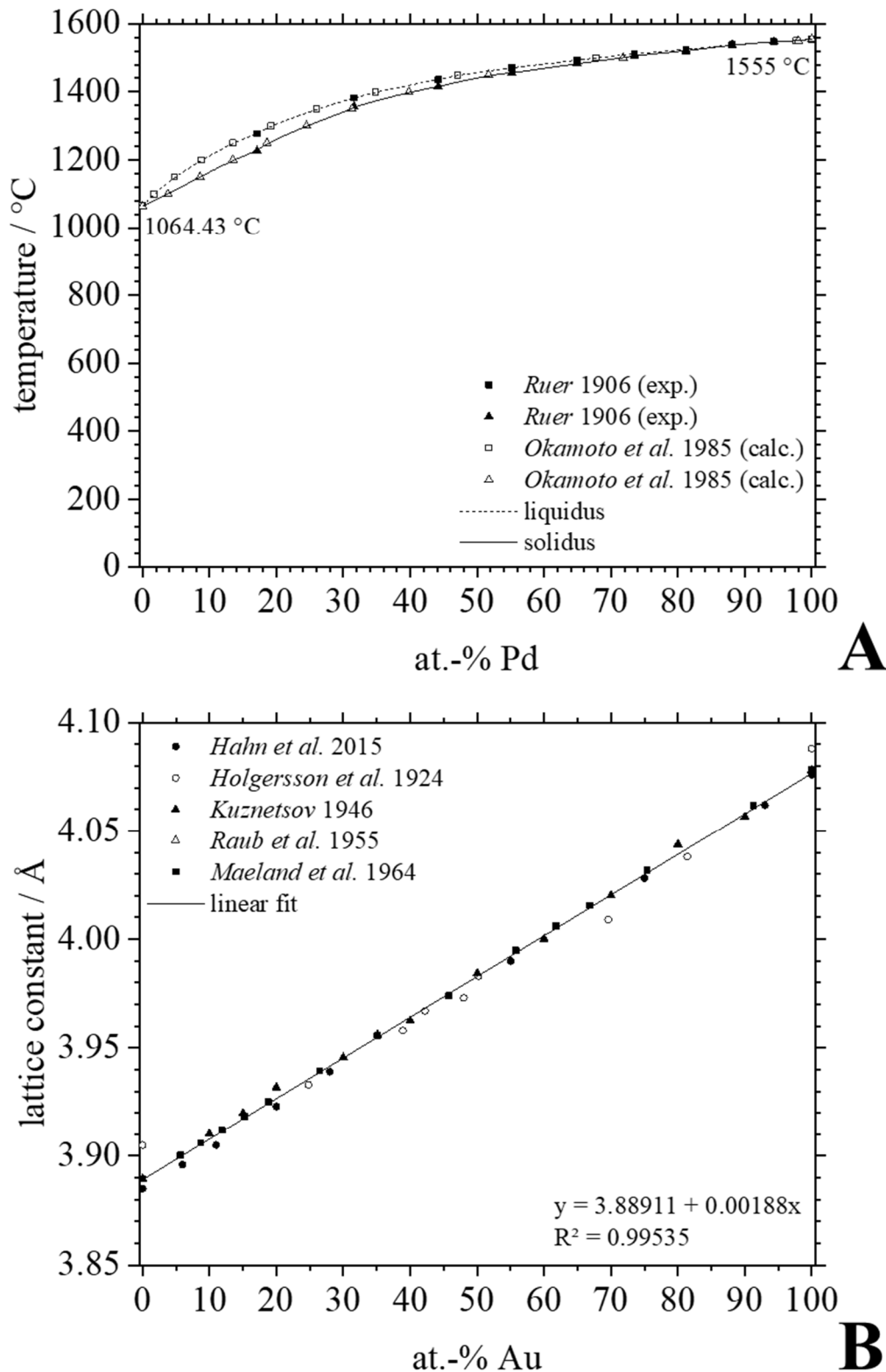


Figure 91: Phase diagram (A) and trend of lattice parameter (B) in the Pd-Au system. Data points are taken from references.^[51, 236-241]

The main reflexes of the (111), (200), (220), and (311) crystallographic plane of the fcc phases of palladium and gold can be observed and assigned to the reference (Table 16 and Table 17). The sharp reflexes originate from additional lanthanum hexaboride (LaB_6 , marked with asterisks, Figure 92) for investigation of the instrumental broadening, which is negligible.

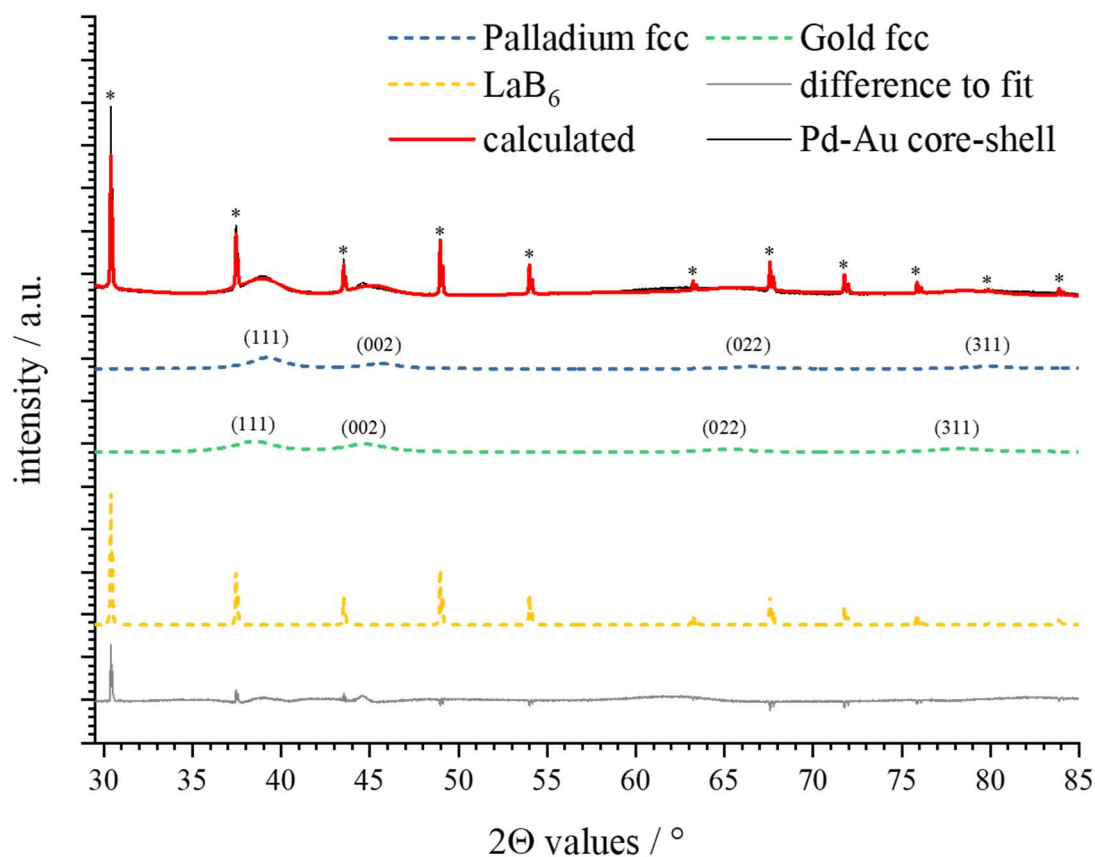


Figure 92: Powder diffraction pattern (not $K\alpha$ stripped) and Rietveld refinement of PVP-stabilised Pd-Au core-shell nanoparticles synthesised by reduction with *D*-glucose. The peak profile is calculated using the fcc phases of palladium and gold, respectively. The asterisks mark the lanthanum hexaboride (LaB_6 , PDF 00-034-0427).^[122] The reflexes of palladium and gold are compared to powder diffraction file 00-004-0784 (Au)^[222] and 00-046-1043 (Pd), respectively.^[148]

Table 16: Overview of the palladium fcc reflex position between 35-90° from Rietveld refinement in comparison to the ICDD database (Pd fcc, PDF 00-046-1043).^[148]

Reflex position (observed) $2\Theta / ^\circ$	Reflex position (reference) $2\Theta / ^\circ$	Lattice plane (hkl)
39.221	40.122	(111)
45.503	46.664	(200)
66.436	68.118	(220)
79.998	82.099	(311)

Table 17: Overview of the gold fcc reflex positions between 35-90° from Rietveld refinement in comparison to the ICDD database (Au fcc, PDF 00-004-0748).^[222]

Reflex position (observed) $2\Theta / ^\circ$	Reflex position (reference) $2\Theta / ^\circ$	Lattice plane (hkl)
38.526	38.178	(111)
44.608	44.397	(200)
65.092	64.565	(220)
78.274	77.547	(311)

The slightly shift of the observed gold reflex positions to higher 2Θ values (Table 17) suggests a small compression of the unit cell and results in a decrease in the lattice parameter of Au. In contrast, the palladium reflex positions are shifted to lower 2Θ values (Table 16), which implies an expansion of the unit cells. As result, an increase in the lattice parameter of Pd can be observed.^[174, 175]

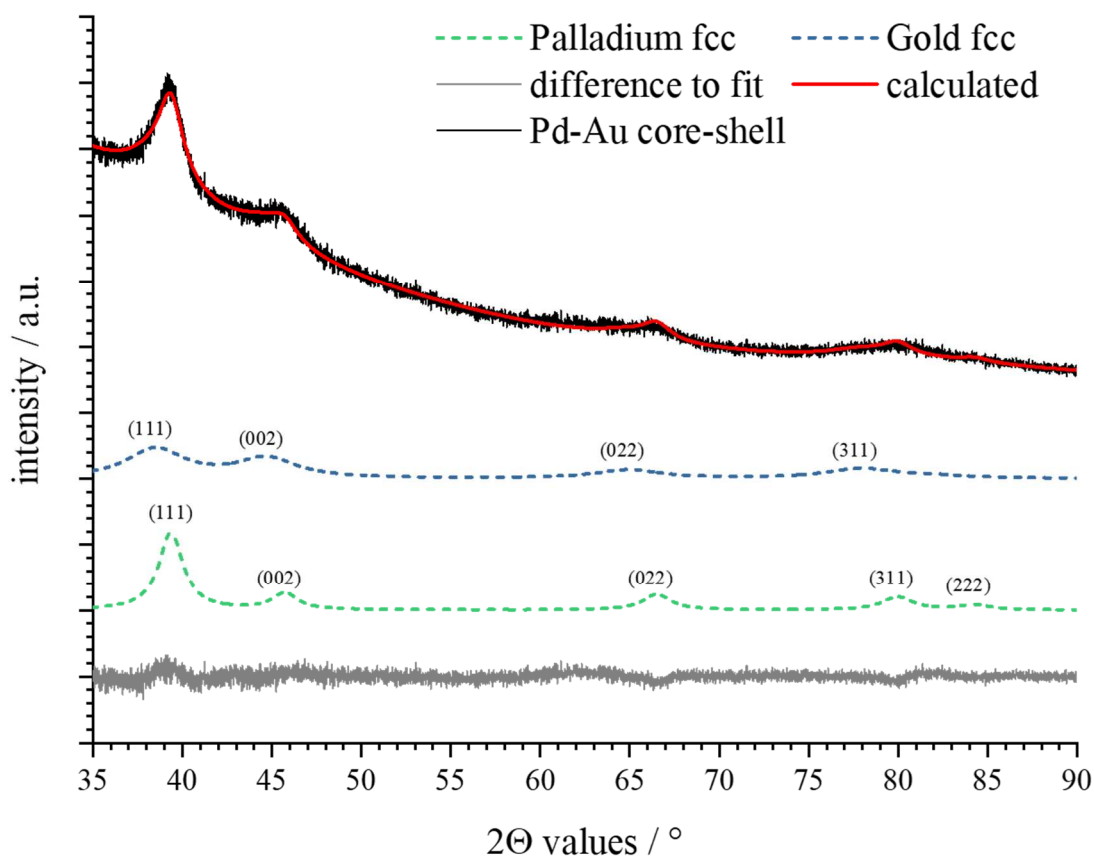


Figure 93: Rietveld refinement of the X-ray powder diffraction pattern of freeze-dried Pd-Au core-shell nanoparticles for the investigation of the structural parameters.

The calculated lattice parameter, especially for Pd, as well as the EDX line scan analysis indicate an alloying inside the particle. A gradual elemental distribution leads to a palladium-rich core and a gold-rich shell with a partial alloying at the phase boundary. This behaviour is consistent with the TEM results.

Table 18: Results of the Rietveld refinement from X-ray powder diffraction analysis of freeze-dried Pd-Au core-shell nanoparticles. The reference values for the lattice parameter a were taken from ICDD database PDF 00-004-0784 (Au fcc)^[222] and PDF 00-046-1043 (Pd fcc), respectively.^[148]

Parameter	Au fcc	Pd fcc
Tabulated lattice parameter a (bulk metals) / Å	4.07860	3.89019
Calculated lattice parameter a / Å	4.07 ± 0.06	3.97 ± 0.06
Calculated cell volume / Å ³	68 ± 3	63 ± 3
Calculated crystallite size / nm	2.5 ± 0.4	5.2 ± 0.4
Calculated crystal density / g cm ⁻³	19.4	11.3

Notably, the computed lattice parameters are related to a comparatively large error due to the wide peak broadening in the diffraction pattern. In consequence, a calculation of the microstrain that also contributes to the peak broadening is not possible.

In summary, the wet-chemical synthesis of Pd-Au core-shell nanoparticles with *D*-glucose yields spherical nanoparticles within a size range of 6-8 nm and a core diameter between 5 nm and 7 nm. The elemental mapping from energy-dispersive X-ray spectroscopy clearly illustrates the presence of a core-shell system consisting of a palladium core and a gold shell (1-2 nm thickness). The successful epitaxial overgrowth of Au on the Pd surface could be also verified by UV/vis spectroscopy. The electromagnetic spectrum shows an absorption in the visible region after addition of Au corresponding to the SPR of nanosized gold. Investigations by PXRD and Rietveld refinement could show that the obtained core-shell nanoparticles have a gradual elemental distribution. The particles are composed of a palladium-rich core and a gold-rich shell with a partial alloying at the phase boundary.

4.2.2 Au-Pd core-shell nanoparticles by sequential reduction

The reaction parameters of the previously described synthesis of Pd-Au core-shell nanoparticles were transferred to the Au-Pd core-shell system.

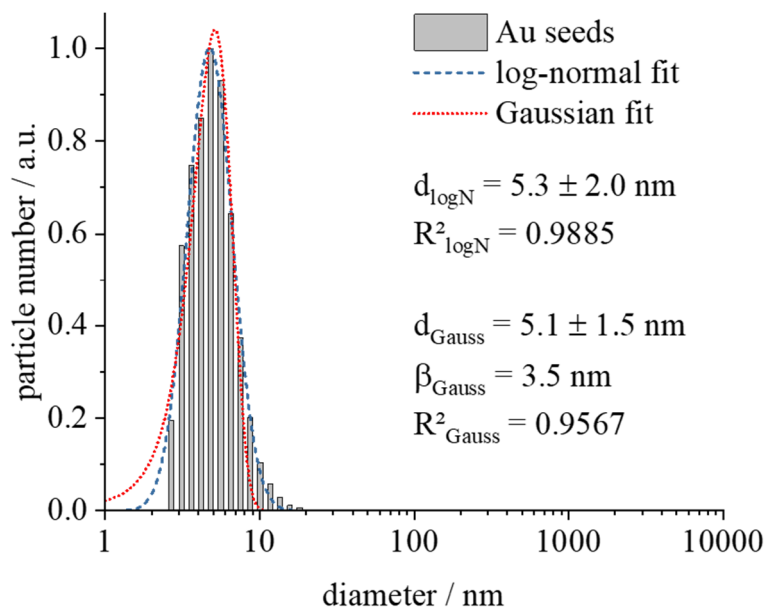


Figure 94: Number-weighted size distribution of Au seeds synthesised by reduction with *D*-glucose determined by DLS. The peak profile is analysed by a log-normal as well as a Gaussian distribution fit. The PDI is 0.47.

The hydrodynamic diameter of the initial Au seeds synthesised by reduction with *D*-glucose is 5.2 nm with a standard deviation of ± 1.8 nm (Figure 94). The PDI is 0.47. Note that the dispersion is not purified which strongly influences the determination of size by DLS as well as the calculated polydispersity index. However, neither sedimentation nor aggregation of particles can be observed.

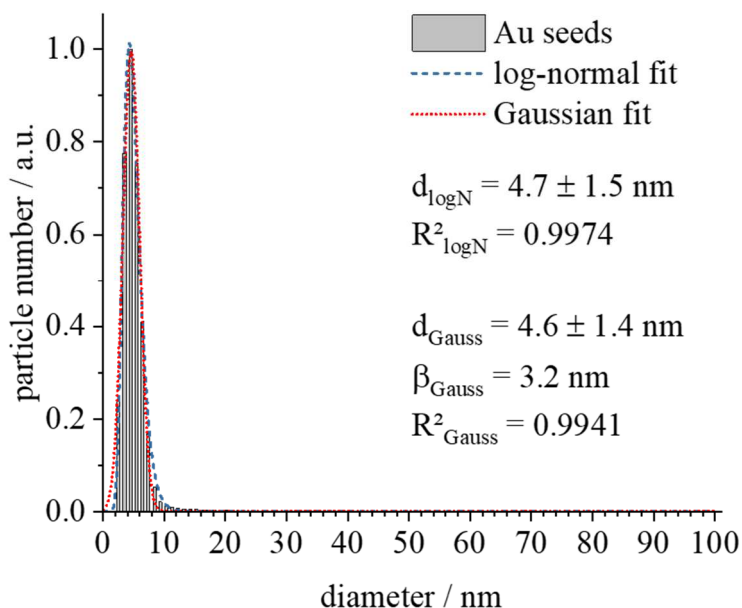


Figure 95: Number-weighted size distribution of Au seeds synthesised by reduction with citrate and tannic acid determined by DCS. The peak profile is analysed by a log-normal as well as a Gaussian distribution fit. The PDI is 0.48.

The diameter from DCS is 4.7 nm with a standard deviation of 1.5 nm and a PDI value of 0.48 (Figure 95). Subsequently, Pd²⁺ ions are added to the dispersion of small Au seeds to form a palladium shell in the presence of remaining *D*-glucose. The average particle size determined by DLS is 18.0 nm with a standard deviation of ± 5.1 nm in diameter (Figure 96). The PDI is 0.37. The diameter of Au-Pd core-shell particles from DCS is 6.9 nm with a standard deviation of ± 1.5 nm and a PDI value of 0.43 (Figure 97). The UV/vis spectra of the Au seeds and the Au-Pd core-shell nanoparticles suggest the presence of a dense palladium shell around a gold core because of the absence of the SPR absorption band of gold after addition of Pd. Additionally, there is no further absorption in the visible range (400 to 800 nm) which correlates to pure palladium.^[115]

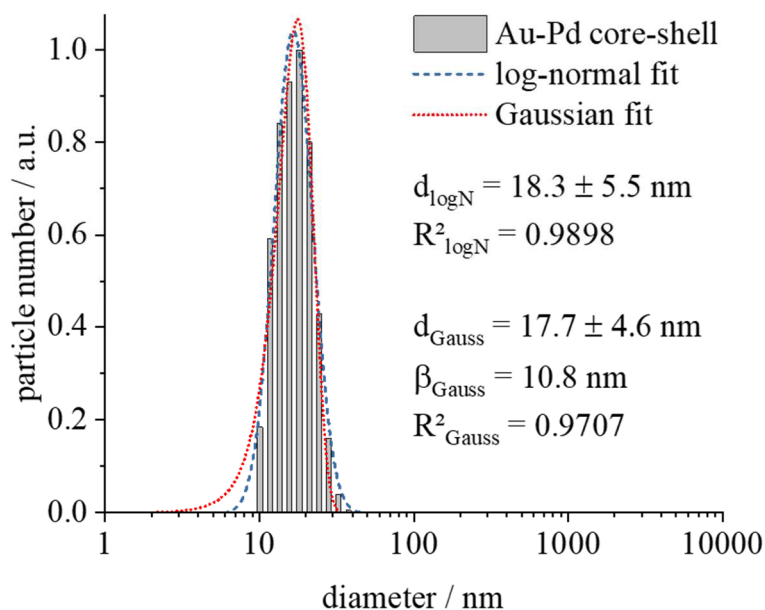


Figure 96: Number-weighted size distribution of Au-Pd core-shell nanoparticles synthesised by reduction with *D*-glucose determined by DLS. The peak profile is analysed by a log-normal as well as a Gaussian distribution fit. The PDI is 0.37.

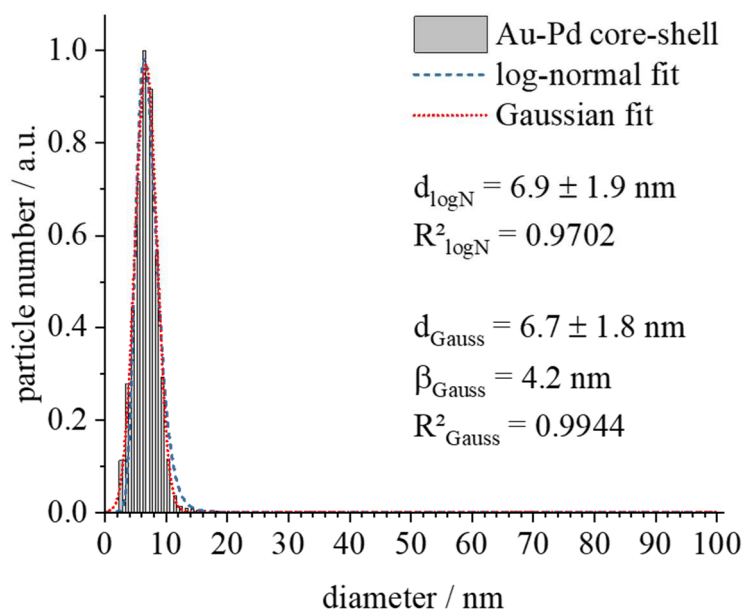


Figure 97: Number-weighted size distribution of PVP-stabilized Au-Pd core-shell nanoparticles synthesised by sequential reduction with citrate and tannic acid determined by DCS. The peak profile is analysed by a log-normal as well as a Gaussian distribution fit. The PDI is 0.43

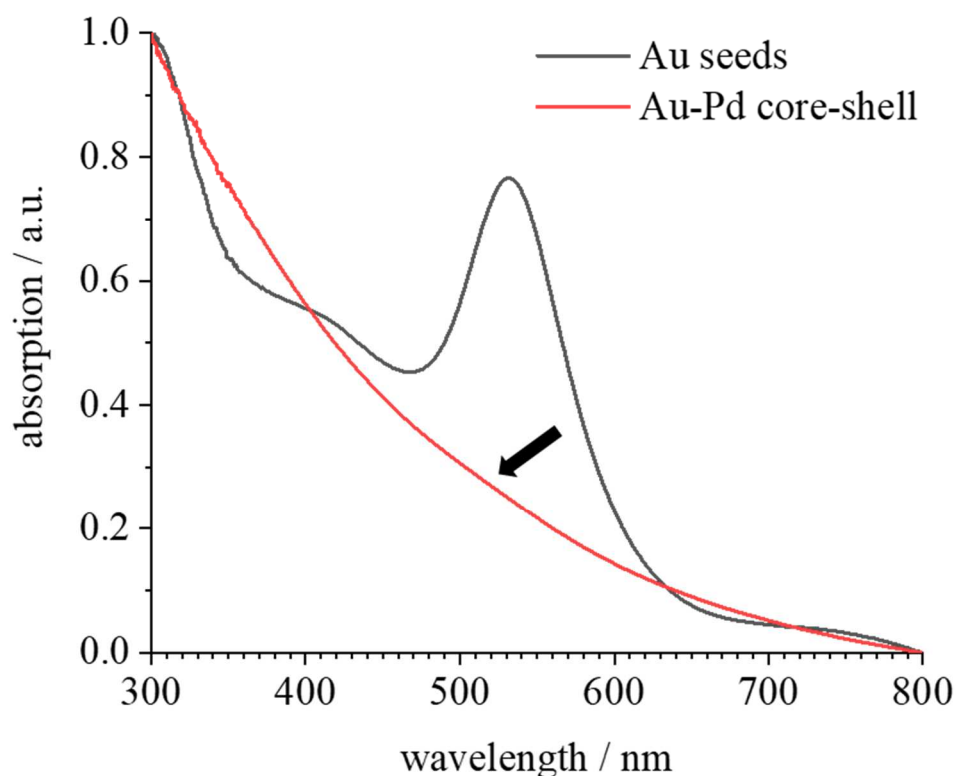


Figure 98: UV/vis spectra of Au seeds and of the Au-Pd core-shell nanoparticles. The absence of an SPR absorption band of Au after addition of palladium is marked with a black arrow. The data is normalised for better comparison.

The HAADF-STEM images show almost spherical particles with a defined core-shell structure indicated by elemental mapping from EDX analysis (Figure 100). However, some small particles consisting only of palladium can also be found (see white arrow in Figure 100). The particle size of Au-Pd core-shell nanoparticles is determined manually by measuring the size of 100 particles. The data is compiled in a histogram (Figure 99). The size of Au-Pd core-shell nanoparticles from electron microscopy is 5.7 nm with a standard deviation of ± 1.2 nm in diameter. The thickness of the palladium shell is approximately 1 to 1.5 nm as determined manually from HAADF-STEM images.

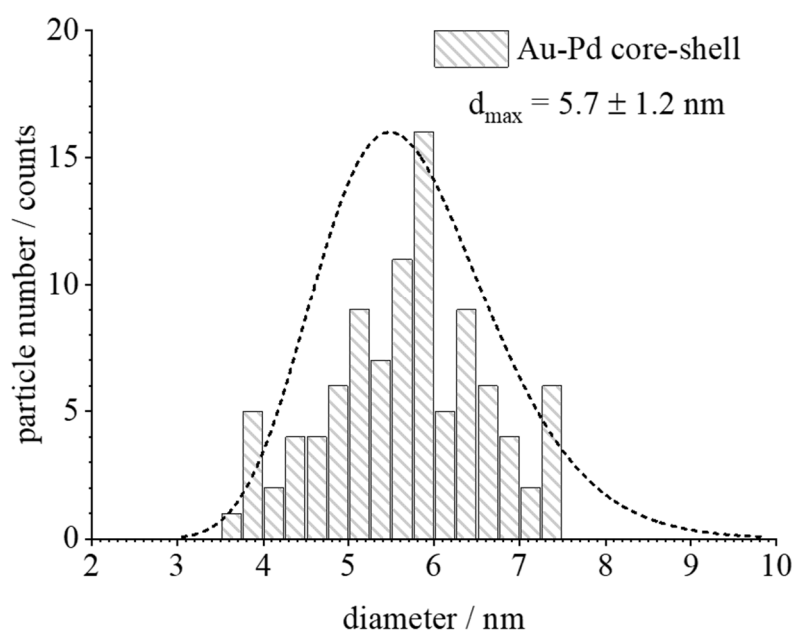


Figure 99: Histogram of particle size analysis from HAADF-STEM of PVP-stabilised Au-Pd core-shell nanoparticles. The size distribution was analysed by a log-normal distribution fit.

Dynamic light scattering, differential centrifugal sedimentation analysis and HAADF-STEM each probe different particles sizes. This can be explained by the different physical principles and/or detection characteristic of each method. Additionally, TEM probes particles in the dry state (and of course in vacuum), i.e. the dense metallic core only, whereas the DLS and DCS probe the hydrodynamic diameter which is generally larger.^[95] The difference between DLS and analytical disc centrifugation also originates from on the method characteristics. It is noteworthy that the particle diameter from DCS is slightly smaller than this determined by dynamic light scattering. This is probably due to the polymer shell around the particles, which shifts the effective density of the particles towards lower values. In consequence of a lower effective density, the sedimentation time is increasing, which results in smaller particle sizes.^[113]

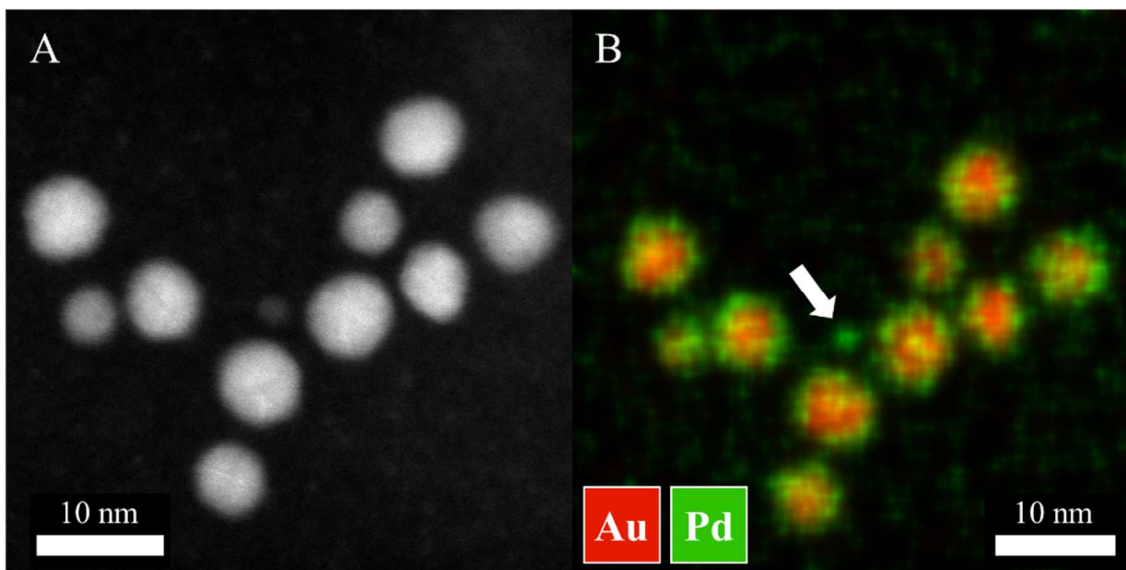


Figure 100: Representative HAADF image of Au-Pd core-shell nanoparticles and the corresponding elemental mapping from EDX analysis. The EDX maps clearly illustrate the co-presence of a gold core (red) and a palladium shell (green), but also show some small Pd nanoparticles (white arrow).

The more or less pronounced boundary between the Au core and the Pd shell indicates a sequential overgrowth with partial alloying at the interface. Gold and palladium provide an unlimited row of mixed crystals, with a perfect match to Vegard's law concerning the lattice parameter a for the face-centred cubic (fcc) crystal system (Figure 91).^[51, 236-241] X-ray powder diffraction on freeze-dried samples is carried out to investigate the internal structure of core-shell nanoparticles and an extensive Rietveld refinement is performed for quantitative phase analysis and calculation of the lattice parameters, the crystallite sizes, the crystal density, and cell volume. Despite the epitaxial overgrowth of palladium, the two metal phases can be clearly distinguished in the diffraction pattern due to their different lattice parameters. The results of the Rietveld refinement are summarised in Table 21.

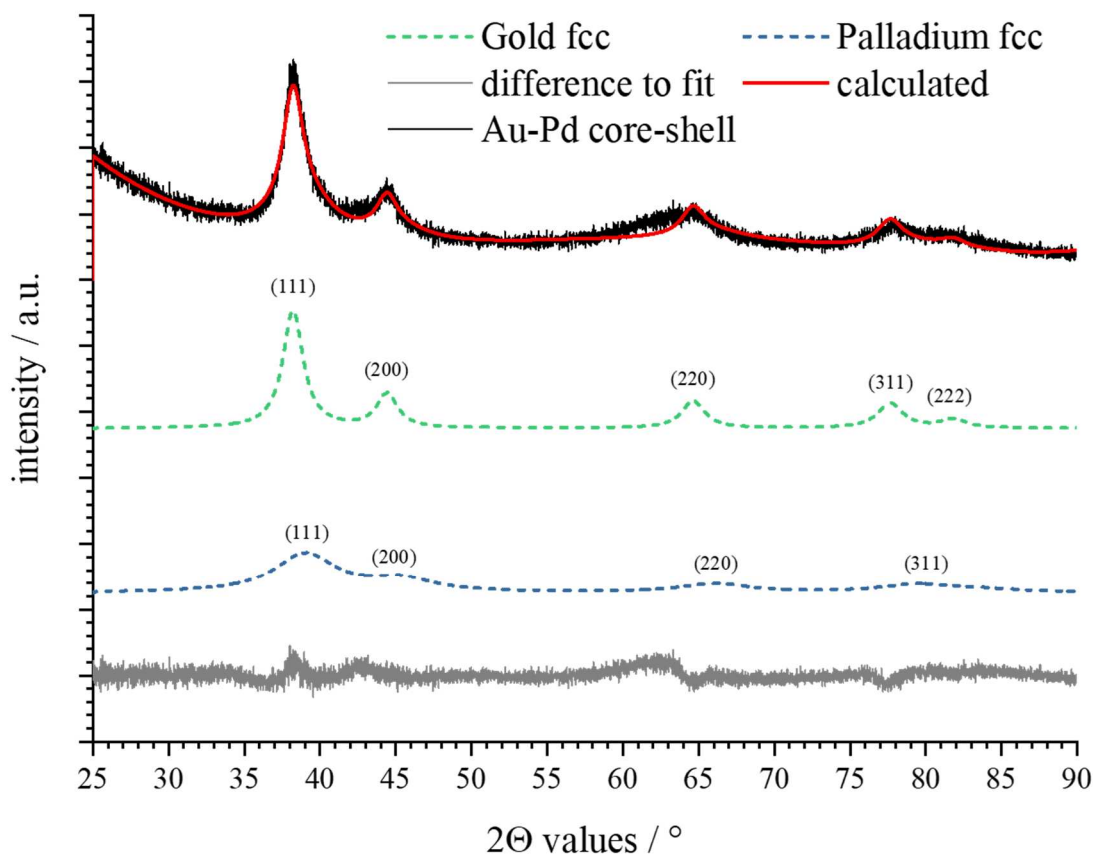


Figure 101: Rietveld refinement of the X-ray powder diffraction pattern of freeze-dried Au-Pd core-shell nanoparticles for the investigation of the structural parameters. The peak profile is calculated using the fcc phases of palladium and gold, respectively. The reflexes of palladium and gold are compared to powder diffraction file 00-004-0784 (Au)^[222] and 00-046-1043 (Pd), respectively.^[148]

The main reflexes of the (111), (200), (220), and (311) crystallographic plane of the fcc phases of palladium and gold can be observed and assigned to the reference (Table 19 and Table 20). The slightly shift of the observed gold reflex positions to higher 2θ values (Table 17) indicates a small compression of the unit cell and results in a slightly decrease in the lattice parameter of Au. In contrast, the palladium reflex positions are shifted to lower 2θ values (Table 16), which implies an expansion of the unit cells. As result, an increase in the lattice parameter of Pd can be observed.^[174, 175]

Table 19: Overview of the palladium fcc reflex position between 35-90° from Rietveld refinement in comparison to the ICDD database (Pd fcc, PDF 00-046-1043).^[148]

Reflex position (observed) $2\Theta / ^\circ$	Reflex position (reference) $2\Theta / ^\circ$	Lattice plane (hkl)
39.141	40.122	(111)
44.902	46.664	(200)
66.144	68.118	(220)
80.044	82.099	(311)

Table 20: Overview of the gold fcc reflex positions between 35-90° from Rietveld refinement in comparison to the ICDD database (Au fcc, PDF 00-004-0748).^[222]

Reflex position (observed) $2\Theta / ^\circ$	Reflex position (reference) $2\Theta / ^\circ$	Lattice plane (hkl)
38.2018	38.178	(111)
44.387	44.397	(200)
64.640	64.565	(220)
77.678	77.547	(311)
81.577	81.725	(222)

The calculated lattice parameter, especially for palladium, as well as the elemental mapping from EDX indicate a partial alloying at the phase boundary. This behaviour is consistent with the HAADF-STEM results. Notably, the computed lattice parameters are related to a comparatively large error due to the wide peak broadening in the diffraction pattern. In consequence, a calculation of the microstrain that also contributes to the peak broadening is not possible.

Table 21: Results of the Rietveld refinement from X-ray powder diffraction analysis of freeze-dried Au-Pd core-shell nanoparticles. The reference values for the lattice parameter a were taken from ICDD database PDF 00-046-1043 (Pd fcc)^[148] and PDF 00-004-1043 (Au fcc), respectively.^[222]

Parameter	Au fcc	Pd fcc
Tabulated lattice parameter a (bulk metals) / Å	4.07860	3.89019
Calculated lattice parameter a / Å	4.07 ± 0.01	3.99 ± 0.08
Calculated cell volume / Å ³	67.8 ± 0.1	63.9 ± 0.4
Calculated crystallite size / nm	5.9 ± 0.2	1.89 ± 0.8
Calculated crystal density / g cm ⁻³	19.3	11.1

In summary, the synthesis of Au-Pd core-shell nanoparticles leads to quasi-spherical particles with a size of about 7 nm and a core diameter between 4-5 nm. The elemental mapping from energy-dispersive X-ray spectroscopy clearly illustrates the presence of a core-shell system consisting of a palladium core and a gold shell (2-3 nm thickness). Investigations by PXRD and Rietveld refinement could show that the obtained core-shell nanoparticles have a partial alloying at the phase boundary. The successful epitaxial overgrowth of Pd on the Au surface could be also verified by UV/vis spectroscopy. The electromagnetic spectrum shows no distinct absorption in the visible region after addition of Pd corresponding to the bulk material of palladium.

4.2.4 Summary

Whereas Pd-Au and Au-Pd core-shell nanoparticles can be easily prepared by a one-pot synthesis based on a seed-and-growth method, the wet-chemical synthesis of bimetallic (alloyed) AuPd nanostructures using *D*-glucose as reducing agent has not been successful. The co-reduction of Pd²⁺ and Au³⁺ in the presence of PVP leads to an undefined mixture of differently shaped particles (triangle, decahedrons, spheres) with a more or less distinct core-shell like structure. Additionally, many small palladium nanoparticles are formed. The successful syntheses of Pd-Au and Au-Pd core-shell nanoparticles can be confirmed by spectroscopic and high-resolution TEM techniques as well as X-ray diffraction. The overall hydrodynamic particle sizes are 6 to 8 nm in diameter as determined by analytical disc centrifugation. UV/vis spectroscopy allows the examination of the shell growth according to the presence or absence of SPR absorption bands of gold (Figure 102).

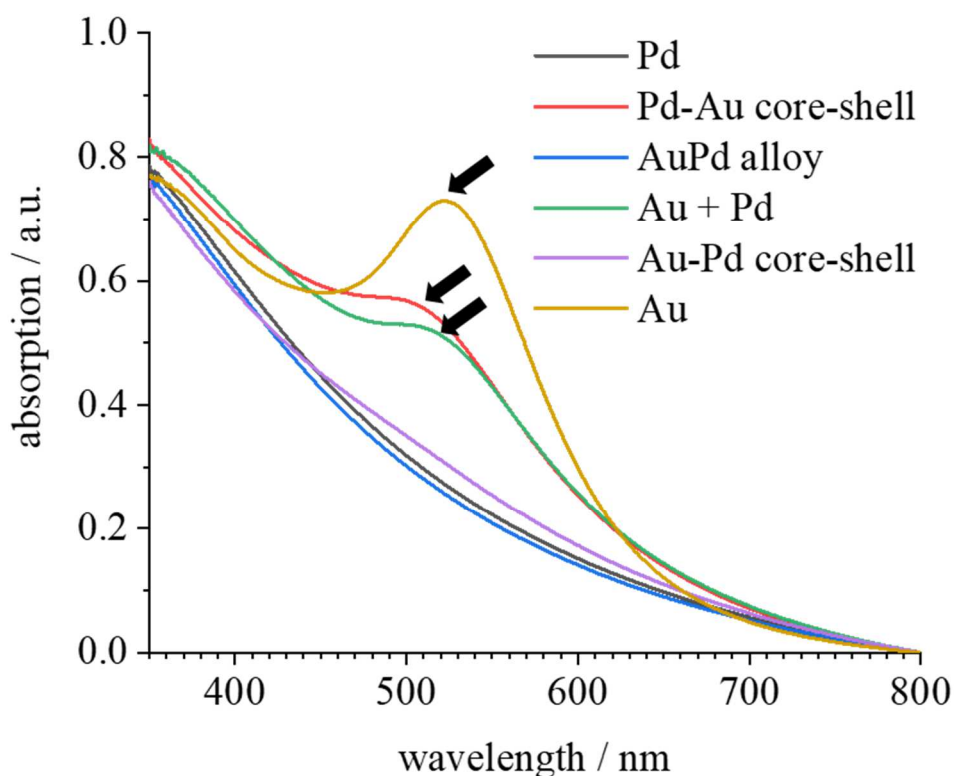


Figure 102: UV-vis spectra of Pd-Au core-shell, AuPd alloyed, and Au-Pd core-shell nanoparticles compared to Pd, Au, and a physical mixture of both. The development of absorption bands according to the SPR of Au is marked with black arrows.

Except for the bimetallic (alloyed) AuPd nanoparticles, the HAADF-STEM images show (almost) spherical nanoparticles. Notably, some particles have a triangular shape. Especially in the case of Pd-Au core-shell nanoparticles, the core-shell structure can also be confirmed by the Z-contrast and can be quantified by elemental mapping from EDX analysis. Most of the particles are single crystalline, despite the presence of the core-shell structure and some isolated twins and grain boundaries. Thus, an epitaxial growth of gold and palladium onto the core occurs, respectively. However, a galvanic replacement of palladium by gold cannot be observed. The particle formation is illustrated in Figure 103.

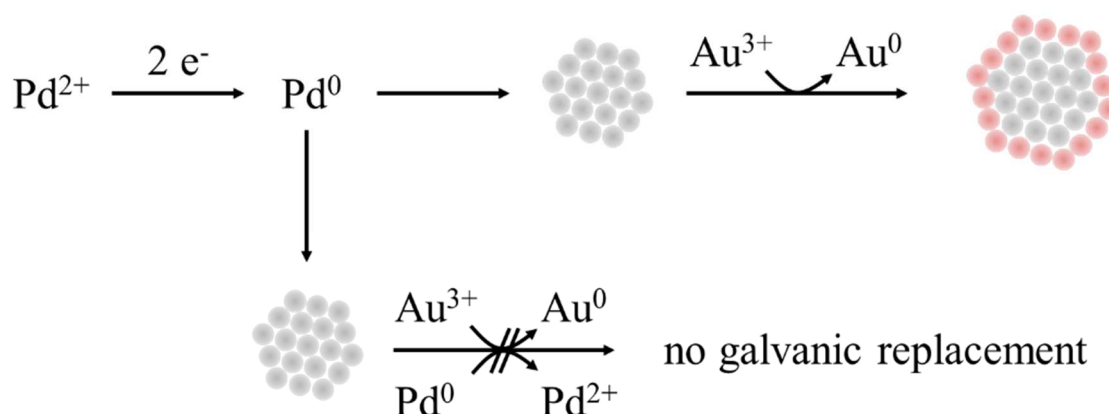


Figure 103: Schematic illustration of the formation of Pd-Au core-shell nanoparticles. A dissolution of initial Pd seeds by a redox reaction (galvanic replacement) cannot be observed.

The structural behaviour of Pd-Au and Au-Pd core-shell nanoparticles was studied by powder X-ray diffraction and Rietveld refinement analysis. The results clearly show the presence of the formation of core-shell structure. Additionally, the presence of only a core-shell system was verified by a powder diffraction pattern of a physical mixture of gold and palladium nanoparticles. For the detailed characterisation of the Pd and Au nanoparticles see chapter 4.1.3 and 4.1.8, respectively. X-ray powder diffraction on freeze-dried samples was carried out after a physical mixture of two dispersions of gold and palladium nanoparticles. The main reflexes of the (111), (200), (220), and (311) crystallographic planes of the fcc phases of palladium and gold can be identified and assigned to the reference (Table 22 and Table 23). Furthermore, a distinct decrease in the intensity between the reflex position of both (111) crystallographic planes could be observed (Figure 104).

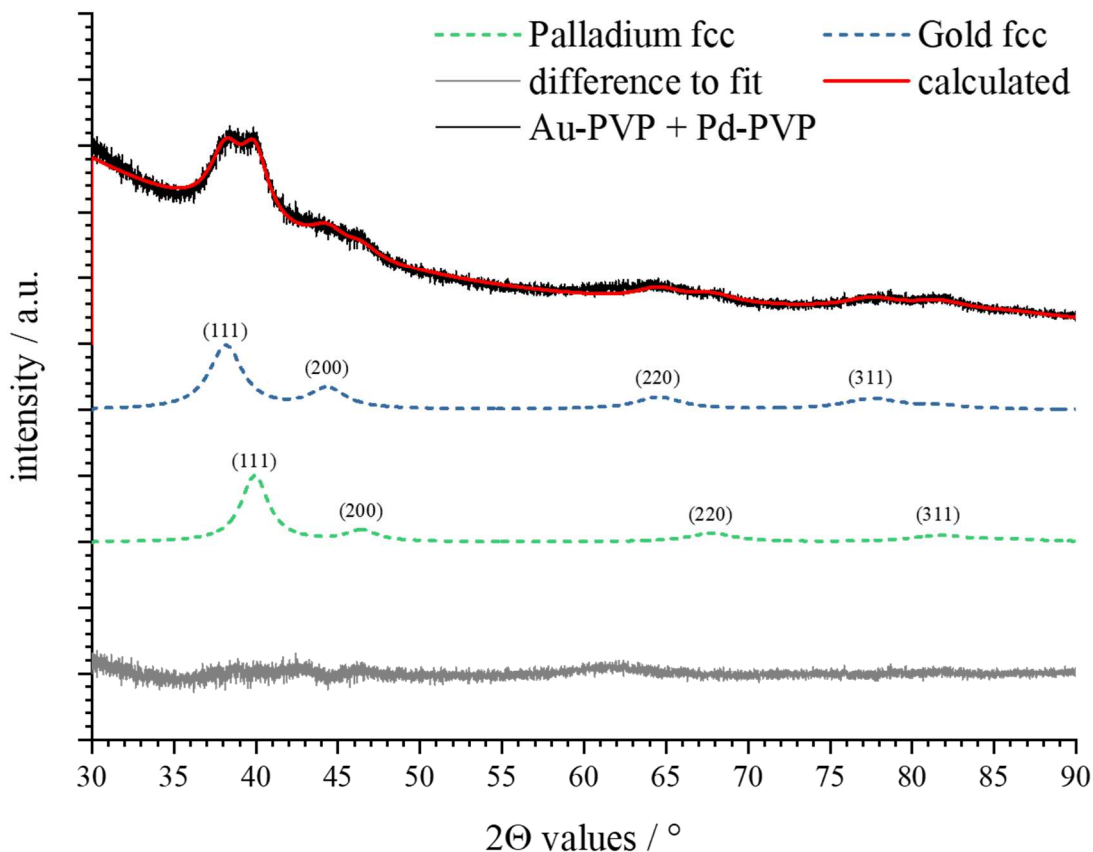


Figure 104: Powder diffraction pattern (not $K\alpha$ stripped) and Rietveld refinement of a physical mixture of PVP-stabilised Au and Pd. The peak profile is calculated using the fcc phases of palladium and gold, respectively. The reflexes of palladium and gold are compared to powder diffraction file 00-004-0784 (Au)^[222] and 00-046-1043 (Pd), respectively.^[148]

An extensive Rietveld refinement is performed for quantitative phase analysis and calculation of the lattice parameters, the crystallite sizes, the crystal density, and cell volume. The two metal phases can be clearly distinguished in the diffraction pattern due to their different lattice parameters. The results of the Rietveld refinement analysis are summarised (Table 24).

Table 22: Overview of the palladium fcc reflex position between 35-90° from Rietveld refinement in comparison to the ICDD database (Pd fcc, PDF 00-046-1043).^[148]

Reflex position (observed) $2\Theta / ^\circ$	Reflex position (reference) $2\Theta / ^\circ$	Lattice plane (hkl)
39.977	40.122	(111)
46.496	46.664	(200)
67.863	68.118	(220)
81.771	82.099	(311)

Table 23: Overview of the gold fcc reflex positions between 35-90° from Rietveld refinement in comparison to the ICDD database (Au fcc, PDF 00-004-0748).^[222]

Reflex position (observed) $2\Theta / ^\circ$	Reflex position (reference) $2\Theta / ^\circ$	Lattice plane (hkl)
38.253	38.178	(111)
44.463	44.397	(200)
64.697	64.565	(220)
77.720	77.547	(311)

The calculated crystallographic properties of the palladium phase correlate with the data of the bulk material (space group $Fm\bar{3}m$, lattice constant $a = 3.8930 \text{ \AA}$, cell volume $V_{\text{cell}} = 59.000 \text{ \AA}^3$, crystal density $\rho_{\text{crystal}} = 11.979 \text{ g cm}^{-3}$).^[149] The lattice parameter of the phase analysis of gold also corresponds to the face-centred cubic (fcc) phase of the bulk material. (space group $Fm\bar{3}m$, lattice constant $a = 4.072 \text{ \AA}$, cell volume $V_{\text{cell}} = 67.519 \text{ \AA}^3$, crystal density $\rho_{\text{crystal}} = 19.377 \text{ g cm}^{-3}$).^[223]

Table 24: Results of the Rietveld refinement from X-ray powder diffraction analysis of a physical mixture of Au and Pd nanoparticles. The reference values for the lattice parameter a were taken from ICDD database PDF 00-046-1043 (Pd fcc)^[148] and PDF 00-004-1043 (Au fcc), respectively.^[222]

Parameter	Au fcc	Pd fcc
Tabulated lattice parameter a (bulk metals) / \AA	4.07860	3.89019
Calculated lattice parameter a / \AA	4.072 ± 0.002	3.903 ± 0.001
Calculated cell volume / \AA^3	67.51 ± 0.08	59.46 ± 0.05
Calculated crystallite size / nm	6.3 ± 0.5	5.1 ± 0.3
Calculated crystal density / g cm^{-3}	19.4	11.9

Overall, a phase separation in the core-shell system could be excluded by evaluation of the diffraction data and calculated crystallographic properties. In addition, *in-situ* small-angle X-ray scattering (SAXS) measurements are carried out to monitor the core-shell formation during the synthesis of Pd-Au core-shell nanoparticles. The Pd seeds are formed immediately as shown by the time-resolved evolution of the average size in diameter (Figure 105). After the addition of gold (at $t = 50 \text{ min}$), an increase in diameter is observed. Both, the size of initial Pd seeds as well as the final size of Pd-Au core-shell nanoparticles correspond very well to the results from DLS, DCS, TEM, and PXRD. Notably, the evolution of agglomerates is detected by those SAXS experiments and small fractions of aggregates can be verified from the data analysis.^[242]

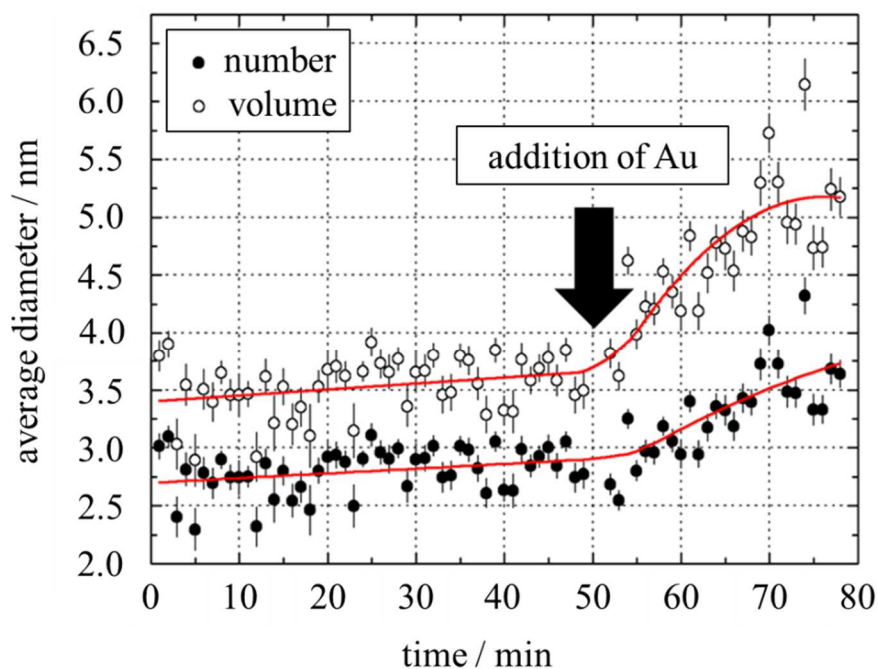


Figure 105: Time-resolved evolution of the average size in diameter during the synthesis of Pd-Au core-shell nanoparticles determined by in-situ small-angle X-ray scattering (SAXS). The trend lines are only a guidance. The graph is taken from reference.^[242]

The investigation of potential cytotoxic effects after unintended exposure to Pd-Au core-shell nanoparticles is carried out via incubation of hMSCs with total metal concentration from 2.5 to 50 $\mu\text{g ml}^{-1}$ for 24 h. Concerning the biological action, there is no significant effect on hMSCs (Figure 106).

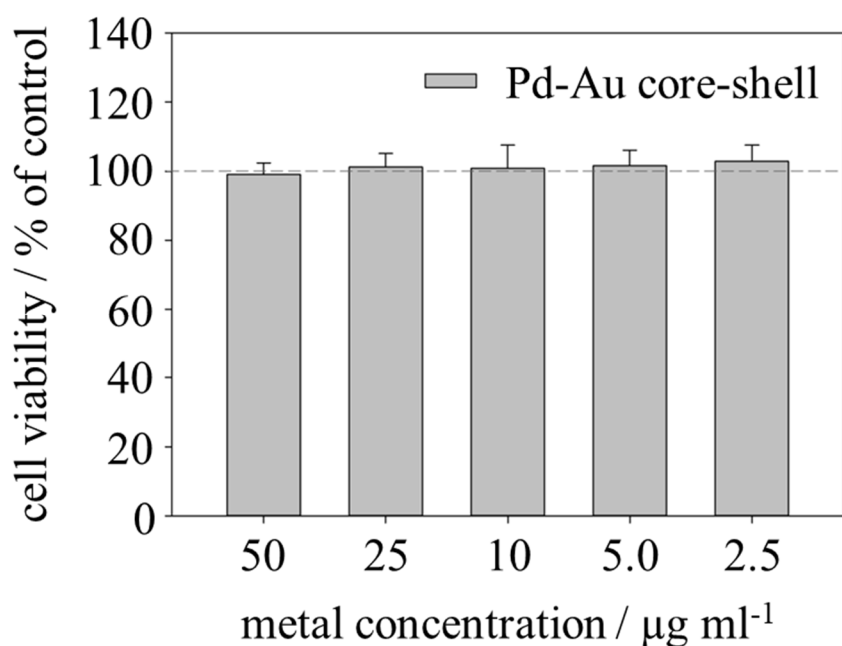


Figure 106: Effect of PVP-stabilised Pd-Au core-shell nanoparticles on the viability of hMSCs. The cells are treated with particles ($c(\text{metal})$: 2.5 to 50 $\mu\text{g ml}^{-1}$) for 24 h under cell culture conditions. Vital cells (green fluorescence) are quantified by digital image processing (phase analysis). The data is expressed as mean value \pm standard deviation ($n = 6$ independent experiments) given as the percentage of the control (hMSCs without nanoparticles). The graph is taken from reference.^[242]

4.3 Characterisation of bimetallic Ag-Pd nanoparticles

The last part of the present work is concerned with the syntheses and characterisation of bimetallic nanostructures of silver and palladium. In general, a water-based simultaneous reduction approach is carried out to obtain alloyed AgPd nanoparticles. Additionally, a seed-and-growth method is utilized to prepare Ag-Pd particles with a core-shell construction. For that, a sequential reduction of Ag^+ and Pd^{2+} with a suitable reductant, here *D*-glucose, in the presence of PVP as stabilizing agent is pursued. The purified nanoparticles are characterised by dynamic light scattering and analytical disc centrifugation with respect to their size. The validation of the successful preparation of bimetallic nanostructures is performed by using electron microscopic techniques, i.e. HAADF with additional EDX spectroscopic analysis. The optical properties were measured by UV/vis spectroscopy. Dr. Kateryna Loza performed the high-resolution and scanning transmission electron microscopy including HAADF imaging and EDX spectroscopic analysis in cooperation with Dr. Marc Heggen's group at the Ernst-Ruska Centre for Microscopy and Spectroscopy with Electrons in Jülich

4.3.1 Bimetallic AgPd (alloyed) nanoparticles by simultaneous reduction

PVP-stabilised bimetallic AgPd nanoparticles with an expected alloyed structure are synthesised by a simultaneous co-reduction approach using *D*-glucose. The average hydrodynamic diameter as determined by DLS is 17.0 nm with a standard deviation of ± 3.1 nm (Figure 107).

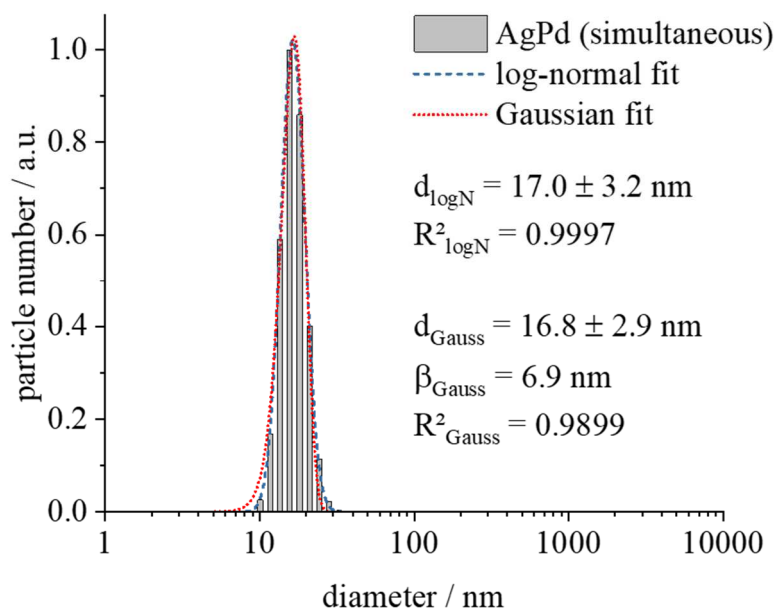


Figure 107: Number-weighted size distribution of bimetallic AgPd (alloyed) nanoparticles synthesised by simultaneous reduction with *D*-glucose determined by DLS. The peak profile is analysed by a log-normal as well as a Gaussian distribution fit. The PDI is 0.17.

The number-weighted size distribution determined by DCS results in an average diameter of 4.6 nm with a standard deviation of ± 0.7 nm (Figure 108). Both polydispersity indices of 0.17 and 0.13 indicate a well-dispersed system, respectively. In addition, neither sedimentation nor aggregation of particles can be observed.

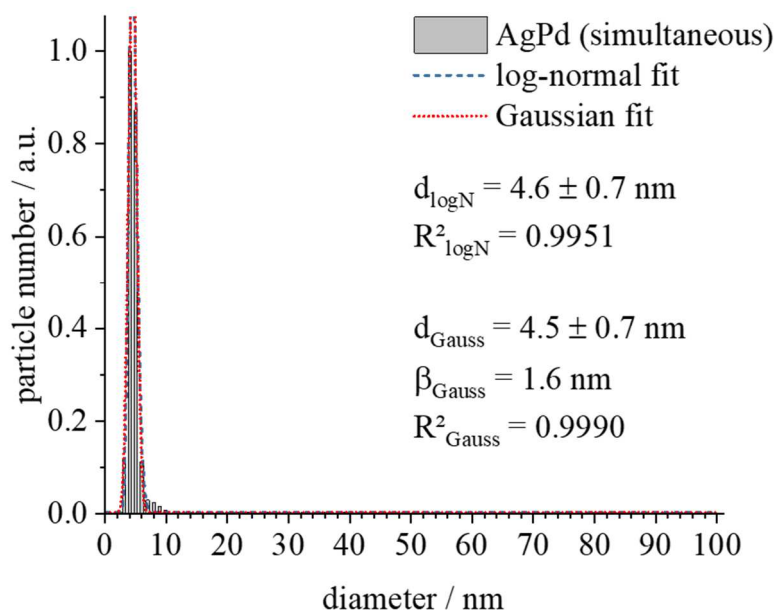


Figure 108: Number-weighted size distribution of bimetallic AgPd (alloyed) nanoparticles synthesised by simultaneous reduction with *D*-glucose determined by DCS. The peak profile is analysed by a log-normal as well as a Gaussian distribution fit. The PDI is 0.13.

Dynamic light scattering, differential centrifugal sedimentation analysis and HAADF-STEM each probe different particles sizes. This can be explained by the different physical principles and/or detection characteristic of each method. Additionally, TEM probes particles in the dry state (and of course in vacuum), i.e. the dense metallic core only, whereas the DLS and DCS probe the hydrodynamic diameter which is generally larger.^[95] The difference between DLS and analytical disc centrifugation also originates from on the method characteristics. It is noteworthy that the particle diameter from DCS is slightly smaller than the one determined by dynamic light scattering. This is probably due to the polymer shell around the particles, which affects the effective density of the particles and leads to lower values. In consequence of a lower effective density, the sedimentation time is increasing, which results in smaller particle sizes.^[113]

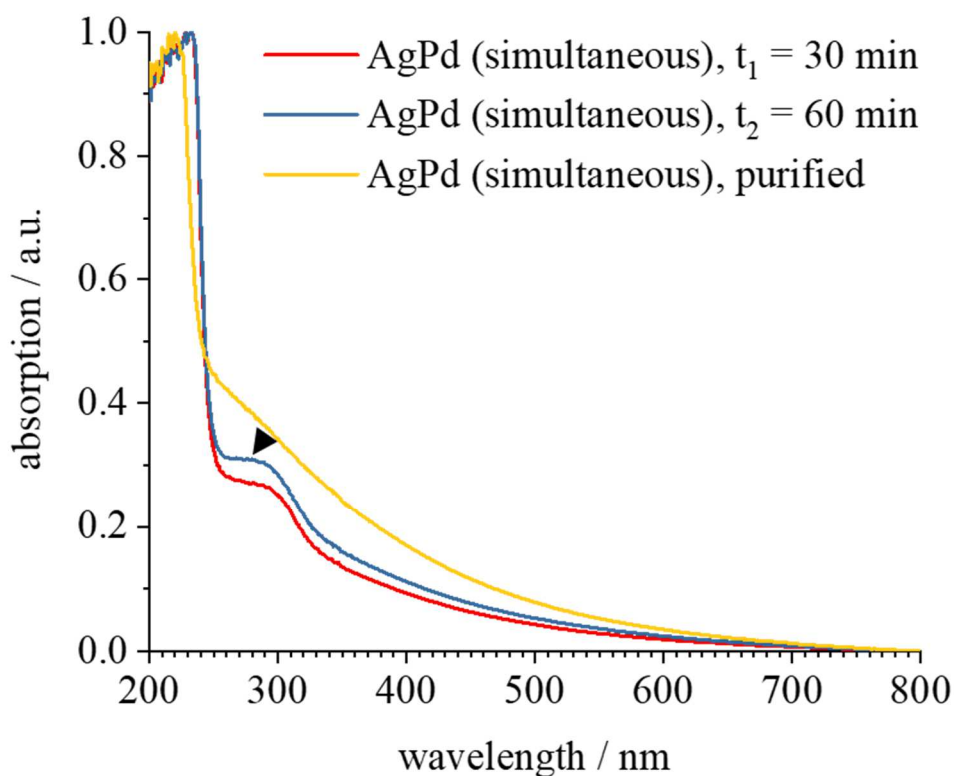


Figure 109: Time-resolved UV/vis spectra of bimetallic AgPd (alloyed) nanoparticles during the synthesis. The data is normalised for better comparison. The black arrow shows the absorption of the $\text{Pd}(\text{NO}_2)_4^{2-}$ complex from the precursor $\text{Pd}(\text{NO}_3)_2$ in aqueous medium.

The time-resolved UV/vis spectra are measured at the half ($t_1 = 30$ min) and the end of the reaction ($t_2 = 60$ min) as well as after purification (Figure 109). The presence of $\text{Pd}(\text{NO}_3)_2$ during the synthesis leads to a small absorption in the near ultraviolet region below 300 nm which is caused by the square planar Pd complex $\text{Pd}(\text{NO}_2)_4^{2-}$ (Figure 109, marked with a black arrow).^[147] Silver nitrate shows also slightly absorption in this region because of the NO_3^- anion.^[164, 165] The purified dispersion show no distinct absorption in the visible range (400 to 800 nm) which correlates either to the absorption behaviour of pure palladium or to the presence of alloyed AgPd nanoparticles. In the case of alloyed nanostructures, Pd is in the position to prevent the absorption by surface plasmon resonance of silver.^[115, 234]

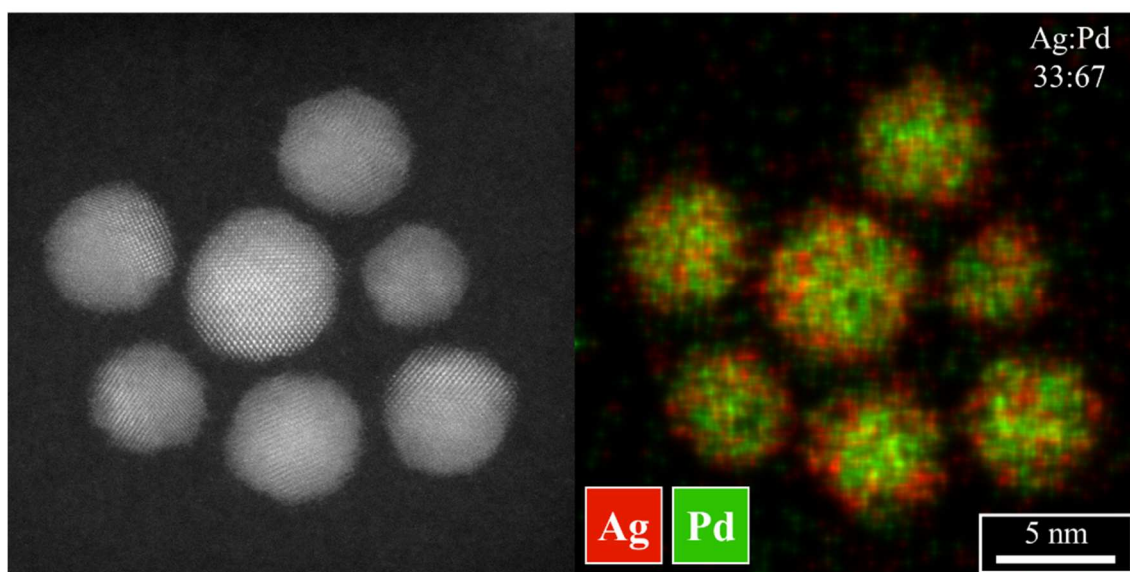


Figure 110: Representative HAADF image of bimetallic AgPd nanoparticle synthesised by simultaneous reduction with *D*-glucose. The corresponding elemental mapping from EDX analysis show core-shell structures with a Pd-rich core (green) and a silver shell (red). The molar Ag:Pd ratio is 33:67 at%.

The particle size is determined manually by measuring the size of 8 particles and compiling a histogram. The HAADF-STEM images show spherical-like nanoparticles with an average diameter of $5.7 \text{ nm} \pm 1.2 \text{ nm}$. Notably, the significance of the size distribution determined by TEM is not given due to small amount of measured nanoparticles. The elemental mapping from EDX analysis gives an average Ag:Pd ratio of 30-33:67-70 at% that is quite different to the initial molar ratio of 50:50 at% (Ag:Pd). This leads to believe that an incomplete reduction of Ag^+ is occurred in the presence of $\text{Pd}(\text{NO}_3)_2$. Furthermore, the obtained particles reveal a core-shell structure with an enrichment of Pd in the inner sphere (Figure 110). A partial alloying cannot be excluded. A more or less closed silver shell can be identify by a higher magnification of a single particle (Figure 111).

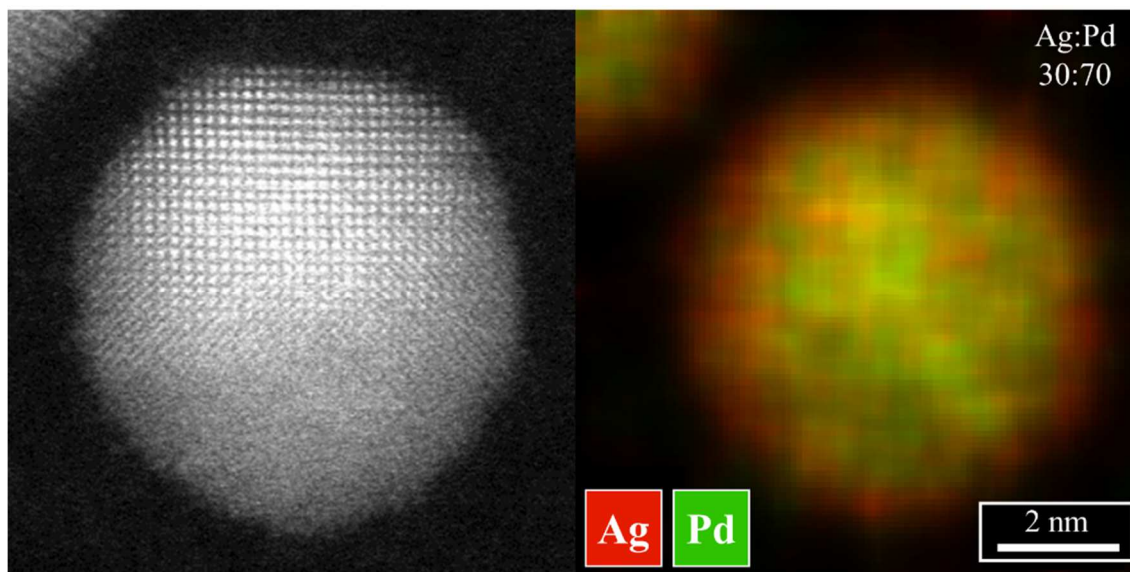


Figure 111: HAADF image of a single AgPd nanoparticle synthesised by simultaneous reduction with *D*-glucose. The corresponding elemental mapping from EDX analysis clearly illustrate the co-presence of a Pd-rich core (green) and a silver shell (red). The molar Ag:Pd ratio is 30:70 at%.

The occurrence of a palladium-rich core and a silver-rich shell in bimetallic AgPd nanoparticles from simultaneous co-reduction of ionic Pd²⁺ and Ag⁺ species indicates a faster reduction of Pd due to its more noble character (Figure 112). The standard potential E^0 of palladium (Pd²⁺/Pd⁰) under acidic conditions (pH = 0) is +0.915 V and is slightly higher than the standard potential of silver (E^0 (Ag⁺/Ag⁰) = +0.799 V at pH = 0).^[243] The enrichment of the nobler metal inside bimetallic nanoparticles from co-reduction can be observed on the AgAu system.^[91] In the case of gold (E^0 (Au³⁺/Au⁰) = +1.498 V at pH = 0) and silver, the difference in the standard potential is much more higher than in the Ag:Pd system.^[243] In non-aqueous solution an alloying with an even elemental distribution throughout the AgPd nanoparticles can be obtained.^[63]

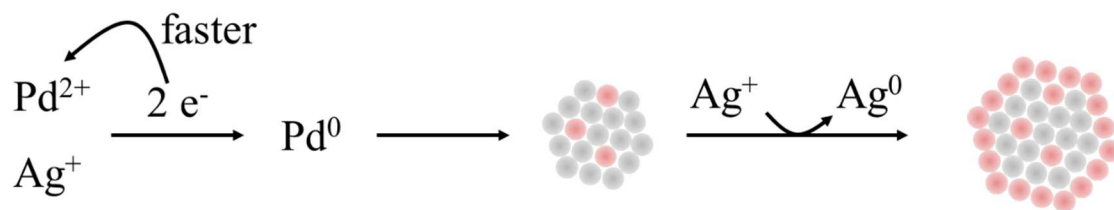


Figure 112: Reaction scheme of the core-shell structure formation in the synthesis of bimetallic AgPd nanoparticles by simultaneous reduction with *D*-glucose.

In summary, the simultaneous reduction of Ag^+ and Pd^{2+} in aqueous medium yields spherical-like nanoparticles with a core-shell structure. The obtained particles are about 17 nm in hydrodynamic diameter determined by DLS. The size from differential centrifugal sedimentation analysis is 4 to 5 nm, which correlates with the STEM data. The metallic core size is about 6 nm. The HAADF-STEM shows uniform particles with a core-shell structure. The palladium forms the core, whereas the silver forms a thin shell. The molar Ag: Pd ratio shows a silver deficiency compared to the initial amount. The Ag-Pd nanoparticles show no distinct absorption in the visible range, which also suggests the formation of only a very thin Ag layer.

4.3.2 Ag-Pd core-shell nanoparticles by sequential reduction

Ag-Pd nanoparticles with an expected core-shell construction are prepared by seed-and-growth approach through sequential reduction. First, silver seeds are prepared by reduction of AgNO_3 with *D*-glucose in the presence of PVP as stabilizing agent. The hydrodynamic diameter of initial Ag seeds is 9.2 nm with a standard deviation of ± 1.3 nm (Figure 113). The PDI of 0.10 is very low and indicates highly dispersed nanoparticles.

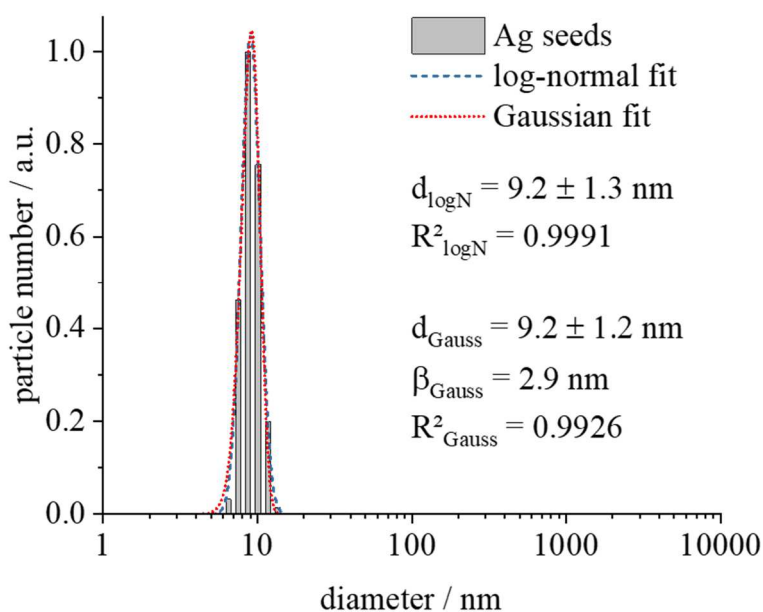


Figure 113: Number-weighted size distribution of initial Ag seeds synthesised by reduction with *D*-glucose determined by DLS. The peak profile is analysed by a log-normal as well as a Gaussian distribution fit. The PDI is 0.10.

Note that the size measurements are carried out using the unpurified dispersion. The size determination of initial Ag seeds by DCS leads to a very broad and bimodal size distribution. The mean diameter is $8 \text{ nm} \pm 6 \text{ nm}$. Additionally, a broad fraction of bigger particles or aggregates (in the size range between 40 to 90 nm) can be observed. Nevertheless, neither aggregation nor sedimentation of particles can be observed. The hydrodynamic diameter of obtained bimetallic Ag-Pd nanoparticles is 38.8 nm with a standard deviation of ± 10.1 nm as determined by DLS (Figure 115). The polydispersity index is 0.32. Furthermore, the size of Ag-Pd nanoparticles are verified by DCS (Figure 116). The average

size is 6.3 nm with a standard deviation of ± 1.3 nm in diameter. The PDI is 0.20, indicating well-dispersed particular system.

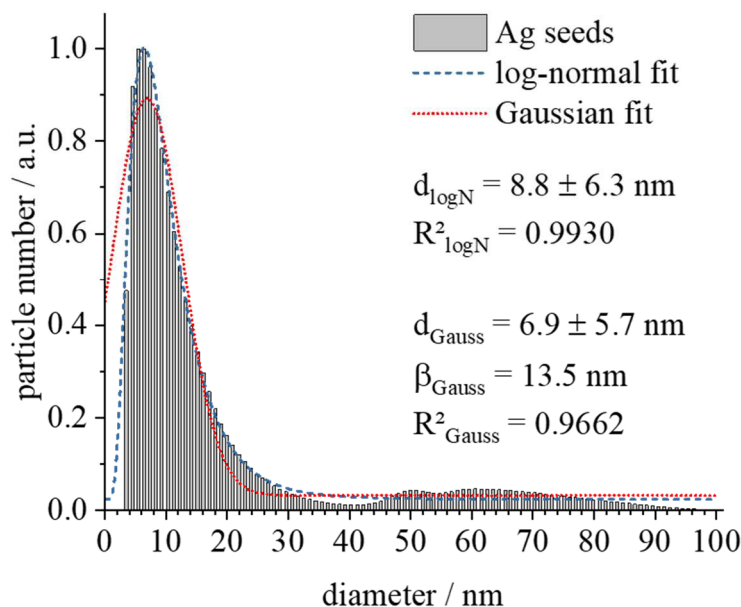


Figure 114: Number-weighted size distribution of initial Ag seeds synthesised by reduction with *D*-glucose determined by DCS. The peak profile is analysed by a log-normal as well as a Gaussian distribution fit. The PDI is 3.85.

The difference in sizes originate from the underlying method principles. Electron microscopy requires dried samples and gives information mainly about the metallic core of the particles because the hydration shell and adsorbed polymer collapsed in the high vacuum. The dynamic light scattering is based on measuring the intensity of the Rayleigh scattering and is carried out in the dispersed state. Hence, the obtained particle sizes are always larger than the metallic core due to the presence of the hydrated polymeric layer that influences the hydrodynamic diameter of the particles.^[95] In addition, the polymer shell lowers the effective density of the particles, which affect the sedimentation behaviour during the DCS analysis. The increased sedimentation time leads to obviously smaller particle sizes compared to the results from DLS.^[113]

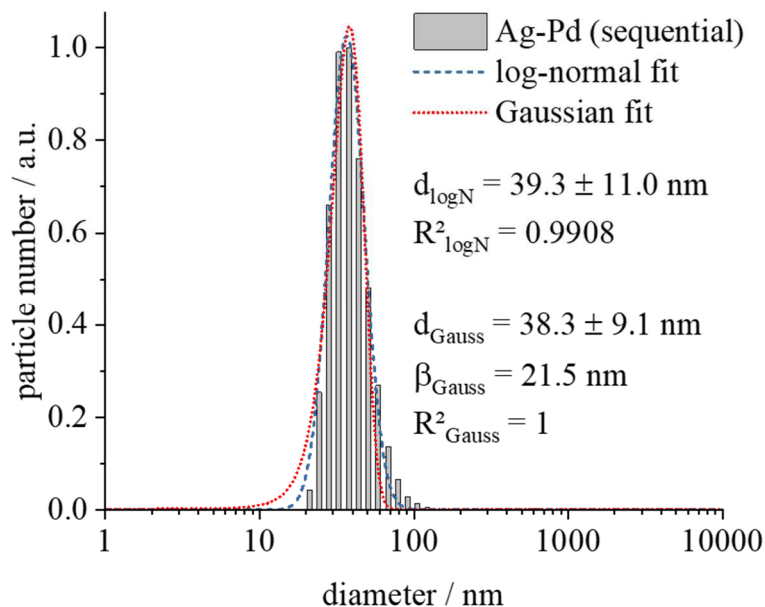


Figure 115: Number-weighted size distribution of bimetallic Ag-Pd nanoparticles synthesised by sequential reduction with *D*-glucose determined by DLS. The peak profile is analysed by a log-normal as well as a Gaussian distribution fit. The PDI is 0.32.

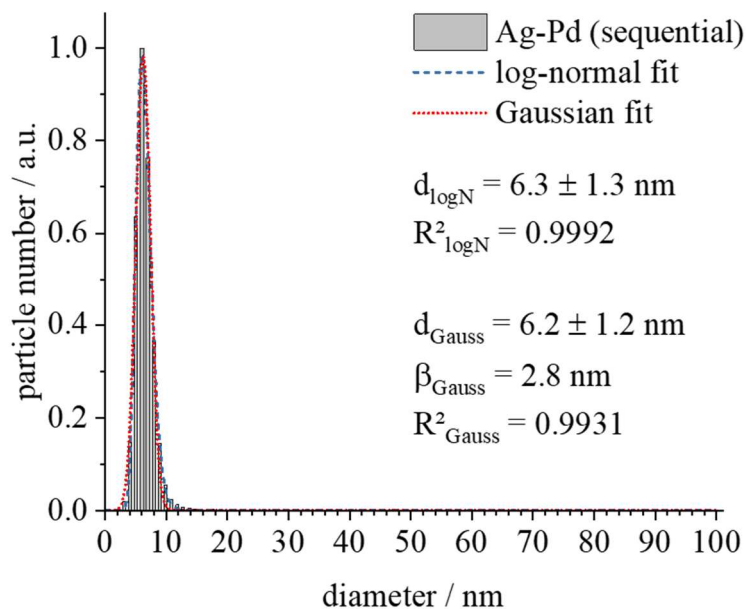


Figure 116: Number-weighted size distribution of bimetallic Ag-Pd nanoparticles synthesised by sequential reduction with *D*-glucose determined by DCS. The peak profile is analysed by a log-normal as well as a Gaussian distribution fit. The PDI is 0.20.

The time-resolved UV/vis spectra are measured at four different times and after purification of the bimetallic Ag-Pd (core-shell) nanoparticles by ultracentrifugation (Figure 118). Pd(NO₃)₂ as well as AgNO₃ lead to small absorption in the near ultraviolet region below 300 nm which is caused by the square planar Pd complex Pd(NO₂)₄²⁻ and the NO₃⁻ anion of silver nitrate.^[147, 164, 165] The purified dispersion shows no distinct absorption in the visible range (400 to 800 nm). Thus, palladium might be formed a dense shell because Pd is in the position to prevent the absorption by surface plasmon resonance of silver.^[234]

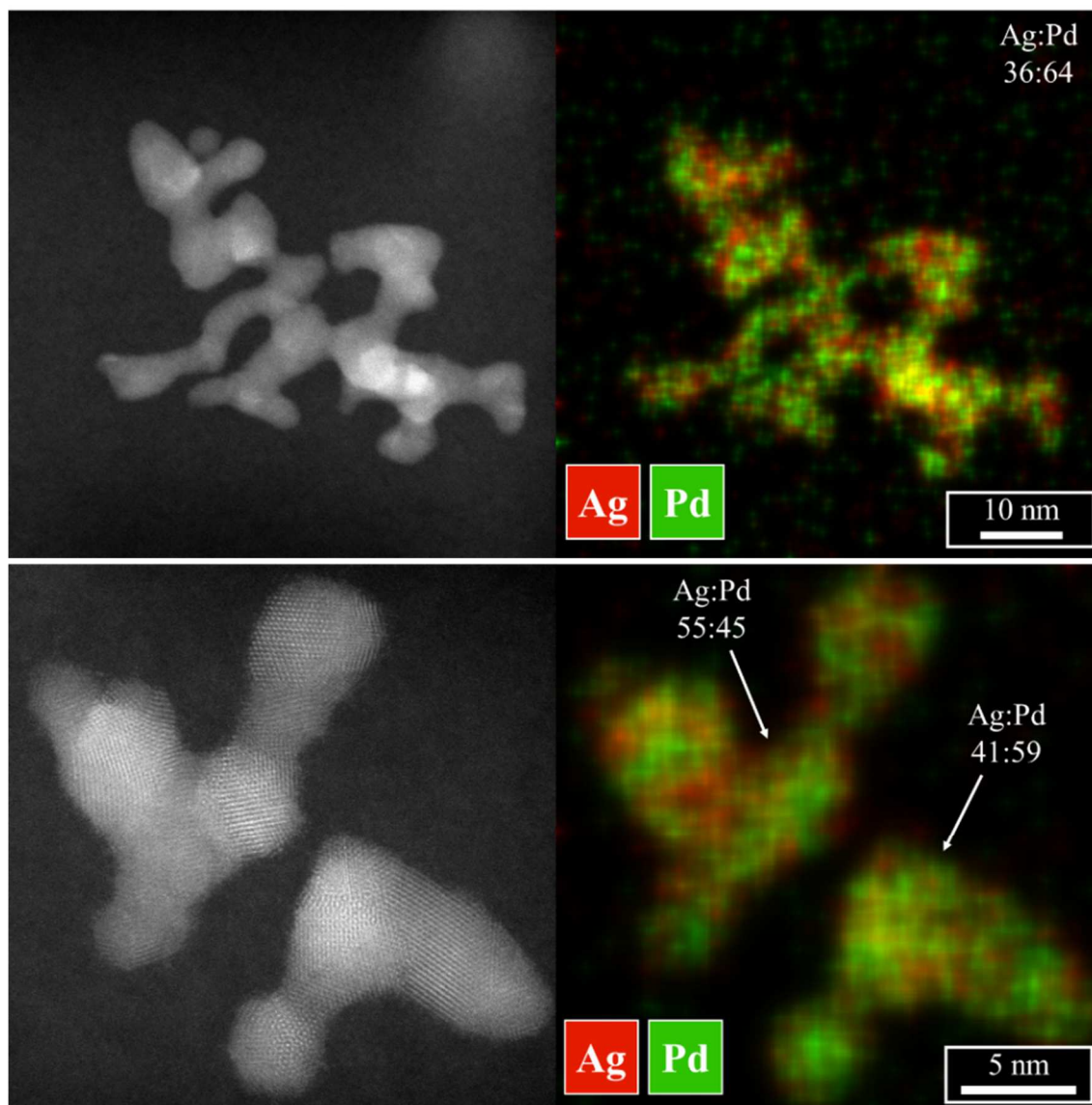


Figure 117: Representative HAADF images of bimetallic Ag-Pd nanoparticle synthesised by sequential reduction with *D*-glucose. The overall molar Ag:Pd ratio is 44:56 at%.

The HAADF images show branched aggregated structures of silver and palladium with some indications of partial alloying (Figure 117). However, neither the dynamic light scattering nor the analytical disc centrifugation of bimetallic Ag-Pd (core-shell) nanoparticles cause to an assumption of aggregation. The size distribution as well as the polydispersity indices indicate a well-dispersed, stable dispersion. Considering the difference in the standard potential between Ag and Pd, a galvanic replacement of initial Ag seeds may be occurred.

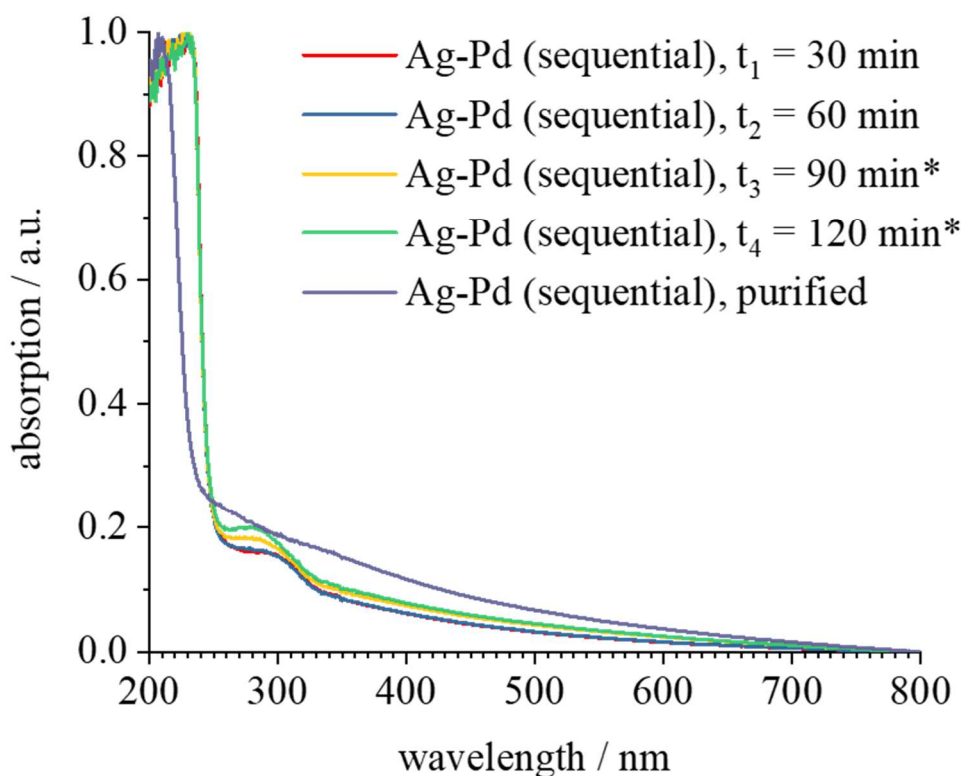


Figure 118: Time-resolved UV/vis spectra of bimetallic Ag-Pd (core-shell) nanoparticles during the synthesis. The asterisks marked the presence of Ag^+ after addition of AgNO_3 at $t = 60$ min.

Due to the fact that Pd^{2+} as well as NO_3^- are strong oxidising under acidic conditions, the galvanic replacement reaction is critical in this two-step synthesis because it leads to dissolution of the less noble silver in the presence of Pd^{2+} ions. In aqueous solution $\text{Pd}(\text{NO}_3)_2$ are present in form of square planar Pd- L_4 complexes, e.g. $[\text{Pd}(\text{H}_2\text{O})_4]^{2+}$. This behaviour leads to a decrease in the standard potential. For example, the square planar $[\text{PdCl}_4]^{2-}$ and $[\text{Pd}(\text{NO}_2)_4]^{2-}$ complexes have standard potentials $\text{PdCl}_4^-/\text{Pd}^0$ of $+0.591$ V^[244] and

$\text{Pd}(\text{NO}_2)_4^{2-}/\text{Pd}^0$ of $-0.340 \text{ V}^{[245]}$ at room temperature which are even lower than of Ag^+/Ag^0 . However, the solution is heated up to $100 \text{ }^\circ\text{C}$, the aqueous complexes decomposed and Pd^{2+} ions are disposable.^[246] The standard potential $\text{Pd}^{2+}/\text{Pd}^0$ of $+0.915 \text{ V}$ is higher than of Ag^+/Ag^0 which leads to an oxidation of initial silver nanoparticles. The oxidation of Ag^0 and the release of Ag^+ ions come to the dissolution of silver particles in consequence of the galvanic replacement reaction. Furthermore, the oxidation potential of NO_3^-/NO is $+0.960 \text{ V}$ (at $\text{pH} = 0$) and might also oxidise Ag .^[243] Afterwards, the excess of the reducing agent *D*-glucose leads to a renewed reduction and reforming of bimetallic nanoparticles with a random structure (Figure 119).

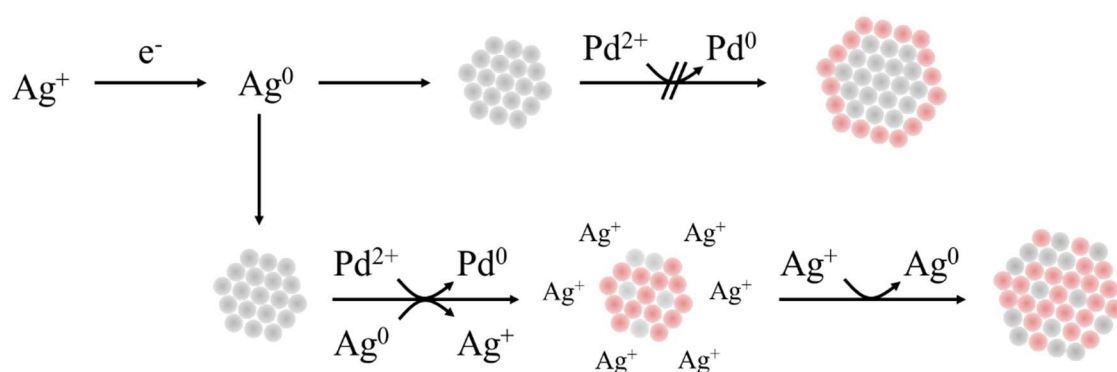


Figure 119: Schematic illustration of the possible redox reaction (galvanic replacement) of initial Ag seeds during the synthesis of bimetallic Ag-Pd nanoparticles by sequential reduction with *D*-glucose.

In summary, the synthesis of bimetallic AgPd nanostructures via a seed and growth approach by sequential reduction does not lead to the expected core-shell structure with an Ag core and a Pd shell. The obtained nanostructures show strong aggregation.

4.3.3 Pd-Ag core-shell nanoparticles by sequential reduction

A sequential reduction approach is chosen to obtain bimetallic Pd-Ag nanoparticles with an expected core-shell structure. The hydrodynamic diameter of the initial Pd seeds is 9.6 nm with a standard deviation of ± 2.4 nm determined by DLS (Figure 120). The polydispersity index of the size distribution is 0.29 indicating a well-dispersed system.

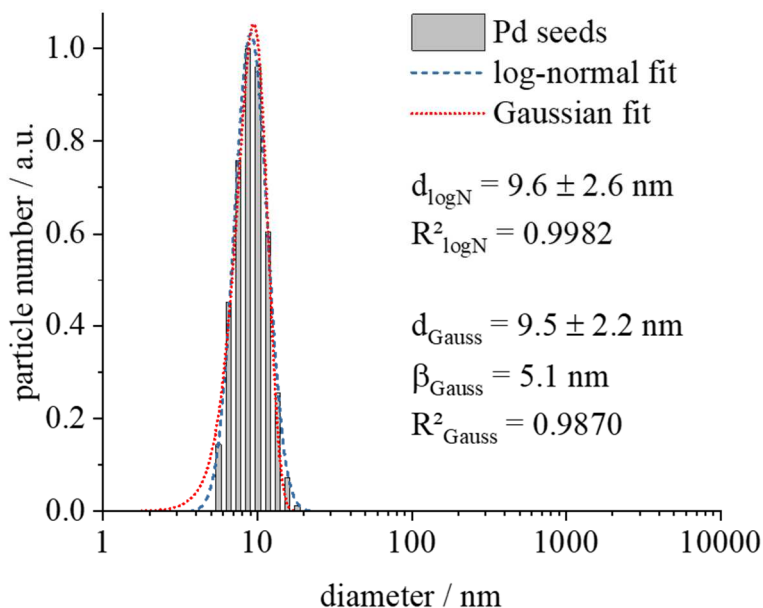


Figure 120: Number-weighted size distribution of initial Pd seeds nanoparticles synthesised by reduction with *D*-glucose determined by DLS. The peak profile is analysed by a log-normal as well as a Gaussian distribution fit. The PDI is 0.29.

The size of initial palladium seeds is verified by analytical disc centrifugation. The size according to DCS is 3.3 nm ± 0.8 nm in diameter with a PDI of 0.27. Note that those measurements are taken out from the unpurified reaction solution.

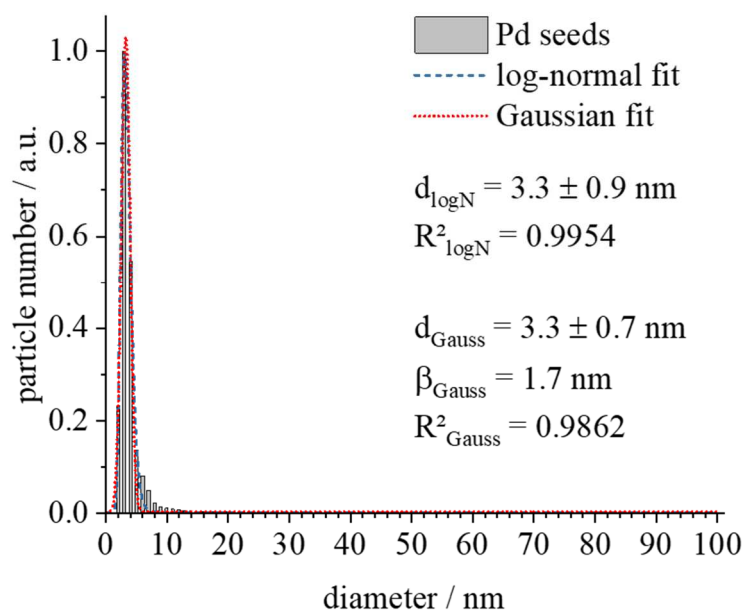


Figure 121: Number-weighted size distribution of initial Pd seeds synthesised by reduction with *D*-glucose determined by DCS. The peak profile is analysed by a log-normal as well as a Gaussian distribution fit. The PdI is 0.27.

The hydrodynamic diameter of bimetallic Ag-Pd nanoparticles is $11.9 \text{ nm} \pm 3.8 \text{ nm}$ determined by DLS (Figure 122). The PdI is 0.47, indicating an unstable dispersion. Nevertheless, no sedimentation or aggregation can be observed. The size from DCS is 4.4 nm with a standard deviation of $\pm 1.0 \text{ nm}$ in diameter (Figure 123). In contrast to the PdI from DLS, the polydispersity index is 0.26 indicating a well-dispersed system (Figure 123). The increase of about 1 nm in diameter is not significant, but might imply a formation of a silver shell. The verification of those expectations is taken out by HAADF imaging with additional energy-dispersive X-ray spectroscopy.

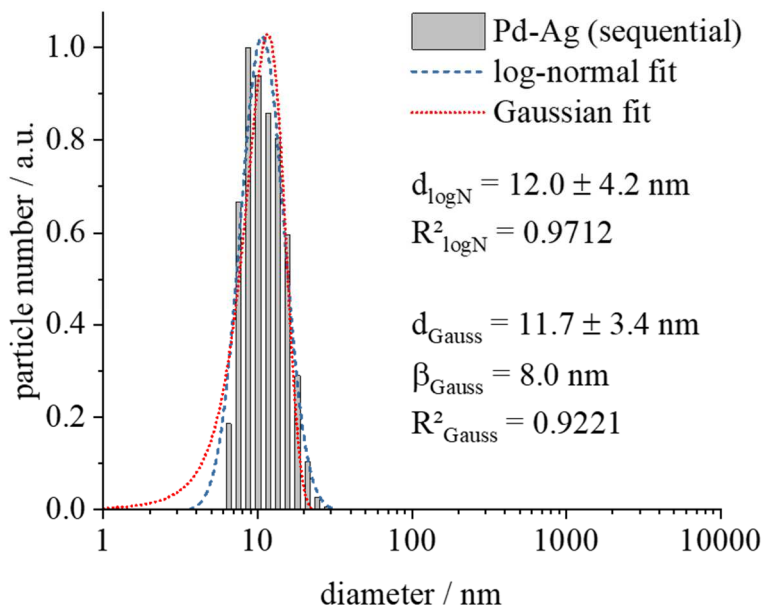


Figure 122: Number-weighted size distribution of bimetallic Pd-Ag nanoparticles synthesised by sequential reduction with *D*-glucose determined by DLS. The peak profile is analysed by a log-normal as well as a Gaussian distribution fit. The PDI is 0.47.

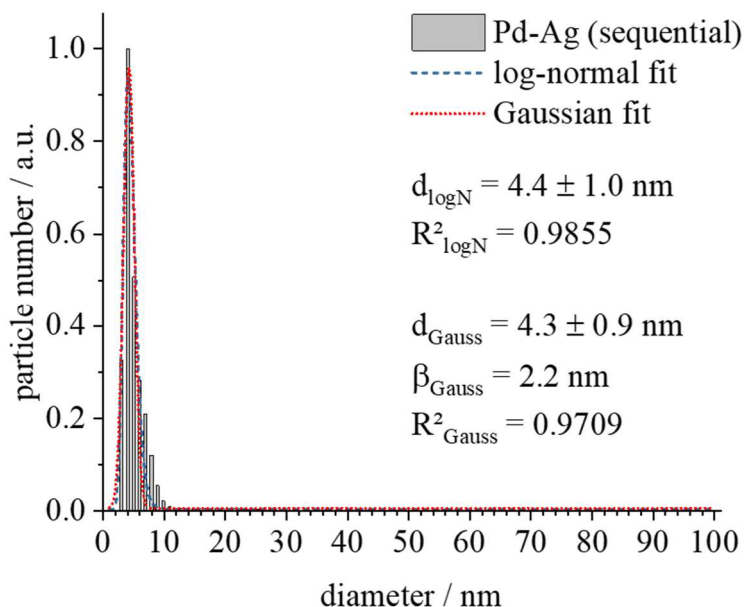


Figure 123: Number-weighted size distribution of bimetallic Pd-Ag nanoparticles synthesised by sequential reduction with *D*-glucose determined by DCS. The peak profile is analysed by a log-normal as well as a Gaussian distribution fit. The PDI is 0.26.

The time-resolved UV/vis spectra are measured at four different times and after purification of the bimetallic Pd-Ag (core-shell) nanoparticles by ultracentrifugation (Figure 124). Both, AgNO_3 and $\text{Pd}(\text{NO}_3)_2$ lead to small absorption in the near ultraviolet region below 300 nm which is caused by the presence of the NO_3^- anion of silver nitrate and the square planar Pd complex $\text{Pd}(\text{NO}_2)_4^{2-}$.^[147, 164, 165]

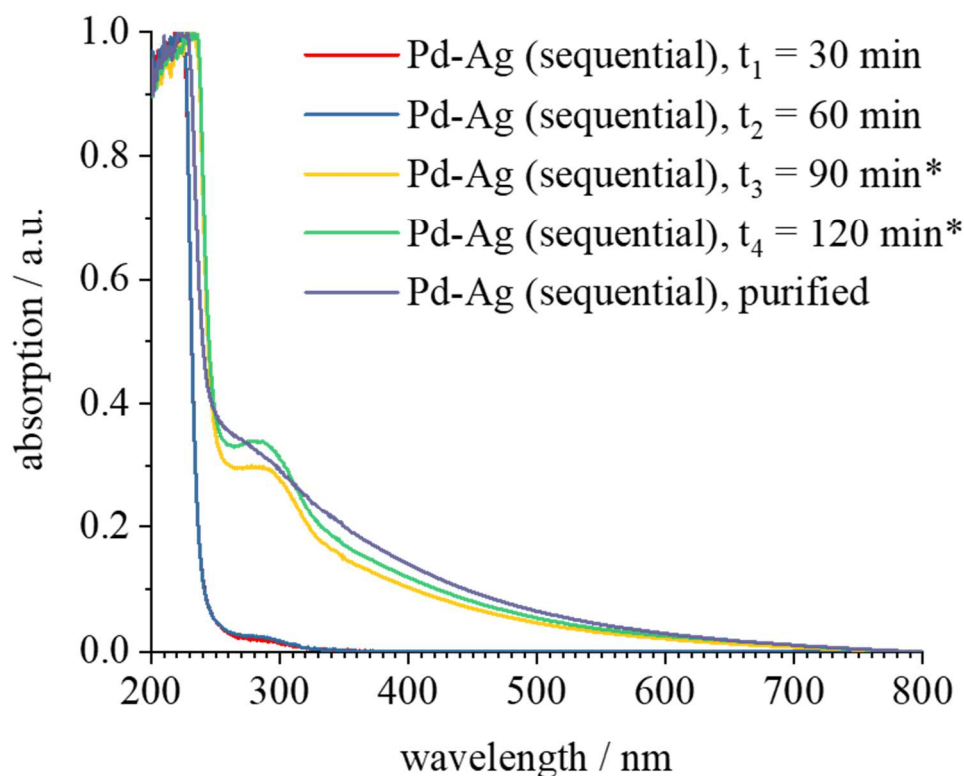


Figure 124: Time-resolved UV/vis spectra of bimetallic Pd-Ag (core-shell) nanoparticles during the synthesis. The asterisks marked the presence of Pd^{2+} after addition of $\text{Pd}(\text{NO}_3)_2$ at $t = 60$ min

The purified dispersion shows no distinct absorption in the visible range (400 to 800 nm). Thus, silver might not be reduced or formed a dense shell. Additionally, a partial alloying of the whole particle or at the phase boundary might be occurred because Pd is in the position to prevent the absorption by surface plasmon resonance of silver.^[234] The high-angle annular dark field imaging as well as the elemental mapping from EDX analysis show spherical-like particles with an implied core-shell construction which consist of a palladium core and a thin Ag shell (Figure 125).

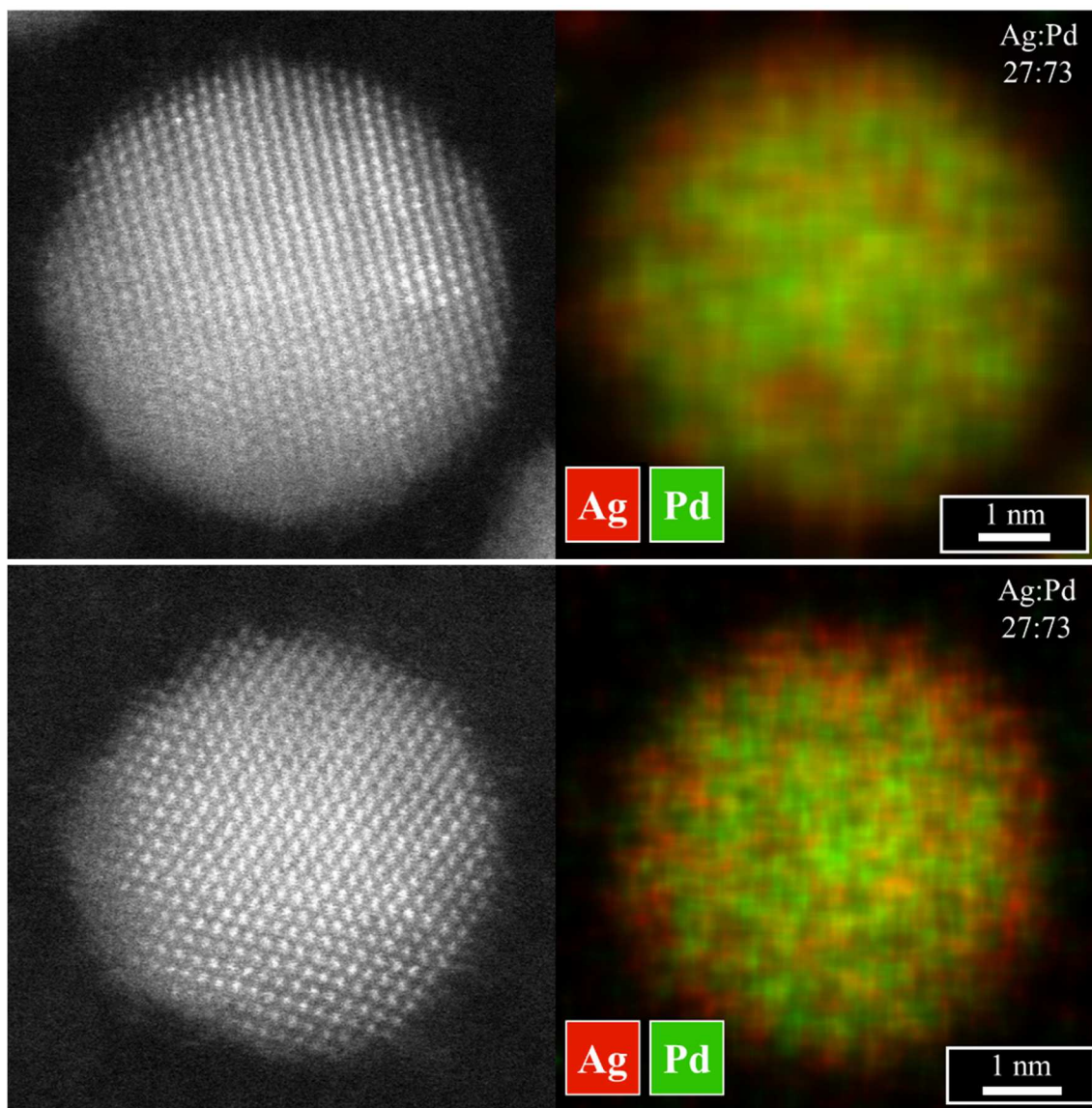


Figure 125: Representative HAADF images of single bimetallic Pd-Ag nanoparticle synthesised by sequential reduction with *D*-glucose. The corresponding elemental mapping from EDX analysis clearly illustrate the co-presence of a Pd-rich core (green) and a silver shell (red). The molar Ag:Pd ratio is 27:73 at%.

The size of Pd-Ag core-shell nanostructures is 6.2 nm with a standard deviation of ± 0.5 nm in diameter. These results correspond very well to the observation from colloid-chemical characterisation by DLS and DCS. The assessment of the shell thickness from HAADF images leads to similar values of approximately 0.5 nm, which correlates to the estimated thickness from DCS. Furthermore, the silver layer seems to be imperfectly and a partial alloying on the phase boundary cannot be excluded. Whereas the nominal molar ratio of the synthesis has been 50:50 at% (Ag:Pd), the obtained particles show a molar

ratio of 27:73 at% (Ag:Pd). These results evidence an incomplete reduction of the silver species. The spherical morphology of initial Pd seeds is maintained after adding silver.

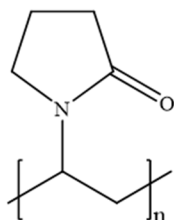
In summary, the sequential reduction of Pd²⁺ (1st) and Ag⁺ (2nd) in aqueous medium yields spherical-like nanoparticles with a core-shell structure. The obtained particles are about 12 nm in hydrodynamic diameter determined by DLS. The size from differential centrifugal sedimentation analysis are around 4 nm, which correlates with the STEM data. The metallic core size is approximately 3 nm. The HAADF-STEM shows uniform particles with a core-shell structure. The initial palladium seeds form the core. An epitaxial overgrowth of silver can be observed. The molar Ag:Pd ratio shows a silver deficiency compared to the initial amount. The Pd-Ag core-shell nanoparticles show no distinct absorption in the visible range, which also suggests the formation of only a very thin Ag layer.

4.3.4 Summary

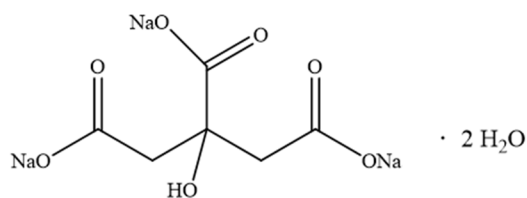
In general, bimetallic AgPd nanostructures (4 to 8 nm) can be wet-chemically prepared by simultaneous and sequential reduction with *D*-glucose in the presence of PVP. The simultaneous reduction of Ag^+ and Pd^{2+} leads to nanoparticles with a core-shell structure. According to the standard potential of both metals, the more noble palladium is reduced faster which results in a Pd-rich core and an Ag-rich shell. The synthesis yields spherical-like nanoparticles with a monodisperse size distribution determined by DLS, DCS and TEM. The molar ratio of 30:70 at% (Ag:Pd) deviates from the nominal ratio of 50:50 at% (Ag:Pd) which reveals an incomplete reduction of the silver. This correlates to the electrochemical properties of both metals and the reaction conditions. The presence of oxidising species like Pd^{2+} and NO_3^- slows the reduction kinetics of Ag^+ and enables the formation of a core-shell structure. Additionally, Pd-Ag core-shell nanoparticles can be prepared in a water-based synthesis by an initial formation of Pd seeds, followed by the addition of a silver shell. There is an epitaxial overgrowth of the silver shell onto the palladium core, leading to a molar ratio of 30:70 at% (Ag:Pd), while the nominal molar ratio was 50:50 at% (Ag:Pd). Neither pure Ag nanoparticles nor galvanic replacement of silver by palladium can be observed. Thus, an incomplete reduction of the Ag^+ species is assumed. Compared to the simultaneous reduction of both metal precursors, the sequential seed-and-growth method leads also to spherical particles with a narrow size distribution and low PdI values. In contrast, Ag-Pd core-shell nanoparticles cannot be prepared in a water-based synthesis by formation of initial silver seeds, followed by the addition of palladium shell. The initial Ag seeds are oxidised, leading to the concurrent release of Ag^+ ions and reduction of Pd^{2+} to Pd^0 . This entails that the seeds reform to an alloyed, branched structure with a random distribution of both elements.

5 Experimental section

5.1 Chemicals



Poly(*N*-vinylpyrrolidone)



Trisodium citrate dihydrate

Figure 126: Molecular formula of poly(*N*-vinylpyrrolidone (PVP; (C₆H₉NO)_n n ≈ 370, M_w = 30,000 g mol⁻¹) and trisodium citrate dihydrate (Na₃C₆H₅O₇ · 2 H₂O, M_w = 294.09 g mol⁻¹).

All chemicals were used without further purification. HAuCl₄ and H₂PtCl₆ were prepared by dissolution of gold and platinum in hot aqua regia, followed by removing the solvent to dryness and multiple re-dissolution and precipitation in HCl.

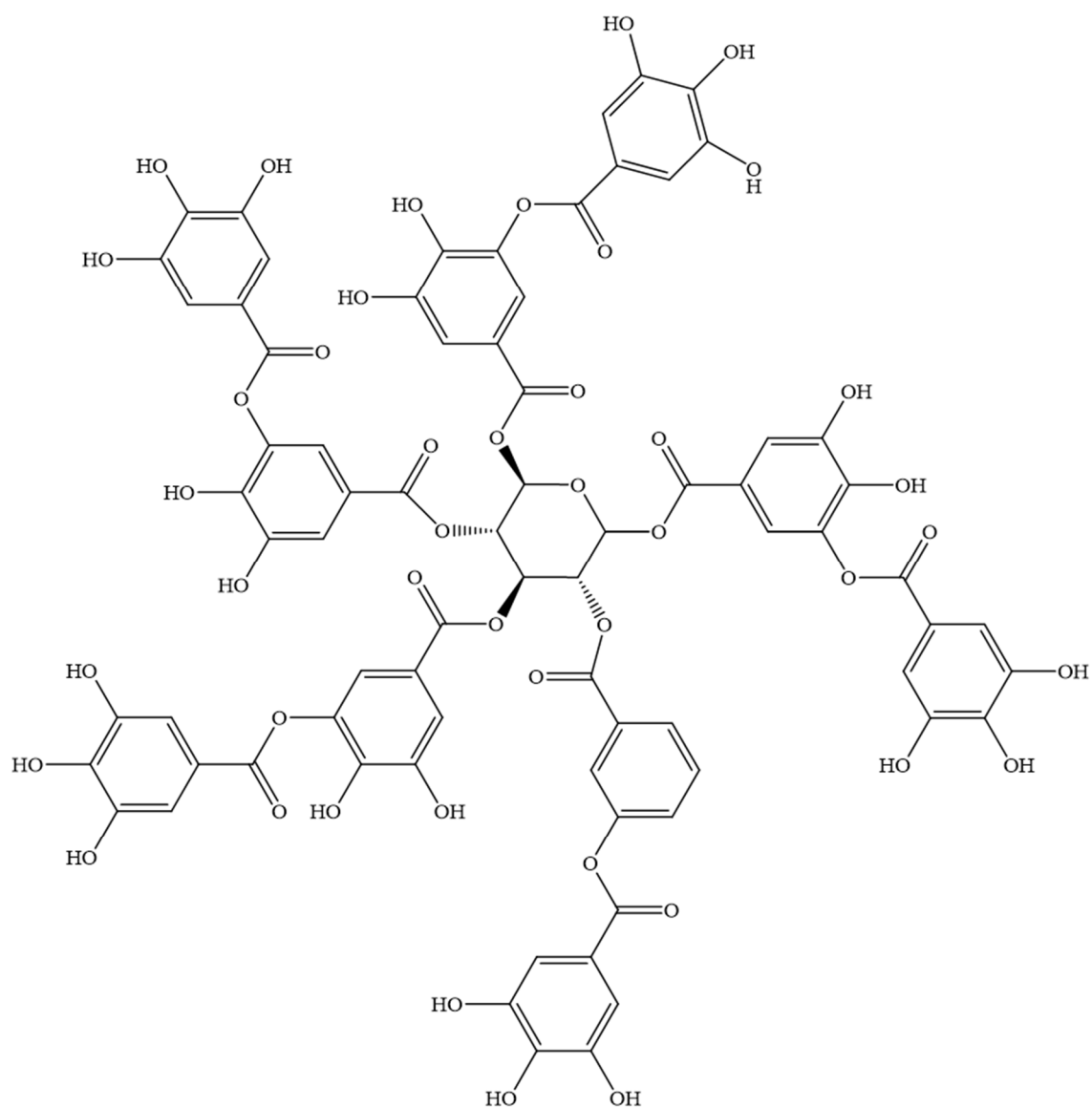


Figure 127: Chemical formula of tannic acid ($C_{76}H_{52}O_{46}$, $M_w = 1,700.38 \text{ g mol}^{-1}$) with its phenolic groups.

Table 25: List of chemicals used.

Chemical	Manufacturer/Distributor	Purity
<i>D</i> -glucose	J. T. Baker / Fisher Scientific GmbH	p.a.
Ethanol	Fisher Chemicals / Fisher Scientific GmbH	p.a.
Gold	Umicore AG & Co. KG	99.99 %
Hexachloridplatonic acid	Self-made by dissolution of platinum bar	
Hexachloridoplatinic acid (ICP standard)	Bernd Kraft GmbH	p.a., traceable to NIST
Hydrochloric acid	Bernd Kraft GmbH	p.a.
Nitric acid	Bernd Kraft GmbH	p.a.
Osmium chloride	Sigma-Aldrich Chemie GmbH	
Palladium nitrate (ICP standard)	Bernd Kraft GmbH	p.a., traceable to NIST
Platinum	Umicore AG & Co. KG	99.99 %
Poly(<i>N</i> -vinylpyrrolidone) ($M_w = 40,000 \text{ g mol}^{-1}$)	Sigma-Aldrich Chemie GmbH	p.a.
Rhodium chloride	Sigma-Aldrich Chemie GmbH	
Ruthenium chloride	Sigma-Aldrich Chemie GmbH	
Silver nitrate	Carl Roth GmbH + Co. KG	
Sodium borohydride	Sigma-Aldrich Chemie GmbH	>96 %

Sodium hydroxide	VWR International GmbH	
Tannic acid	AcrosOrganics / Fisher Scientific GmbH	95 %
Tetrachloridoauric acid	Self-made by dissolution of gold bar	
Trisodium citrate dihydrate	AppliChem GmbH	p.a.

5.2 Software / Databases

Table 26: List of used software and databases. The asterisks (*) marked the databases.

Software/database	Purpose	Editor/reference
ChemDraw Prime 16.0	Molecular formula design	PerkinElmer Informatics, Inc.
Endnote X8	Citation manager	Thomson Reuters Corp.
DIFFRAC.EVA	Phase analysis	Bruker Corp.
Topas 5.0	Rietveld refinement	Bruker Corp.
ImageJ	Graphical particle size analysis	Wayne Rasband, National Institutes of Health, USA
GIMP 2.8	Graphic design	Spencer Kimball, Peter Mattis
Photoshop CS4 V 11.0	Graphic design	Adobe System, Inc.
OriginPro 2018	Graphing and analysis	OriginLab Corp.
American Mineralogist Crystal Structure Database (AMCSD)*	Crystallographic data	[247]
Crystallographic Open Database (COD)*	Crystallographic data	[248]
ICDD*	Crystallographic data	International Centre of Diffraction Data, USA

5.3 Devices

Table 27: List of equipment used.

Method	Device	Manufacturer
AAS	Atomic absorption spectrometer M-Series	Thermo Electron Corp.
Centrifugation	Lab centrifuge Rotofix 32A	Andreas Hettich GmbH & Co. KG
DCS	Disc centrifuge DC24000	CPS Instruments, Inc.
DLS	Zetasizer Nano ZS ZEN 3600	Malvern Panalytical, Ltd.
HR-TEM	FEI Titan G2 80-200 CREWLEY ^[99]	Thermo Fisher Scientific, Inc.
Lyophilisation	Lyophilizer Christ Alpha 2-4 LSC	Martin Christ Gefriertrocknungsanlagen GmbH
PXRD	X-Ray powder diffractometer Bruker D8 ADVANCE	Bruker Corp.
Rotary evaporation	Rotavapor R-114	Buechi Labortechnik GmbH
STEM (incl. HAADF, and EDX)	FEI Titan 80-300 ChemiSTEM ^[100, 101]	Thermo Fisher Scientific, Inc.
Ultracentrifugation	Ultracentrifuge Sorvall™ WX Ultra Series	Thermo Fisher Scientific, Inc.

Ultrasonification	Ultrasonic cleaner Elmasonic S10	Elma Schmidbauer GmbH
UV/vis	Spectrophotometer Varian Cary 300	Agilent Technologies, Inc.
Vortex	Vortex-Genie 2	Scientific Industries, Inc.

5.4 Synthesis

Ultrapure water (Purelab ultra instrument from ELGA) was used in all experiments. All glassware was cleaned with boiling *aqua regia* before use to eliminate possible crystallisation nuclei. For the experiments containing silver, separate glassware was used which was cleaned with boiling nitric acid to eliminate possible crystallisation nuclei and to prevent the precipitation of insoluble silver chloride during synthesis. Afterwards, all flasks were carefully rinsed with ultrapure water several times.

5.4.1 Synthesis of monometallic Ru, Rh, Pd, Os, Ir, and Pt nanoparticles with *D*-glucose

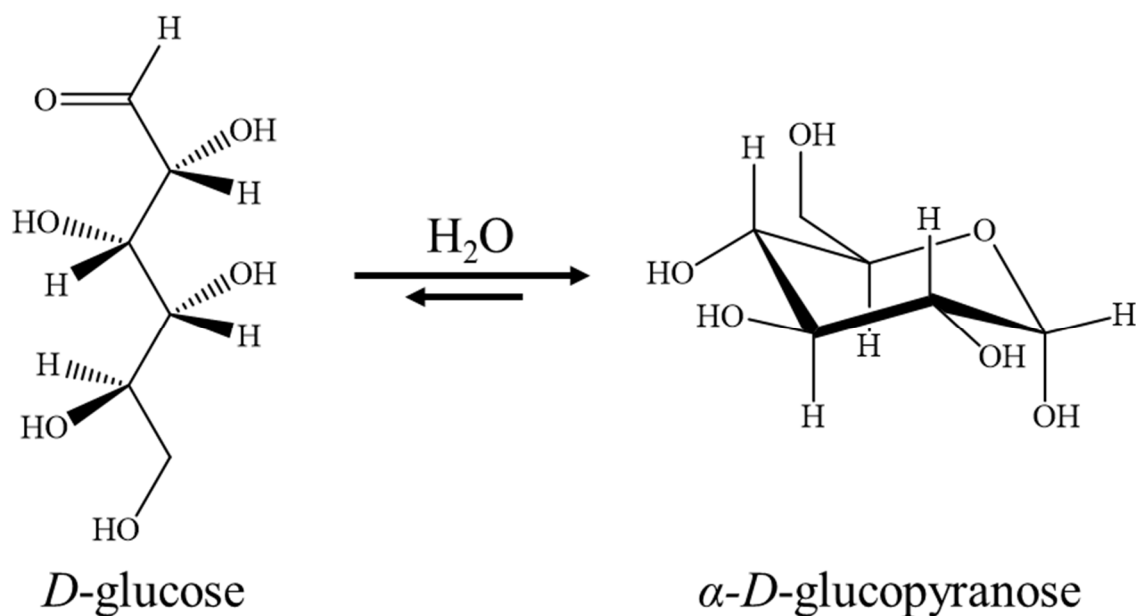


Figure 128: The equilibrium in water between the open chain form of *D*-glucose and the cyclic form α -*D*-glucopyranose.

In solution, *D*-glucose is in equilibrium between the open chain and cyclic forms. In aqueous media the preferred conformation (> 99 %) is the cyclic form α -*D*-glucopyranose (Figure 128).^[249] The proposed redox reaction of *D*-glucose in the presence of metal ions is as follows (Figure 129).^[250]

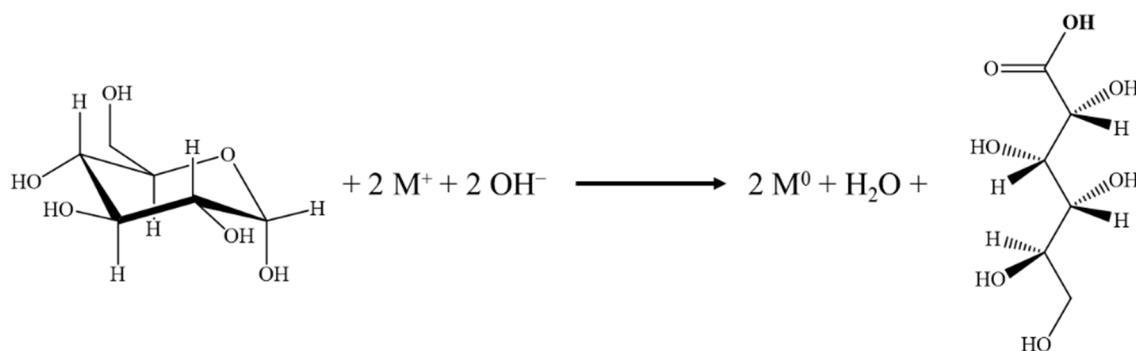


Figure 129: Scheme of the redox reaction of *D*-glucose and metal ions.

In a 100 ml two-neck round-bottom flask, 600 mg (3 mmol) *D*-glucose and 50 mg (0.125 μ mol) poly(*N*-vinylpyrrolidone) (PVP) were dissolved in 50 ml water under stirring (700 rpm) and heated to 100 °C under reflux. Then an aqueous solution (5 ml) of the corresponding metal precursor (25 μ mol for Os, Ir, and Pt; 50 μ mol for Ru, Rh, and Pd) was rapidly added. The mixture was boiled under reflux temperature for 60 min (Pd), 120 min (Ru, Rh), and 240 min (Os, Ir, Pt), respectively. At the end of reaction time, the mixture was rapidly cooled to room temperature in an ice bath. Most of the water and the synthesis by-products were removed by centrifugation (4,000 rpm) in a spin filter tube (Millipore; molecular weight cut-off 3 kDa). The nanoparticles were purified by a final centrifugation step at 66,000 g (30,000 rpm) for 30 min, followed by redispersion in ultrapure degassed water. The dispersion was stored under argon at 4 °C to avoid oxidation. For X-ray powder diffraction, the nanoparticle dispersion was isolated, shock-frozen with liquid nitrogen, and lyophilized to remove the frozen water.

5.4.2 Synthesis of monometallic Ag nanoparticles with sodium borohydride

In general, one sodium borohydride molecule can release eight electrons, which can potentially reduce metal ions. The number of reduced species depends on the oxidation state of the metal precursor molecule. A general proposed mechanism of the redox reaction of sodium borohydride and a monovalent metal cation is as follows.



In a 500 ml two-neck round-bottom flask, 18 mg (60 μmol) AgNO_3 and 18 mg (90 μmol) trisodium citrate were dissolved in 350 ml water. The mixture was rapidly cooled in an ice bath with stirring (700 rpm). Then 10 ml of a 10 mM NaBH_4 solution (4 mg; dissolved in cold water) were added rapidly to the reaction mixture. After 1 min, an aqueous solution of 25 mM PVP (10 ml, 150 mg) was added and the mixture was stirred for 3 h. The PVP-stabilized Ag nanoparticles were purified by centrifugation at 66,000 g (30,000 rpm) for 30 min and redispersion in ultrapure degassed water two times. The dispersion was stored under argon at 4 $^\circ\text{C}$ to avoid oxidation. For X-ray powder diffraction, the nanoparticle dispersion was isolated, shock-frozen with liquid nitrogen, and lyophilized to remove the frozen water.

5.4.3 Synthesis of monometallic Au nanoparticles with trisodium citrate and tannic acid

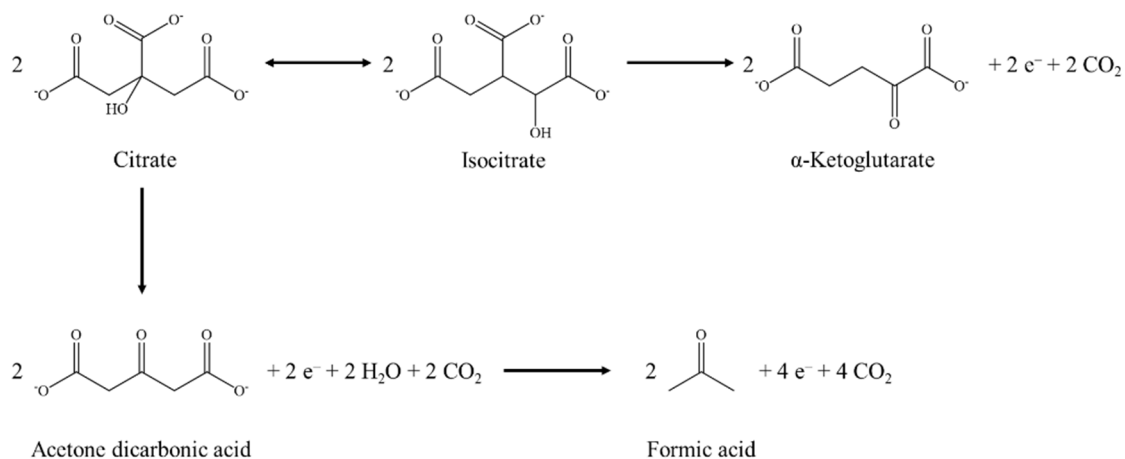
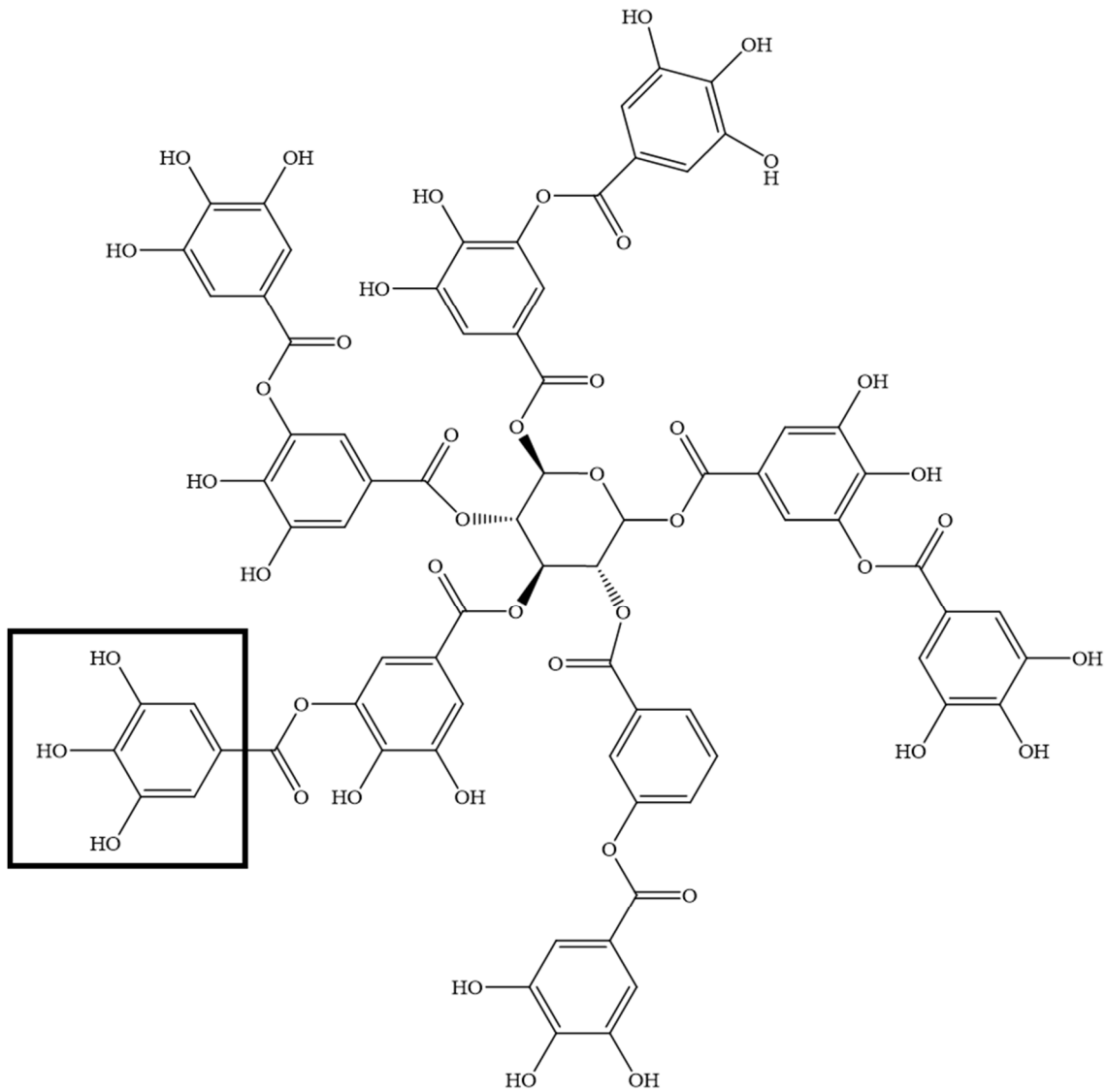


Figure 130: Scheme of possible reaction of the oxidation of citrate. The preferred pathway at higher temperature is the complete decarboxylation with the formation of formic acid.^[251, 252]

Both, trisodium citrate as well as tannic acid act as reducing agent in the synthesis of metal nanoparticles. The oxidation of citrate leads to the formation of α -ketoglutarate, acetone dicarboxylic acid, formic acid, and carbon dioxide (Figure 130).^[249, 251] In the presence of tannic acid, the citrate molecules mainly stabilise the initial particles because tannic acid possesses the higher reducing strength and contributes up to ten electrons per molecule (Figure 131).^[253]



Tannic acid

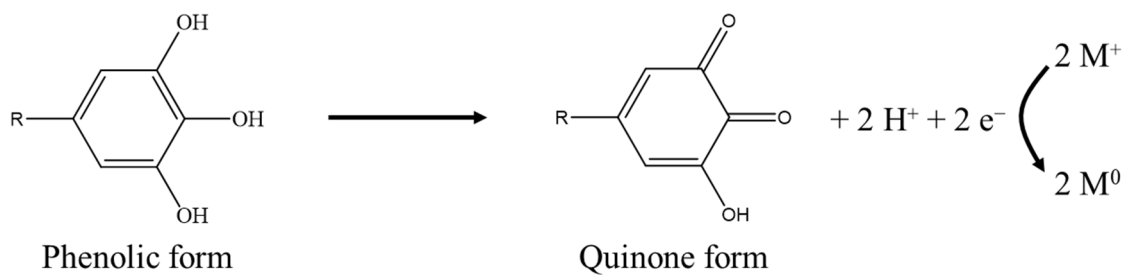


Figure 131: The molecular structure of tannic acid and the reaction scheme of the redox reaction between tannic acid and metal ions. The oxidation of the phenolic groups in the tannic acid (marked with the black box) to quinones leads to a subsequent release of electrons which can reduce metal ions.

In a 250 ml two-neck round-bottom flask, 600 mg (2 mmol) trisodium citrate and 50 mg (0.03 mmol) tannic acid were dissolved in 150 ml water under stirring (700 rpm) and heated to 100 °C under reflux. Then, 5 ml of an aqueous H_{AuCl}₄ solution (containing 25 μmol Au; 5 mg) were added rapidly to the boiling solution. After 5 min, the reaction mixture was rapidly cooled to room temperature in an ice bath. 50 mg (0.125 μmol) PVP dissolved in 5 ml H₂O were added for stabilization and the mixture was stirred for at least 12 h. Most of the water and the by-products were removed by centrifugation (4,000 rpm) in a spin filter tube. The nanoparticles were purified by a final centrifugation step at 66,000 g for 30 min and redispersed in ultrapure degassed water. The dispersion was stored under argon at 4 °C to avoid oxidation. For X-ray powder diffraction, the nanoparticle dispersion was isolated, shock-frozen with liquid nitrogen, and lyophilized to remove the frozen water.

5.4.4 Synthesis of bimetallic AuPd alloyed nanoparticles

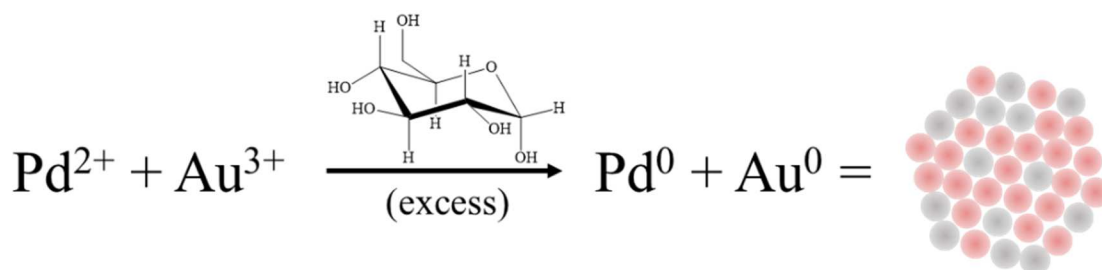


Figure 132: Possible reaction scheme of the formation of bimetallic AuPd alloyed nanoparticles.

Bimetallic AuPd (alloyed) nanoparticles were prepared by dissolving 600 mg (3 mmol) D-glucose and 50 mg (0.125 μmol) PVP in 50 ml water in a 100 ml two-neck round bottom flask. The mixture was stirred (700 rpm) and heated to 100 $^{\circ}\text{C}$ under reflux. Meanwhile, 2.5 ml of an aqueous solution of $\text{Pd}(\text{NO}_3)_2$ (containing 2.5 mg/25 μmol Pd) and 2.5 ml of an aqueous solution of HAuCl_4 (containing 2.5 mg/25 μmol Au) were mixed in a 5 ml Eppendorf tube. Then the mixture was added and the solution was stirred for 30 min at 100 $^{\circ}\text{C}$ under reflux. The reaction mixture was cooled to room temperature with an ice bath. The dispersion was centrifuged with a Millipore Spin Filter (molecular weight cut-off 3 kDa, remaining volume 500 μl) at 4,000 rpm for 45 min. The remaining concentrated dispersion was taken up, centrifuged twice at 66,000 g (30,000 rpm) for 30 min, and redispersed in ultrapure water. For X-ray powder diffraction, the nanoparticle dispersion was isolated, shock-frozen with liquid nitrogen, and lyophilized to remove the frozen water.

5.4.5 Synthesis of bimetallic Pd-Au core-shell nanoparticles

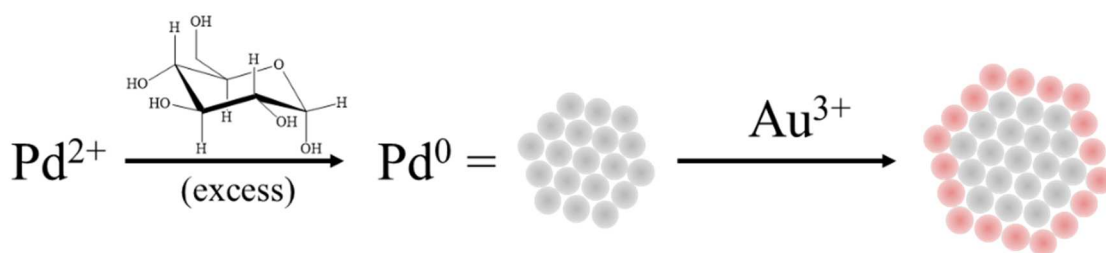


Figure 133: Reaction scheme of the possible formation of Pd-Au core-shell nanoparticles.

In a 250 ml two-neck round-bottom flask, 600 mg (2 mmol) trisodium citrate, 50 mg (0.03 mmol) tannic acid and 50 mg (0.125 μ mol) PVP were dissolved in 150 ml water under stirring (700 rpm) and heated to 100 °C under reflux. Then, 5 ml of an aqueous HAuCl₄ solution (containing 25 μ mol Au; 5 mg) were added rapidly to the boiling solution. Then 5 ml of an aqueous solution containing Pd²⁺ (either Pd(NO₃)₂ or Na₂PdCl₄ with no notable difference between the two precursors; containing 5 mg/0.05 mmol Pd) were added and the reaction mixture was heated for 1 h at 100 °C under reflux. Afterwards, the reaction mixture was rapidly cooled to room temperature in an ice bath. Most of the water and the by-products were removed by centrifugation (4,000 rpm) in a spin filter tube for 45 min. The nanoparticles were purified by a final centrifugation step at 66,000 g (30,000 rpm) for 30 min and redispersed in ultrapure degassed water. The dispersion was stored under argon at 4 °C to avoid oxidation. . For X-ray powder diffraction, the nanoparticle dispersion was isolated, shock-frozen with liquid nitrogen, and lyophilized to remove the frozen water.

For the analysis of the gold seeds, the synthesis was terminated before the addition of palladium, and the Au nanoparticles were isolated in the same way as the Au-Pd nanoparticles.

5.4.6 Synthesis of bimetallic Au-Pd core-shell nanoparticles

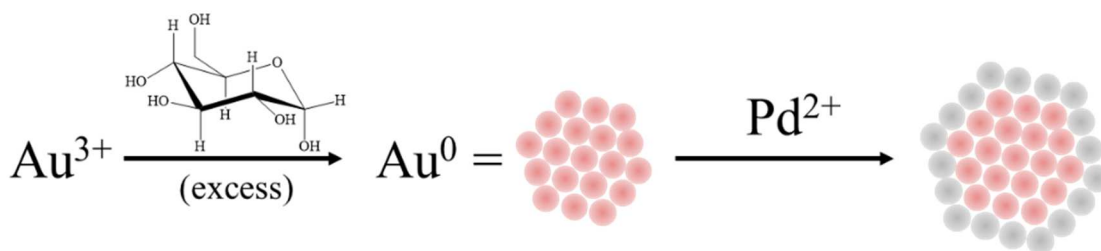


Figure 134: Reaction scheme of the possible formation of Au-Pd core-shell nanoparticles.

Pd-Au core-shell nanoparticles were prepared by dissolving 600 mg (3 mmol) *D*-glucose and 50 mg (0.125 μmol) PVP in 50 ml water in a two-neck round bottom flask. The mixture was stirring (700 rpm) and heated to 100 $^{\circ}\text{C}$ under reflux. First, 5 ml of an aqueous solution containing Pd^{2+} (either $\text{Pd}(\text{NO}_3)_2$ or Na_2PdCl_4 with no notable difference between the two precursors; containing 5 mg/0.05 mmol Pd) were added and the reaction mixture was heated for 1 h at 100 $^{\circ}\text{C}$ under reflux. Then 5 ml of HAuCl_4 solution (containing 9.85 mg/0.05 mmol Au) were rapidly added. The mixture was kept boiling for another 5 min at 100 $^{\circ}\text{C}$. Then, the reaction mixture was cooled to room temperature with an ice bath. The dispersion was centrifuged with a Millipore Spin Filter (molecular weight cut-off 3 kDa, remaining volume 500 μl) at 4000 rpm for 45 min. The remaining concentrated dispersion was taken up, centrifuged twice at 66,000 g (30,000 rpm) for 30 min, and redispersed in ultrapure water. For X-ray powder diffraction, the nanoparticle dispersion was isolated, shock-frozen with liquid nitrogen, and lyophilized to remove the frozen water.

For the analysis of the palladium seeds, the synthesis was terminated before the addition of gold, and the palladium nanoparticles were isolated in the same way as the Pd-Au nanoparticles.

5.4.7 Synthesis of bimetallic AgPd (alloyed) nanoparticles

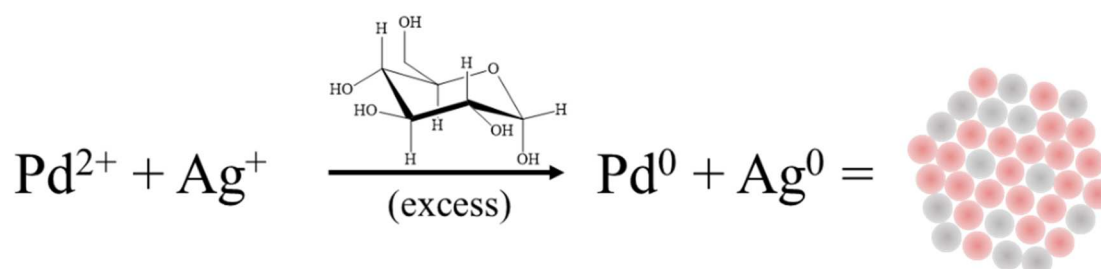


Figure 135: Reaction scheme of the possible formation of alloyed AgPd nanoparticles.

Bimetallic AgPd (alloyed) nanoparticles were prepared by dissolving 600 mg (3 mmol) *D*-glucose and 50 mg (0.125 μmol) PVP in 50 ml water in a 100 ml two-neck round bottom flask. The mixture was stirred (700 rpm) and heated to 100 $^{\circ}\text{C}$ under reflux. Meanwhile, 2.5 ml of an aqueous solution of $\text{Pd}(\text{NO}_3)_2$ (containing 2.5 mg/0.025 mmol Pd) and 2.5 ml of an aqueous solution of AgNO_3 (containing 2.5 mg/0.025 Ag) were mixed in a 5 ml Eppendorf tube. Then the mixture was added and the solution was heated for 1 h at 100 $^{\circ}\text{C}$ under reflux. The reaction mixture was cooled to room temperature with an ice bath. The dispersion was centrifuged with a Millipore Spin Filter (molecular weight cut-off 3 kDa, remaining volume 500 μl) at 4,000 rpm for 45 min. The remaining concentrated dispersion was taken up, centrifuged twice at 66,000 g (30,000 rpm) for 30 min, and re-dispersed in ultrapure water.

5.4.8 Synthesis of Ag-Pd core-shell nanoparticles

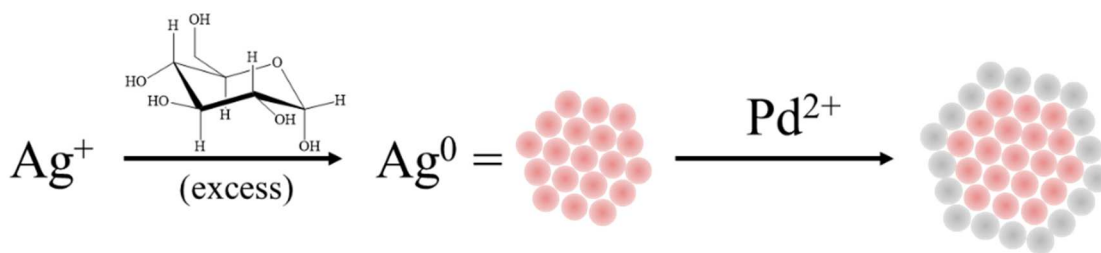


Figure 136: Reaction scheme of the possible formation of Ag-Pd core-shell nanoparticles.

Ag-Pd core-shell nanoparticles were prepared by dissolving 600 mg (3 mmol) *D*-glucose and 50 mg (0.125 μmol) PVP in 50 ml water in a 100 ml two-neck round bottom flask. The mixture was stirred (700 rpm) and heated to 100 $^{\circ}\text{C}$ under reflux. First, 2.5 ml of an aqueous solution of $\text{Pd}(\text{NO}_3)_2$ (containing 2.5 mg/0.025 mmol Pd) was added rapidly to the boiling solution and kept at 100 $^{\circ}\text{C}$ for 1 h. Afterwards, 2.5 ml of an aqueous solution of AgNO_3 (containing 2.5 mg/0.025 Ag) was added and the solution was heated for 60 min at 100 $^{\circ}\text{C}$ under reflux. The reaction mixture was cooled to room temperature with an ice bath. The dispersion was centrifuged with a Millipore Spin Filter (molecular weight cut-off 3 kDa, remaining volume 500 μl) at 4,000 rpm for 45 min. The remaining concentrated dispersion was taken up, centrifuged twice at 66,000 g (30,000 rpm) for 30 min, and redispersed in ultrapure water.

5.4.9 Synthesis of Pd-Ag core-shell nanoparticles

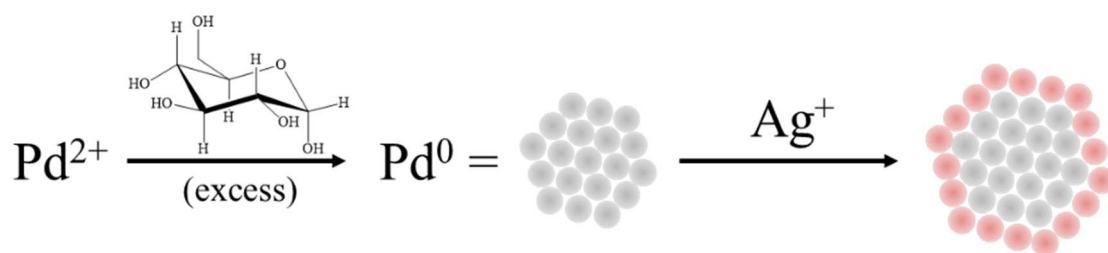


Figure 137: Reaction scheme of the possible formation of Pd-Ag core-shell nanoparticles.

Pd-Ag core-shell nanoparticles were prepared by dissolving 600 mg (3 mmol) *D*-glucose and 50 mg (0.125 μmol) PVP in 50 ml water in a 100 ml two-neck round bottom flask. The mixture was stirred (700 rpm) and heated to 100 $^{\circ}\text{C}$ under reflux. First, 2.5 ml of an aqueous solution of AgNO_3 (containing 2.5 mg/0.025 mmol Ag) was added rapidly to the boiling solution and kept at 100 $^{\circ}\text{C}$ for 60 min. Afterwards, 2.5 ml of an aqueous solution of $\text{Pd}(\text{NO}_3)_2$ (containing 2.5 mg/0.025 Pd) was added and the solution was heated for 1 h at 100 $^{\circ}\text{C}$ under reflux. The reaction mixture was cooled to room temperature with an ice bath. The dispersion was centrifuged with a Millipore Spin Filter (molecular weight cut-off 3 kDa, remaining volume 500 μl) at 4,000 rpm for 45 min. The remaining concentrated dispersion was taken up, centrifuged twice at 66,000 g (30,000 rpm) for 30 min, and re-dispersed in ultrapure water.

6 Conclusion

One main aim of the present work was the establishment of reproducible, water-based syntheses of mono- and bimetallic nanoparticles with an equal surface-functionalisation and similar diameter. Moreover, a detailed characterisation according to size, shape, composition, and (crystallographic) structure as well as the investigation of their physical, chemical, biological and optical properties are an integral component of this work. Based on the classical *Turkevich*^[252] and comparable methods^[218, 254, 255] as well as the glucose synthesis^[250], the wet-chemical syntheses are transferred to the other metal systems and modified to obtain the desired results. Numerous chemical, physico-chemical and physical methods to synthesise noble metal nanoparticles are reported in literature.^[8, 256, 257] In the last years the development of sustainable synthesis routes, namely green syntheses, of such particular systems has become more prominent.^[258, 259] Additionally, physical methods like laser ablation are more frequently used for the generation of nanostructures.^[46, 75, 76, 260-262] One of the major challenges is the shape-controlled synthesis of metal nanostructures (spheres, cubes, rods, etc.) which can be achieved by various experimental approaches. The focus is on the nucleation control, crystal growth and colloidal stabilisation.^[5, 43, 44, 263] In contrast, most of the syntheses of rhodium^[125, 264], palladium^[265, 266], platinum^[267-269] and silver^[155, 270, 271] are based on the prominent polyol process. Organic compounds like ethylene glycol serve as the solvent, reductant and stabilising agent.^[45, 272] The complexity with the use of non-aqueous compounds and solvents is the transfer to biological systems. In the case of ruthenium and osmium, another problem is the possible formation of toxic species like RuO₄ and OsO₄ during the synthesis or characterisation. Common synthesis of Ru and Os nanoparticles starts from organometallic precursors^[111, 273] or is carried out in ionic liquids.^[177, 178] Iridium nanoparticles can be also obtained in ionic liquids^[187], by the polyol process^[189] or using superhydride.^[188]

Here, spherical-like, uniform nanoparticles of the noble metals with an average diameter between 4 and 8 nm were synthesised in aqueous media with the help of suitable reducing agents (*D*-glucose, sodium borohydride, and a mixture of citrate and tannic acid), stabilised with poly(*N*-vinylpyrrolidone), and purified by ultracentrifugation and redispersion in ultrapure water. Additionally, a careful and extensive characterisation has been performed. All dispersions of the platinum metals (Ru, Rh, Pd, Os, Ir, and Pt) had a brownish to almost black colour without any distinct absorption in the visible range (400 to 800

nm). Silver and gold showed characteristic absorption behaviour of their surface plasmon resonance (SPR).^[115] The sizes of the obtained particles were determined by different colloid-chemical methods as well as high-resolution transmission electron microscopy. Dynamic light scattering (DLS) and differential centrifugal sedimentation (DCS) analysis were used to measure the hydrodynamic diameter, i.e. the size of the particle including the hydration shell of adsorbed ligands, ions and polymer, whereas TEM depicts only the metallic core because of the collapse of the polymer in the high vacuum. Recognisable, the differences in the hydrodynamic size from DLS and DCS are caused by the physical measuring principle. While the DLS overestimates the particle size due to the swollen polymer in aqueous solution, the DCS displayed smaller diameter because of the high effective density of the metal core compared to the hydration shell.^[95, 113] High-resolution TEM showed spherical-like nanoparticles with diameters that are in good agreement with the results from analytical disc centrifugation and dynamic light scattering. All eight systems had a neutral to slightly negative ζ -potential, which supposedly results from synthesis by-products. PVP at its own is a neutral polyelectrolyte which does not greatly influence the electrophoretic mobility of dispersed particles.^[274] However, it is known that citrate and other ligands like tris(sodium-*m*-sulfonato-phenyl)phosphine (TPPTS) are often not completely replaced by the stabilizing polymer PVP which results in a measurable (negative) ζ -potential.^[224] The crystallographic structure was studied by powder X-ray diffraction. Additionally, the crystallite sizes, lattice parameters and cell volumes were calculated by an in-depth Rietveld refinement. Considering the influence of the nanocrystallinity on the experimental data, all results correspond to the data of the bulk materials and the successful synthesis of the monometallic nanoparticles can be confirmed.

Except ruthenium, osmium, and iridium, the nanoparticles are stable in cell culture media and were examined in a comparative cell biological study. Human mesenchymal stem cells (hMSCs) were cultured in the presence of noble metal nanoparticles (with a metal concentration up to $50 \mu\text{g ml}^{-1}$) under cell culture conditions (RPMI + 10 % FCS). Rhodium, palladium, platinum, and gold have did not shown an adverse effect. In particular, no negative effect and no oxidative release of ions have been observed up to 50 ppm. Silver nanoparticles had an influence on the viability of hMSCs after 24 h of exposure, which became noticeable in form of a cytotoxic effect starting from $25 \mu\text{g ml}^{-1}$. Furthermore, the cell viability decreased with increasing Ag concentration. Silver chloride and silver ions show similar effects, which are well known in literature.^[230-232, 275] Whereas subtoxic concentrations (2.5 to $10 \mu\text{g ml}^{-1}$) of silver had no discernible cell biological

effect, cell detachment could be observed at toxic concentration of Ag nanoparticles (25 to 50 $\mu\text{g ml}^{-1}$). This is correlated to the cytotoxic action. Additionally, a subtoxic concentration of silver had an adverse effect on the differentiation of hMSCs.^[233] Overall, the cytotoxicity of silver nanostructures is due to the oxidative release of Ag^+ .^[32, 34, 35, 231, 275-281] For the more noble metals, such dissolution effects do not supposedly occur and an oxidation by dissolved oxygen species is not expected from the electrochemical point of view.

As mentioned in the introduction, bimetallic nanostructures might reveal a promising mechanism to suspend the careless use of antibiotics and open the field of new antimicrobial and bactericidal mechanisms. Metals with antibacterial action like copper and silver hold a lot of promise and are well characterised. It could be shown that the combination of silver with a nobler metal, e.g. gold or platinum, lead to a higher Ag^+ release by a sacrificial anode effect caused by the electrochemical polarisation of silver.^[36-38] In the present work, gold and palladium represent the proof-of-principle system due to their similar electrochemical behaviour with respect to such systems with silver. Pd-Au and Au-Pd core-shell nanoparticles (core diameter about 5 to 6 nm, shell thickness of about 1-1.5 nm) were prepared in a wet-chemical synthesis based on a seeded growth approach.^[282, 283] In the first step, palladium particles were synthesised by reduction with *D*-glucose in the presence of PVP. Those seeds acted as core to which gold was epitaxial overgrown in a one-pot synthesis. Due to the presence of excess glucose, a galvanic replacement of initial Pd seeds by gold could be prevented. The size of the palladium as well as of the obtained core-shell nanoparticles were determined by dynamic light scattering, analytical disc centrifugation and high-resolution TEM. UV/vis spectroscopy was used to verify the epitaxial overgrowth of gold. After the addition of Au, the electromagnetic spectrum showed an absorption band which corresponds to the absorption of the surface plasmon resonance (SPR) of gold. This observation validated the successful overgrowth and the presence of a dense gold layer on the palladium particle. The development of an absorption band after the addition of Au on Pd is well reported.^[56, 284] The presence of two separate phases was confirmed by elemental mapping from EDX analysis and HAADF-STEM. Additionally, the crystallographic parameters were determined by X-ray powder diffraction and Rietveld refinement. Both, the palladium and the gold phase could be identified and the crystallite sizes, lattice constants, cell volumes and crystal densities could be calculated using the face-centre cubic (fcc) phases. With respect to the lattice

constant of the pure metals, a partial alloying at the phase boundary could not be completely excluded. However, the water-based synthesis of alloyed AuPd nanoparticles by co-reduction of the ionic precursors has not been successful, yet. Gold nanoparticles are normally inert regarding biological and bactericidal effects.^[285] Nevertheless, a size-dependent cytotoxicity of gold is known, especially if they are very small (e.g. cluster-like Au particles).^[286-288] Au nanoparticles (< 5 nm) can achieve nuclear entry in fibroblasts, while larger particles (> 9 nm) cannot penetrate the nuclear pores and remain inside the cytoplasm.^[289] In contrast, palladium shows potential risks due to catalytic effects and the generation of reactive oxygen species (ROS).^[290-292] Nevertheless, there is no data available on the biological effects of bimetallic gold-palladium nanostructures. Therefore, biological activity tests of Pd-Au core-shell nanoparticles are carried out in this study. The investigations revealed that there is no significant effect on hMSCs (up to a total metal concentration of 50 $\mu\text{g ml}^{-1}$) after exposure for 24 h. Similar effects are observed for PVP-stabilised Au nanoparticles (6 nm) exposed to hMSCs^[293] and for peripheral blood mononuclear cells (PBMCs) after incubation in the presence of palladium nanoparticle with a particle size of 9 nm.^[294]

Bimetallic palladium-silver nanoparticles (core diameter of about 5 to 6 nm, shell thickness of approx. 0.5 nm) with a core-shell construction were obtained in two different synthesis approaches. First, the co-reduction of AgNO_3 and $\text{Pd}(\text{NO}_3)_2$ with *D*-glucose in the presence of PVP yielded spherical nanoparticles with a thin Ag shell onto a Pd-rich core. Second, the stepwise reduction by initial formation of palladium seeds, followed by an epitaxial overgrowth of silver onto the Pd surface also led to a core-shell structure. The silver shell could however be characterised only to some extent by UV/vis spectroscopy and HAADF-STEM.

The optimisation of the synthesis conditions, especially for ruthenium, osmium, and iridium, as well as the variation of parameters, i.e. temperature, pH value and concentrations, will be the next step to get a simple, transferable, and variable basic framework of a water-based synthesis useful for obtaining metal nanoparticles with an easily accessible variation in size, shape and crystal structure. In addition, the extension of the syntheses to other bimetallic particles with different element ratios may be possible by variation of the synthesis conditions and will be a main goal in the future. Nevertheless, one of the major challenge will be the prevention of the galvanic replacement in aqueous media of the less noble silver in the presence of a more noble metal.

7 Summary

In summary, it can be stated that monometallic nanoparticles of group VIII to XI elements can be easily prepared by a water-based synthesis, leading to uniform spherical-like nanoparticles with an average diameter between 4 and 8 nm and the same surface-functionalisation. Except ruthenium, osmium, and iridium, all syntheses result in reasonable yields, high reproducibility, and monodisperse size distribution. An extensive characterisation of size and shape is performed using common colloid-chemical (DLS, DCS) and microscopic methods (HR-TEM). Considering the measurement characteristics of each method, the hydrodynamic diameters determined by DLS and DCS correspond very well to the sizes from high-resolution TEM analysis. The composition and optical properties are studied by UV/vis spectroscopy. Monometallic silver and gold particles show the typical absorption behaviour of the surface plasmon resonance, while all other metals have no distinct absorption in the visible range (400 to 800 nm). Further, the structural investigation is carried out by additional microscopic techniques (HAADF-STEM, EDX) and X-ray powder diffraction. The platinum metals seem to form single-crystalline particles. In the case of silver, a second phase can be identified by Rietveld refinement that corresponds to the increased amount of stacking faults (< 10 %). Gold shows typical penta-fold twinned crystals, which can be depicted by high-resolution TEM imaging. The calculated crystallite sizes are in accordance with the particle diameter and confirm the regularly crystallographic structure. No obvious effect on hMSCs can be observed after exposure with Rh, Au, Pd and Pt nanoparticles after 24 h (up to a total metal concentration of 50 $\mu\text{g ml}^{-1}$). Silver shows a concentration-dependent cytotoxic effect, which is noticeable starting from an Ag content of 25 $\mu\text{g ml}^{-1}$. Noteworthy, ruthenium, osmium and iridium are not stable in cell culture media (RPMI + 10 % FCS) which is generally observable in form of aggregation and precipitation during cell experiments (not shown).

Bimetallic Au-Pd and Pd-Au core-shell nanoparticles are obtained via a one-pot synthesis based on a seeded-growth method. In contrast, the synthesis of alloyed gold-palladium nanoparticles in aqueous media using *D*-glucose was not successful. UV/vis spectroscopy, PXRD and HR-TEM including supplemental techniques like energy-dispersive X-ray spectroscopy (EDX) and high-angle annular dark field imaging (HAADF) confirm the epitaxial overgrowth of a metallic layer on the surface of initial seeds. In the case of Pd-Au core-shell nanoparticles additional *in-situ* small-angle X-ray scattering (SAXS) is

performed to monitor the core-shell formation during the wet-chemical synthesis. Pd-Au core-shell nanoparticles have no significant effect on the viability of human mesenchymal stem cells (hMSCs) up to a total metal concentration of $50 \mu\text{g ml}^{-1}$.

Palladium-silver nanoparticles with a suggested core-shell structure are available using two different one-pot synthesis approach. On the one hand, the sequential reduction of the corresponding ionic metal precursors based on a seeded-growth method results in palladium particles with a thin Ag layer, on the other hand the simultaneous reduction of both metals leads to an enrichment of Pd in the core region and the formation of a silver shell. A galvanic replacement of initial Ag seeds can be observed by adding Pd^{2+} ions.

8 German Summary

Zusammenfassend lässt sich sagen, dass mono- und bimetallische Nanopartikel der Elemente der Gruppe VIII bis XI leicht mit Hilfe einer wasser-basierten Synthese dargestellt werden können, welche zu kugelförmigen, gleichförmigen und gleichgroßen Nanopartikeln mit einer durchschnittlichen Größe von 4 bis 8 nm im Durchmesser und gleicher Oberflächen-Funktionalisierung führt. Mit Ausnahme von Ruthenium, Osmium und Iridium, resultieren alle Synthesen in passablen Ausbeuten, hoher Reproduzierbarkeit und hoher Monodispersität. Eine ausführliche Charakterisierung bezüglich Größe, Form und Zusammensetzung ist mit gängigen kolloidchemischen (DLS, DCS), spektroskopischen (UV/vis) und mikroskopischen Methoden (HR-TEM) erfolgt. Des Weiteren ist eine strukturelle Untersuchung mit Hilfe zusätzlichen mikroskopischen Techniken (HAADF-STEM, EDX) und der Röntgenbeugung durchgeführt worden. Die Nanopartikel scheinen einkristallin mit einigen wenigen Stapelfehlern, insbesondere bei Silber, zu sein und besitzen berechnete Kristallitgrößen ähnlich der Partikeldurchmesser. Gold hingegen zeigt typische fünffach verzwilligte Kristalle. Die hydrodynamischen Durchmesser, die mittel DLS und DCS ermittelt worden sind, sind vergleichbar mit den Größen aus der Analyse der hochaufgelösten Transmissionselektronenmikroskopischen Daten. Unter Berücksichtigung der Messeigenschaften der einzelnen Verfahren entsprechen die von DLS und DCS ermittelten hydrodynamischen Durchmesser sehr gut den Größen aus der TEM-Analyse. Die Zusammensetzung und die optischen Eigenschaften wurden mittels UV/vis-Spektroskopie untersucht. Silber und Gold zeigen das typische Absorptionsverhalten, das durch die Oberflächenplasmonenresonanz hervorgerufen wird, während alle anderen Metalle keine deutliche Absorption im sichtbaren Bereich (400 bis 800 nm) hatten. Darüber hinaus wurde eine Strukturuntersuchung durch zusätzliche mikroskopische Techniken (HAAD-STEM, EDX) und Röntgenpulverdiffraktometrie durchgeführt. Die Platin-Metalle scheinen einkristalline Partikel zu bilden. Bei Silber kann eine zweite Phase durch die Rietveld-Verfeinerung identifiziert werden, die mit der erhöhten Anzahl von Stapelfehlern (< 10 %) korreliert. Gold zeigt typische fünffach verzwilligte Kristalle, die durch hochaufgelöste TEM-Bilddarstellung dargestellt werden konnten. Die berechneten Kristallitgrößen entsprechen dem Partikeldurchmesser und bestätigen die empirisch beobachtbare Kristallstruktur. Nach einer 24-stündigen Exposition mit Rh, Pd, Pt und Au (bis zu einer Gesamtmetallkonzentration von $50 \mu\text{g ml}^{-1}$) ist keine offensichtliche Wirkung auf

hMSCs zu erkennen. Silber zeigt einen konzentrationsabhängigen zytotoxischen Effekt, der sich ab einem Ag-Gehalt von $25 \mu\text{g ml}^{-1}$ bemerkbar macht. Erwähnenswert ist, dass Ruthenium, Osmium und Iridium in Zellkulturmedien (RPMI + 10 % FCS) nicht stabil sind, was typischerweise in Form von Aggregation und Niederschlagsbildung in den Zellversuchen zu beobachten ist (wurde hier nicht gezeigt).

Bimetallische Au-Pd und Pd-Au Kern-Schale-Nanopartikel werden durch eine Eintopfsynthese auf der Grundlage eines Impfkristallwachstumsverfahrens erhalten. Im Gegensatz dazu war die Synthese von legierten Gold-Palladium-Nanopartikeln in wässrigem Medium mit *D*-Glucose nicht erfolgreich. UV/vis-Spektroskopie, PXRD und HR-TEM einschließlich ergänzender Techniken wie energiedispersiver Röntgenspektroskopie (EDX) und spezieller Abbildungstechnik (engl. high-angle annular dark field (HAADF) imaging) bestätigen das epitaktische Überwachsen einer metallischen Schicht auf der Oberfläche der Ausgangskeime. Bei Pd-Au Kern-Schale-Nanopartikeln wird eine zusätzliche *in-situ* Kleinwinkel-Röntgenstreuung (SAXS) durchgeführt, um die Kern-Schale-Bildung während der nasschemischen Synthese zu überwachen. Pd-Au Kern-Schale-Nanopartikel haben bis zu einer Gesamtmetallkonzentration von $50 \mu\text{g ml}^{-1}$ keinen signifikanten Einfluss auf die Viabilität humaner mesenchymaler Stammzellen (hMSCs).

Palladium-Silber-Nanopartikel mit einer implizierten Kern-Schale-Struktur sind mit zwei verschiedenen Eintopfverfahren erhältlich. Zum einen führt die auf einem Impfkristallwachstumsverfahren basierende sequentielle Reduktion der entsprechenden ionischen Metallvorläufer zu Palladiumpartikeln mit einer dünnen Ag-Schicht, zum anderen führt die gleichzeitige Reduktion beider Metalle zu einer Anreicherung von Pd in der Kernregion und die Bildung einer Silberhülle. Ein galvanischer Ersatz der ursprünglichen Ag-Kerne kann durch Zugabe von Pd^{2+} -Ionen beobachtet werden.

9 Appendix

9.1 List of publications

- 2019 M. Breisch, V. Grasmik, K. Loza, K. Pappert, A. Rostek, N. Ziegler, A. Ludwig, M. Heggen, M. Epple, J.C. Tiller, T.A. Schildhauer, M. Köller, C. Sengstock, *Bimetallic silver-platinum nanoparticles with combined osteo-promotive and antimicrobial activity* **2019** (submitted)
- 2019 P.R.A.F. Garcia, K. Loza, S. Daumann, V. Grasmik, K. Pappert, A. Rostek, J. Helmlinger, O. Prymak, M. Epple, C.L.P. Oliveira, *Combining small-angle X-ray scattering and X-ray powder diffraction to investigate size, shape, and crystallinity of silver, gold, and alloyed silver-gold nanoparticles*, *Braz. J. Phys.* **2019** (doi: 10.1007/s13538-019-00642-z)
- 2018 A. Rostek, M. Breisch, K. Pappert, K. Loza, M. Heggen, M. Köller, C. Sengstock, M. Epple, *Comparative biological effects of spherical noble metal nanoparticles (Rh, Pd, Ag, Pt, Au) with 4-8 nm diameter*, *Beilstein J. Nanotechnol.* **2018**, 9, 2763-2774 (doi: 10.3762/bjnano.9.258)
- 2018 A. Rostek, M. Breisch, K. Loza, P.R.A.F. Garcia, C.L.P. Oliveira, O. Prymak, M. Heggen, M. Köller, C. Sengstock, M. Epple, *Wet-chemical synthesis of Pd-Au core-shell nanoparticles (8 nm): From nanostructure to biological properties*, *ChemistrySelect* **2018**, 3, 4994-5001 (doi: 10.1002/slct.201800638)
- 2016 I. Schremmer, A. Brik, D.G. Weber, N. Rosenkranz, A. Rostek, K. Loza, T. Brüning, M. Epple, J. Bünger, G.A. Westphal, *Chemotaxis, cytokine and chemokine release of NR8383 macrophages after exposure to amorphous silica, crystalline quartz, barium sulfate and titanium dioxide*, *Toxicol. Lett.* **2016**, 263, 68-75 (doi: 10.1016/j.toxlet.2016.08.014)

- 2015 G.A. Westphal, I. Schremmer, A. Rostek, K. Loza, N. Rosenkranz, T. Brüning, M. Epple, J. Bünger, *Particle-induced cell migration assay (PICMA): A new in vitro assay for inflammatory particle effects based on permanent cell lines*, *Toxicol. In Vitro* **2015**, 29, 997-1005 (doi: 10.1016/j.tiv.2015.04.005)
- 2014 O. Prymak, S. Ristig, W. Meyer-Zaika, A. Rostek, L. Ruiz, J.M. Gonzalez-Calbet, M. Vallet-Regi, M. Epple, *X-ray powder diffraction as a tool to investigate the ultrastructure of nanoparticles*, *Russ. Phys. J.* **2014**, 56, 1111-1115 (doi: 10.1007/s11182-014-0149-2)
- 2011 A. Rostek, D. Mahl, M. Epple, *Chemical composition of surface-functionalized gold nanoparticles*, *J. Nanopart. Res.* **2011**, 13, 4809-4814 (doi: 10.1007/s11051-011-0456-2)

9.2 List of scientific conferences, poster contributions and oral presentations

- 25.11. – 2018 MRS Fall Meeting and Exhibit, Boston (United States of America)
30.11.2018
- A. Rostek, M. Breisch, K. Loza, V. Grasmik, K. Pappert, M. Heggen, M. Köller, C. Sengstock, M. Epple: “*Mono- and bimetallic nanoparticles of noble metals – The influence of the composition and nanostructure on biological effects*” (**oral presentation**)
- 05.03. – 26th Annual Meeting of the German Crystallographic Society (DGK),
08.03.2018 Essen (Germany)
- A. Rostek, K. Loza, O. Prymak, P.R.A.F. Garcia, C.L.P. Oliveira, M. Heggen, M. Epple: “*In-situ small-angle X-ray scattering (SAXS) and powder X-ray diffraction (PXRD): Complementary tools to investigate the structural behaviour and the composition of mono- and bimetallic nanoparticles*” (**oral presentation/poster contribution**)
- 09.11. – Jahrestagung der Deutschen Gesellschaft für Biomaterialien, Würzburg (Germany)
11.11.2017
- A. Rostek, I. Föhring, K. Loza, A. Brik, D.G. Weber, C. Sengstock, M. Köller, T. Brüning, G. Johnen, G.A. Westphal, J. Bünger, M. Epple: “*The particle-induced cell migration assay (PICMA): An in vitro tool to assess the effect of inflammatory particles*” (**poster contribution**)
- 03.03. – Abschlusskolloquium des Schwerpunktprogramms “Biological Response to Nanoscale Particles” (SPP1313), Fulda (Germany)
05.03.2014
- S. Ristig, J. Helmlinger, K. Loza, A. Rostek, B. Schütze, M. Epple: “*Possibilities in Synthesis and Functionalization of Inorganic Nanoparticles: Silver and Silver Chloride Nanoparticles*” (**poster contribution**)
- B. Schütze, J. Helmlinger, K. Loza, S. Ristig, A. Rostek, M. Epple: “*Possibilities in Synthesis and Functionalization of Metallic and Bimetallic Nanoparticles: Gold and Silver-Gold alloyed Nanoparticles*” (**poster contribution**)

- A. Rostek, J. Helmlinger, K. Loza, S. Ristig, B. Schütze, M. Epple: “*Survey on Analysis Tools for the Characterization of Inorganic Nanoparticles: Chemical Composition and Ligand Shell*“ (**poster contribution**)
- J. Helmlinger, K. Loza, S. Ristig, A. Rostek, B. Schütze, M. Epple: “*Survey on Analysis Tools for the Characterization of Inorganic Nanoparticles: Size and Morphology*“ (**poster contribution**)
- K. Loza, J. Helmlinger, S. Ristig, A. Rostek, B. Schütze, M. Epple, C. Sengstock, M. Köller: “*Biological Action of Inorganic Nanoparticles*“ (**poster contribution**)
- A. Rostek, J. Helmlinger, K. Loza, S. Ristig, B. Schütze, M. Epple, C. Sengstock, M. Köller: “*Inorganic Nanoparticles (Ag, AgCl, Au and Ag-Au alloys): Synthesis, Characterization and Cell Biological Studies*“ (**oral presentation**)
- 08.09. – 25th European Symposium on Biomaterials, Madrid (Spain)
- 12.09.2013 A. Rostek, M. Malissek, S. Langolf, L. Treuel, C. Schmuck, M. Epple: “*The influence of surface-functionalized gold nanoparticles on the enzymatic activity and structure of trypsin*” (**poster contribution**)
- 01.11. – Jahrestagung der Deutschen Gesellschaft für Biomaterialien, Hamburg (Germany)
- 03.11.2012 A. Rostek, J. Diendorf, S. Ristig, C. Greulich, M. Köller, M. Epple: “*Silber-, Gold- und Silber-Gold-Nanopartikel: Vergleichende zellbiologische Untersuchungen*” (**poster contribution**)
- 11.09. – International Conference on Biological Response to Nanoscale Particles, Essen (Germany)
- 15.09.2011 A. Rostek, D. Mahl, M. Epple: “*Chemical composition of surface-functionalized gold nanoparticles*” (**poster contribution**)

9.3 Curriculum vitae

The CV is not included in the online version for privacy reasons.

Der Lebenslauf ist in der Online-Version aus datenschutzrechtlichen Gründen nicht enthalten.

9.4 Acknowledgement

I would like to express my sincere gratitude to

Prof. Dr. Matthias Epple for the supervision of the PhD, master, and bachelor thesis, for providing me with interesting research topics, scientific support during my academic career, the opportunities of research stays abroad, and possibilities of presenting my results on scientific conferences,

Prof. Dr. Stephan Barcikowski for the assessment of my thesis and fruitful discussion within the priority program SPP1313,

Prof. Dr. Manfred Köller, Jun.-Prof. Dr. Christina Sengstock, née Greulich, and Ms. Marina Breisch from Surgical Research at the University Hospital Bergmannsheil of the Ruhr-University Bochum for long-time cooperation and fruitful scientific discussions,

Dr. Marc Heggen from the Ernst-Ruska Centre for Microscopy and Spectroscopy with Electrons in the Forschungszentrum Jülich for outstanding collaboration,

Dr. Kateryna Loza for transmission electron microscopy investigations, fruitful scientific discussions and pleasant research stays in Fulda and Berlin,

Dr. Isabell Föhring, née Schremmer, Ms. Nina Rosenkranz, Dr. Götz A. Westphal, Prof. Dr. Jürgen Bünger for outstanding collaboration and the insight in toxicological research,

Ms. Kerstin Brauner and Mr. Robin Meya for all AAS measurements,

Ms. Carola Fischer, Ms. Sabine Kiefer, Ms. and Sabine Bollmann with organisation and technical assistance,

Dr. Oleg Prymak and Mr. Dietrich Tönnies for technical assistance and XRPD measurements,

Ms. Selina van der Meer for a pleasant time as lab mate,

Dr. Viktoria Grasmik, Mr. Sebastian Kollenda, Ms. Alwina Lübke, Mr. Kevin Pappert, Ms. Tatjana Ruks, Ms. Karolin Wey, all other colleagues and alumni of the working group for lab assistance, fruitful discussion, scientific advice, and the atmosphere,

Dr. Dirk Mahl for the support at the beginning of my academic career, fruitful scientific discussion and advice,

My parents, parents-in-law, family and friends for their love, helpfulness, and support.

Furthermore, I would thank Dr. Simon Ristig for being a great friend and for the pleasant time at university, for being my roommate at several research stays and conferences in New York City, Madrid, Fulda, Gießen, and Berlin, and for all the time out of science and beyond.

I would thank Dr. Raphaela Ristig (and of course Greta) for all the enjoyable time out of lab and for amusing evenings at the Tapas bar.

At finally yet importantly, I would express my lovely gratitude to my wife Miriam for her love, warmness and indispensable support during my study.

9.5 Statutory declaration / Eidesstaatliche Erklärung

I hereby declare that the presented thesis with the following title

“Wet-chemical synthesis of mono- and bimetallic nanoparticles of group VIII to XI metals and their detailed characterisation”

is my own work and independently written. I further declare that I neither used the help of second individuals nor other tools and references as listed. I also declare that the presented thesis has never been submitted in any other possible way to other faculties.

Hiermit versichere ich, die vorliegende Arbeit mit dem Titel

„Wet-chemical synthesis of mono- and bimetallic nanoparticles of group VIII to XI metals and their detailed characterisation”

selbst verfasst und unabhängig niedergeschrieben habe. Des Weiteren erkläre ich keine außer den angegebenen Hilfsmitteln und Quellen verwendet zu haben. Zudem erkläre ich, dass ich die Arbeit in dieser oder einer ähnlichen Form bei keiner anderen Fakultät eingereicht habe.

Essen, den 12.03.2019

Alexander Rostek

10. References

- [1] J. J. Giner-Casares, M. Henriksen-Lacey, M. Coronado-Puchau, L. M. Liz-Marzán, *Mater. Today* **2016**, *19*, 19.
- [2] H. Goesmann, C. Feldmann, *Angew. Chem. Int. Ed. Engl.* **2010**, *49*, 1362.
- [3] S. E. Lohse, C. J. Murphy, *J. Am. Chem. Soc.* **2012**, *134*, 15607.
- [4] W. J. Stark, P. R. Stoessel, W. Wohlleben, A. Hafner, *Chem. Soc. Rev.* **2015**, *44*, 5793.
- [5] Y. Xia, Y. Xiong, B. Lim, S. E. Skrabalak, *Angew. Chem. Int. Ed. Engl.* **2009**, *48*, 60.
- [6] R. Yu, L. M. Liz-Marzán, F. J. García de Abajo, *Chem. Soc. Rev.* **2017**, *46*, 6710.
- [7] P. K. Jain, X. Huang, I. H. El-Sayed, M. A. El-Sayed, *Acc. Chem. Res.* **2008**, *41*, 1578.
- [8] J. Li, T. Zhao, T. Chen, Y. Liu, C. N. Ong, J. Xie, *Nanoscale* **2015**, *7*, 7502.
- [9] H.-l. Liu, F. Nosheen, X. Wang, *Chem. Soc. Rev.* **2015**, *44*, 3056.
- [10] R. M. Wang, O. Dmitrieva, M. Farle, G. Dumpich, H. Q. Ye, H. Poppa, R. Kilaas, C. Kisielowski, *Phys. Rev. Lett.* **2008**, *100*, 017205.
- [11] Y. Xu, L. Chen, X. Wang, W. Yao, Q. Zhang, *Nanoscale* **2015**, *7*, 10559.
- [12] W. Aki, K. Masashi, K. Juewon, K. Atsuhiko, T. Kyoko, M. Tadahiko, M. Yusei, *Nanotechnology* **2009**, *20*, 455105.
- [13] C. M. Cobley, J. Chen, E. C. Cho, L. V. Wang, Y. Xia, *Chem. Soc. Rev.* **2011**, *40*, 44.

- [14] W. He, X. Han, H. Jia, J. Cai, Y. Zhou, Z. Zheng, *Sci. Rep.* **2017**, *7*, 40103.
- [15] J. Li, W. Liu, X. Wu, X. Gao, *Biomaterials* **2015**, *48*, 37.
- [16] J. Wei, X. Chen, S. Shi, S. Mo, N. Zheng, *Nanoscale* **2015**, *7*, 19018.
- [17] T. Wen, W. He, Y. Chong, Y. Liu, J.-J. Yin, X. Wu, *Phys. Chem. Chem. Phys.* **2015**, *17*, 24937.
- [18] L. Gan, M. Heggen, R. O'Malley, B. Theobald, P. Strasser, *Nano Lett.* **2013**, *13*, 1131.
- [19] M. B. Gawande, A. Goswami, T. Asefa, H. Guo, A. V. Biradar, D.-L. Peng, R. Zboril, R. S. Varma, *Chem. Soc. Rev.* **2015**, *44*, 7540.
- [20] G. Guisbiers, R. Mendoza-Cruz, L. Bazán-Díaz, J. J. Velázquez-Salazar, R. Mendoza-Perez, J. A. Robledo-Torres, J.-L. Rodriguez-Lopez, J. M. Montejano-Carrizales, R. L. Whetten, M. José-Yacamán, *ACS Nano* **2016**, *10*, 188.
- [21] K. McNamara, S. A. M. Tofail, *Phys. Chem. Chem. Phys.* **2015**, *17*, 27981.
- [22] C. K. Narula, X. Yang, C. Li, A. R. Lupini, S. J. Pennycook, *J. Phys. Chem. C* **2015**, *119*, 25114.
- [23] V. Petkov, B. Prasai, Y. Ren, S. Shan, J. Luo, P. Joseph, C.-J. Zhong, *Nanoscale* **2014**, *6*, 10048.
- [24] M. Auffan, J. Rose, J.-Y. Bottero, G. V. Lowry, J.-P. Jolivet, M. R. Wiesner, *Nat. Nanotechnol.* **2009**, *4*, 634.
- [25] W. Zimmerli, *J. Intern. Med.* **2014**, *276*, 111.
- [26] D. Campoccia, L. Montanaro, C. R. Arciola, *Biomaterials* **2006**, *27*, 2331.
- [27] M. Hans, A. Erbe, S. Mathews, Y. Chen, M. Solioz, F. Mücklich, *Langmuir* **2013**, *29*, 16160.

- [28] N. Matsumoto, K. Sato, K. Yoshida, K. Hashimoto, Y. Toda, *Acta Biomater.* **2009**, *5*, 3157.
- [29] G. Grass, C. Rensing, M. Solioz, *Appl. Environ. Microbiol.* **2011**, *77*, 1541.
- [30] W. K. Jung, H. C. Koo, K. W. Kim, S. Shin, S. H. Kim, Y. H. Park, *Appl. Environ. Microbiol.* **2008**, *74*, 2171.
- [31] V. De Matteis, M. A. Malvindi, A. Galeone, V. Brunetti, E. De Luca, S. Kote, P. Kshirsagar, S. Sabella, G. Bardi, P. P. Pompa, *Nanomed. Nanotechnol. Biol. Med.* **2015**, *11*, 731.
- [32] S. Kittler, C. Greulich, J. Diendorf, M. Köller, M. Epple, *Chem. Mater.* **2010**, *22*, 4548.
- [33] A. M. Königs, H.-C. Flemming, J. Wingender, *Front. Microbiol.* **2015**, *6*.
- [34] J. Liu, D. A. Sonshine, S. Shervani, R. H. Hurt, *ACS Nano* **2010**, *4*, 6903.
- [35] J. Helmlinger, C. Sengstock, C. Groß-Heitfeld, C. Mayer, T. A. Schildhauer, M. Köller, M. Epple, *RSC Adv.* **2016**, *6*, 18490.
- [36] D. P. Dowling, A. J. Betts, C. Pope, M. L. McConnell, R. Eloy, M. N. Arnaud, *Surf. Coat. Technol.* **2003**, *163-164*, 637.
- [37] M. Köller, P. Bellova, S. M. Javid, Y. Motemani, C. Khare, C. Sengstock, K. Tschulik, T. A. Schildhauer, A. Ludwig, *Mater. Sci. Eng. C* **2017**, *74*, 536.
- [38] M. Köller, C. Sengstock, Y. Motemani, C. Khare, P. J. S. Buenconsejo, J. Geukes, T. A. Schildhauer, A. Ludwig, *Mater. Sci. Eng. C* **2015**, *46*, 276.
- [39] C. Dhand, N. Dwivedi, X. J. Loh, A. N. Jie Ying, N. K. Verma, R. W. Beuerman, R. Lakshminarayanan, S. Ramakrishna, *RSC Adv.* **2015**, *5*, 105003.
- [40] L. Polavarapu, S. Mourdikoudis, I. Pastoriza-Santos, J. Pérez-Juste, *CrystEngComm* **2015**, *17*, 3727.

- [41] G. Schmid (ed.), *Nanoparticles - From Theory to Application*, 2nd ed., WILEY-VCH Verlag GmbH & Co. KGaA, Weinheim (Germany), **2010**.
- [42] K. D. Gilroy, J. Puibasset, M. Vara, Y. Xia, *Angew. Chem.* **2017**, *129*, 8773.
- [43] Y. Xia, X. Xia, H.-C. Peng, *J. Am. Chem. Soc.* **2015**, *137*, 7947.
- [44] Y. Xia, X. Xia, Y. Wang, S. Xie, *MRS Bull.* **2013**, *38*, 335.
- [45] H. Dong, Y. C. Chen, C. Feldmann, *Green Chem.* **2015**, *17*, 4107.
- [46] D. Zhang, B. Gökce, S. Barcikowski, *Chem. Rev.* **2017**, *117*, 3990.
- [47] S. I. Sanchez, M. W. Small, J.-m. Zuo, R. G. Nuzzo, *J. Am. Chem. Soc.* **2009**, *131*, 8683.
- [48] L. Zhang, Z. Xie, J. Gong, *Chem. Soc. Rev.* **2016**, *45*, 3916.
- [49] L. Zhang, J. Zhang, Q. Kuang, S. Xie, Z. Jiang, Z. Xie, L. Zheng, *J. Am. Chem. Soc.* **2011**, *133*, 17114.
- [50] P. Kunal, H. Li, B. L. Dewing, L. Zhang, K. Jarvis, G. Henkelman, S. M. Humphrey, *ACS Catalysis* **2016**, *6*, 4882.
- [51] C. Hahn, D. N. Abram, H. A. Hansen, T. Hatsukade, A. Jackson, N. C. Johnson, T. R. Hellstern, K. P. Kuhl, E. R. Cave, J. T. Feaster, T. F. Jaramillo, *J. Mater. Chem. A* **2015**, *3*, 20185.
- [52] J. Li, Y. Zheng, J. Zeng, Y. Xia, *Chem. Eur. J.* **2012**, *18*, 8150.
- [53] C. J. DeSantis, A. C. Sue, M. M. Bower, S. E. Skrabalak, *ACS Nano* **2012**, *6*, 2617.
- [54] A. Spitale, M. A. Perez, S. Mejía-Rosales, M. J. Yacamán, M. M. Mariscal, *Phys. Chem. Chem. Phys.* **2015**, *17*, 28060.

- [55] A. Gopalan, D. Ragupathy, H. T. Kim, K. M. Manesh, K. P. Lee, *Spectrochim. Acta A Mol. Biomol. Spectrosc.* **2009**, *74*, 678.
- [56] B. Lim, H. Kobayashi, T. Yu, J. Wang, M. J. Kim, Z.-Y. Li, M. Rycenga, Y. Xia, *J. Am. Chem. Soc.* **2010**, *132*, 2506.
- [57] V. Mazumder, M. Chi, K. L. More, S. Sun, *Angew. Chem. Int. Ed. Engl.* **2010**, *49*, 9368.
- [58] C. Zhu, J. Zeng, J. Tao, M. C. Johnson, I. Schmidt-Krey, L. Blubaugh, Y. Zhu, Z. Gu, Y. Xia, *J. Am. Chem. Soc.* **2012**, *134*, 15822.
- [59] J. Zeng, C. Zhu, J. Tao, M. Jin, H. Zhang, Z.-Y. Li, Y. Zhu, Y. Xia, *Angew. Chem. Int. Ed. Engl.* **2012**, *51*, 2354.
- [60] Y. Yang, J. Liu, Z.-W. Fu, D. Qin, *J. Am. Chem. Soc.* **2014**, *136*, 8153.
- [61] S. Xie, S.-I. Choi, N. Lu, L. T. Roling, J. A. Herron, L. Zhang, J. Park, J. Wang, M. J. Kim, Z. Xie, M. Mavrikakis, Y. Xia, *Nano Lett.* **2014**, *14*, 3570.
- [62] J. Li, J. Liu, Y. Yang, D. Qin, *J. Am. Chem. Soc.* **2015**, *137*, 7039.
- [63] D. Sun, P. Li, B. Yang, Y. Xu, J. Huang, Q. Li, *RSC Adv.* **2016**, *6*, 105940.
- [64] H. Kahri, M. Sevim, Ö. Metin, *Nano Res.* **2017**, *10*, 1627.
- [65] S. Zhang, Ö. Metin, D. Su, S. Sun, *Angew. Chem. Int. Ed. Engl.* **2013**, *52*, 3681.
- [66] K. Kim, K. L. Kim, K. S. Shin, *J. Phys. Chem. C* **2011**, *115*, 14844.
- [67] E. A. Bakr, H. G. El-Attar, M. A. Salem, *Res. Chem. Intermed.* **2018**.
- [68] H. Keskinen, J. M. Mäkelä, M. Vippola, M. Nurminen, J. Liimatainen, T. Lepistö, J. Keskinen, *J. Mater. Res.* **2004**, *19*, 1544.
- [69] W. G. Kreyling, M. Semmler-Behnke, Q. Chaudhry, *Nano Today* **2010**, *5*, 165.

- [70] J. Bridges, K. Dawson, W. de Jong, T. Jung, A. Proykova, Q. Chaudhry, R. Duncan, E. Gaffet, K. Jensen, W. Kreyling, B. Quinn, *Scientific basis for the definition of the term "nanomaterial"*, European Commission, **2012**.
- [71] T. Cosgrove, *Colloid Science: Principles, methods and applications*, 2nd ed., John Wiley & Sons Ltd., **2010**.
- [72] G. J. Lauth, J. Kowalczyk, *Einführung in die Physik und Chemie der Grenzflächen und Kolloide (german)*, Springer-Verlag GmbH, Berlin (Germany), **2016**.
- [73] G. Schmid (ed.), *Nanoparticles: From Theory to Application*, 2nd ed., Wiley-VCH Verlag GmbH & Co. KGaA, Weinheim (Germany), **2010**.
- [74] R. B. Gupta, U. B. Kompella (ed.), *Nanoparticle Technology for Drug Delivery, Vol. 159*, Taylor & Francis Group, LLC, New York, **2006**.
- [75] V. Amendola, S. Polizzi, M. Meneghetti, *J. Phys. Chem. B* **2006**, *110*, 7232.
- [76] S. Barcikowski, G. Compagnini, *Phys. Chem. Chem. Phys.* **2013**, *15*, 3022.
- [77] N. Hastrup, G. M. O'Connor, *Physics Procedia* **2011**, *12*, 46.
- [78] B. Derjaguin, L. D. Landau, *Acta Physicochem U.R.S.S.* **1941**, *14*, 633.
- [79] E. W. Verwey, J. T. G. Overbeek, *Theory of Stability of Lyophobic Colloids*, Elsevier, Amsterdam, **1948**.
- [80] T. F. Tadros (ed.), *Colloid Stability - The Role of Surface Forces - Part I*, WILEY-VCH Verlag GmbH & Co. KGaA Weinheim (Germany), **2007**.
- [81] V. K. LaMer, R. H. Dinegar, *J. Am. Chem. Soc.* **1950**, *72*, 4847.

- [82] E. M. Zaiser, V. K. LaMer, *J. Colloid Sci.* **1948**, *3*, 571.
- [83] S. K. Ghosh, T. Pal, *Chem. Rev.* **2007**, *107*, 4797.
- [84] K. L. Kelly, E. Coronado, L. L. Zhao, G. C. Schatz, *J. Phys. Chem. B* **2003**, *107*, 668.
- [85] E. Le Ru, P. Etchegoin, *Principles of Surface Enhanced Raman Spectroscopy and related plasmonics effect*, Elsevier, Amsterdam (Netherlands), **2009**.
- [86] S. Schlücker (ed.), *Surface Enhanced Raman Spectroscopy - Analytical, Biophysical and Life Science Applications*, WILEY-VCH GmbH & Co. KGaA, Weinheim (Germany), **2011**.
- [87] P. Hou, H. Liu, J. Li, J. Yang, *CrystEngComm* **2015**, *17*, 1826.
- [88] K. Kamata, Y. Lu, Y. Xia, *J. Am. Chem. Soc.* **2003**, *125*, 2384.
- [89] S. Kumar-Krishnan, M. Estevez-González, R. Pérez, R. Esparza, M. Meyyappan, *RSC Adv.* **2017**, *7*, 27170.
- [90] M. Kamundi, L. Bromberg, E. Fey, C. Mitchell, M. Fayette, N. Dimitrov, *J. Phys. Chem. C* **2012**, *116*, 14123.
- [91] S. Ristig, O. Prymak, K. Loza, M. Gocyla, W. Meyer-Zaika, M. Heggen, D. Raabe, M. Epple, *J. Mater. Chem. B* **2015**, *3*, 4654.
- [92] K. K. Nanda, *Pramana* **2009**, *72*, 617.
- [93] W. Schärfl, *Light scattering from polymer solutions and nanoparticle dispersions*, Springer-Verlag, Berlin (Germany), **2007**.
- [94] H. G. Zachmann, A. Jüngel, *Mathematik für Chemiker (german)*, Vol. 6, WILEY-VCH Verlag GmbH & Co. KGaA, Weinheim (Germany), **2007**.

- [95] D. Mahl, J. Diendorf, W. Meyer-Zaika, M. Epple, *Colloids Surf. A* **2011**, 377, 386.
- [96] S. Banerjee, K. Loza, W. Meyer-Zaika, O. Prymak, M. Epple, *Chem. Mater.* **2014**, 26, 951.
- [97] N. Kläntschi, P. Lienemann, P. Richner, H. Vonmont, *Elementanalytik - Instrumenteller Nachweis und Bestimmung von Elementen und deren Verbindungen*, Spektrum Akad. Verl., Heidelberg / Berlin / Oxford, **1996**.
- [98] S. Amelinckx, D. v. Dyck, J. v. Landyut, G. v. Tendeloo (ed.), *Electron Microscopy - Principles and Fundamentals*, VCH Verlagsgesellschaft mbH, Weinheim (Germany), **1997**.
- [99] A. Kovács, R. Schierholz, K. Tillmann, *Journal of large-scale research facilities JLSRF* **2016**, 2, A43.
- [100] A. Thust, J. Barthel, K. Tillmann, *Journal of large-scale research facilities JLSRF* **2016**, 2, A41.
- [101] M. Heggen, M. Luysberg, K. Tillmann, *Journal of large-scale research facilities JLSRF* **2016**, 2, A42.
- [102] M. T. Otten, *J. Electron Microsc. Techn.* **1991**, 17, 221.
- [103] V. K. Pecharsky, P. Y. Zavalij, *Fundamentals of Powder Diffraction and Structural Characterization of Materials*, Springer Science+Business Media, Inc., **2003**.
- [104] P. Scherrer, *Nachr. Ges. Wiss. Göttingen, Math.-Phys. Kl.* **1918**, 2, 98.
- [105] A. R. Stokes, A. J. C. Wilson, *Proc. Phys. Soc. London* **1944**, 56, 174.
- [106] M. Harada, S. Takahashi, *J. Colloid Interface Sci.* **2008**, 325, 1.

- [107] Y. Zhang, J. Yu, H. Niu, H. Liu, *J. Colloid Interface Sci.* **2007**, *313*, 503.
- [108] X. Yan, H. Liu, K. Y. Liew, *J. Mater. Chem.* **2001**, *11*, 3387.
- [109] S. H. Joo, J. Y. Park, J. R. Renzas, D. R. Butcher, W. Huang, G. A. Somorjai, *Nano Lett.* **2010**, *10*, 2709.
- [110] J. Shen, X. Yin, D. Karpuzov, N. Semagina, *Catal. Sci. Technol.* **2013**, *3*, 208.
- [111] C. Pan, K. Pelzer, K. Philippot, B. Chaudret, F. Dassenoy, P. Lecante, M.-J. Casanove, *J. Am. Chem. Soc.* **2001**, *123*, 7584.
- [112] N. G. García-Peña, R. Redón, A. Herrera-Gomez, A. L. Fernández-Osorio, M. Bravo-Sanchez, G. Gomez-Sosa, *Appl. Surf. Sci.* **2015**, *340*, 25.
- [113] H. Fissan, S. Ristig, H. Kaminski, C. Asbach, M. Epple, *Anal. Methods* **2014**, *6*, 7324.
- [114] A. G. F. Shoair, *J. Mol. Liq.* **2015**, *206*, 68.
- [115] J. A. Creighton, D. G. Eadon, *J. Chem. Soc., Faraday Trans.* **1991**, *87*, 3881.
- [116] B. Kumar, G. Kaur, S. B. Rai, *Spectrochim. Acta A Mol. Biomol. Spectrosc.* **2017**, *187*, 75.
- [117] J. Kowalonek, H. Kaczmarek, *Eur. Polym. J.* **2010**, *46*, 345.
- [118] X.-f. Qian, J. Yin, S. Feng, S.-h. Liu, Z.-k. Zhu, *J. Mater. Chem.* **2001**, *11*, 2504.
- [119] M. Ravi, S. Bhavani, K. Kiran Kumar, V. V. R. Narasimaha Rao, *Solid State Sci.* **2013**, *19*, 85.
- [120] J.-F. Zhu, G.-H. Tao, H.-Y. Liu, L. He, Q.-H. Sun, H.-C. Liu, *Green Chem.* **2014**, *16*, 2664.

- [121] American Mineralogist Crystal Structure Database (AMCSD), AMCSD 0020237 (Ru)
- [122] International Centre of Diffraction Data (ICDD), Powder Diffraction File (PDF) 00-034-0427 (LaB₆)
- [123] International Centre of Diffraction Data (ICDD), Powder Diffraction File (PDF) 00-006-0663 (Ru)
- [124] H. P. Klug, L. E. Alexander, *X-ray diffraction procedures for polycrystalline and amorphous materials*, Wiley Interscience, New York, **1974**.
- [125] A. J. Biacchi, R. E. Schaak, *ACS Nano* **2011**, *5*, 8089.
- [126] S. Xie, X. Y. Liu, Y. Xia, *Nano Res.* **2015**, *8*, 82.
- [127] E. Ramírez-Meneses, K. Philippot, M. A. Domínguez-Crespo, M. Ibrahim, I. Betancourt, A. M. Torres-Huerta, A. Ezeta-Mejia, *J. Mater. Sci.* **2018**, *53*, 8933.
- [128] M. Marín-Almazo, J. A. Ascencio, M. Pérez-Álvarez, C. Gutiérrez-Wing, M. José-Yacamán, *Microchem. J.* **2005**, *81*, 133.
- [129] W. Alsalahi, W. Tylus, A. M. Trzeciak, *ChemCatChem* **2018**, *10*, 2051.
- [130] F. Durap, M. Zahmakıran, S. Özkar, *Appl. Catal. A* **2009**, *369*, 53.
- [131] W. C. Wolsey, C. A. Reynolds, J. Kleinberg, *Inorg. Chem.* **1963**, *2*, 463.
- [132] M. H. Abou_Taleb, *J. Appl. Polym. Sci.* **2009**, *114*, 1202.
- [133] M. T. Razzak, Zainuddin, Erizal, S. P. Dewi, H. Lely, E. Taty, Sukirno, *Radiat. Phys. Chem.* **1999**, *55*, 153.
- [134] W. H. Eisa, E. Al-Ashkar, S. M. El-Mossalamy, S. S. M. Ali, *Chem. Phys. Lett.* **2016**, *651*, 28.

- [135] International Centre of Diffraction Data (ICDD), Powder Diffraction File (PDF) 00-005-0685 (Rh)
- [136] International Centre of Diffraction Data (ICDD), Powder Diffraction File (PDF) 00-005-0628 (Halite, NaCl)
- [137] American Mineralogist Crystal Structure Database (AMCSD), AMCSD 0011159 (Rh)
- [138] I. Saldan, Y. Semenyuk, I. Marchuk, O. Reshetnyak, *J. Mater. Sci.* **2015**, *50*, 2337.
- [139] A. Chen, C. Ostrom, *Chem. Rev.* **2015**, *115*, 11999.
- [140] S. C. Jung, Y.-K. Park, H.-Y. Jung, S. C. Kim, *J. Nanosci. Nanotechnol.* **2017**, *17*, 2833.
- [141] W. Lu, B. Wang, K. Wang, X. Wang, J. G. Hou, *Langmuir* **2003**, *19*, 5887.
- [142] S.-W. Kim, J. Park, Y. Jang, Y. Chung, S. Hwang, T. Hyeon, Y. W. Kim, *Nano Lett.* **2003**, *3*, 1289.
- [143] N. Viet Long, N. Duc Chien, H. Hirohito, O. Michitaka, H. Tomokatsu, N. Masayuki, *Adv. Nat. Sci. Nanosci. Nanotechnol.* **2010**, *1*, 035012.
- [144] J. D. Senra, L. F. B. Malta, R. C. Michel, Y. Cordeiro, R. A. Simão, A. B. C. Simas, L. C. S. Aguiar, *J. Mater. Chem.* **2011**, *21*, 13516.
- [145] M. Tsuji, K. Ikedo, M. Matsunaga, K. Uto, *CrystEngComm* **2012**, *14*, 3411.
- [146] L. I. Elding, L. F. Olsson, *J. Phys. Chem.* **1978**, *82*, 69.
- [147] M. Benkhaled, S. Morin, C. Pichon, C. Thomazeau, C. Verdon, D. Uzio, *Appl. Catal. A* **2006**, *312*, 1.

- [148] International Centre of Diffraction Data (ICDD), Powder Diffraction File (PDF) 00-046-1043 (Pd)
- [149] American Mineralogist Crystal Structure Database (AMCSD), AMCSD 0014146 (Pd)
- [150] J. Zeng, Y. Zheng, M. Rycenga, J. Tao, Z.-Y. Li, Q. Zhang, Y. Zhu, Y. Xia, *J. Am. Chem. Soc.* **2010**, *132*, 8552.
- [151] Y. Sun, *Chem. Soc. Rev.* **2013**, *42*, 2497.
- [152] D. Aherne, D. M. Ledwith, M. Gara, J. M. Kelly, *Adv. Funct. Mater.* **2008**, *18*, 2005.
- [153] S. H. Im, Y. T. Lee, B. Wiley, Y. Xia, *Angew. Chem. Int. Ed. Engl.* **2005**, *44*, 2154.
- [154] W. M. Schuette, W. E. Buhro, *ACS Nano* **2013**, *7*, 3844.
- [155] Y. Sun, B. Mayers, T. Herricks, Y. Xia, *Nano Lett.* **2003**, *3*, 955.
- [156] Y. Sun, B. Mayers, Y. Xia, *Adv. Mater.* **2003**, *15*, 641.
- [157] Y. Sun, Y. Xia, *Science* **2002**, *298*, 2176.
- [158] B. Wiley, Y. Sun, B. Mayers, Y. Xia, *Chem. Eur. J.* **2005**, *11*, 454.
- [159] A. V. Girão, P. C. Pinheiro, M. Ferro, T. Trindade, *RSC Adv.* **2017**, *7*, 15944.
- [160] C. M. Gonzalez, Y. Liu, J. C. Scaiano, *J. Phys. Chem. C* **2009**, *113*, 11861.
- [161] J. Huang, Y. Zhu, C. Liu, Y. Zhao, Z. Liu, M. N. Hedhili, A. Fratalocchi, Y. Han, *Small* **2015**, *11*, 5214.
- [162] Z. Ren, X. Li, J. Guo, R. Wang, Y. Wu, M. Zhang, C. Li, Q. Han, J. Dong, H. Zheng, *Opt. Comm.* **2015**, *357*, 156.

- [163] P. E. J. Saloga, C. Kästner, A. F. Thünemann, *Langmuir* **2018**, *34*, 147.
- [164] J. Mack, J. R. Bolton, *J. Photochem. Photobiol. A* **1999**, *128*, 1.
- [165] K. O. Shittu, O. Ihebunna, *Adv. Nat. Sci. Nanosci. Nanotechnol.* **2017**, *8*, 045003.
- [166] H. J. Lee, M. A. Do, E. J. Kim, J. H. Yeum, H. D. Ghim, J. H. Choi, *Adv. Mater. Res.* **2008**, *47-50*, 1080.
- [167] S. W. Chaikin, W. G. Brown, *J. Am. Chem. Soc.* **1949**, *71*, 122.
- [168] H. I. Schlesinger, H. C. Brown, A. E. Finholt, J. R. Gilbreath, H. R. Hoekstra, E. K. Hyde, *J. Am. Chem. Soc.* **1953**, *75*, 215.
- [169] International Centre of Diffraction Data (ICDD), Powder Diffraction File (PDF) 00-004-0783 (Ag)
- [170] V. Bansal, V. Li, A. P. O'Mullane, S. K. Bhargava, *CrystEngComm* **2010**, *12*, 4280.
- [171] B. Wang, G. T. Fei, Y. Zhou, B. Wu, X. Zhu, L. Zhang, *Cryst. Growth Des.* **2008**, *8*, 3073.
- [172] American Mineralogist Crystal Structure Database (AMCSD), AMCSD 0013118 (Ag fcc)
- [173] American Mineralogist Crystal Structure Database (AMCSD), AMCSD 0018575 (Ag hcp)
- [174] W. H. Qi, M. P. Wang, *J. Nanopart. Res.* **2005**, *7*, 51.
- [175] Y. Zhao, J. Zhang, *J. Appl. Crystallogr.* **2008**, *41*, 1095.
- [176] A. Pitto-Barry, L. M. A. Perdigao, M. Walker, J. Lawrence, G. Costantini, P. J. Sadler, N. P. E. Barry, *Dalton Trans.* **2015**, *44*, 20308.

- [177] J. Krämer, E. Redel, R. Thomann, C. Janiak, *Organometallics* **2008**, *27*, 1976.
- [178] C. Vollmer, C. Janiak, *Coord. Chem. Rev.* **2011**, *255*, 2039.
- [179] E. Borja-Arco, O. Jiménez-Sandoval, J. Escalante-García, L. Magallón-Cacho, P. J. Sebastian, *Int. J. Electrochem.* **2011**, *2011*, 8.
- [180] E. M. Glebov, I. P. Pozdnyakov, S. G. Matveeva, A. A. Melnikov, S. V. Chekalin, M. V. Rogozina, V. V. Yudanov, V. P. Grivin, V. F. Plyusnin, *Photochem. Photobiol. Sci.* **2017**, *16*, 220.
- [181] O. V. Rudnitskaya, E. K. Kultyshkina, E. V. Dobrokhotova, V. S. Podvoyskaya, P. V. Dorovatovskii, V. A. Lazarenko, Y. V. Zubavichus, V. N. Khrustalev, *Polyhedron* **2017**, *134*, 114.
- [182] American Mineralogist Crystal Structure Database (AMCSD), AMCSD 0016737 (Os)
- [183] International Centre of Diffraction Data (ICDD), Powder Diffraction File (PDF) 00-006-0662 (Os)
- [184] A. L. Brown, H. Winter, A. M. Goforth, G. Sahay, C. Sun, *Nanoscale Res. Lett.* **2018**, *13*, 208.
- [185] M. Cui, Y. Zhao, C. Wang, Q. Song, *Microchim. Acta* **2016**, *183*, 2047.
- [186] V. W. Faria, M. F. Brunelli, C. W. Scheeren, *RSC Adv.* **2015**, *5*, 84920.
- [187] G. S. Fonseca, G. Machado, S. R. Teixeira, G. H. Fecher, J. Morais, M. C. M. Alves, J. Dupont, *J. Colloid Interface Sci.* **2006**, *301*, 193.
- [188] C. K. Yee, R. Jordan, A. Ulman, H. White, A. King, M. Rafailovich, J. Sokolov, *Langmuir* **1999**, *15*, 3486.
- [189] F. Bonet, V. Delmas, S. Grugeon, R. Herrera Urbina, P. Y. Silvert, K. Tekaia-Elhsissen, *Nanostruct. Mater.* **1999**, *11*, 1277.

- [190] F. Scholz, C. J. Pickett (ed.), *Inorganic Electrochemistry, Vol. 7a*, John Wiley & Sons, **2006**.
- [191] P. Borja, C. Vicent, M. Baya, H. García, J. A. Mata, *Green Chem.* **2018**, *20*, 4094.
- [192] M. Dusselier, P. Van Wouwe, A. Dewaele, E. Makshina, B. F. Sels, *Energy Environ. Sci.* **2013**, *6*, 1415.
- [193] C. B. Rasrendra, I. G. B. N. Makertihartha, S. Adisasmito, H. J. Heeres, *Top. Catal.* **2010**, *53*, 1241.
- [194] Z. Zhang, G. W. Huber, *Chem. Soc. Rev.* **2018**, *47*, 1351.
- [195] H. Lodish, A. Berk, C. A. Kaiser, M. Krieger, A. Bretscher, H. Ploegh, A. Amon, K. C. Martin, *Molecular Cell Biology*, W. H. Freeman and Company, New York, **2016**.
- [196] Y. Zhao, E. A. Hernandez-Pagan, N. M. Vargas-Barbosa, J. L. Dysart, T. E. Mallouk, *J. Phys. Chem. Lett.* **2011**, *2*, 402.
- [197] X.-M. Wang, J.-M. Hu, J.-Q. Zhang, *Electrochim. Acta* **2010**, *55*, 4587.
- [198] I. A. Poulsen, C. S. Garner, *J. Am. Chem. Soc.* **1962**, *84*, 2032.
- [199] S. R. Mellsop, A. Gardiner, A. T. Marshall, *Electrocatal.* **2016**, *7*, 226.
- [200] J. C. Chang, C. S. Garner, *Inorg. Chem.* **1965**, *4*, 209.
- [201] G. Li, S. Li, M. Xiao, J. Ge, C. Liu, W. Xing, *Nanoscale* **2017**, *9*, 9291.
- [202] International Centre of Diffraction Data (ICDD), Powder Diffraction File (PDF) 00-046-1044 (Ir)

- [203] American Mineralogist Crystal Structure Database (AMCSD), AMCSD 0011147 (Ir)
- [204] Y. Kang, J. B. Pyo, X. Ye, R. E. Diaz, T. R. Gordon, E. A. Stach, C. B. Murray, *ACS Nano* **2013**, 7, 645.
- [205] C. Salzemann, F. Kameche, A.-T. Ngo, P. Andreatza, M. Calatayud, C. Petit, *Faraday Discuss.* **2015**, 181, 19.
- [206] H. Nagao, M. Ichiji, I. Hirasawa, *Chem. Eng. Technol.* **2017**, 40, 1242.
- [207] B. Escobar Morales, S. A. Gamboa, U. Pal, R. Guardián, D. Acosta, C. Magaña, X. Mathew, *Int. J. Hydrogen Energy* **2010**, 35, 4215.
- [208] C. Wang, H. Daimon, T. Onodera, T. Koda, S. Sun, *Angew. Chem. Int. Ed. Engl.* **2008**, 47, 3588.
- [209] V.-L. Nguyen, M. Ohtaki, V. N. Ngo, M.-T. Cao, M. Nogami, *Adv. Nat. Sci. Nanosci. Nanotechnol.* **2012**, 3, 025005.
- [210] H. Song, F. Kim, S. Connor, G. A. Somorjai, P. Yang, *J. Phys. Chem. B* **2005**, 109, 188.
- [211] N. Viet-Long, O. Michitaka, N. Van Nong, C. Minh-Thi, N. Masayuki, *Adv. Nat. Sci. Nanosci. Nanotechnol.* **2012**, 3, 025005.
- [212] D. S. Shen, D. Philip, J. Mathew, *Spectrochim. Acta A Mol. Biomol. Spectrosc.* **2013**, 114, 267.
- [213] C. K. Jørgensen, *Mol. Phys.* **1959**, 2, 309.
- [214] R. M. Garcia, Y. Song, R. M. Dorin, H. Wang, A. M. Moreno, Y.-B. Jiang, Y. Tian, Y. Qiu, C. J. Medforth, E. N. Coker, F. van Swol, J. E. Miller, J. A. Shelnut, *Phys. Chem. Chem. Phys.* **2011**, 13, 4846.

- [215] International Centre of Diffraction Data (ICDD), Powder Diffraction File (PDF) 00-001-1194 (Pt)
- [216] American Mineralogist Crystal Structure Database (AMCSD), AMCSD 0011157 (Pt)
- [217] D. Mahl, J. Diendorf, S. Ristig, C. Greulich, Z.-A. Li, M. Farle, M. Köller, M. Epple, *J. Nanopart. Res.* **2012**, *14*, 1153.
- [218] J. Piella, N. G. Bastús, V. Puntès, *Chem. Mater.* **2016**, *28*, 1066.
- [219] Y. Shang, C. Min, J. Hu, T. Wang, H. Liu, Y. Hu, *Solid State Sci.* **2013**, *15*, 17.
- [220] X. Liang, Z.-j. Wang, C.-j. Liu, *Nanoscale Res. Lett.* **2009**, *5*, 124.
- [221] É. G. A. Miranda, A. Tofanello, A. M. M. Brito, D. M. Lopes, L. J. C. Albuquerque, C. E. de Castro, F. N. Costa, F. C. Giacomelli, F. F. Ferreira, J. C. Araújo-Chaves, I. L. Nantes, *Front. Chem.* **2016**, *4*, 13.
- [222] International Centre of Diffraction Data (ICDD), Powder Diffraction File (PDF) 00-004-0784 (Au)
- [223] American Mineralogist Crystal Structure Database (AMCSD), AMCSD 0013108 (Au)
- [224] A. Rostek, D. Mahl, M. Epple, *J. Nanopart. Res.* **2011**, *13*, 4809.
- [225] S. Ino, *J. Phys. Soc. Jpn.* **1969**, *27*, 941.
- [226] F. Baletto, R. Ferrando, *Rev. Mod. Phys.* **2005**, *77*, 371.
- [227] D. Pohl, A. Surrey, L. Schultz, B. Rellinghaus, *Appl. Phys. Lett.* **2012**, *101*, 263105.
- [228] A. Rostek, M. Breisch, K. Pappert, K. Loza, M. Heggen, M. Köller, C. Sengstock, M. Epple, *Beilstein J. Nanotechnol.* **2018**, *9*, 2763.

- [229] S. Ahlberg, A. Antonopoulos, J. Diendorf, R. Dringen, M. Epple, R. Flöck, W. Goedecke, C. Graf, N. Haberl, J. Helmlinger, F. Herzog, F. Heuer, S. Hirn, C. Johannes, S. Kittler, M. Köller, K. Korn, W. G. Kreyling, F. Krombach, J. Lademann, K. Loza, E. M. Luther, M. Malissek, M. C. Meinke, D. Nordmeyer, A. Pailliant, J. Raabe, F. Rancan, B. Rothen-Rutishauser, E. Rühl, C. Schleh, A. Seibel, C. Sengstock, L. Treuel, A. Vogt, K. Weber, R. Zellner, *Beilstein J. Nanotechnol.* **2014**, *5*, 1944.
- [230] S. Chernousova, M. Epple, *Angew. Chem. Int. Ed. Engl.* **2013**, *52*, 1636.
- [231] K. Loza, J. Diendorf, C. Sengstock, L. Ruiz-Gonzalez, J. M. Gonzalez-Calbet, M. Vallet-Regi, M. Köller, M. Epple, *J. Mater. Chem. B* **2014**, *2*, 1634.
- [232] K. Loza, C. Sengstock, S. Chernousova, M. Köller, M. Epple, *RSC Adv.* **2014**, *4*, 35290.
- [233] C. Sengstock, J. Diendorf, M. Epple, T. A. Schildhauer, M. Köller, *Beilstein J. Nanotechnol.* **2014**, *5*, 2058.
- [234] X. Li, T. Odoom-Wubah, J. Huang, *RSC Adv.* **2018**, *8*, 30340.
- [235] K. E. MacArthur, T. J. A. Slater, S. J. Haigh, D. Ozkaya, P. D. Nellist, S. Lozano-Perez, *Microsc. Microanal.* **2016**, *22*, 71.
- [236] R. Ruer, *Z. Anorg. Chem.* **1906**, *51*, 391.
- [237] E. Raub, G. Vorwag, *Z. Metallkd.* **1955**, *46*, 513.
- [238] H. Okamoto, T. B. Massalski, *Bull. Alloy Phase Diagr.* **1985**, *6*, 229.
- [239] A. Maeland, T. B. Flanagan, *Can. J. Phys.* **1964**, *42*, 2364.
- [240] V. G. Kuznetsov, *Struct. Rep.* **1946**, *10*, 54.
- [241] S. Holgersson, E. Sedström, *Ann. Phys.* **1924**, *380*, 143.

- [242] A. Rostek, M. Breisch, K. Loza, P. R. A. F. Garcia, C. L. P. Oliveira, O. Prymak, M. Heggen, M. Köller, C. Sengstock, M. Epple, *ChemistrySelect* **2018**, *3*, 4994.
- [243] A. F. Holleman, N. Wiberg, *Lehrbuch der Anorganischen Chemie (german)*, Vol. 102, Walter de Gruyter & Co., Berlin, **2007**.
- [244] H. Jing, H. Wang, *Chem. Mater.* **2015**, *27*, 2172.
- [245] R. N. Goldberg, L. G. Hepler, *Chem. Rev.* **1968**, *68*, 229.
- [246] M. Tsuji, T. Kidera, A. Yajima, M. Hamasaki, M. Hattori, T. Tsuji, H. Kawazumi, *CrystEngComm* **2014**, *16*, 2684.
- [247] R. T. Downs, M. Hall-Wallace, *Am. Mineral.* **2003**, *88*, 247.
- [248] S. Gražulis, D. Chateigner, R. T. Downs, A. F. T. Yokochi, M. Quirós, L. Lutterotti, E. Manakova, J. Butkus, P. Moeck, A. Le Bail, *J. Appl. Crystallogr.* **2009**, *42*, 726.
- [249] P. C. Heinrich, M. Müller, L. Graeve (ed.), *Löffler/Petrides Biochemie and Pathobiochemie (german)*, Vol. 9, Springer-Verlag GmbH, Berlin (Germany), **2014**.
- [250] H. Wang, X. Qiao, J. Chen, X. Wang, S. Ding, *Mater. Chem. Phys.* **2005**, *94*, 449.
- [251] A. C. Kuyper, *J. Am. Chem. Soc.* **1933**, *55*, 1722.
- [252] J. Turkevich, P. C. Stevenson, J. Hillier, *Discuss. Faraday Soc.* **1951**, *11*, 55.
- [253] T. Ahmad, *J. Nanotechnol.* **2014**, *2014*, 11.
- [254] N. G. Bastús, F. Merkoçi, J. Piella, V. Puntès, *Chem. Mater.* **2014**, *26*, 2836.

- [255] K. Ranoszek-Soliwoda, E. Tomaszewska, E. Socha, P. Krzyczmonik, A. Ignaczak, P. Orlowski, M. Krzyzowska, G. Celichowski, J. Grobelny, *J. Nanopart. Res.* **2017**, *19*, 273.
- [256] A. Abedini, A. A. A. Bakar, F. Larki, P. S. Menon, M. S. Islam, S. Shaari, *Nanoscale Res. Lett.* **2016**, *11*, 287.
- [257] V. Pareek, A. Bhargava, R. Gupta, N. Jain, J. Panwar, *Adv. Sci. Eng. Med.* **2017**, *9*, 527.
- [258] M. Chandra, P. K. Das, *Int. J. Green Nanotechnol. Phys. Chem.* **2009**, *1*, P10.
- [259] P. Dauthal, M. Mukhopadhyay, *Ind. Eng. Chem. Res.* **2016**, *55*, 9557.
- [260] S. Barcikowski, A. Menéndez-Manjón, B. Chichkov, M. Brikas, G. Račiukaitis, *Appl. Phys. Lett.* **2007**, *91*, 083113.
- [261] E. G. Gamaly, A. V. Rode, B. Luther-Davies, V. T. Tikhonchuk, *Phys. Plasmas* **2002**, *9*, 949.
- [262] A. V. Kabashin, M. Meunier, *J. Appl. Phys.* **2003**, *94*, 7941.
- [263] Y. Xia, K. D. Gilroy, H.-C. Peng, X. Xia, *Angew. Chem.* **2017**, *129*, 60.
- [264] T. Ikeda, A. Xiong, T. Yoshinaga, K. Maeda, K. Domen, T. Teranishi, *J. Phys. Chem. C* **2013**, *117*, 2467.
- [265] H. Huang, Y. Wang, A. Ruditskiy, H.-C. Peng, X. Zhao, L. Zhang, J. Liu, Z. Ye, Y. Xia, *ACS Nano* **2014**, *8*, 7041.
- [266] Y. Xiong, J. Chen, B. Wiley, Y. Xia, S. Aloni, Y. Yin, *J. Am. Chem. Soc.* **2005**, *127*, 7332.
- [267] J. Chen, T. Herricks, M. Geissler, Y. Xia, *J. Am. Chem. Soc.* **2004**, *126*, 10854.
- [268] T. Herricks, J. Chen, Y. Xia, *Nano Lett.* **2004**, *4*, 2367.

- [269] S. Komarneni, D. Li, B. Newalkar, H. Katsuki, A. S. Bhalla, *Langmuir* **2002**, *18*, 5959.
- [270] Y. Sun, Y. Xia, *Adv. Mater.* **2002**, *14*, 833.
- [271] B. Wiley, T. Herricks, Y. Sun, Y. Xia, *Nano Lett.* **2004**, *4*, 1733.
- [272] A. R. Tao, S. Habas, P. Yang, *Small* **2008**, *4*, 310.
- [273] K. Pelzer, O. Vidoni, K. Philippot, B. Chaudret, V. Collière, *Adv. Funct. Mater.* **2003**, *13*, 118.
- [274] I. W. Kellaway, N. M. Najib, *Int. J. Pharm.* **1981**, *9*, 59.
- [275] K. Loza, M. Epple, *RSC Adv.* **2018**, *8*, 24386.
- [276] Z. Adamczyk, M. Oćwieja, H. Mrowiec, S. Walas, D. Lupa, *J. Colloid Interface Sci.* **2016**, *469*, 355.
- [277] C. Graf, D. Nordmeyer, C. Sengstock, S. Ahlberg, J. Diendorf, J. Raabe, M. Epple, M. Köller, J. Lademann, A. Vogt, F. Rancan, E. Rühl, *Langmuir* **2018**, *34*, 1506.
- [278] C.-M. Ho, C.-K. Wong, S. K.-W. Yau, C.-N. Lok, C.-M. Che, *Chem. Asian J.* **2011**, *6*, 2506.
- [279] R. D. Kent, P. J. Vikesland, *Environ. Sci. Technol.* **2012**, *46*, 6977.
- [280] J. Liu, R. H. Hurt, *Environ. Sci. Technol.* **2010**, *44*, 2169.
- [281] J. M. Zook, S. E. Long, D. Cleveland, C. L. A. Geronimo, R. I. MacCuspie, *Anal. Bioanal. Chem.* **2011**, *401*, 1993.
- [282] C. Gao, J. Goebel, Y. Yin, *J. Mater. Chem. C* **2013**, *1*, 3898.
- [283] P. Hou, H. Liu, J. Li, J. Yang, *Cryst. Eng. Comm* **2015**, *17*, 1826.

- [284] E. A. Larios-Rodríguez, F. F. Castellón-Barraza, D. J. Borbón-González, R. Herrera-Urbina, A. Posada-Amarillas, *Adv. Sci. Eng. Med.* **2013**, *5*, 665.
- [285] M. Homberger, U. Simon, *Philos. Trans. Royal Soc. A* **2010**, *368*, 1405.
- [286] S. K. Boda, J. Broda, F. Schiefer, J. Weber-Heynemann, M. Hoss, U. Simon, B. Basu, W. Jahnen-Dechent, *Small* **2015**, *11*, 3183.
- [287] A. Leifert, Y. Pan-Bartnek, U. Simon, W. Jahnen-Dechent, *Nanoscale* **2013**, *5*, 6224.
- [288] Y. Pan, S. Neuss, A. Leifert, M. Fischler, F. Wen, U. Simon, G. Schmid, W. Brandau, W. Jahnen-Dechent, *Small* **2007**, *3*, 1941.
- [289] C. C. Berry, J. M. de la Fuente, M. Mullin, S. W. Chu, A. S. Curtis, *IEEE Trans. Nanobiosci.* **2007**, *6*, 262.
- [290] I. Iavicoli, M. Farina, L. Fontana, D. Lucchetti, V. Leso, C. Fanali, V. Cufino, A. Boninsegna, K. Leopold, R. Schindl, D. Brucker, A. Sgambato, *Toxicol. In Vitro* **2017**, *42*, 191.
- [291] L. Fontana, V. Leso, A. Marinaccio, G. Cenacchi, V. Papa, K. Leopold, R. Schindl, B. Bocca, A. Alimonti, I. Iavicoli, *Nanotoxicology* **2015**, *9*, 843.
- [292] N. Neubauer, J. Palomaeki, P. Karisola, H. Alenius, G. Kasper, *Nanotoxicology* **2015**, *9*, 1059.
- [293] D. Mahl, C. Greulich, W. Meyer-Zaika, M. Köller, M. Epple, *J. Mater. Chem.* **2010**, *20*, 6176.
- [294] C. Petrarca, E. Clemente, L. Di Giampaolo, R. Mariani-Costantini, K. Leopold, R. Schindl, L. V. Lotti, R. Mangifesta, E. Sabbioni, Q. Niu, G. Bernardini, M. Di Gioacchino, *J. Immunol. Res.* **2014**, *2014*, 295092.